IDŐJÁRÁS

QUARTERLY JOURNAL
OF THE HUNGARIAN METEOROLOGICAL SERVICE

Special Issue: Severe weather events and their impact on society

Guest Editors: **Balázs Szintai** and **Tamás Weidinger**

CONTENTS

VOL. 119 * NO. 2 * APRIL – JUNE 2015

IDŐJÁRÁS

Quarterly Journal of the Hungarian Meteorological Service

Editorial Office: Kitaibel P.u. 1, H-1024 Budapest, Hungary
P.O. Box 38, H-1525 Budapest, Hungary
E-mail: journal.idojaras@met.hu
Fax: (36-1) 346-4669

Indexed and abstracted in Science Citation Index Expanded™ and Journal Citation Reports/Science Edition
Covered in the abstract and citation database SCOPUS®

Subscription by mail:
IDŐJÁRÁS, P.O. Box 38, H-1525 Budapest, Hungary
E-mail: journal.idojaras@met.hu

Editorial

Special Issue: Severe weather events and their impact on society

According to the latest reports of the Intergovernmental Panel on Climate Change (IPCC), it is expected that the occurrence of severe weather events like long heatwaves or strong thunderstorms will significantly increase by the end of the 21st century in Europe. Consequently, it is getting more and more important to study the underlying scientific basics and to develop such forecasting systems which are able to accurately predict these events. Noting the increasing relevance of this topic, the theme of the 39th Meteorological Scientific Days was chosen to be severe weather events and their impact on society. The Scientific Days were organized during autumn 2013 at the Hungarian Academy of Sciences by the Subcommittee for Atmospheric Dynamics and Synoptic Meteorology of the Meteorological Scientific Committee. The program consisted of 21 oral presentations, and as a new and successful initiative, a poster session was also organized with 7 posters (see at www.met.hu/omsz/rendezvenyek). The large number of presentations allowed to give an extensive overview on the topic of severe weather events and present several applications. Similarly to previous years, the opening presentation was a foreign invited speaker, who presented the nowcasting systems applied at European national meteorological services. This was followed by an overview talk about the evolution of nowcasting systems in Hungary. The next couple of presentations investigated severe weather events on large time and spatial scales. Furthermore, a presentation highlighted the actual challenges of hydrology. The following speakers presented the numerical modeling aspects of the forecasting of severe weather events. The first day was closed with three presentations showing interesting examples of research connected to severe precipitation events. The second day was devoted to the applications presenting different areas in society (e.g., aviation, defense, transportation) where severe weather could have a large impact, and accurate forecasting of such events is essential.

Similarly to previous years, the present special issue of IDŐJÁRÁS devoted to papers based on the presentations of the Meteorological Scientific Days. A high number of 11 papers were accepted, which well reflects the increasing interest in the topic of severe weather events from both scientific and application oriented communities. The organization of the papers follows the structure of the Scientific Days itself. The first two papers deal with severe weather events on large time and spatial scales, followed by two studies about the climatology cyclones and thunderstorms. Three papers are dedicated to the numerical modeling systems predicting severe weather events. The last four papers are dealing with applications like weather warnings at the Hungarian Defense Forces, forecasting of blowing snow, usage of unmanned meteorological aircrafts, and urban human comfort. It is important to note that due to the high number of papers, the last two presentations dealing with aviation and urban meteorology – are going to be included in the next issue of IDŐJÁRÁS.

Finally, we would like to thank the Editor-in-Chief of IDŐJÁRÁS for making it possible to publish the present special issue, and all the authors who contributed to the 39th Meteorological Scientific Days. Careful work of the Executive Editor of the journal by compiling the present issue is also appreciated.

Balázs Szintai and *Tamás Weidinger*
Guest Editors

IDŐJÁRÁS

Quarterly Journal of the Hungarian Meteorological Service
Vol. 119, No. 2, April–June, 2015, pp. 129–142

Projected changes of extreme precipitation using multi-model approach

Judit Bartholy, **Rita Pongrácz**, and **Anna Kis**

Department of Meteorology, Eötvös Loránd University,
Pázmány Péter sétány 1/A, H-1117 Budapest, Hungary

E-mail: bartholy@caesar.elte.hu, prita@nimbus.elte.hu,
kisanna@nimbus.elte.hu

(Manuscript received in final form October 6, 2014)

Abstract—Excessive precipitation may result in different environmental and socio-economical damages. In order to mitigate or avoid the potential losses associated to these, it is essential to provide estimations of precipitation tendencies for the future, which facilitate to build appropriate adaptation strategies in time. In this paper we used bias-corrected daily precipitation outputs of 11 regional climate model (RCM) simulations to determine the projected precipitation trends for the Carpathian Basin. According to the results of the analysis of precipitation indices, frequency of extreme precipitation will generally increase in the entire Central/Eastern European domain, except in summer, when decreasing trend is very likely in Hungary as well as in the southern regions.

Key-words: regional climate change, heavy precipitation, precipitation intensity, percentile values, climate index

1. Introduction

In the recent years, extreme precipitation events have become more frequent as well as more intense in many regions of Europe, e.g., in the western part of Central Europe since 1961 (*Kyselý*, 2009; *Seneviratne et al.*, 2012). This is especially valid for winter. In other seasons and other regions, including the

Carpathian Basin, the observed trends are not significant and inconsistent for the past (e.g., *Klein Tank* and *Können*, 2003; *Bartholy* and *Pongrácz*, 2005; 2007). In order to be prepared for the coming changes and make appropriate plans in various socio-economic sectors, it is essential to provide future estimates of mean precipitation trends and extreme events. Different sectors, different activities consider extreme precipitation very differently. Therefore, several types of extreme indices can be defined for describing these events (*Zhang et al.*, 2011). One of the most widely used types is based on exceeding various threshold values, which can be an absolute value (e.g., 10 mm, 20 mm, etc.) or a given (e.g., 90th, 95th, etc.) percentile of long climatological time series. Other more complex indices consider duration, intensity, and/or persistence of the events. Extreme indices usually focus on daily scale using daily precipitation totals. Despite the huge demand of sub-daily scale extreme analysis, there is a lack of such studies due to reliable data availability.

Climate model simulations for the future suggest that number of heavy precipitation days is likely to increase in the northern mid-latitudes in the 21st century, especially in winter (*IPCC*, 2012). Furthermore, in some regions more heavy precipitation days are likely to occur despite of the projected decrease in total precipitation amount. For instance, in Europe, more frequent extreme precipitation events are likely to occur in the coming decades (e.g., *Kyselý et al.*, 2011; 2012; *Rajczak et al.*, 2013). For Hungary, PRUDENCE (*Christensen et al.*, 2007) simulation results suggest that extreme precipitation events are projected to increase in winter, whereas a general decrease is estimated in summer (*Bartholy et al.*, 2008).

Intense precipitation may lead to a severe flood event, which is considered one of the major possible natural hazards on society. Specifically, in Central Europe, river flood risk and vulnerability are likely to have grown in many areas in the recent years (*Kundzewicz et al.*, 2005). As Working Group II of the Intergovernmental Panel on Climate Change (IPCC) pointed out in the Fifth Assessment Report (*IPCC*, 2014), river management is the main factor determining the flood trends of the past. Although the detected regional flood trends in Europe are inconsistent and statistically not significant for the past (*Renard et al.*, 2008, *Stahl et al.*, 2010), it is important to estimate the future change of precipitation, especially extremes, in order to develop appropriate river management strategies. According to the results of *Dankers* and *Feyen* (2008), extreme discharge levels are projected to occur in many European rivers.

In this paper, extreme precipitation is analyzed for Hungary using climate model simulations output. For this purpose, precipitation-related climate indices calculated from bias-corrected time series serve as main indicators for future climate change. First, the data and the applied indices are described. Results are discussed for indices based on (i) absolute value thresholds, (ii) percentile-based thresholds, and for intensity-based indices.

2. *Data and methods*

In order to estimate the future extreme precipitation trends, outputs from 11 regional climate models (RCMs) embedded in global climate models (GCMs) are analyzed taken into account the intermediate SRES A1B emission scenario (*Nakicenovic* and *Swart*, 2000). According to this scenario, the population is estimated to increase up to 8.7 billions and decline after the middle of the 21st century. The energy demand is assumed to be covered from both fossil fuels and renewable/nuclear energy sources. Thus, global mean CO_2 concentration level is estimated to reach 717 ppm by 2100. Simulation datasets are available with 25 km horizontal resolution on daily scale for 1951–2100 from the ENSEMBLES project (*van der Linden* and *Mitchell*, 2009). Due to the general underestimation of summer precipitation and overestimation of winter precipitation (*Pongrácz et al.*, 2011), raw data have to be bias-corrected prior to the detailed analysis. The applied correction (*Pongrácz et al.*, 2014) is based on a quantile matching technique (*Formayer* and *Haas*, 2010) for which E-OBS datasets (*Haylock et al.*, 2008) serve as reference for the 1951–2000 time period. The 25 km horizontal resolution gridded daily E-OBS data were created in the framework of the ENSEMBLES project by interpolating measured datasets of meteorological stations from all over Europe. For the area focused in this analysis, data from about 400 stations were used (note that the spatial coverage is not homogeneous).

After the correction, several precipitation-related climate indices are calculated. This paper focuses on excessive precipitation, whereas analysis of the lack of precipitation, i.e., drought-related indices can be found in *Pongrácz et al.* (2014). Among the indices connected to extreme precipitation (*Table 1*), two indices are defined by using different absolute threshold values (RR10, RR20), two indices indicate precipitation intensity (RX1, RX5) for different durations, and six indices are based on percentiles of daily precipitation amount (R90p, R95p, R99p, R90pGT, R95pGT, R99pGT). The grid cell values of all the 10 indices are calculated from the 11 bias-corrected RCM simulations for Central/Eastern Europe (covering the area of 43.625°–50.625°N, 13.875°–26.375°E) for the whole 1951–2100 simulation period. In this analysis, mean seasonal changes for the 2021–2050 and 2071–2100 periods are determined relative to the 1961–1990 reference period. Moreover, nine subregions are defined in the selected domain (Southeastern Czech Republic, Eastern Austria, Slovakia, Southwestern Ukraine, Slovenia, Hungary, Romania, Croatia, and Northern Serbia), for which the spatial average of annual and seasonal mean changes are calculated.

Table 1. Name, definition, and unit of the analyzed precipitation-related climate indices

Index	Definition	Unit
RR10	Number of heavy precipitation days ($R_{day} \geq 10$ mm)	day
RR20	Number of very heavy precipitation days ($R_{day} \geq 20$ mm)	day
RX1	Highest 1-day precipitation amount ($R_{max,1day}$)	mm
RX5	Highest 5-day precipitation amount ($R_{max,5day}$)	mm
R90p	The 90th percentile of daily precipitation time series	mm
R95p	The 95th percentile of daily precipitation time series	mm
R99p	The 99th percentile of daily precipitation time series	mm
R90pGT	Fraction of total precipitation above the base period's 90th percentile ($\sum(R_{2071-2100} > R90p_{1961-1990})/\sum R_{2071-2100}$)	%
R95pGT	Fraction of total precipitation above the base period's 95th percentile ($\sum(R_{2071-2100} > R95p_{1961-1990})/\sum R_{2071-2100}$)	%
R99pGT	Fraction of total precipitation above the base period's 99th percentile ($\sum(R_{2071-2100} > R99p_{1961-1990})/\sum R_{2071-2100}$)	%

3. Results and discussion

First, analysis of exceeding absolute daily precipitation threshold values is presented for the mid- and late-century compared to the reference period 1961–1990. Then, the projected changes of percentile-based indices are evaluated. Finally, intensity-type precipitation indices are analyzed.

3.1. Estimated future changes of precipitation indices using absolute threshold values

On a daily scale, 10 mm and 20 mm precipitation amounts are usually considered as heavy and very heavy precipitation days, respectively. Due to the different processes resulting in rainfall or snowfall, these days occur generally more often in summer than in winter, i.e., more precipitation occur from convective systems in the summer months. Two indices (RR10 and RR20) are analyzed in this paper and compared seasonally for the three selected time slices (1961–1990, 2021–2050, and 2071–2100). The average numbers of days are very different for the two indices, therefore, different scales and units are used in *Fig. 1*, i.e., RR10 and RR20 are shown as the mean frequency in 10 and 30 years, respectively. In July and August both indices are projected to decrease relative to the reference period 1961–1990, moreover, in May and June, RR10 is likely to decrease by the end of the 21st century. In all the other months, indices are projected to increase on average.

If we consider the estimated changes between the middle and late 21st century, the two indices differ in the three autumn months, namely, RR10 is projected to increase in September and October, whereas RR20 is likely to decrease in these two months. In November, the opposite is projected: RR10 tends to decrease and RR20 tends to increase.

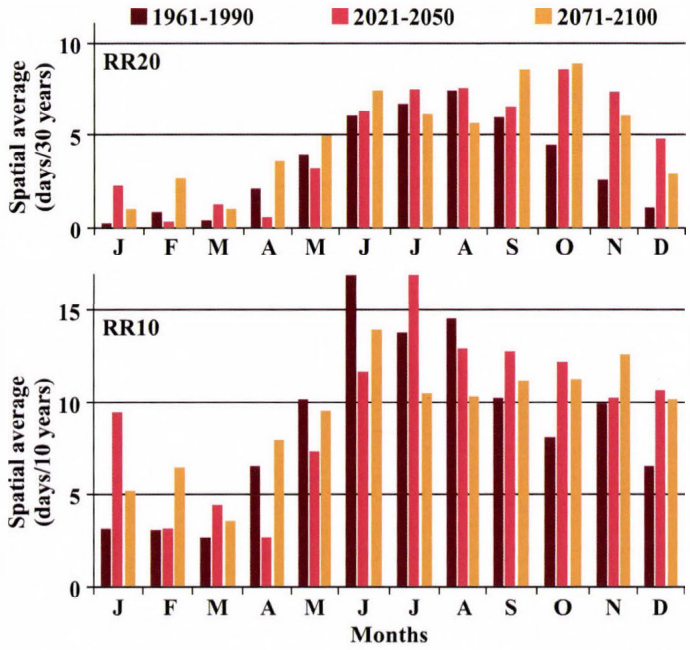

Fig. 1. Multi-model monthly average values of RR20 (upper panel) and RR10 (lower panel) for Hungary in 1961–1990, 2021–2050, and 2071–2100. Original units from Table 1 are modified to show simulated occurrence frequencies in longer time periods, 30 and 10 years, respectively.

Higher values are projected for 2021–2050 relative to 1961–1990 for both RR10 and RR20 in January, March, July, and December (which implies dominantly the winter half-year). This is followed by the decrease of average index values in the second half of the century. On the contrary, in April and May, both RR10 and RR20 are projected to decrease first, and then, increase by the last few decades of the century (in case of RR10, the estimated mean changes are similar also for June).

3.2. *Estimated future changes of percentile-based precipitation indices*

From the aspect of excessive precipitation, this paper focuses on large percentiles, i.e., the 90th, 95th, and 99th percentile values themselves, and the precipitation totals above these percentile thresholds relative to the entire precipitation totals. The seasonal mean changes of these percentile-based precipitation indices by the end of the 21st century compared to the reference period are summarized in *Fig. 2* for Hungary.

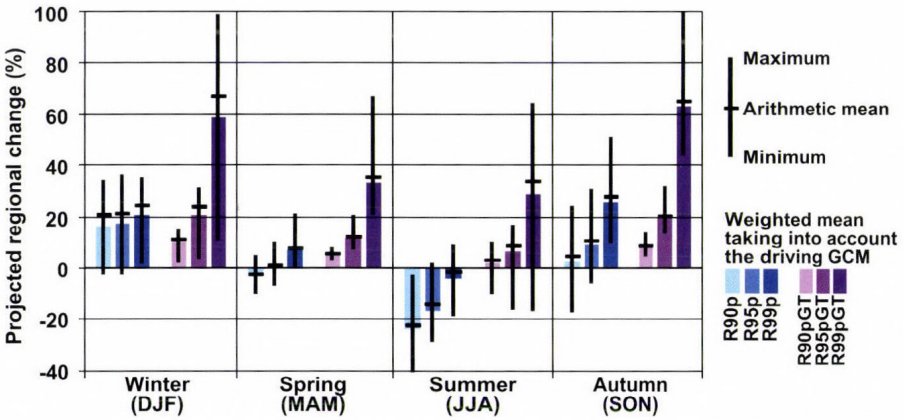

Fig. 2. Projected seasonal mean changes (%) of the percentile-based precipitation indices for Hungary by 2071–2100 relative to the reference period 1961–1990. The thicker bars indicate the average changes on the basis of RCM projections using equal weights to the driving GCMs. The thinner bars indicate the total ranges of RCM projections.

The fractions of the extreme daily precipitation totals from the entire precipitation totals are dominantly projected to increase, only two RCM (HIRHAM/ARPEGE and HadRM/HadCM3) simulations estimate decrease of summer index values. RCM simulations suggest quite similar changes of R90pGT, the entire multi-model uncertainty is less than 15%. Estimated spatial average changes of R95pGT are less similar compared to those of R90pGT, however, the uncertainty due to the different RCM use does not exceed 33%. The largest multi-model uncertainty in relative changes is projected in case of R99pGT exceeding 45% in all the seasons, moreover, it is 88.5% in winter. Similarly to the uncertainty ranges of multi-model estimations, the projected increases of the fractions of the higher extreme daily precipitation totals are also larger than those of the smaller extremes, i.e., estimated seasonal changes of R90pGT (2–10% on average) are smaller than changes of R95pGT (6–21% on average), which are considerably smaller than changes of R99pGT (33–63% on average). For all the

three indices, the largest increase is projected generally in winter and autumn, and the smallest increases are likely to occur in summer and spring.

The spatial structures of the projected seasonal mean changes for the entire domain are shown in *Fig. 3*. The composite maps clearly suggest that the estimated increases are larger in the northern part of the domain than in Hungary, and generally smaller in the southern regions. In summer, overall slight decreases are projected for all the three indices in the southwestern regions. Within Hungary, the projected average changes of all the three indices are generally larger in the eastern lowlands than in the western Transdanubian part of the country. However, in spring, the smallest increases are estimated in the middle subregions of the country.

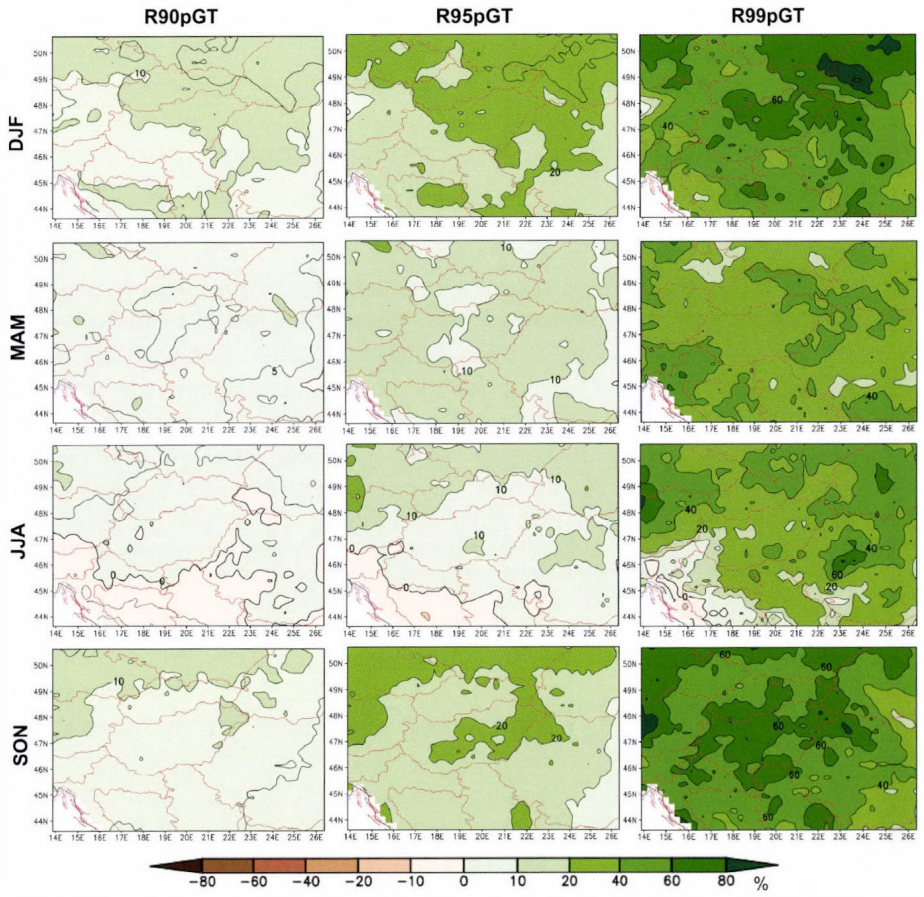

Fig. 3. Projected multi-model mean changes (%) of the fraction of total precipitation greater than the 90th, 95th, and 99th percentiles of daily precipitation in the four seasons (from top to bottom: winter, spring, summer, autumn) for 2071–2100 relative to the reference period 1961–1990.

The entire ranges of the estimated changes of high percentile values of daily precipitation are relatively large, mostly exceeding 25%, except in spring when they are 15–20% (*Fig. 2*). These large ranges suggest quite large uncertainty within the multi-model ensemble, when even the signs of the projected trends can be different (i.e., both increasing and decreasing). However, in winter, all the three percentile values in Hungary are very likely to increase, the estimated multi-model mean changes are 21%, 21%, and 24% for R90p, R95p, and R99p, respectively. In autumn, the higher the extreme percentile, the larger the projected increase. For instance, R99p is projected to increase by about 26% by the end of the 21st century relative to the reference period. In summer, the multi-model ensemble projects clear decrease of R90p (by 23% on average) in Hungary, mainly decrease of R95p (by 15% on average), whereas higher uncertainty is associated to the estimation of changes in R99p: the majority of the RCMs project slight increase (not exceeding 9%), nevertheless, some of the RCMs project relatively high decrease (10–19%), resulting in an overall slight decrease of R99p. Finally, in spring, slight changes are projected in general, which do not exceed 10%. However, note that R99p is estimated to clearly increase (by 7% on average), since all the RCMs project positive changes by 2071–2100 compared to 1961–1990.

The spatial structures of the projected seasonal mean changes are shown in *Fig. 4*. The estimated summer decreases show clear zonal differences, the largest decrease in percentile values of daily precipitation exceeds 40% and 20% in the southern part of the entire domain in case of R90p and R95p, respectively. The summer values of R99p tend to increase in the northern (and especially the northwestern) part of the domain, and decreases of R99p values are projected only in the southern part (the largest average decreases exceed 10%). Within Hungary, the quasi-zonal structure can be recognized as well, as in the entire domain. All the three indices are projected to decrease in summer in the whole country, the largest decreases are likely to occur along the southern border of Hungary. In winter, increases of the indices are estimated in the entire domain, the largest changes are likely to occur in the northern part, especially in the mountainous subregions. Percentile values in the northern part of Hungary are also projected to increase more than in the southern subregions. R99p – representing the very high extreme daily precipitation – is projected to increase in the entire domain also in spring and autumn, however, the projected seasonal average changes are generally smaller than in winter. In the equinox seasons, R90p values are projected to increase in the northern part and decrease in the southern part of the domain, whereas R95p is estimated to increase dominantly (except in small regions in the southern part).

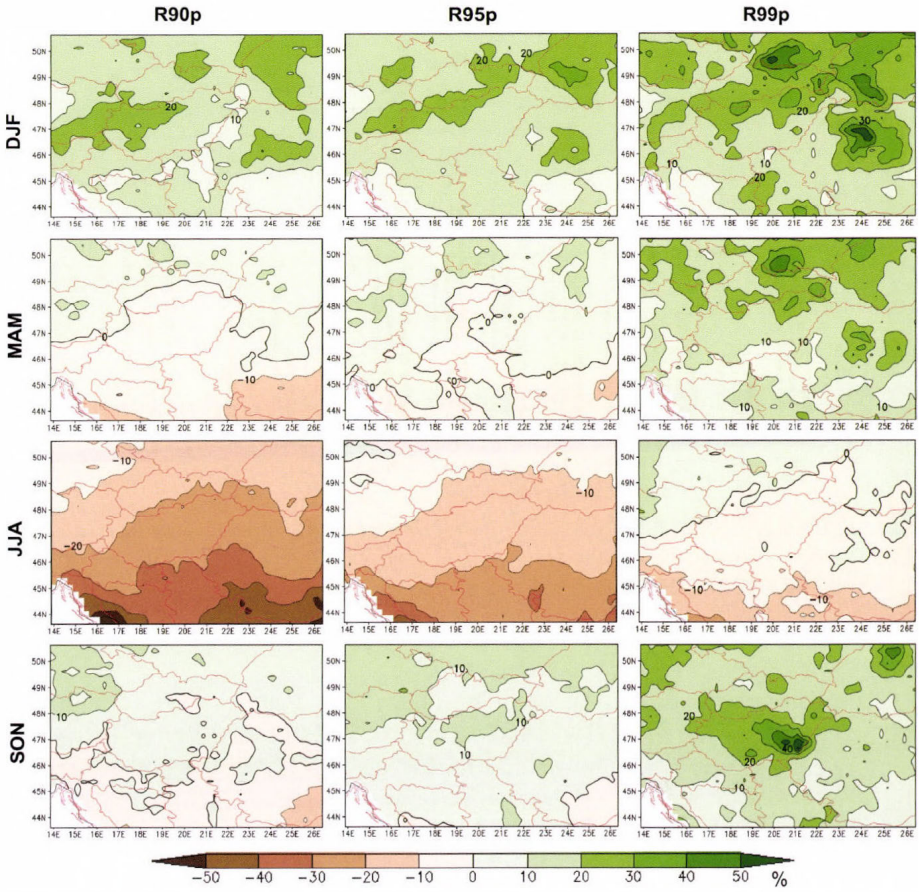

Fig. 4. Projected multi-model mean changes (%) of the 90th, 95th, and 99th percentiles of daily precipitation in the four seasons (from top to bottom: winter, spring, summer, autumn) for 2071–2100 relative to the reference period 1961–1990.

3.3. Estimated future trends of precipitation intensity indices

The precipitation intensity is represented in this paper by the highest precipitation totals during 1 day and 5 days (i.e., RX1 and RX5, respectively). The summary of multi-model monthly estimations of spatial average for Hungary is shown in *Fig. 5* for RX5 (similar changes are projected for RX1). These results clearly suggest that the maximum 5-day precipitation totals are projected to increase in the 21st century in all months, except August. The inter-model variability of the estimated RX5 values is much higher in July, August, and September than in the rest of the year (the entire RX5 ranges of RCM-estimations for the winter months do not exceed 20 mm). In general, the inter-

model variability of RX5 is projected to increase in the 21st century compared to the reference period.

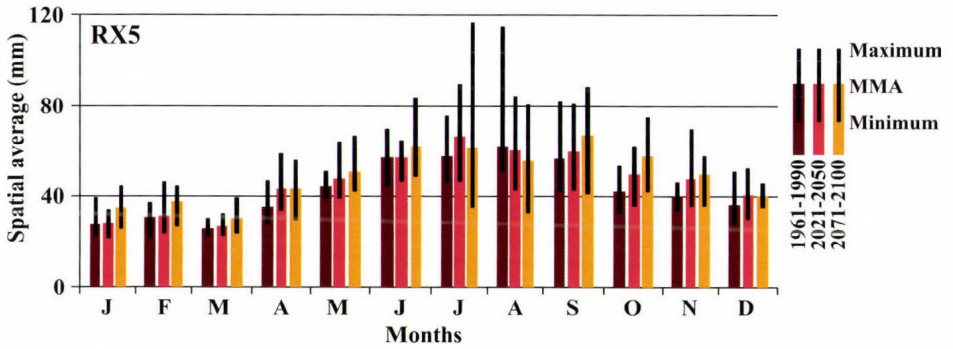

Fig. 5. Comparison of estimated monthly average values of RX5 for Hungary in 1961–1990, 2021–2050, and 2071–2100 using 11 RCM simulation outputs. MMA indicates the multi-model average.

Composite maps of the projected seasonal mean changes of RX1 show the spatial structures of the estimated changes by 2071–2100 relative to 1961–1990 (*Fig. 6*). Increasing trends are projected for all seasons, except in summer in the southern part of the domain, where the estimated negative changes on average imply decreasing trends for the future. The estimated spatial average changes of RX1 for the whole domain are 20%, 11%, 2%, and 23% in winter, spring, summer, and autumn, respectively. In summer, a zonal structure similarly to the changes of the summer percentile values can be recognized: in the northern part of the selected domain RX1 is projected to increase, whereas in the southern subregions it is projected to decrease. Specifically, the estimated multi-model average changes by the late 21st century in summer are +11% and –8% in the southeastern Czech Republic and in Croatia, respectively. In Hungary, the largest increase is estimated in autumn (+23%), when projected changes calculated from 9 individual RCM simulations (out of 11 total experiments studied in this paper) are statistically significant.

Since the largest increases are likely to occur in winter and autumn, more detailed temporal analysis is presented for these two seasons in *Fig. 7* showing the average decadal values of RX1 from the 1950s to the 2090s for Hungary. The ensemble of the individual RCM simulations clearly suggest increasing trends in the multi-model mean as well as in the 1st, 2nd, and 3rd maximum and minimum decadal values of RX1. All these trend coefficients are statistically significant at 0.05 level. The estimated overall change of the multi-model mean between the 1950s and 2090s is 30% in winter, and 33% in autumn, when the

decadal average of the highest daily precipitation amount is very likely to exceed 24 mm in the 2090s (and it was about 18 mm in the 1950s according to the RCM simulations).

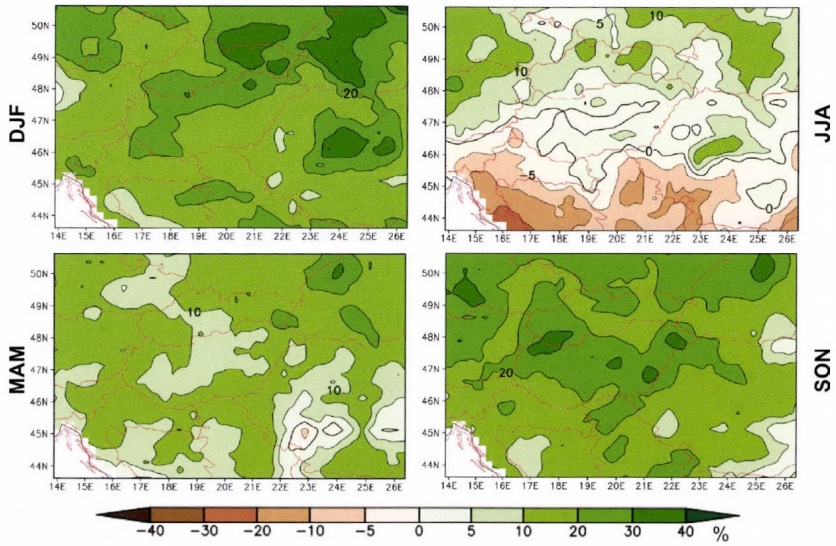

Fig. 6. Composite maps of the projected seasonal mean changes (%) of RX1 by 2071–2100 relative to the reference period 1961–1990. Average changes are calculated on the basis of RCM projections using equal weights to the driving GCMs.

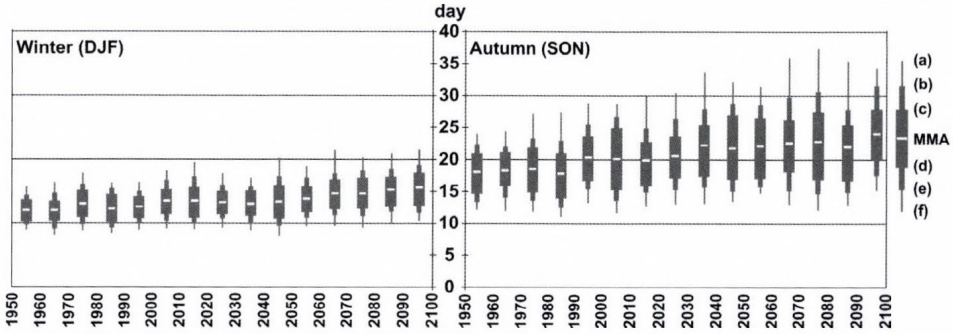

Fig. 7. Average decadal values of RX1 for Hungary in winter (left panel) and autumn (right panel), 1951–2100. MMA indicates the multi-model average. (a) and (f) indicate the maximum and minimum RX1 values, respectively. (b) and (e) indicate the second largest and smallest RX1 values, respectively. (c) and (d) indicate the third largest and smallest RX1 values, respectively.

4. Conclusions

Estimated changes of extreme precipitation conditions in Central/Eastern Europe (with special focus on Hungary) have been analyzed in this paper using bias-corrected daily precipitation outputs of 11 RCM simulations from the ENSEMBLES project considering the intermediate A1B scenario. Based on the results, the following conclusions can be drawn for the late 21st century relative to the reference period.

(i) Excessive precipitation (R90p, R95p, R99p) is mostly estimated to increase, except in summer, when decrease is projected both in Hungary and in the southern regions of the entire domain.

(ii) The fraction of the excessive precipitation relative to the total amount (R90pGT, R95pGT, R99pGT) is projected to increase in general. Only a few RCMs estimate slight decrease in summer for Hungary, and the multi-model average change in summer is slightly negative in the southwestern part of the entire domain.

(iii) Frequency of heavy precipitation (RR10, RR20) is projected to decrease in summer, and increase in the rest of the year.

(iv) Precipitation intensity (RX1, RX5) is likely to increase overall. However, in summer decreasing trend is estimated in the southern parts of the selected domain.

Overall, remarkable increasing trends of precipitation extremes are projected for Central/Eastern Europe by 2071–2100 relative to the 1961–1990 reference period. These changes may result in more frequent and more severe river flooding, therefore, in order to mitigate the vulnerability of the region, it is highly suggested to develop appropriate flood protection and management strategies in time considering these estimated changes.

Acknowledgements–Research leading to this paper has been supported by the following sources: the Hungarian Scientific Research Fund under grants K-78125 and K109109, the European Union and the European Social Fund through project FuturICT.hu (TÁMOP-4.2.2.C-11/1/KONV-2012-0013), and the AGRÁRKLIMA2 project (VKSZ_12-1-2013-0001). The ENSEMBLES data used in this work was funded by the EU FP6 Integrated Project ENSEMBLES (Contract number 505539), whose support is gratefully acknowledged. Furthermore, we acknowledge the E-OBS dataset from the EU-FP6 project ENSEMBLES (http://ensembles-eu.metoffice.com), and the data providers in the ECA&D project (http://eca.knmi.nl).

References

Bartholy, J. and *Pongrácz, R.*, 2005: Tendencies of extreme climate indices based on daily precipitation in the Carpathian Basin for the 20th century. *Időjárás 109*, 1–20.

Bartholy, J. and *Pongrácz, R.*, 2007: Regional analysis of extreme temperature and precipitation indices for the Carpathian Basin from 1946 to 2001. *Global Planet. Change 57*, 83–95.

Bartholy, J., Pongrácz, R., Gelybó, Gy., and *Szabó, P.*, 2008: Analysis of expected climate change in the Carpathian Basin using the PRUDENCE results. *Időjárás 112*, 249–264.

Christensen, J.H., Carter, T.R., Rummukainen, M., and *Amanatidis, G.*, 2007: Evaluating the performance and utility of regional climate models: The PRUDENCE project. *Climatic Change 81*, 1–6.

Dankers, R. and *Feyen, L.*, 2008: Climate change impact on flood hazard in Europe: An assessment based on high resolution climate simulations. *J. Geophys. Res. 113*, D19105, 17.

Formayer, H. and *Haas, P.*, 2010: Correction of RegCM3 model output data using a rank matching approach applied on various meteorological parameters. Deliverable D3.2 RCM output localization methods (BOKU-contribution of the FP 6 CECILIA project). http://www.cecilia-eu.org/

Haylock, M.R., Hofstra, N., Klein Tank, A.M.G., Klok, E.J., Jones, P.D., and *New, M.*, 2008: A European daily high-resolution gridded dataset of surface temperature and precipitation for 1950–2006. *J. Geophys. Res (Atmospheres) 113*, D20119,

IPCC, 2012: Managing the Risks of Extreme Events and Disasters to Advance Climate Change Adaptation. A Special Report of Working Groups I and II of the Intergovernmental Panel on Climate Change. (Eds. *Field, C. B., Barros, V., Stocker, T. F., Dahe, Q., Dokken, D. J., Plattner, G-K., Ebi, K. L., Allen, S. K., Mastandrea, M. D., Tignor, M., Mach, K. J., Midgley, P. M.*), Cambridge University Press, Cambridge, UK and New York, NY, USA,

IPCC, 2014: Climate Change 2014: Impacts, Adaptation, and Vulnerability. Part A: Global and Sectoral Aspects. Contribution of Working Group II to the Fifth Assessment Report of the Intergovernmental Panel on Climate Change (Eds. *Field, C.B., Barros, V.R., Dokken, D.J., Mach, K.J., Mastrandrea, M.D., Bilir, T.E., Chatterjee, M., Ebi, K.L., Estrada, Y.O., Genova, R.C., Girma, B., Kissel, E.S., Levy, A.N., MacCracken, S., Mastrandrea, P.R., White, L.L.*) Cambridge University Press, Cambridge, United Kingdom and New York, NY, USA,

Klein Tank, A.M.G. and *Können, G.P.*, 2003: Trends in indices of daily temperature and precipitation extremes in Europe, 1946-1999. *J. Climate 16*, 3665–3680.

Kundzewicz, Z.W., Ulbrich, U., Brücher, T., Graczyk, D., Krüger, A., Leckebusch, G.C., Menzel, L., Pinskwar, I., Radziejewski, M., and *Szwed, M.*, 2005: Summer floods in Central Europe – Climate change track? *Nat. Hazards 36*, 165–189.

Kyselý, J., 2009: Trends in heavy precipitation in the Czech Republic over 1961–2005. *Int. J. Climatol. 29*, 1745–1758.

Kyselý, J., Gaál, L., Beranová, R., and *Plavcová, E.*, 2011: Climate change scenarios of precipitation extremes in Central Europe from ENSEMBLES regional climate models. *Theor. Appl. Climatol. 104*, 529–542.

Kyselý, J., Santiago, B., Beranová, R., Gaál, L., and *Lopez-Moreno, H.I.*, 2012: Different patterns of climate change scenarios for short-term and multi-day precipitation extremes in the Mediterranean. *Global Planet. Change 98–99*, 63–72.

van der Linden, P. and *Mitchell, J.F.B.*, (Eds.), 2009: ENSEMBLES: Climate Change and Its Impacts: Summary of research and results from the ENSEMBLES project. UK Met Office Hadley Centre, Exeter, UK.

Nakicenovic, N. and *Swart, R.*, (Eds.) 2000: Emissions Scenarios. A special report of IPCC Working Group III. Cambridge University Press, UK, 570p.

Pongrácz, R., Bartholy, J., and *Miklós, E.*, 2011: Analysis of projected climate change for Hungary using ENSEMBLES simulations. *Appl. Ecol. Environ. Res. 9*, 387–398.

Pongrácz, R., Bartholy, J., and *Kis, A.*, 2014: Estimation of future precipitation conditions for Hungary with special focus on dry periods. *Időjárás 118*, 305–321.

Rajczak, J., Pall, P., and *Schar, C.*, 2013: Projections of extreme precipitation events in regional climate simulations for Europe and the Alpine Region. *J. Geophys. Res. Atmos. 118*, 3610–3626.

Renard, B., Lang, M., Bois, P., Dupeyrat, A., Mestre, O., Niel, H., Sauquet, E., Prudhomme, C., Parey, S., Paquet, E., Neppel, L., and *Gailhard, J.*, 2008: Regional methods for trend detection: Assessing field significance and regional consistency. *Water Resour. Res. 44*, W08419.

Seneviratne, S.I., Nicholls, N., Easterling, D., Goodess, C.M., Kanae, S., Kossin, J., Luo, Y., Marengo, J., McInnes, K., Rahimi, M., Reichstein, M., Sorteberg, A., Vera, C., and *Zhang, X.*, 2012: Changes in climate extremes and their impacts on the natural physical environment. In: (Eds. *Field, C.B., Barros, V., Stocker, T.F., Dahe, Q., Dokken, D.J., Plattner, G-K., Ebi, K.L., Allen,*

S.K., Mastandrea, M.D., Tignor, M., Mach, K.J., Midgley, P.M.) Managing the Risks of Extreme Events and Disasters to Advance Climate Change Adaptation A Special Report of Working Groups I and II of the Intergovernmental Panel on Climate Change (IPCC). Cambridge University Press, Cambridge, UK, and New York, NY, USA, 109–230.

Stahl, K., Hisdal, H., Hannaford, J., Tallaksen, L.M., van Lanen, H.A.J., Sauquet, E., Demuth, S., Fendekova, M., and *Jódar, J.,* 2010: Streamflow trends in Europe: Evidence from a dataset of nearnatural catchments. *Hydrol. Earth Syst. Sci. 14*, 2367–2382.

Zhang, X., Alexander, L., Hegerl, G.C., Jones, P., Klein Tank, A., Peterson, T.C., Trewin, B., and *Zwiers, F.W.,* 2011: Indices for monitoring changes in extremes based on daily temperature and precipitation data. *Wiley Interdis. Rev. Clim. Change 2*, 851–870.

IDŐJÁRÁS

Quarterly Journal of the Hungarian Meteorological Service
Vol. 119, No. 2, April–June, 2015, pp. 143–158

Assessment of heat-related mortality in Budapest from 2000 to 2010 by different indicators

János Bobvos*, Balázs Fazekas, and **Anna Páldy**

National Institute of Environmental Health, Budapest, Hungary
Albert Flórián u. 2-6, H-1097 Budapest, Hungary
E-mails: bobvos.janos@oki.antsz.hu;
fazekasbalazshu@gmail.com; paldy.anna@oki.antsz.hu

**Corresponding author*

(Manuscript received in final form April 17, 2014)

Abstract—The increase of the temperature and frequency of extreme weather events are predicted as the most visible effects of expected climate change. The number of publications dealing with heat-related mortality has been increasing for the last 20 years. They concluded that no formal definition of a heat wave existed, so the definition of such events would be very important. A more consistent methodology for calculating excess mortality would enhance comparisons between studies.

It is a growing demand to elaborate and use indicators which can provide comparable information of the impact of heat on mortality in different geographic and climatic regions. Therefore, the World Health Organization developed a set of climate change related health indicators in the CEHAPIS (Climate, Environment and Health Action Plan Information System) project. The authors aimed to assess heat related excess mortality by using this methodology, in addition to indicators used in the Hungarian Heat Alert System, in order to provide a recommendation for a more precise detection of health effects in Budapest.

In this paper, the heat wave related daily excess mortality is analyzed for the summer periods of 2000–2010 in Budapest. Mortality is characterized by the daily total mortality and that of the age group 65 years and over. Meteorological variables of the Pestszentlőrinc station, regarded as an urban background meteorological station, were used. Daily temperature was characterized by four indicators: mean and maximum daily temperatures, and mean and maximum daily apparent temperatures. The impact on mortality was compared in relation to the different temperature indicators and threshold values. A method was developed to define the optimal threshold range where the excess mortality could be identified effectively.

The recommended method is capable to detect the changes of temperature and to assess the impact of heat waves on daily mortality. The results are in accordance with previous studies. Concerning the indicators, the application of daily mean temperature values seems to be optimal for Budapest. Further analyses are required to answer the question to what extent the Budapest findings can be used in other cities.

Key-words: heat indicators, heat-related mortality, heat-health warning system, climate change, health effects of climate change

1. Introduction

The number of publications dealing with heat related mortality has been increasing for the last 20 years. These studies have been reviewed from different points of view. In a review article, *Basu* (2009) analyzed the epidemiological studies dealing with the association of ambient temperature and mortality published in the period of 2001–2008. The majority of the studies used time series analysis or case-crossover methods and proved the impact of heat on mortality. Several studies identified cause- or age-specific vulnerable subgroups. In their critical review, *Hajat* and *Kosatsky* (2010) identified the comparable multicenter studies in order to explore the heterogeneity of the effects. Heat-related mortality could be detected in the majority of cities, the older age groups were more vulnerable, and the bigger heat effect was associated with higher population density. A higher threshold value was found in cities with higher summer temperatures.

The majority of studies call attention to the negative impacts of predicted climate change. According to the latest report of IPCC (Intergovernmental Panel on Climate Change, AR5 Fifth Assessment Report), the global mean surface temperature change for the period 2016–2035 relative to 1986–2005 will likely be in the range of 0.3 °C to 0.7 °C. The increase of global mean surface temperatures for 2081–2100 relative to 1986–2005 is projected to likely be in the ranges 0.3 °C to 4.8 °C (*IPCC,* 2013). A greater likelihood of injury, disease, and death due to more intense heat waves and fires is expected (*IPCC,* 2014). In his critical review, *Gosling et al.* (2009a) examined present temperature-mortality relationships and discussed climate change issues. He concluded that no formal definition of a heat wave existed, so the definition of such events would be very important. A more consistent methodology for calculating excess mortality would enhance comparisons between studies. There is evidence that climate change will affect temperature-related mortality heterogeneously, so there is a need for inter-regional comparisons that account for changes in the mean and variance of temperature.

Several studies analyzed the Budapest data as well. *Paldy et al.* (2005) investigated the effect of weather on daily mortality in Budapest, 1970–2000. *Hajat et al.* (2006) and *Gosling et al.* (2007) analyzed the same period by different methods. The data from the nineties were evaluated by *Ishigami et al.* (2008) and *Baccini et al.* (2008); a cause- and age-specific analysis was carried out by *D'Ippoliti et al.* (2010). Besides the Budapest data, a comparison of heat related mortality was carried out between the urban and rural populations in Hungary (*Bobvos* and *Paldy,* 2009). The excess mortality due to the strongest heat wave ever recorded in 2007 was analyzed at regional (*Paldy* and *Bobvos,* 2009) and small area levels (*Paldy et al.,* 2011). The predicted heat related excess mortality due to climate change was assessed by *Gosling et al.* (2009b), *Baccini et al.* (2011), and *Bobvos et al.* (2011) using a regional climate model.

Based on the studies, the proven impact of heat on mortality is a great burden on society. In order to decrease the negative effects, heat-health warning systems have been developed by public health services all around the world. These systems are based on meteorological forecasts and include different measures during warnings. *Kovats* and *Ebi* (2006) reviewed the public health aspects of heat waves and evaluated the relative effectiveness of public health responses. *Kovats* and *Hajat* (2008) emphasize the important differences in vulnerability existing between populations, depending on climate, culture, infrastructure (housing), and other factors. Based on the forecasts of the Hungarian Meteorological Service, the Hungarian Heat Alert System was introduced in Hungary in 2005. The system has three levels: a 1st warning, a 2nd alert, and a 3rd alarm level. The threshold temperature of the alert is 25 °C daily mean temperature. A heat wave is defined as three or more consecutive days with temperatures above this threshold. During the heat waves, the health care services and the local authorities launch previously prepared measures.

The above cited studies used a great variety of heat-related indices. It is a growing demand to develop and use indicators which can provide comparable information of the impact of heat on mortality in different geographic and climatic regions. Therefore, the WHO – in collaboration with WHO Member States – developed a set of climate change related health indicators (categorized into exposure, effect, and action) within the frame of the CEHAPIS project (*WHO*, 2011). This project recommends using two types of temperature indicators for heat exposure. The authors aimed to assess heat-related excess mortality by using the CEHAPIS methodology in addition to indicators used in the Hungarian Heat Alert System in order to provide a recommendation for a more precise detection of the health effects in Budapest.

2. Data and methods

In this paper, the heat wave-related daily excess mortality was analyzed for the summer period (May 16–Sept 15) of 2000–2010 for Budapest. Daily mortality data were gained from the Central Statistical Office of 1995–2010 for Budapest. All natural cause mortality (International Classification of Diseases codes ICD-9: 1–799) was characterized by the daily total mortality (M 0-X) and that of the age group 65 years and above (M 65+). Meteorological variables of the Pestszentlőrinc measuring station were retrieved from the Global Surface Summary of the Day Data (*GSOD,* 2010) archived in the National Climatic Data Centre (NCDC) at National Oceanic and Atmospheric Administration (NOAA) for 1990–2010. The Pestszentlőrinc monitoring station was regarded as an urban background meteorological station of Budapest. Daily temperature was characterized by four indicators: mean (T) and maximum daily temperatures

(Tx), and mean (AT) and maximum (ATx) daily apparent temperatures in °C. Apparent mean and maximum temperatures (*Kalkstein* and *Valimont,* 1986) were used as indices of thermal discomfort based on air temperature (T) and dew point temperature (T_{dp}) according to the following formula:

$$AT = -2.653 + 0.994(T) + 0.0153\left(T_{dp}\right)^2. \quad (1)$$

To follow the changes in the temperature, a 10-year fixed reference period of 1990–1999 was chosen. The hot days were identified by the 90th percentile of the frequency distribution of temperature indicators, where the daily mean temperature value was 25 °C, being a threshold of the Hungarian Heat Alert System. A heat wave was defined as three or more consecutive days with temperatures above this threshold.

After the initial description of the data, linear trend analyses were carried out to detect the changes in time. An assessment was done to compare the number of heat waves identified by the different temperature indicators in relation to the threshold. The number of heat waves and the number of days of heat waves corresponding to the 90th percentile threshold were defined by year, respectively for the whole period.

The effect of heat waves on daily mortality – absolute excess mortality (EM, in case number) – was defined as the difference of the mortality during heat waves (observed mortality: M_o) and the expected mortality (M_e) computed form the daily mortality of the previous five years (reference periods of mortality) excluding the daily mortality of days of heat waves in the given years:

$$EM = \sum(M_0 - M_e). \quad (2)$$

The relative excess mortality was also computed in a similar way, defining the percent increase of mortality during the heat waves of a given summer period. The mean relative excess mortality ($EM\%$, in percent) of the heat wave days (L) of a summer period can be computed by the following formula:

$$EM\% = 100\sum(M_0 - M_e)L^{-1}. \quad (3)$$

To characterize the whole period, the sum and mean of excess mortality due to heat wave days were calculated above different percentiles in case of each indicator. To define the optimal threshold ranges, the product of the two data was used.

3. Results

3.1. Characteristics of mortality data and temperature indicators

Mortality data of the investigated period are shown in *Table 1*. The summer mean daily mortality of the whole period was 60.8 of the total population and 44.7 of the age group 65 years and over. Maximum daily mortalities were recorded in both age groups in 2007. The standard deviation (SD) was also the highest in that year. Total mortality showed a significant decreasing tendency by 0.33 cases per year in the total population and by 0.21 cases in the older age group.

Table 1. Yearly descriptive statistics of daily mortality of the total population and age group 65 and over years in the summer (cases), periods of 2000–2010 in Budapest

	2000	2001	2002	2003	2004	2005	2006	2007	2008	2009	2010	mean
M 0-X min	43	46	38	38	40	39	36	35	35	39	36	38.6
M 0-X mean	62.9	62.9	61.3	58.8	61.3	60.8	62.6	61.2	58.2	57.5	60.8	60.8
M 0-X max	106	93	97	89	83	93	99	113	80	82	107	94.7
M 0-X SD	10.5	8.5	10.0	9.7	9.0	9.2	10.9	12.7	9.4	7.7	10.7	9.8
M 65+ min	29	33	28	26	28	29	25	22	22	26	25	26.6
M 65+ mean	46.1	46.7	45.2	43.1	44.9	44.4	45.1	44.9	42.3	42.7	45.8	44.7
M 65+ max	77	72	77	67	65	68	77	95	61	64	78	72.8
M 65+ SD	8.6	7.5	8.4	8.1	6.9	7.3	8.3	10.8	7.2	6.6	8.9	8.0

Table 2 contains the temperature data of the period. The mean of the daily mean temperatures were between 20 °C and 21 °C, the mean of the maximum daily temperatures was around 25–26 °C. Based on the daily mean temperature, the hottest year was 2003, while the daily maximum value was the highest in 2007, when the daily mean temperature was over 32 °C and the daily maximum was over 40 °C. The strongest heat wave was recorded in 2007, when several new record temperature values were measured.

3.2. Associations between the threshold values of temperature indicators and the number of defined heat wave days.

Fig 1 shows the values of the four temperature indicators in relation to different percentiles (p%) of the reference period – between 1990 and 1999 – of the study.

The shapes of the curves of the corresponding indicator pairs were similar in the range of p50–p80. The values of apparent temperature were lower in the cooler periods; the difference reached 2 °C in relation to the values of simple temperature indicators. The threshold values of the apparent temperature were somewhat greater, by 0.2–0.3 °C, in the hottest range. The value of the 90th percentile corresponded to the threshold temperature of the Hungarian Heat Alert System (mean daily temperature, T=25 °C), the exact threshold values were T=25.1 °C, AT=25.5°C, Tx=32.8 °C, and ATx=32.0°C.

Table 2. Yearly descriptive statistics of temperature indicators (°C) in the summer, periods of 2000–2010 in Budapest

	2000	**2001**	**2002**	**2003**	**2004**	**2005**	**2006**	**2007**	**2008**	**2009**	**2010**	**mean**
T min	11.8	10.4	12.9	13.2	10.7	9.9	11.2	9.3	11.7	10.1	8.8	10.9
T mean	20.8	20.2	21.5	22.3	19.7	20.2	20.4	21.7	21.0	21.1	20.0	20.8
T max	29.6	28.8	28.7	29.5	28.2	28.6	28.5	32.3	27.1	27.7	28.7	28.9
Tx min	14.7	14.5	16.1	16.1	14.0	11.7	13.1	11.1	14.6	12.7	10.1	13.5
Tx mean	26.9	25.6	27.0	28.5	25.4	25.2	26.0	27.8	27.0	26.9	24.9	26.5
Tx max	38.0	36.0	35.4	38.3	34.4	35.2	35.9	40.6	36.1	35.0	35.2	36.4
AT min	10.3	8.4	10.7	10.6	8.0	8.0	9.6	7.5	9.1	8.3	6.6	8.8
AT mean	19.8	19.7	21.4	21.8	19.0	20.0	20.5	21.3	20.6	20.4	20.5	20.5
AT max	29.9	30.0	29.1	28.9	28.6	31.5	31.8	32.6	28.4	29.1	31.9	30.2
ATx min	13.2	12.7	13.9	15.2	11.3	10.3	11.5	9.3	12.0	10.9	7.9	11.6
ATx mean	25.9	25.1	26.9	27.9	24.7	25.1	26.1	27.4	26.5	26.2	25.4	26.1
ATx max	37.0	37.2	36.8	37.7	34.8	37.6	37.5	40.7	37.4	35.7	38.3	37.3

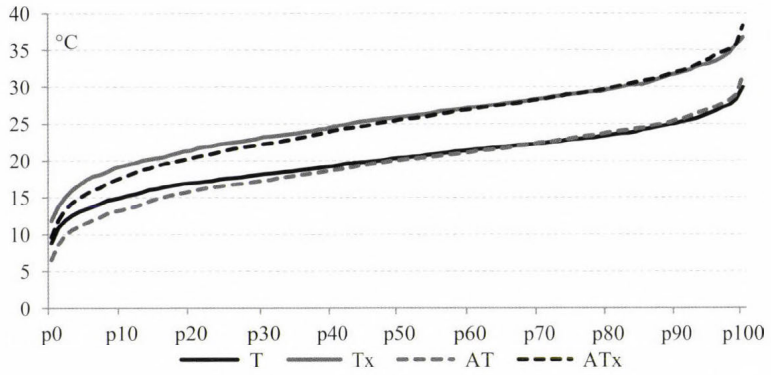

Fig. 1. Values of the four temperature indicators (°C) in relation to the percentiles between 1990 and 1999 in Budapest.

The temperature indicators identified different numbers of heat wave days in the period of 2000–2010. *Fig. 2* demonstrates the numbers of heat wave days by different threshold values in the warmer intervals. It can be observed that apparent temperature indicators defined more heat wave days. This means that the different indicators identified the same number of heat waves by different percentiles. The curves of the *T-Tx* and *AT-ATx* indicator pairs crossed each other several times in relation to threshold values.

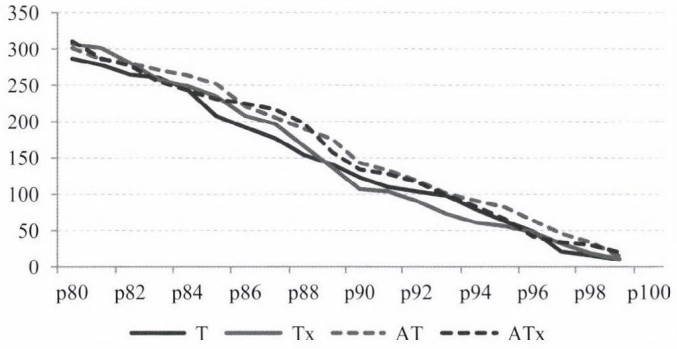

Fig. 2. Number of heat wave days defined by the four indicators in relation to percentiles between 2000 and 2010 in Budapest.

Fig. 3 represents the number of heat waves lasting for three or more days defined by the 90th percentile by different indicators. In some years, the number of heat waves defined by different indicators was the same (2001, 2005); however, the number of heat waves was different in most of the years. In the period from 2006 to 2010, the differences in the number of heat waves became bigger and more frequent. The yearly mean numbers of heat waves were 1.9–2.5 events.

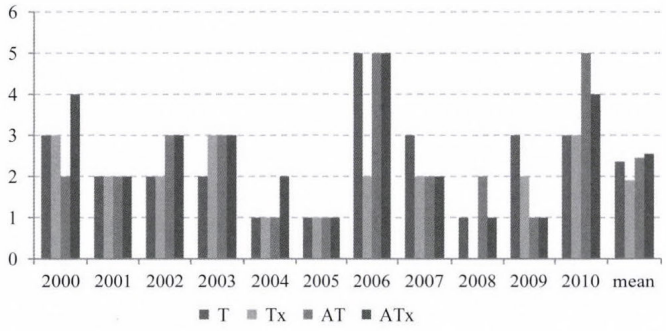

Fig. 3. The number of heat waves defined by the 90th percentile of indicators between 2000 and 2010 in Budapest.

Fig. 4 represents the number of heat wave days defined by the 90th percentile by different indicators. The numbers of heat wave days were different in each year. The differences became greater and more frequent in the last five years. The yearly mean numbers of heat wave days were between 10 and 13 days.

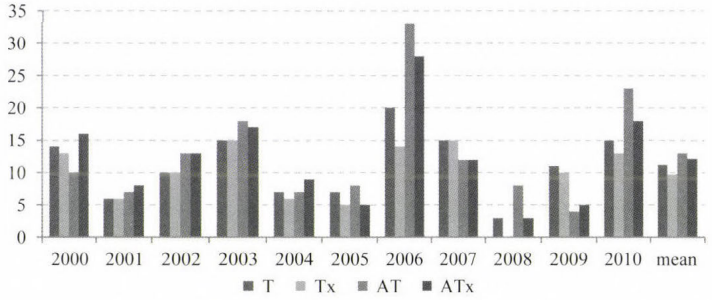

Fig. 4. The number of heat wave days defined by the 90th percentile of indicators between 2000 and 2010 in Budapest.

Based on the previous results, we can state that different heat wave days were identified by the different indicators. It was necessary to test to what extent the heat wave days were defined by the indicators as identical. *Fig. 5* shows the number of heat wave days defined by the indicator pairs, furthermore, the number of identical heat wave days defined by both indicators for the whole study period. The most heat wave days were identified by the indicator pairs *AT* and *ATx* (143 and 134 days, respsctively), while 123 and 107 days were identified by *T* and *Tx*. The number of identical heat wave days was between 88 and 129 days, meaning a correspondence of a range of 66–87% by indicators.

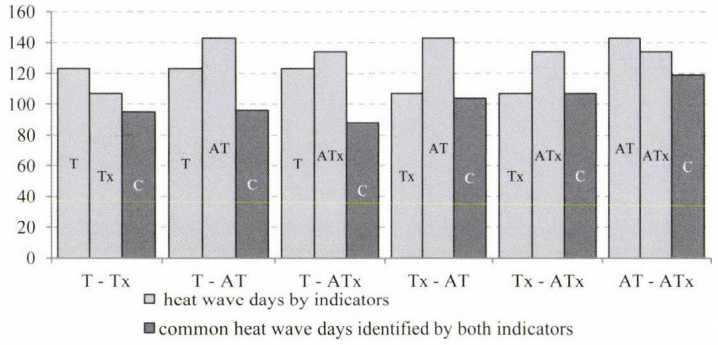

Fig. 5. The number of heat wave days identified by indicator pairs at the 90th percentile threshold value and the number of common heat wave days identified by both indicators between 2000 and 2010 in Budapest.

3.3. *Associations of heat and mortality*

The association between daily mortality and temperature has a U or J shape in general. In case of Budapest, the curve has a typical J shape. *Fig. 6* shows the difference of the daily mortality from the mean mortality in relation to daily mean temperature in the total population and in the group over 65 years. The approximate curve was produced by a cubic spline function having 4 degrees of freedom. The shape of the curves were similar, however, the effect of the temperature was somewhat bigger in the older age group. There was a higher mortality on cooler (<10 °C mean temperature), and warmer days (>23 °C mean temperature). The daily mortality significantly increased on days with higher mean temperature; the difference was greater than 40% on the hottest days. Concerning daily mortality, the optimal temperature range was between 17–20 °C. The shapes of the curves of the other indicators were similar.

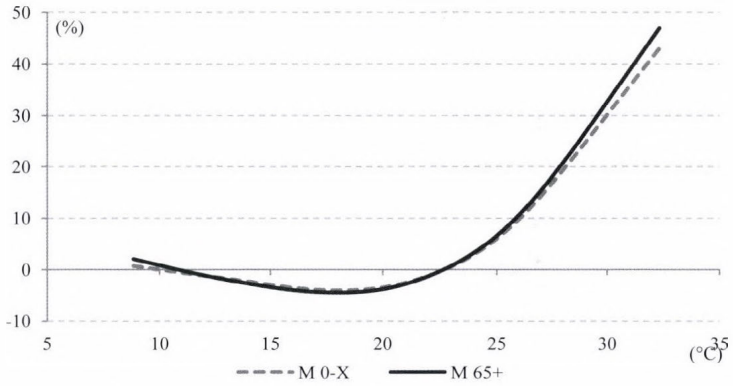

Fig. 6. Characteristics of association of daily mortality (percent differences from mean mortality) and daily mean temperature between 2000 and 2010 in Budapest.

3.4. *Effect of heat waves on mortality*

Fig. 7 shows the calculated daily expected total mortality (M_e) during the studied period and the total observed mortality (M_o) of the heat wave days by years. The expected daily mortality calculated on the basis of a 5-year moving reference period showed a decreasing tendency in relation to time. An excess mortality could be observed on the heat wave days in each year. In 2008, no heat wave was defined by the *Tx* indicator; therefore, no excess mortality was shown. The observed mortality was higher than expected mortality in every year. The association was similar in the older age group as well (not shown).

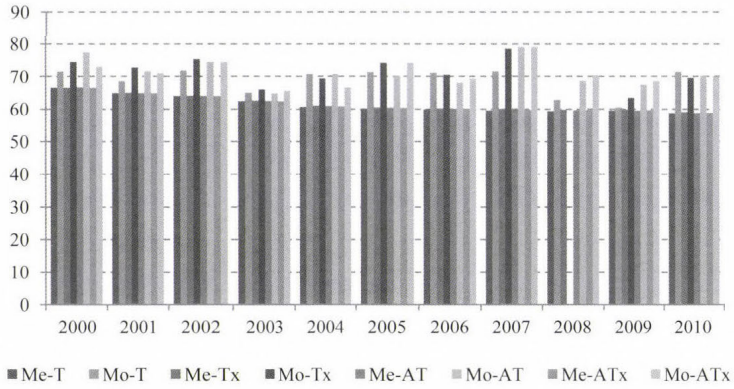

Fig. 7. The expected daily total mortality (M_e) and the observed total mortality (M_o) during the heat wave days defined by the four indicators between 2000 and 2010 in Budapest.

Fig. 8 shows the difference between observed and expected mortality: the excess mortality by years. The yearly numbers of excess mortality due to heat waves showed great variability. The lowest excess mortality was observed in 2008, and it was also very low in 2009 and 2001. The highest excess mortality was recorded in 2007, due to the strongest heat wave ever recorded. In that year, the number of excess death cases was 230–270 in the total population and 202–240 cases in the older age group during the 15 heat wave days by the different indicators. Similarly high excess mortality was observed in 2006 and 2010. There were great differences in the number of excess death cases in those years, when the indicators identified considerably different numbers of heat wave days (in 2006, 2008, and 2010). An average of 102–122 excess mortality cases could be attributed to heat waves in the total population, whereas there were 86–96 cases in the older age group defined by the different indicators. The mean percent excess mortality was between 15–18%; however, it surpassed 30% in 2007.

3.5. The relationship of excess mortality and different threshold values

The sum of death cases decreased by the increase of temperature threshold values as the number of identified heat wave days decreased. On the other hand, excess mortality increased on days with increasing temperature, while the mean excess mortality on identified heat wave days increased in relation to threshold values. To define the proper threshold, the product of the corresponding values of the two curves can be used. At the maximum range of the product curve, the two opposite processes were equally considered. *Fig. 9* represents the sum of total excess mortality, the mean excess mortality above different percentiles, as well as the product of the two datasets in case of daily mean temperature

indicator. The shapes of the curves of the sum of total excess mortality and the mean excess mortality changed more steeply over the 80th percentile, the value of their product started to increase over this percentile. Above the 95th percentile, the total excess mortality started to decrease significantly, while the excess mortality on heat wave days changed in the opposite direction. The range between the 85th and 95th percentiles met the criteria of the threshold value the best. The chosen threshold of daily mean temperature is 25 °C, which is the national alert threshold, corresponding to the 90th percentile seemed to be a suitable cut-off point. The shapes of the curves of the other indicators were similar (not shown).

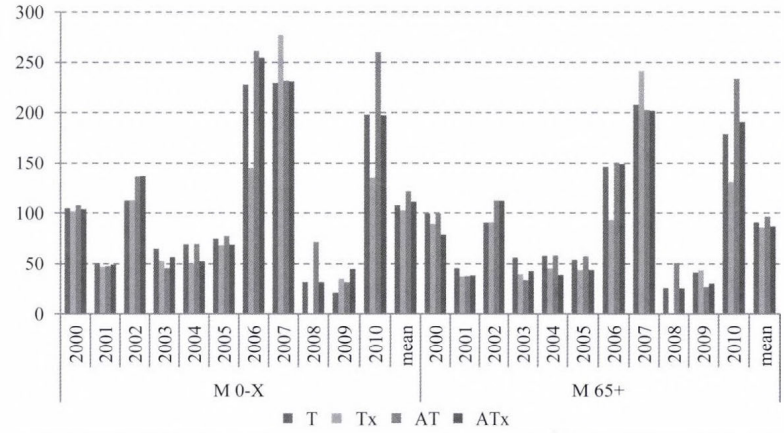

Fig. 8. The difference between expected and observed mortality in the total population and in the older age group between 2000 and 2010 in Budapest.

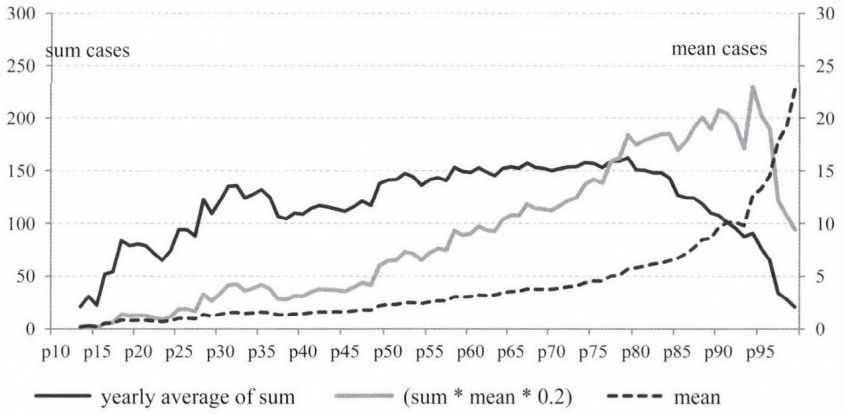

Fig. 9. The sum of total excess mortality, the mean excess mortality of heat wave days above thresholds, as well as their product in case of daily mean temperature indicator between 2000 and 2010 in Budapest.

The increase of the mean excess mortality on heat wave days in relation to the threshold values differed by the different temperature indicators (*Fig 10*). Similar values of excess mortality could be observed within the range of 85th–92nd percentiles of temperature indicators. In the range of higher temperatures, the differences between the shapes of the curves were bigger, the highest excess mortality could be observed when using the daily mean temperature indicator. In case of the other three indictors, considerably lower increase of excess mortality was related to the increase of threshold values. Excess mortality increased only over the threshold value corresponding to the 99th percentile.

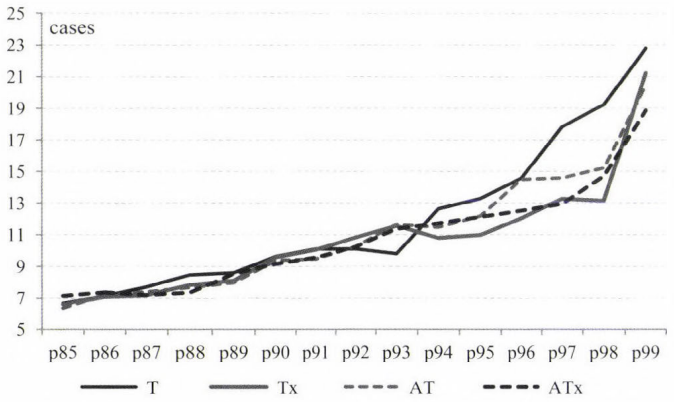

Fig. 10. The mean excess mortality on days above threshold by different indicators between 2000 and 2010 in Budapest.

4. Discussion

Heat related mortality was studied very intensively in the last two decades all around the world. The adverse impact was shown with great certainty. Several methods were used to characterize heat waves; different indicators were elaborated and applied.

The majority of studies used simple temperature parameters to characterize the impact of heat, while others applied more complex thermal indices based on different meteorological factors like humidity, radiation, wind speed, etc. Many papers tested several indicators in order to find the most suitable temperature predictor to detect heat-related excess mortality (*Barnett et al.,* 2010; *Kim et al.,* 2011; *Vaneckova et al.,* 2011; *Yu et al.,* 2011; *Morabito et al.,* 2014). The results could not identify the best indicator, the use of complex indices did not prove to be more efficient in determining the impact. Furthermore, the computation of complex indices is troublesome, their forecast is more ambiguous.

There is no universal definition of heat waves; the threshold values also show great variability. Health endpoints also vary, different age and cause-specific mortalities, as well as different groups (sex, race, socio-economic state, etc.) are studied. The results within multicenter studies can be compared due to the applied common methodology.

There is an increasing need to have comparable results in the public health system. The CEHAPIS methodology aims to monitor the change of heat related mortality in relation to climate change in the long run. The major concept was to develop simple indicators and computation for wide range use and comparability. Similarly to climate models, a 10-year reference period of the temperature indicators (daily maximum and daily apparent maximum temperature) is used in order to follow the future changes. The methodology describes heat waves as days with at least three consecutive days above the threshold value of temperature indicators defined as the 95th percentile of the reference temperature. The methodology recommends assessing the impact on cities with more than 500,000 inhabitants. Mortality, excluding external causes of the total and the 65 years and older population, is used to characterize vulnerability. A moving reference period (five years prior to the year of study year) of mortality is chosen to follow the changes of sensitivity (aging, adaptation, etc.). The expected (baseline) mortality, i.e., the average daily number of deaths is calculated using daily mortality in the reference period excluding the daily number of deaths on heat wave days. In the present paper, two simple temperature indices (T, Tx) and two other ones including humidity (AT, ATx) were used. The calculations did not need sophisticated statistical methods.

The mortality data of Budapest showed a significantly decreasing tendency. The use of a moving reference period could handle this tendency when calculating the expected values, i.e., the baseline decreased from year to year. No trend could be observed in the temperature data, as well as in the number of heat waves or heat wave days. It can be supposed that the increasing tendency of temperature due to heat waves will be detectable by these indicators using longer time series.

The different indicators identified different numbers of heat wave days by different threshold values in the warmer intervals. Using the same percentiles, the number of heat waves and the number of heat wave days were different in most of the years. Furthermore, the number of identical heat wave days defined by the indicator pairs showed great variability. This meant that the chosen temperature indicator considerably defined the length and number of heat waves and consequently, influenced the number of excess death cases of the given year. This phenomenon was detected in case of defined threshold as the result of calculated excess mortality showed. It should always be taken into consideration; however, this is a general feature of each other methodology as well.

The product function provides help to determine the optimal indicator and threshold. The range between the 85th and 95th percentiles was found to meet the criteria of the threshold values the best. This range is wide enough to make a choice based on several criteria. If we would like to detect the most cases of excess mortality, then we should choose a lower threshold value that can identify more heat waves. If we would like to identify heat waves with bigger numbers of excess death cases, then we have to choose a threshold of a higher percentile. When we would like to compare the impact of heat in several cities, we should choose a common threshold suitable for each city. Further analyses are necessary to test the applicability of the method in multicenter studies.

The mean excess mortality on days above threshold by different indicators can provide further assistance to choose the suitable indicator. Similar values of excess mortality can be observed within the range of the 85th – 92nd percentiles of temperature indicators. Within this range, the indicators are similarly sensitive and effective. In the range of higher temperatures above the 92nd percentile, the differences of the shapes of curves are bigger. The highest excess mortality can be observed when using the daily mean temperature indicator, therefore, it is more effective. On the other hand, the other three indicators are less sensitive in the range of the 94th–98th percentiles; they can effectively identify excess mortality on very hot days. Further analyses are required to answer the question, to what extent the Budapest findings can be used in other cities.

The threshold in this study – the national alert threshold, which is the 25 °C daily mean temperature, corresponding to the 90th percentile – seems to be a suitable cut-off point. This threshold, lower than the one recommended by the CEHAPIS methodology, was chosen, while an excess death rate of 7% was detected at this cut off point of the sensitivity curve. This increase of mortality already requires actions according to the public health authorities.

5. Conclusion

The aim of the study was to develop a simpler method than time series analysis to identify excess mortality attributable to heat. The methodology is suitable to assess the changes of weather and climatic conditions to follow the impact of heat on daily mortality. The results are in accordance with the findings of previous studies.

At the chosen threshold value of 90th percentile, the mean excess mortality of the whole period computed by using the four indicators did not differed considerably, although the identified heat wave days varied to some extent. The use of apparent temperature indicators is not more advantageous and their prediction is more complicated. The apparent temperatures as well as the maximum temperature indicator are able to identify high excess mortality mainly on very hot days, while the daily mean temperature indicator is effective

in a wider threshold range. Based on these results, the use of daily mean temperature is recommended.

The thorough analysis of threshold values is desirable using longer time series of the data of different cities. By this comparative analysis, we can get an answer to whether the system based on the daily mean temperature can be generalized.

References

Baccini, M., Biggeri, A., Accetta, G., Kosatsky, T., Katsouyanni, K., Analitis, A., Anderson, H. R., Bisanti, L., D'Ippoliti, D., Danova, J., Forsberg, B., Medina, S., Paldy, A., Rabczenko, D., Schindler, C., and *Michelozzi, P.,* 2008: Heat effects on mortality in 15 European cities. *Epidemiology 19,* 711–719.

Baccini M., Kosatsky T., Analitis A., Anderson H. R., D'Ovidio M., Menne B., Michelozzi P., and *Biggeri, A.,* 2011: PHEWE Collaborative Group. Impact of heat on mortality in 15 European cities: attributable deaths under different weather scenarios. *J Epidemiol. Commun. Health 65,* 64–70.

Barnett, A.G., Tong, S., and *Clements, A.C.A.,* 2010: What measure of temperature is the best predictor of mortality? *Environ. Res. 110,* 604–611.

Basu, R., 2009: High ambient temperature and mortality: a review of epidemiologic studies from 2001 to 2008. *Environ. Health 8,* 40.

Bobvos, J. and *Paldy, A.,* 2009: Impact of Heat on the Urban and Rural Population in Hungary. *Epidemiology 20, S127.*

Bobvos, J., Solymosi, N., and *Paldy, A.,* 2011: Climate change and heat-related mortality in Budapest - comparative methods of impact estimation of temperature change. *Environ. Health Perspect.* Available at: http://ehp.niehs.nih.gov/isee/, accessed 15 April 2014.

D'Ippoliti, D., Michelozzi, P., Marino, C., de'Donato, F., Menne, B., Katsouyanni, K., Kirchmayer, K., Analitis, A., Medina-Ramón, M., Paldy, A., Atkinson, R., Kovats, R.S., Bisanti, L., Schneider, A., Lefranc, A., Iñigue. C., and *Perucci, C.A.,* 2010: The impact of heat waves on mortality in 9 European cities: results from the EuroHEAT project. *Environ. Health 9,* 37.

Gosling, S.N., McGregor, G.R., and *Paldy, A.,* 2007: Climate change and heat-related mortality in six cities Part 1: model construction and validation. *Int. J. Biometeorol. 51,* 525–540.

Gosling, S.N., Lowe, J.A., McGregor, G.R., Pelling, M., and *Malamud, B.D.,* 2009a: Associations between elevated atmospheric temperature and human mortality: a critical review of the literature. *Climatic Change 92,* 299–341.

Gosling, S N., McGregor, G.R., and *Lowe, J.A.,* 2009b: Climate change and heat-related mortality in six cities Part 2: climate model evaluation and projected impacts from changes in the mean and variability of temperature with climate change. *Int. J. Biometeorol. 53,* 31–51.

GSOD, 2010: Global surface summary of the day data Version 7. At National Climatic Data Centre (NCDC). Available at: ftp://ftp.ncdc.noaa.gov/pub/data/gsod/, accessed 15 April 2014.

Hajat, S., Armstrong, B., Baccini, M., Biggeri, A., Bisanti, L., Russo, A., Paldy, A., Menne, B., and *Kosatsky, T.,* 2006: Impact of high temperatures on mortality: is there an added heat wave effect? *Epidemiology 17,* 632–638.

Hajat, S., Kosatky, T., 2010: Heat-related mortality: a review and exploration of heterogeneity. *J. Epidemiol. Commun. Health 64,* 753–760.

IPCC, 2013: Climate Change 2013: The Physical Science Basis. Summary for Policymakers. In: (Eds.: *Stocker, T.F., Qin, D., Plattner, G.K., Tignor, M., Allen, S.K., Boschung, J., Nauels, A., Xia, Y., Bex, V., Midgley, P.M.*) Contribution of Working Group I to the Fifth Assessment Report of the Intergovernmental Panel on Climate Change. Cambridge University Press, Cambridge, United Kingdom and New York, NY, USA.

IPCC, 2014: Climate Change 2014: Impacts, Adaptation, and Vulnerability. Summary for Policymakers. In: (Eds. *Aldunce, P., Ometto, J.P., Raholijao, N., Yasuhara, K.*) Final draft of Working Group II to the Fifth Assessment Report of the Intergovernmental Panel on Climate Change. Available at: http://ipcc-wg2.gov/AR5/images/uploads/IPCC_WG2AR5_SPM_Approved.pdf, accessed 15 April 2014.

Ishigami, Ai., Hajat, S., Kovats, R. S., Bisanti, L., Rognoni, M., Russo, A., Paldy, A., 2008: An ecological time-series study of heat-related mortality in three European cities. *Environ. Health . 7,* 5.

Kalkstein, L.S. and *Valimont, K.M.,* 1986: An evaluation of summer discomfort in the United States using a relative climatological index. *Bull. Am. Meteorol. Soc. 67,* 842–848.

Kim, Y.M., Kim, S., Cheong, H.K., Kim, E.H., 2011: Comparison of temperature indexes for the impact assessment of heat stress on heat-related mortality. *Environ. Health Toxicol. 26,* Available at: http://dx.doi.org/10.5620/eht.2011.26.e2011009, accessed 15 April 2014.

Kovats, R S. and *Ebi, K.L.,* 2006: Heatwaves and public health in Europe. *Eur. J. Publ.Health 16,* 592–599.

Kovats, R.S. and *Hajat, S.,* 2008: Heat stress and public health: a critical review. *Ann. Rev. Publ. Health 29,* 41–55.

Morabito, M., Crisci, A., Messeri, A., Capecchi, V., Modesti, P. A., Gensini, G. F., and *Orlandini, S.,* 2014: Environmental Temperature and Thermal Indices: What Is the Most Effective Predictor of Heat-Related Mortality in Different Geographical Contexts? *Sci. World J.* Available at: http://dx.doi.org/10.1155/2014/961750 , accessed 15 April 2014.

Paldy, A., Bobvos, J., Vamos, A., Kovats, R.S., and *Hajat, S.,* 2005: The effect of temperature and heat waves on daily mortality in Budapest, Hungary, 1970–2000. In: (Eds. *Kirch, W., Menne, B., Bertollini, R.*) Extreme weather events and public health responses. Springer, New York, 99–107.

Paldy, A. and *Bobvos, J.,* 2009: Impact of the Unusual Heatwave of 2007 on Mortality in Hungary . *Epidemiology 20(6),* S126–S127.

Paldy, A., Juhasz, A., Bobvos, J., and *Nagy, CS.,* 2011: Modelling of the association of health impacts of exposure to 2007-heatwave and the effect modifiers at small area level in Hungary . *Environ. Health Perspect.* Available at: http://ehp.niehs.nih.gov/isee/, accessed 15 April 2014.

Vaneckova, P., Neville, G., Tippett, V., Aitken, P., Fitzgerald, G., Tong, S., 2011: Do biometeorological indices improve modeling outcomes of heat-related mortality? *J. Appl. Meteorol. Climatol. 50,* 1165–1176.

WHO, 2011: Tools for the monitoring of Parma Conference commitments. Report of the meeting 25–26 November 2010. Available at:http://www.euro.who.int/data/assets/pdf_file /0019/134380/e94788.pdf, accessed 15 April 2014.

Yu, W., Guo, Y., Ye, X., Wang, X., Huang, C., Pan, X., and *Tong, S.,* 2011: The effect of various temperature indicators on different mortality categories in a subtropical city of Brisbane, Australia. *Sci.Total Environ. 409,* 3431–3437.

IDŐJÁRÁS

Quarterly Journal of the Hungarian Meteorological Service
Vol. 119, No. 2, April – June, 2015, pp. 159–184

Multivariable cyclone analysis in the Mediterranean region

Fanni Dóra Kelemen*, **Judit Bartholy**, and **Rita Pongrácz**

Eötvös Loránd University, Department of Meteorology
Pázmány P. sétány 1/A, 1117 Budapest, Hungary

**Corresponding author E-mail: kelemenf@nimbus.elte.hu*

(Manuscript received in final form September 22, 2014)

Abstract—This paper analyzes midlatitude cyclones identified and tracked in the Mediterranean region for the recent past, between 1981 and 2010. The Mediterranean region is especially interesting since the complex land orography favors lee cyclogenesis, and the warm sea area provides latent heat for the developing cyclones. These cyclones may result in heavy precipitation, even flood events affecting southern and central Europe, including Hungary.

Cyclones are identified using two different reanalyses, the ERA Interim reanalysis from ECMWF at 0.75° horizontal resolution and the NCEP-DOE R2 reanalysis at 2.5° horizontal resolution. For the identification, a multivariable approach is used to eliminate and assess the uncertainties rising from the choice of a specific variable, which is particularly important in the Mediterranean, where the systems are tend to be weak and shallow. Mean sea level pressure (MSLP), geopotential heights of the 1000 hPa, and the 850 hPa isobaric levels are used as main variables, and relative vorticity at 850 hPa isobaric level serves, an additional variable. The applied algorithm has uni- and bivariate modes. In the bivariate mode, relative vorticity at 850 hPa is added to the main variable.

The results suggest that time series of annual number of cyclones using the two reanalyses correlate significantly, however, using the higher resolution dataset, more cyclones can be identified. The largest and the smallest frequency of cyclones over the entire domain occur in spring and summer, respectively. The largest spread of the multivariable ensemble is in summer, probably caused by non-frontal thermal lows. Furthermore, summer is mostly dominated by short-lived cyclones. The main cyclogenesis regions are the Gulf of Genoa and the Cyprus region, with some minor centers at the Adriatic Sea, the northern part of the Black Sea, and the Iberian Peninsula. The cyclone frequency trend is slightly increasing in most parts of the region, especially over the Adriatic Sea and near Cyprus. Hungary is affected annually by approximately 30 cyclones from the Mediterranean area, most frequently in spring.

Key-words: cyclone identification, cyclone tracking, cyclone climatology, Mediterranean region, reanalysis, MSLP, geopotential height, relative vorticity

1. Introduction

Mid-latitude cyclones play a major role in the general circulation of the atmosphere, they largely contribute to the energy transfer between the equatorial and the polar regions. The potential energy derived from the temperature differences of air masses along the frontal surface is transformed by cyclones into kinetic energy. Cyclones are basically large vortices, in which warm and moist air mixes with cold and dry air. Through this process, energy is transformed and released.

In the Mediterranean region, the presence of large warm sea surface almost completely surrounded by land (the Mediterranean sea is connected to the ocean only through narrow straits) and the orography both induce the evolution of cyclones. The cyclones occurring in this region transfer moist and warm air over the continental regions, then, as mixing with colder air, the embedded moisture condensates, often resulting in intensive precipitation. *Jansa et al.* (2001) showed that the majority of heavy rain events in the Mediterranean occurred in the vicinity of a cyclone center. Thus, these cyclones determine substantially the local weather and climate.

The cyclones associated with intensive precipitation can cause floods, or other severe weather events, like on March 15th, 2013 when a snowstorm hit Hungary. The snow even caused power-cut in some regions of the country. In large areas of Hungary snowdrift occurred, which resulted in chaotic traffic conditions, especially due to the coincidence of the storm with a national holiday. Also in 2013, severe flood occurred in Central Europe, which was mainly caused by the precipitation of three consecutive cyclones triggered by a cut-off at the upper level of the atmosphere (*Grams et al.*, 2014). The relationship between Mediterranean cyclones and Central European floods is often mentioned, i.e., the Vb cyclone track from the *van Bebber* (1891) categories is usually associated with flood events (*Hofstätter et al.*, 2012), for example the Danube flood in Central Europe in 2002 (*Ulbrich et al.*, 2003).

The aim of this study is (i) to analyze objectively the cyclones in the Mediterranean region with particular focus on the Genoa lows, (ii) to investigate the performance of the multivariable cyclone identification method, and (iii) to overview the climatology of those cyclones coming from the Mediterranean region, which directly affect Hungary.

The exact identification of a mid-latitude cyclone is difficult since there are no generally accepted criteria. Cyclone identification and tracking can be done by manually analyzing meteorological fields, however, for comprehensive analyses, objective methods must be used. The most commonly used method for cyclone identification is to search local extremes in a selected variable field, and connect the successive centers according to some constraints.

One of the most commonly used variable for cyclone identification is the mean sea level pressure (MSLP) (*Serezze*, 1995; *Lionello et al.*, 2002; *Hanson et*

al., 2004; *Bartholy et al.*, 2008), which refers to the pressure information at a specific surface reduced from the geographic surface by using a temperature profile. This reduction estimates the pressure at sea level sometimes below the actual surface level. Since temperature profiles affect the MSLP values and they can be unusual at high elevations, the fields can produce anomalous patterns in the area of mountains. In addition to MSLP, some detecting algorithms calculate the gradient of MSLP as well, to find a cyclone center (*Picornell et al.*, 2001; *Jansa et al.,* 2001). Others investigate the Laplacian of MSLP (*Murray* and *Simmonds,* 1991), which can be interpreted as the quasi-geostrophic relative vorticity (*Pinto et al.,* 2005). Besides quasi-geostrophic relative vorticity, relative vorticity at 850 hPa can also be used to identify cyclones (*Hodges et al.*, 2011*; Catto et al.,* 2010; *Woollings et al.,* 2010). 850 hPa isobaric level can be considered as the lowermost level of the free atmosphere. Relative vorticity has an advantage over MSLP, namely, it is more independent from the direct effects of topography. *Hoskins* and *Hodges* (2002) compared several cyclone climatology results using different fields, and they showed that relative vorticity is especially good when describing smaller-scale systems, which are typical in the Mediterranean region. On the other hand, the disadvantage of using relative vorticity is that at high resolution it becomes a very noisy field (*Hodges et al.,* 2011). Hence, a truncation of the field is necessary if relative vorticity field is the key element of the identification algorithm. Besides MSLP and relative vorticity, geopotential height of the 1000 hPa is also used to identify cyclones (*Trigo et al.,* 1999, 2000; *Alpert et al.*, 1990).

Most of the studies considered only one specific variable to identify cyclones, sometimes including its derivatives, too. An exception is found in *König et al.* (1993), who used both the 850 hPa relative vorticity and 1000 hPa geopotential height, however, their algorithm considered these fields separately and later combined the information from the two fields along the lifecycle of a specific cyclone.

All Lagrangian cyclone identification methods are based on a search for local extremes in a selected gridded field. The most common approach is to investigate the neighboring points of a grid point. In many cases, only the 8 nearest neighboring points are analyzed (*Alpert et al.,* 1990; *Trigo et al.*, 1999; *Hanson et al.,* 2004; *Maheras et al.*, 2001) whether the values are larger or smaller than in the central point. Sometimes the evaluated area covers a larger region, i.e., 5×5 grid points or even more (*Bartholy et al.*, 2008). Obviously, the investigated region size depends on the grid's horizontal resolution. For a 2.5° horizontal resolution grid, the investigation of the 8 neighboring points is adequate for cyclone center identification. In case of higher resolution grid, the investigated area should cover the same sized region, which evidently includes more grid points. Another way to find local minima in a gridded field is used by *Lionello et al.* (2002). They identified at each time step the sets of the steepest decreasing paths, which led to the same MSLP minimum by comparing the

neighboring point values. *Picornell et al.* (2001) and *Jansa et al.* (2001) used MSLP for their studies, where the search of MSLP minimum was extended with the analysis of pressure gradients around the already found minimum points along eight major directions (E, NE, N, NW, W, SW, S, SE). If the gradient exceeds a threshold along at least six directions then the system is considered to an open cyclone, whereas if the gradients are sufficiently large along all the eight directions then the system is considered to be a closed cyclone. Open and closed systems have been distinguished at other studies, too (e.g., *Sinclair*, 1994; *Murray* and *Simmonds*, 1991; *Picornell et al.*, 2001). *Sinclair* (1994) analyzed the geostrophic relative vorticity (calculated from 1000 hPa geopotential height) and used MSLP to decide whether a system is closed or not. He considered a system to be closed in the Southern Hemisphere if its vorticity minimum was closer than 5° latitude to a pressure minimum.

To get a more comprehensive picture about cyclones, the identified centers are usually tracked by a criterion to follow the center along the lifecycle of the cyclone. In some studies the tracking is not included (e.g., *Jansa et al.*, 2001; *Finnis et al.*, 2007). The most common tracking technique is the nearest neighbor concept, where the continuation of one specific cyclone is that center in the following time step, which is located the nearest to the center of the preceeding step. The search for the nearest neighbor is sometimes specified in an area often asymmetric to the center, taking into account the typical eastward movement of the mid-latitude cyclones. For example, when a rectangular area around the center is evaluated, its west-east axis is longer than the north-south axis (*König et al.*, 1993). *Trigo et al.* (1999) used a method, which searches for the next cyclone center within an area determined by the maximum cyclone velocity (33 km/h westward and 90 km/h in any other direction). Another tracking approach (i.e., *Murray* and *Simmonds*,1991; *Sinclair,* 1994; *Pinto et al.*, 2005; *Wernli* and *Schwierz*, 2006) pre-estimates the new position of a cyclone, evaluates all the cyclone centers being close to this first guess location, and selects the most likely candidate. This technique is a good solution when the available time steps are not too frequent, so the cyclones' separation and displacement should be considered together. Tracking method of *Muskulus* and *Jacob* (2005) uses the Kalman filter approach, in which the matching is carried out by minimizing a weighted prediction error function. This technique has several advantages: (i) besides one previous time step, it can consider the whole lifetime of the cyclone, and (ii) estimating the error, which predicts the maximum distance for the next match.

Depending on the identification technique and the aim of a particular study, additional filtering of the identified cyclones is possible. The most common filtering is to use thresholds for the cyclones' lifetime and/or for the MSLP of their centers. For instance, the lifetime of accepted cyclones should last longer than 12 hours (*Trigo et al.*, 1999), and the pressure of the cyclone center should be lower than 1000 hPa (*Gulev et al.*, 2001; *Muskulus* and *Jacob*, 2005).

Bartholy et al. (2008) considered different lifetime thresholds for Atlantic-European and Mediterranean cyclones (3 days and 1 day, respectively).

For some special applications, the extension of the cyclone must be calculated, e.g., *Hanson et al.* (2004) and *Trigo et al.* (1999) applied the definition from *Nielsen* and *Dole* (1992), according to which the cyclone radius is the distance between the center and the outermost closed isobar. *Muskulus* and *Jacob* (2005) used a watershed segmentation method for cyclone identification, and also for determining the area of the cyclones. *Piocornell et al.* (2001) defined the cyclone area as the positive geostrophic vorticity area around the center. The zero vorticity line is determined along the four main directions (N, E, S, W), and these points form an ellipse, which is the final cyclone area.

Due to the lack of exact identification of cyclone tracks, several cyclone tracking methods are available, and they can be used for cross-validation. The manual analyses are highly influenced by the subjective choices made by the analyst. The Intercomparison of Mid Latitude Storm Diagnostics (IMILAST) project (*Neu et al.*, 2013) made an effort to investigate the method-related uncertainties of cyclone identifications, and concluded that the results can be sensitive to several aspects of the applied method. They found important differences in the interannual variability and geographical distribution of cyclones in the Mediterranean. That is why we use a multivariable cyclone identification ensemble in this study for this region. In our identifying system, the same algorithm forms several individual methods with different variables used to identify cyclone centers. This way the uncertainties arising from the variable choice are assessed and taken into account in the final conclusions.

The paper briefly presents the used two reanalyses in Section 2. Then, in Section 3, the methodology and composition of the multivariable ensemble are described. In Section 4, the results of the cyclone time series based on the two reanalyses are compared, then, the ERA Interim results are analyzed in detail. The features of the ensemble are investigated, then the annual variability and trends of cyclones are analyzed. The section is closing with a short analysis of the cyclones passing over Hungary. The study ends with the discussions (Section 5) followed by the conclusions (Section 6).

2. Data

The present cyclone analysis is based on reanalysis data forming a spatially and temporally appropriate resolution, regular database, which is needed for the objective. Here, two available reanalyses are selected, the European Centre for Medium-Range Weather Forecasts (ECMWF) Reanalysis (ERA Interim) (*Dee et al.*, 2011) and the reanalysis data from the National Centers for Environmental Prediction (NCEP) and the National Energy Research Supercomputing Center (NERSC) of the Department of Energy (DOE) (*Kanamitsu et al.*, 2002) (NCEP-

DOE R2), which is the updated NCEP/NCAR (National Center for Atmospheric Research) reanalysis. Both datasets are available from 1979 up to the recent past, and we use the data for the 30-year period between 1981 and 2010. Both of the reanalyses are widely used for cyclone climatology studies. Preceding reanalyses of ECMWF (i.e., ERA-15, ERA-40) were earlier used by *Alpert et al.* (1990), *Sinclair* (1994), *Trigo et al.* (1999), *Hoskins* and *Hodges* (2002), *Hanson et al.* (2004), *Wernli* and *Schwierz* (2006), *Bartholy et al.* (2008), *Catto et al.* (2010). Some of these studies, e.g., *Trigo et al.* (1999), *Alpert et al.* (1990) and *Bartholy et al.* (2008) investigated the Mediterranean region. NCEP reanalyses were also used for cyclone analysis in general (e.g., *Hanson et al.*, 2004; *Pinto et al.*, 2005; *Hodges et al.*, 2011), and for the Mediterranean region, too (e.g., *Maheras et al.*, 2001).

ERA Interim is constructed with a use of a spectral model, whose horizontal resolution is expressed by its truncation number T255 indicating the number of waves used to represent the data. This horizontal resolution corresponds with a lat-lon 0.75°×0.75° regular grid, and the data can be downloaded in this interpolated form.

The NCEP-DOE R2 dataset is available on a 2.5°×2.5° horizontal resolution lat-lon grid, which we interpolated to a 0.75°×0.75° grid to achieve the same grid resolution as ERA Interim. The interpolation was made by a bicubic spline method. *Pinto et al.* (2005) showed that the use of spline interpolation improves the localization of cyclones. The improvement is mainly due to the better spatial representation of cyclone centers, however, this method does not add any extra information to the original data. The bicubic spline interpolation produces a smooth field from the original data, since it utilizes both the first and the second derivatives of the original data. The interpolation formula is smooth in the first derivative and continuous in the second derivative.

Both ERA Interim and NCEP-DOE R2 are used with a 6-hour temporal resolution.

The area investigated in this study is the Mediterranean region from 29.25°N to 55.5°N and from 11.25°W to 42.75°E, which is approximately the Med-CORDEX region (*Ruti et al.*, 2015), and thus, it eases future comparison of our reanalysis results to the climate simulations interpolated on the Med-CORDEX domain.

Pressure and geopotential fields are directly available from both database. The relative vorticity field is available only in case of the ERA Interim reanalysis. In order to use similar methodology and ensure consistency in the analysis, we calculate vorticity from the wind fields both from ERA Interim and NCEP-DOE R2.

3. Method

A multivariable ensemble approach is used in this study to assess uncertainties due to the selection of specific cyclone identification method. Several objective methods exist for identifying mid-latitude cyclones using more or less similar (however, not exactly identical) criteria. The advantages of objective methods are shown in *Jansa et al.* (2001), where more cyclones were found with using an objective analysis of high resolution model data than with the human-based subjective analysis. The objective analysis has special advantages in the areas with less measurements and meteorological experiences. Furthermore, the assessment of differences in objective methods is studied in the framework of the IMILAST project (*Neu et al.*, 2013), which is an explicit community effort to intercompare extratropical cyclone detection and tracking algorithms.

The definition of a mid-latitude cyclone is not entirely exact, it is commonly characterized as a low pressure system, which rotates in positive direction (in the Northern Hemisphere). Consequently, the identification of an extratropical cyclone is not standardized either. The different tracking methods capture different aspects of these mid-latitude low pressure systems.

For this presented analysis, we developed our own cyclone identification and tracking method based on previous studies and experiences found in the literature. The uni- and bivariate versions of our method search for extremes in gridded fields. The univariate version uses one specific variable field, which is selected from different variables related to pressure or geopotential height. The bivariate version consists of a combination of two fields, where the second field is always the relative vorticity at 850 hPa isobaric level, whose maxima are located. The relative vorticity is selected on the basis of *Hoskins* and *Hodges* (2002) who showed its importance in case of the Mediterranean small scale systems. The minima of the basis variable field are searched successively in regions of 15×15 grid points corresponding to 11.25°×11.25° area (when using 0.75° horizontal resolution data), which is approximately the typical size of a Mediterranean cyclone. In the relative vorticity field, the maxima are located in regions of 11×11 grid points, which is more appropriate due to the smaller scale structures of this field.

For the univariate version, three variables are selected to find their minima: in addition to the most commonly used MSLP, 1000 hPa and 850 hPa geopotential heights are also considered. The 1000 hPa geopotential height has already been successfully used in the Mediterranean region (e.g., *Trigo et al.*, 1999). The 850 hPa geopotential height is selected, since its tracking statistical characteristics are similar to MSLP's (*Hoskins* and *Hodges*, 2002), and moreover, it represents the same level as the relative vorticity, which might help in the identification of extremes.

The cyclone tracking algorithm is based on a nearest neighbor search procedure, which uses specific search regions to find the sequential steps of a

trajectory. Around each cyclone center a rectangular search region is defined (*König et al.*, 1993), where the continuation of the trajectory is searched in the next time step. The rectangular area extends more in the west-east direction than in the north-south taking into account the mainly eastward propagation of cyclones. If two possible next locations are found within the search region, the nearest one will be selected. The analysis considers only the cyclone tracks exceeding 1 day lifetime threshold similarly to other studies (*Neu et al.*, 2013; *Hanson et al.*, 2004; *Wernli* and *Schwierz*, 2006).

The use of three basic variables, and the uni- and bivariate versions of the method (*Table 1.*) results in six different cyclone track time series, from which an ensemble is formed and analyzed together instead of the difficult decision to identify the one and only ideal method.

Table 1. The set up of the multivariable ensemble for cyclone identification

Univariate	**Bivariate**
U1 Mean sea level pressure (MSLP)	B1 Mean sea level pressure (MSLP) + Relative vorticity at 850 hPa level (RV850)
U2 Geopotential height of the 1000 hPa level (Z1000)	B2 Geopotential height of the 1000 hPa level (Z1000) + Relative vorticity at 850 hPa level (RV850)
U3 Geopotential height of the 850 hPa level (Z850)	B3 Geopotential height of the 850 hPa level (Z850) + Relative vorticity at 850 hPa level (RV850)

For further analysis, the cyclone area for each identified cyclone center is determined. Cyclone domain is defined in a 11.25°×11.25° lat-lon area centered on the cyclone center and located where the relative vorticity is positive. This definition is sufficient for detecting the effect of a passing cyclone, however, it is insufficient for detailed analysis of weather fronts or other smaller scale phenomena.

The cyclones are investigated seasonally, for this purpose their genesis date determines the seasonal membership. We consider December, January, and February as winter, from March until May as spring, June, July, and August as summer, and finally from September till November as autumn.

For the analysis, cyclone track density maps are calculated. Cyclone track density values denote the number of cyclone tracks crossings per 0.75°×0.75° cells in each season during the investigated entire 30 years. Since unequal-area grid is used for the counting of cyclones per grid cells, the effect of changing area per latitude is calculated. However, the difference is negligible considering the scales used in this study. Furthermore, cyclone genesis density maps are calculated similarly to the track densities, except that only the starting points of the trajectories are considered.

In the 30-year time series of track density maps trends are detected in each grid cell. To find the trend coefficient, linear regression is used where the explanatory variable is the year and the dependent variable is the number of cyclones per year. For the trend analysis, the second coefficient of the linear regression is used, which is the slope of the fitted regression line. In each grid point and in case of all ensemble members, the trend coefficients are evaluated whether or not they are statistically significant, and only the significant values are used.

4. Results

4.1. Reanalysis comparison

The above described methodology is applied to construct six cyclone track time series using the ERA Interim and six time series using the NCEP-DOE R2 reanalysis. In our study, first, the differences of the results using the two datasets are evaluated. Overall, more cyclones are found using the ERA Interim reanalysis (around 75 cyclones annually) than the NCEP-DOE R2 (around 64 cyclones annually), which has lower horizontal resolution. Nevertheless, the courses of the time series of the annual numbers of identified cyclones are quite similar (*Fig. 1*), the correlation coefficient is 0.86, which is statistically significant at the 0.05 level. The spreads of both ensembles are 20 in average. In the first half of the time period, the peaks of the lines (i.e., the large cyclone numbers) are in the same years (1984, 1988, 1991, and 1996). In the second half of the period, the peaks are somewhat shifted relative to each other. The results of using the two reanalyses agree on the general growing trend, which is statistically not significant.

The empirical distributions of the cyclone lifetimes are shown in *Fig. 2.* Evidently, less cyclones are found with longer trajectory, this is valid for the identified cyclones using both reanalyses. The largest difference (21%) between the frequencies of cyclones is in case of the shortest living cyclones. These results suggest that more weak and small cyclones can be identified using the ERA Interim reanalysis that typically occur in the Mediterranean region. This can be explained partially by the higher resolution of ERA Interim reanalysis, which affects the representation of orography as well as other small scale physical processes, and these affect the development and appearance of cyclones in the reanalysis.

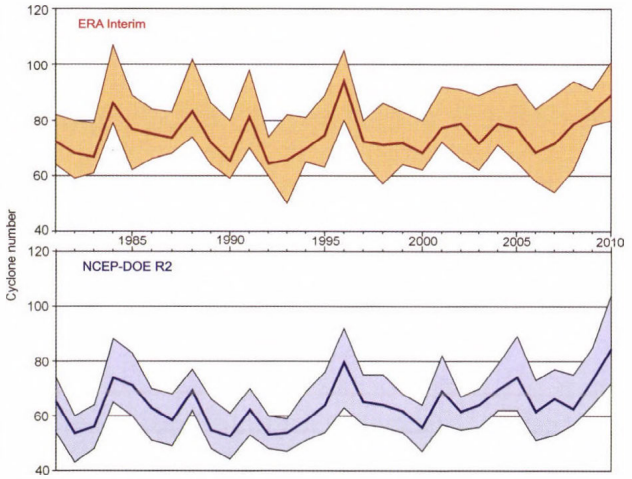

Fig. 1. Time series of the multivariate cyclone identification ensemble from the two reanalyses, ERA Interim (top) and NCEP DOE R2 (bottom). The solid line presents the mean of the ensemble (the average cyclone numbers in each year), and the light colored band presents the spread of the ensemble (the maximum and minimum cyclone numbers in each year).

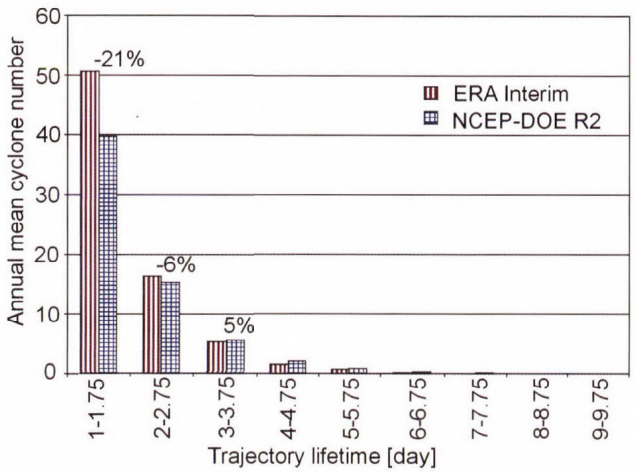

Fig. 2. Histogram of the cyclone lifetime using the two reanalyses. The values above the columns indicate the differences in percentages compared to the results using ERA Interim data.

The results of the comparison suggest, that the higher resolution ECMWF reanalysis is more appropriate for identifying cyclones in the Mediterranean region. Therefore, in the further analyses of cyclones, we use only the ERA Interim based cyclone identification.

4.2. Investigation of the ensemble

The evaluation of the ensemble members are shown through the members' cyclone track density maps and a cyclone lifetime histogram. The comparison presents the features of the different variables, which contributes to the quality of the ensemble mean.

30 years seasonal cyclone track densities are mapped for all the four seasons and all the six members of the multivariable ensemble. Here only the maps for summer (when the ensemble spread is the largest) are shown in *Fig. 3*. The large spread between the ensemble members is most likely caused by the occurrences of thermal lows, which are non-frontal low pressure areas and can not be detected at all levels, neither in the vorticity field. The mean of the ensemble, nevertheless, compensates the effect of using different variables (shown later in *Fig. 7c*). The overall patterns are very similar, the largest cyclone density values occur in the Gulf of Genoa and the southwestern coasts of Turkey, additionally, intense cyclone activity is present over the Iberian Peninsula and the northern part of the Black Sea. The differences between the maps are mainly in the cyclone density values, and not in the spatial patterns, which are basically very similar. The methods using MSLP or geopotential height at 1000 hPa level (i.e., information close to the surface) result in more cyclones, and thus, larger cyclone track density values, which might be the influence of the orography. Furthermore, the limiting effect of the relative vorticity as a second variable is noticeable. The standard deviation of the ensemble mean cyclone track density field in summer is around 2.45 cyclones per 30 years on average over the domain, with the maximum of 87.1 occurring near Cyprus. This means that the largest difference between the two extremes of the entire ensemble is approximately 3 cyclones per grid cell annually, which occurs during the summer months.

After the cyclone track density analysis, the multivariable ensemble is also evaluated in terms of cyclone lifetime. Identified tracks lasting at least 1 day are considered in this analysis. The histogram (*Fig. 4*) clearly shows decreasing numbers for longer-lived cyclones in case of all the six members of the ensemble. In general, the identified numbers of cyclones with 1, 2, 3, ... days lifetime are similar in all members of the ensemble. The only exception is member U2, where considerably more cyclones are identified with less than 2 days lifetime. Furthermore, using relative vorticity at 850 hPa geopotential level as a second variable, B1, B2, B3 identify somewhat less cyclones in each category than the corresponding U1, U2, U3. On higher levels the effects of orography are smaller and the meteorological fields are smoother, therefore, relatively more longer-lived cyclones can be identified in case of U3 and B3 than using the other variables closer to the surface. The difference between U3 and B3 are so small that it cannot be detected on the scale of the histogram, but the limiting effect of using the relative vorticity together with the basic variable

can be detected in this case, too. The small difference might be due to the fact that in both cases the used variables are from the 850 hPa level, which is less sensitive to the orography and does not show the thermal lows. Furthermore, in case of B3, the tilt of the cyclone axis does not complicate the identification of the cyclone centers, unlike in case of B1 and B2, where two different levels are considered and two slightly biased extremes have to be connected to find a cyclone center.

For the further analysis, the mean of the ensemble is used, which incorporates the different characteristics of the ensemble members. Therefore, it gives a more reliable picture about the features of the identified cyclones.

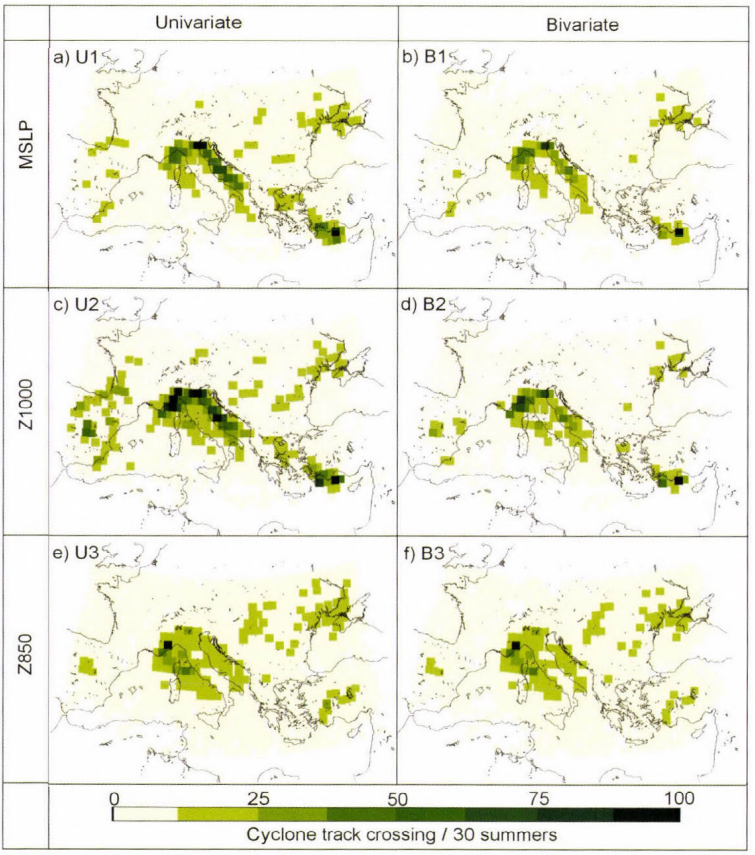

Fig. 3. Cyclone track density maps for summer (1981–2010) from the six members of the multivariable ensemble.

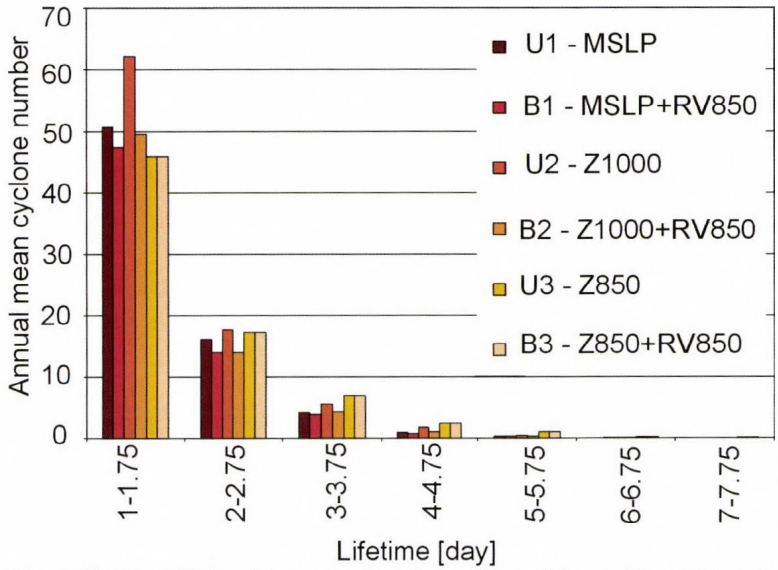

Fig. 4. Cyclone lifetime histogram for all members of the multivariable ensemble.

4.3. Annual cyclone distribution

The annual distribution of cyclones for the whole area is presented in *Fig. 5*. Geographical location and extension of the investigated area highly influence the cyclone frequency and its seasonal distribution. In our study we mainly focused on cyclogenesis areas of the Genoa region, the Aegean Sea, and Cyprus. Other low pressure areas (e.g., over the Iberian Peninsula, the Black Sea) might be also important, however, they are not completely covered here, since their locations are at the border of our domain. Cyclogenesis centers outside Europe (e.g., Saharan lows, Middle East cyclones) are not considered, either. The frequency analysis within the year suggests that the least number of cyclones is in summer. The only exception can be found when the univariate identification is applied using the 1000 hPa geopotential U2 field, in this case the minimum occurred in autumn. The largest and the smallest differences between frequency results of the various identifications occur in summer and winter, respectively. The cyclone identification methods result the maximum cyclone frequency in either spring or winter. Nevertheless, the maximum of the ensemble mean is in spring. Our findings are in a good agreement with those of *Hofstatter* and *Chimani* (2012), who analyzed *van Bebber*'s (1891) track V types between 1961 and 2002, and found their maximum frequency in April and minimum in July.

Cyclogenesis points are counted in every grid cell during the 30 years for every season and for every ensemble member. The results of the members are averaged seasonally, the ensemble means per season are presented in *Fig. 6*. The most active cyclogenesis area is certainly the Gulf of Genoa, which is basically permanent throughout the year. The absolute maximum of genesis event per $0.75°\times0.75°$ grid cell is in the summer near Cyprus (25 cyclogenesis in one particular grid cell per 30 years). Nevertheless, the spatial extensions of genesis centers are small in summer compared to the rest of the year, so the maximum genesis per grid cell is reached by having many genesis episodes in the same relatively small area, and not by having many cyclogenesis overall in the entire domain. The overall seasonal numbers of genesis in the whole area are higher in any other season than summer. The maximum number of cyclogenesis in the whole investigated area occurs in spring. The genesis area near Cyprus is also present throughout the year, but extends less than in the Gulf of Genoa. In both areas, the cyclones are mainly formed over the lee side of the mountains. In winter the Adriatic Sea appears as an additional genesis center, whereas in spring some genesis occur over the Aegean Sea, too. Finally, in summer the Iberian center becomes more prominent. Our findings strengthen the results of *Trigo et al.* (1999).

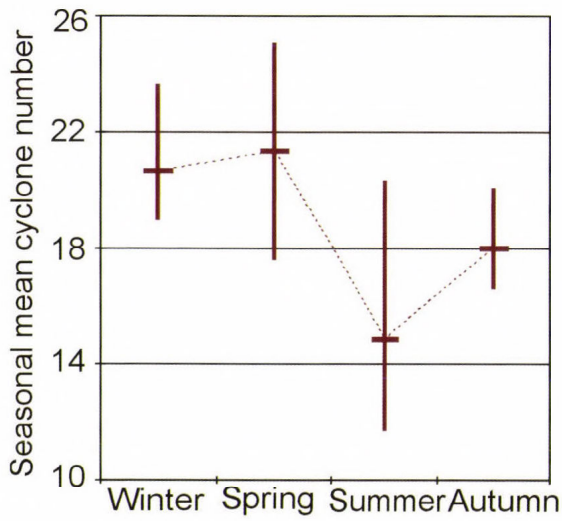

Fig. 5. Mean seasonal frequency of identified cyclone tracks using the 6 time series (horizontal line: ensemble mean, vertical line: ensemble spread).

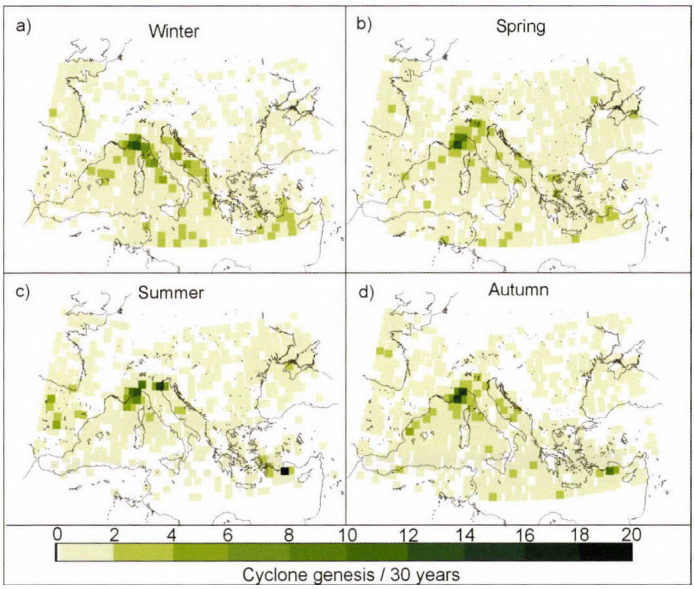

Fig. 6. Seasonal cyclogenesis center numbers from the mean of the multivariable ensemble (1981–2010).

The seasonal track density maps (*Fig. 7*) indicate seasonally the number of cyclone centers crossing each grid cell during the entire 30 years, averaged for the 6 ensemble members. (Note that the whole cyclone areas are not fully represented here, since we focus on the cyclone centers and their close vicinity only.) In general, the most frequent cyclone tracks are the Vd tracks from van Bebber's cyclone track classification (*van Bebber,* 1891), which typically turns south after Gulf of Genoa along the Adriatic Sea. The patterns in the equinox seasons are similar, the main differences listed as follows: (i) in spring the Black Sea cyclone pathway region is more extended and shows its largest activity, (ii) in autumn the region near Cyprus is more active with larger number of cyclones. This can be explained by the temporal extension of the high summer cyclone activity in the Cyprus area. The high track density regions concentrate around the genesis regions, i.e., the Gulf of Genoa, Cyprus, and the northern part of the Black Sea. The spatial extension of the cyclone track density is the largest in winter, whereas the maximum cyclone crossing per grid cell occurs in summer in an isolated point. This implies that the overall cyclone activity in the investigated area is the most intense in winter. The summer cyclones isolated maximum is due to that they tend to follow the same tracks, live shorter, and thus, they affect only the vicinities of their genesis region. This is highlighted in *Fig. 8,* which indicates that the ratio of short trajectories is the largest in summer. In *Fig. 5*, the annual number of spring cyclones is the highest of all season, but this cannot be seen in *Fig. 7*, where winter cyclones are spatially

more extent. This is explained by the fact that in spring the absolute value of short cyclones is maximal (*Fig. 9*). So the difference between the numbers of spring and winter cyclones is compensated by the length of the cyclone lifetime.

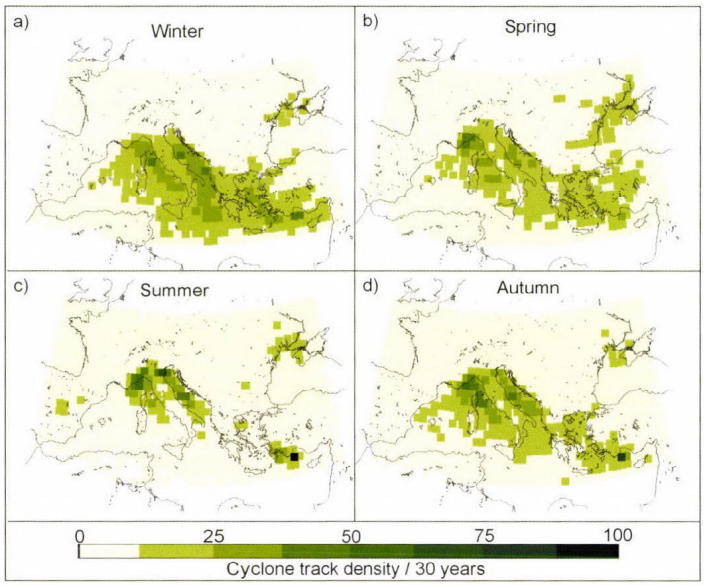

Fig. 7. Seasonal cyclone track density maps from the mean of the multivariable ensemble (1981–2010).

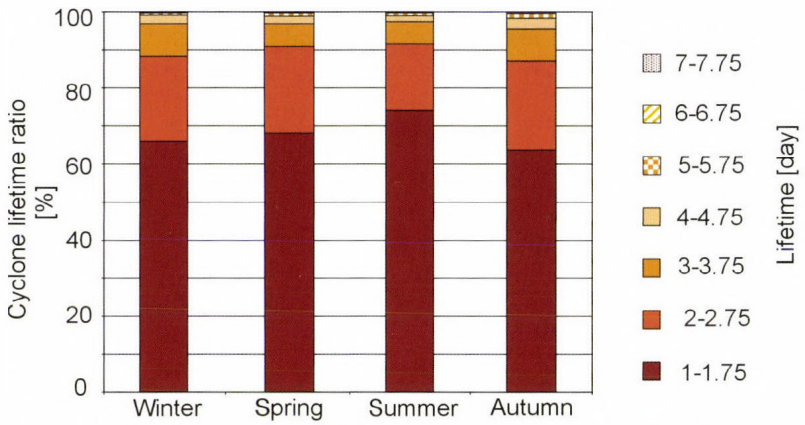

Fig. 8. Seasonal distribution of average cyclone lifetime frequency from the multivariable ensemble.

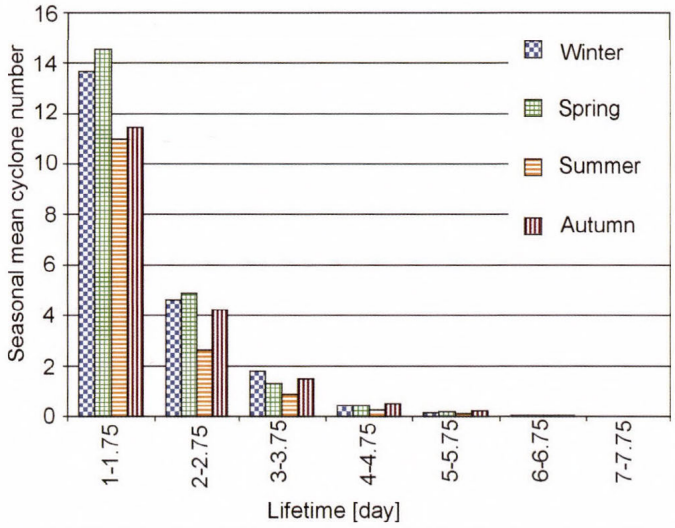

Fig. 9. Histogram of ensemble mean cyclone lifetimes for all seasons.

4.4. Trends

In the investigated 30 years, the changes in annual cyclone numbers are analyzed by calculating the linear trend coefficient of all ensemble members in each grid point. Then, the average value of the individual ensemble members is evaluated. *Fig. 10* shows the significantly positive (top) and negative (bottom) trend coefficients as well as the standard deviation (middle) of the ensemble coefficients. The majority of the significant trend coefficients are positive, located mainly along the Adriatic Sea and southwestern Turkey. Moreover, increasing cyclone numbers are present around the Balearic Island and Sardinia, the Pyrenees, Transylvania, Bulgaria, the Bosporus, and along the coasts of Tunisia. Decreasing tendencies are smaller and more dispersed, they are found at some parts of southern Italy, the region eastward from Malta, the middle part of France, and the northern part of the Black Sea along the Crimean Peninsula. The standard deviation of the ensemble members' trend coefficients shows that the difference between the ensemble members is larger where the detected change is larger.

4.5. Cyclones passing over Hungary

In our study, besides the full domain-based analysis, we also aim to evaluate the comprehensive role of the Mediterranean cyclones on the climate of the Carpathian Basin. For this purpose, those cyclones are selected, whose domain passed over Hungary.

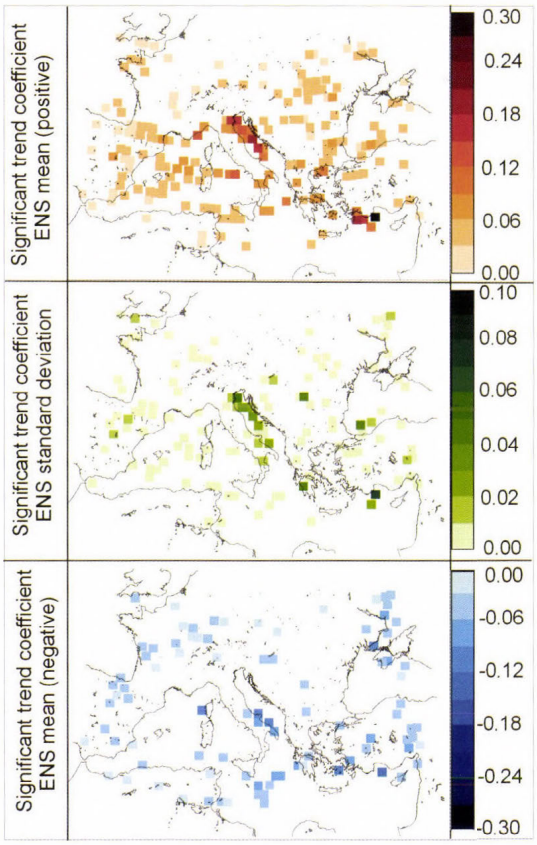

Fig. 10. Spatial distribution of significant trend coefficients (top and bottom: positive and negative coefficients of the ensemble mean, respectively, middle: standard deviation of the significant trend coefficients).

As a result of our analysis, we found that in an average year, roughly 30 cyclones influence the weather in Hungary. This does not include all cyclones affecting Hungary, but mostly the cyclones from the Genoa genesis area, since in our domain we focus on cyclones from the Mediterranean (*Fig. 7*). The time series (*Fig. 11*) correlate strongly with the time series of the whole area (upper part of *Fig. 1*), the correlation coefficient is 0.62, and it is statistically significant at the 0.05 level. The average spread of the ensemble is 11 cyclones/year, which is naturally less than the spread for the whole domain (23 cyclones/year). The local maxima of the cyclones passing over Hungary and the local maxima of all the identified cyclones are not always in the same years. The coincidence of the two maxima is more frequent towards the end of the period (e.g., in 1996, 2001, 2005, and 2010).

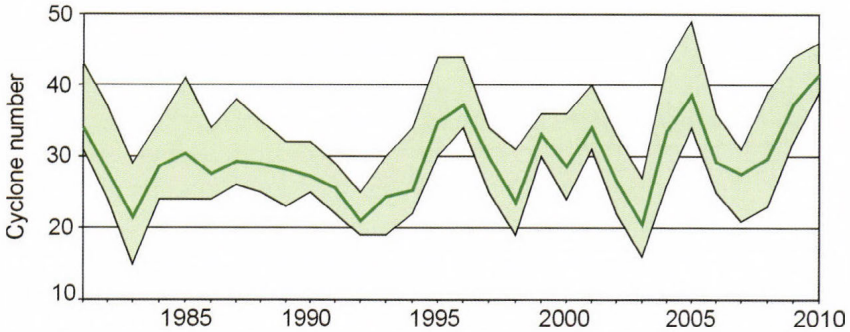

Fig. 11. Time series of the cyclones effecting Hungary from the multivariate cyclone identification ensemble. The solid line presents the mean of the ensembles (the average cyclone numbers in each year), and the light colored band presents the spread of the ensemble (the maximum and minimum cyclone numbers in each year).

The annual distributions of cyclone frequency over Hungary (*Fig. 12*) and the whole domain (*Fig. 5*) are somewhat different. Most of the cyclones occur in spring in both cases, however, the maximum is more robust for the Carpathian Basin, all members of the ensemble have their maximum occurrences in spring, and the relative difference between spring and the other seasons is larger than for the whole domain. Thus, the analysis suggests that the Mediterranean cyclones affect largely the spring weather of the Carpathian Basin. Furthermore, the largest spreads of the ensembles are in summer implying larger uncertainties in this season probably due to thermal lows.

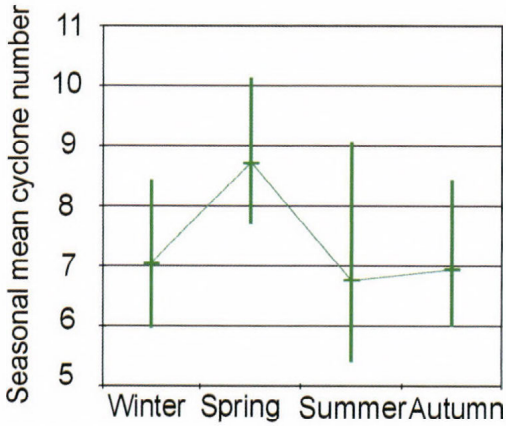

Fig. 12. Mean seasonal frequency of cyclone tracks passing Hungary from the 6 time series (horizontal line: ensemble mean, vertical line: ensemble spread).

5. Discussion

One of the main aims of the study is to develop an adequate cyclone identification method. The evaluation of the method starts by applying it on two different reanalyses, ERA Interim and NCEP-DOE R2, and comparing the results. This comparison provides useful information about the method itself, and also about the datasets. If the pattern or the general features of the results are similar then it can be concluded that the method is not sensitive to the small differences in the reanalyses. However, the differences of the cyclone numbers in the two reanalyses are probably due to general differences of the datasets. These are caused by the different systems used for the production, e.g., data assimilation, physical parameterizations, or the higher/lower resolution of the reanalyses. We found that the correlation is high between the results from the two reanalyses, and ERA Interim datasets include more cyclones. This clearly suggests that the method is adaptable for different datasets. The more cyclones in ERA Interim is probably due to the higher resolution, which better represents the orography, the physical processes, and also their effects. Thus, the primarily orographic cyclogenesis in the Mediterranean is identified more properly in ERA Interim.

Other studies also evaluated the differences between the cyclone climatologies using different reanalyses. For instance, *Hanson et al.* (2004) investigated North Atlantic cyclones between 1979 and 2001, identifying them through MSLP data from NCEP reanalysis (2.5°×2.5°) and from ECMWF ERA-15 reanalysis (1.125°×1.125°) (ERA-15 was extended using operational analyses for the end of the examined period). They concluded that the cyclone climatology from ECMWF data was more comprehensive at all scales. In addition, more very weak and more very strong cyclones were found using the ECMWF data than the NCEP data. *Trigo* (2006) compared storm-tracks using ERA-40 (T159 interpolated to a 1.125°×1.125° regular grid) and NCEP/NCAR (T62 interpolated to a 2.5°×2.5° regular grid) data in the December-March season between 1958 and 2000. It was shown that the main characteristics of genesis and lysis areas in the results of two reanalyses are similar, however, the numbers of storms differ appreciably. Similarly to *Hanson et al.* (2004), the higher resolution ECMWF reanalysis produced more cyclones than the NCEP/NCAR reanalysis. Furthermore, ERA-40 favored the detection of small (sometimes even subsynoptic) scale systems, which are present in the Mediterranean region (*Trigo et al.*, 1999). *Hodges et al.* (2011) compared four reanalyses, i.e., the ERA-Interim (T255), NASA-MERRA (2/3° longitude, 1/2° latitude), NCEP-CFSR (T382), and the JRA25 (T106), focusing on the winter cyclones in both hemispheres between 1989 and 2009. The number, spatial distribution, intensity distribution, track, and lifecycle of cyclones were all compared for the four reanalyses. The conclusions suggest that from a simple intercomparison it is not possible to decide which reanalysis represents the

reality better, only the disagreement between the results can be seen. They found that the spatial differences are small and not significant between the reanalyses, however, there are some orographic regions (e.g., the Mediterranean storm track) where the differences are relatively large. These differences might be the result of the different representation of orography in the reanalyses. Overall, the cyclone numbers and spatial distribution in the new, higher resolution reanalyses are similar, and more realistic than using the lower resolution reanalysis (i.e., JRA25).

According to the previous studies and our own experiences, cyclone identification in the Mediterranean region is difficult due to the frequent occurrence of small and weak systems. The comparisons of reanalyses suggest that (i) the high resolution reanalyses are more appropriate to recognize these systems, and (ii) ECMWF reanalysis is successful in identifying them.

Through the development of the objective cyclone identification method, several variables were tested but no clear distinction could have been made. Different variables have different advantages, so their ensemble are kept and analyzed. MSLP and 1000 hPa geopotential height are both close to the surface, which can be considered as a clear advantage, since a surface-based system is the object of the identification. On the other hand, they are more influenced by the orography, which is a disadvantage. Cyclones are defined as low pressure systems, this is why MSLP is one of the basic variables, but it is a derived field which can cause errors. Cyclones are also rotating systems, this is why relative vorticity at the 850 hPa level is included as a second variable. The advantage of using a second variable, next to the low level values is that only realistic, vertically extent formations are identified. The disadvantage of using the 850 hPa relative vorticity is that it might not be present through the whole lifetime of the cyclone, or it cannot be found in the vicinity of the first level extreme because of the tilt of the cyclone. Thus, the usage of two variables together limits the identified centers. These effects are less obstructive if both variables are from the same level, this is why geopotential height at 850 hPa level is also included. The disadvantage of this configuration is that the shallow, early, or occluding systems are not always detectable. The analysis of the results from the different ensemble members shows the potentials of the multivariable method. In the near-surface variables (Z1000 and MSLP), higher cyclone track densities are present than in the higher level (Z850). It does not necessarily entail that from the near-surface variables more cyclones are identified, just that the cyclones tend to use the same path more frequently. This can be due to the orography, which influences the variable fields, and thus, the tracking too. On the other hand, on the 850 hPa level more numerous longer trajectories are detected, the tracking is more successful than in the lower levels. Besides these differences between the basic variables, in general the use of an additional variable, i.e., relative vorticity, decreases the cyclone

number, but it affects less the longer trajectories. Thus, it serves mainly to omit the weak, short-lived cyclones.

The cyclones in the domain identified by the multivariable ensemble are dominantly the cyclones originated from the Gulf of Genoa, and also include some other genesis areas as southwestern Turkey, the Adriatic Sea and the Iberian Peninsula. The minimum cyclonic activity throughout the year is in summer, when the spread of the ensemble is the largest. The explanation for this probably is the appearance of thermal lows, which are not captured in all variables. They are not aimed to be captured anyway, since they are non-frontal pressure depressions. The most active period is the winter-spring half year. In spring there are more cyclones in our ensemble, but the track density maps show more spatially extent cyclone activity in winter. Although it seems to be a contradiction, winter cyclones have longer lifetimes so they contribute more to the track density maps than spring cyclones. Despite of the largest track density extension in winter, the isolated per grid maximum value is in summer. This means that the summer cyclones' paths more overlap, and produce extreme high track density in a cell than the winter cyclones'. The major cyclone pathway on the track density maps is van Bebber's Vd class, furthermore, Vb and Vc tracks are rare but sometimes occur.

Cyclones transport moisture, heat, and energy, that is why they have an important role in the local weather events of the area hit by their path. Both increase and decrease in their frequency can cause extreme events such as floods or droughts (e.g., *Grams et al.*, 2014). The investigation of trend coefficients in our analysis suggests that in the 30-year period, increasing linear trend is present in larger area than decreasing trend (almost twice as many grid cells). Also, the average of the positive trend coefficients is higher than the negative coefficients'. There are some more pronounced areas where the coefficients are higher, and in many neighboring grid cells the trends are statistically significant, e.g., over the Adriatic Sea. Nevertheless, there is no detectable sign of any north-south or west-east shift in the cyclone track densities.

The average radius of Mediterranean cyclones is between 300 km and 500 km (*Trigo et al.* 1999), their effects on local weather can certainly be observed in the whole area inside their domain not only focusing on their center regions. Therefore to select the cyclones affecting the weather of Hungary, the area where the domain of a cyclone swept through were calculated. The annual variability of these cyclones is a bit different from the general analysis. Namely, the most active season is clearly spring. The difference between spring and winter is almost as large as between spring and summer unlike in case of the entire domain. This implies that among the cyclones originated from the Gulf of Genoa, more cyclones follow northerly paths in spring than in winter.

6. Conclusions

Detailed cyclone analysis covering the time period between 1981 and 2010 was presented in this paper for the Mediterranean region. The spatial focus has been selected on the basis of the importance in influencing local weather throughout Southern and Central Europe, since these cyclones transfer moist air from the sea to the land and are often associated with heavy precipitation and/or flood events. On the basis of the discussed results, the following conclusions can be drawn.

(1) A multivariable cyclone identification and tracking process system was developed, which consists of uni- and bivariate modes of a general method with three basic variables (MSLP, geopotential height at 1000 hPa and 850 hPa), and one additional variable (relative vorticity at 850 hPa) in case of the bivariate mode. Evaluation of the individual ensemble members showed that the use of relative vorticity as a second field has a limiting effect. Furthermore, it was found that the methods using the 850 hPa level geopotential height and/or relative vorticity result in more long-lived cyclone tracks than the others. Overall, our results are in good agreement with previous analyses, highlighting that our developed method is appropriate to use for the identification of cyclones in the Mediterranean region.

(2) Data for the cyclone identification was derived from two reanalyses, i.e., ERA Interim and NCEP DOE R2 to evaluate both the method and the datasets. More cyclones were found using the ERA Interim data, mainly because of more numerous short-lived cyclones, which is probably due to the higher resolution of ERA Interim compared to NCEP DOE R2. Nevertheless, the time series of the two ensemble means from the two reanalyses correlate strongly with each other, therefore, we conclude that the method is not sensitive to small differences in the dataset. Due to the mentioned conclusions detailed analysis was presented only on the basis of cyclone tracks using ERA Interim datasets.

(3) The largest spread of the individual ensemble members occurred in summer possibly because of the presence of thermal lows. However, the spatial distribution of cyclone track density maps of the six ensemble members did not show large differences.

(4) The main cyclogenesis areas in the investigated domain are the Gulf of Genoa and the region around Cyprus, both located on the lee side of a mountain, which enhances cyclogenesis. Moreover, other minor cyclogenesis centrums can be identified over the Iberian Peninsula in summer and the Adriatic Sea in winter.

(5) The largest cyclone number occurred in spring, whereas the analysis of cyclone track density resulted in that the area affected by the cyclones is

the largest in winter, the circulation is more intense in winter. The cyclone lifetime analysis showed that although the number of cyclones is larger in spring than in winter, there are more short cyclones in spring, thus, they do not affect as large areas as winter cyclones. This implies that the cyclonic activity in the Mediterranean is mostly in the winter-spring period. The lowest cyclone activity was found in summer, also the total extension of cyclone passes is the least in summer, although the maximum value of cyclone tracks crossing a grid point occurs in summer. This means that although the number of cyclones is the lowest in summer, they are typically short-lived and they do not get too far from their genesis areas.

(6) The long-term tendencies of cyclone track density for the entire 30-year period are evaluated on the basis of the linear trend coefficients. Considering the whole domain, we found more grid points with statistically significant increasing trends than decreasing, and the absolute mean value of the trend coefficients is slightly higher in case of the positive trends than the negative trends. The most intense growing occurred along the Adriatic Sea and near Cyprus.

(7) In order to investigate the cyclones directly affecting the local weather in Hungary, the cyclone area is defined around the identified cyclone centers, and the cyclones whose domain affects the country are selected. The time series of the cyclones passing over Hungary correlate strongly with the cyclone number time series of the whole domain. The average frequency of Mediterranean cyclones passing over Hungary is 29.5 per year, most of them occurred in spring, similarly to the overall cyclone number in the whole investigated domain.

(8) Our presented results can serve as an adequate reference for further studies using global and regional climate model outputs for the identification of mid-latitude cyclones, which are key elements of the future climatological conditions, especially in Europe. For a complex region like the Mediterranean, the use of regional climate models is especially essential, since they are more appropriate to reconstruct and describe local features compared to the global climate models.

Acknowledgments: Research leading to this paper has been supported by the following sources: the Hungarian Scientific Research Fund under grant K-78125, the European Union and the European Social Fund through project FuturICT.hu (TÁMOP-4.2.2.C-11/1/KONV-2012-0013), also the AGRARKLIMA2 project (VKSZ_12-1-2013-0001).
The NCEP DOE Reanalysis 2 data for this study was provided by the NOAA/OAR/ESRL PSD, Boulder, Colorado, USA, from their website at http://www.esrl.noaa.gov/psd/. The ERA Interim data for this study was downloaded from the website of the European Centre for Medium-Range Weather Forecasts (ECMWF), http://data-portal.ecmwf.int/data/d/interim_full_daily/. We would like to acknowledge the organisations for their efforts to prepare these databases.

References

Alpert, P., Neeman, B.U., and *Shay-El, Y.,* 1990: Climatological analysis of Mediterranean cyclones using ECMWF data. *Tellus, 42,* 65–77.

Bartholy, J., Pongrácz, R., and *Pattantyús-Ábrahám, M.,* 2008: Analyzing the genesis, intensity, and tracks of western Mediterranean cyclones. *Theor. Appl. Climatol. 96,* 133–144.

van Bebber, W.J., 1891: Die Zugstrassen der barometrischen Minima nach den Bahnenkarten der Deutschen Seewarte für den Zeitraum von 1870–1890. *Meteorol. Z. 8,* 361–366.

Catto, J.L., Shaffrey, L.C., and *Hodges, K.I.,* 2010: Can Climate Models Capture the Structure of Extratropical Cyclones? *J. Climate 23,* 1621–1635.

Dee, D.P., Uppala, S.M., Simmons, A.J., Berridford, P., Polis, P., Kobayashi, S., Andrae, U., Balmaseda, M.A., Balsamo, G., Bauer, P., Bechtold, P., Beljaars, A.C.M., van de Berg, L., Bidlot, J., Bormann, N., Delsol, C., Dragani, R., Fuentes, M., Geer, A.J., Haimberger, L., Healy, S.B., Hersbach, H., Holm, E.V., Isaksen, L., Kallberg, P., Kohler, M., Matricardi, M., McNally, A.P., M.Monge-Sanz, B., Morcrette, J.J., Park, B.K., Peubey, C., de Rosnay, P., Tavolato, C., Thepaut, J.N., and *Vitart, F.,* 2011: The ERA-Interim reanalysis: configuration and performance of the data assimilation system. *Q. J. Roy. Meteor. Soc. 137,* 553–597.

Finnis, J., Holland, M.M., Serreze, M C., and *Cassano, J J.,* 2007: Response of Northern Hemisphere extratropical cyclone activity and associated precipitation to climate change, as represented by the Community Climate System Model. *J. Geophys. Res. 112(G4),* G04S42.

Grams, C.M., Binder, H., Pfahl, S., Piaget, N., and *Wernli, H.,* 2014: Atmospheric processes triggering the Central European floods in June 2013. *Nat. Hazard. Earth Sys. Discussions, 2,* 427–458.

Gulev, S.K., Zolina, O., and Grigoriev, S., 2001: Extratropical cyclone variability in the Northern Hemisphere winter from the NCEP/NCAR reanalysis data. *Climate Dynamics 17,* 795–809.

Hanson, C.E., Palutikof, J.P., and *Davies, T.D.,* 2004: Objective cyclone climatologies of the North Atlantic? A comparison between the ECMWF and NCEP Reanalyses. *Climate Dynamics 22,* 757–769.

Hodges, K.I., Lee, R. and *Bengtsson, L.,* 2011: A Comparison of Extra-tropical Cyclones in Recent Re-analyses; ERA-INTERIM, NASA-MERRA, NCEP-CFSR and JRA25. *J. Climate, 24,* 4888–4906.

Hofstätter, M. and *Chimani, B.,* 2012: Van Bebber's cyclone tracks at 700 hPa in the Eastern Alps for 1961–2002 and their comparison to Circulation Type Classifications. *Meteorol. Z. 21,* 459–473.

Hoskins, B.J. and *Hodges, K.I.,* 2002: New Perspectives on the Northern Hemisphere Winter Storm Tracks. *J. Atmos. Sci. 59,* 1041–1061.

Jansa, A., Genoves, A., Picornell, M.A., Campins, J., Riosalido, R., and *Carretero, O.,* 2001: Western Mediterranean cyclones and heavy rain. Part 2: Statistical approach. *Meteorol. Appl. 8,* 43–56.

Kanamitsu, M., Ebisuzaki, W., Woollen, J., Yang, S.-K., Hnilo, J.J., Fiorino, M., and *Potter, G.L.,* 2002: NCEP–DOE AMIP-II Reanalysis (R-2). *Bull. Amer. Meteorol. Soc. 83,* 1631–1643.

König, W., Sausen, R., and *Sielmann, F.,* 1993: Objective Identification of Cyclones in GCM Simulations. *J. Climate 6,* 2217–2231.

Lionello, P., Dalan, F., and *Elvini, E.,* 2002: Cyclones in the Mediterranean region: the present and the doubled CO 2 climate scenarios. *Climate Res. 22,* 147–159.

Maheras, P., Flocas, H.A., Patrikas, I., and *Anagnostopoulou, C.,* 2001: A 40 year objective climatology of surface cyclones in the Mediterranean region: spatial and temporal distribution. *Int. J. Climatol. 21,* 109–130.

Murray, R.J. and *Simmonds, I.,* 1991: A numerical scheme for tracking cyclone centers from digital data Part I: development and operation of the scheme. *Australian Meteorol. Mag. 39,* 155–166.

Muskulus, M., and *Jacob, D.,* 2005: Tracking cyclones in regional model data : the future of Mediterranean storms. *Adv. Geosci. 2,* 13–19.

Neu, U., Akperov, M.G., Bellenbaum, N., Benestad, R., Blender, R., Caballero, R., Cocozza, A., Darce, H.F., Feng, Y., Fraedrich, K., Grieger, J., Gulev, S., Hanley,J., Hewson, T., Inatsu, M., Keay,K., Kew, S.F., Kindem, I., Leckebusch, G.C., Liberato, M.L.R., Lionello, P., Mokhov, I.I., Pinto, J.G., Raible, C.C., Reale, M., Rudeva, I., Schuster, M., Simmonds, I., Sinclair, M., Sprenger, M., Tilinina, N.D., Trigo, I.F., Ulbrich, S.,Ulbrich, U., Wang, X.L., Wernli, H., 2013: IMILAST: A

Community Effort to Intercompare Extratropical Cyclone Detection and Tracking Algorithms. *Bull. Amer. Meteorol. Soc. 94,* 529–547.

Nielsen, J.W. and *Dole, R.M.,* 1992: A survey of extratropical cyclone characteristics during GALE. *Mon Weather Rev 120,* 1156–1167

Picornell, M.A., Jansá, A., Genovés, A., and *Campins, J.,* 2001: Automated database of mesocyclones from the HIRLAM(INM)-0.5° analyses in the western Mediterranean. *Int. J. Climatol. 21,* 335–354.

Pinto, J.G., Spangehl, T., Ulbrich, U., and *Speth, P.,* 2005: Sensitivities of a cyclone detection and tracking algorithm: individual tracks and climatology. *Meteorol. Z. 14, 823–838.*

Ruti, P.M., Somot, S., Giorgi, F., Dubois, C., Flaounas, E., Obermann, A., Dell'Aquila, A., Pisacane, G., Harzallah, A., Lombardi, E., Ahrens, B., Akhtar, N., Alias, A., Arsouze, T., Aznar, R., Bastin, S., Bartholy, J., Béranger, K., Beuvier, J., Bouffies-Cloché, S., Brauch, J., Cabos, W., Calmanti, S., Calvet. J-C., Carillo, A., Conte, D., Coppola, E., Dell'Aquila, A., Djurdjevic, V., Drobinski, P., Elizalde-Arellano, A., Gaertner, M., Galàn, P., Gallardo, C., Gualdi, S., Goncalves, M., Jorba, O., Jordà, G., L'Heveder, B., Lebeaupin-Brossier, C., Li, L., Liguori, G., Lionello, P., Maciàs, D., Nabat, P., Onol, B., Raikovic, B., Ramage, K., Sevault, F., Sannino, G., MV Struglia, Sanna, A., Torma, C., Vervatis, V., 2015: MED-CORDEX initiative for Mediterranean Climate studies *(submitted to BAMS, October 2011, resubmitted in August 2014, resubmitted in March 2015)*

Serreze, M.C., 1995: Climatological aspects of cyclone development and decay in the Arctic. *Atmosphere-Ocean, 33,* 1–23.

Sinclair, M.R., 1994: An objective Cyclone Climatology for Southern Hemisphere. *Month. Weather Rev. 122,* 2239–2256.

Ulbrich, U., Brücher, T., Fink, A.H., Leckebusch, G.C., Krüger, A., and *Pinto, J.G.,* 2003: The central European floods of August 2002: Part 2 –Synoptic causes and considerations with respect to climatic change. *Weather, 58,* 466–471.

Trigo, I.F., Davies, T.D., and *Bigg, G.R.,* 1999: Objective Climatology of Cyclones in the Mediterranean Region. *J. Climate 12,* 1685–1696.

Trigo, I.F., Davies, T.D., and *Bigg, G.R.,* 2000: Decline in Mediterranean rainfall by weakening of Mediterranean cyclones. *Geophys. Res. Lett. 27,* 2913–2916.

Trigo, I.F., 2006: Climatology and interannual variability of storm-tracks in the Euro-Atlantic sector: a comparison between ERA-40 and NCEP/NCAR reanalyses. *Climate Dynamics 26,* 127–143.

Wernli, H. and *Schwierz, C.,* 2006: Surface Cyclones in the ERA-40 Dataset (1958 – 2001). Part I: Novel Identification Method and Global Climatology. *J. Atmos. Sci. 63,* 2486–2507.

Woollings, T., Hoskins, B., Blackburn, M., Hassell, D., and *Hodges, K.,* 2010: Storm track sensitivity to sea surface temperature resolution in a regional atmosphere model. *Climate Dynamics 35,* 341–353.

IDŐJÁRÁS

Quarterly Journal of the Hungarian Meteorological Service
Vol. 119, No. 2, April – June, 2015, pp. 185–196

Thunderstorm climatology in Hungary using Doppler radar data

András Tamás Seres[1]* and **Ákos Horváth**[2]

[1]*Hungarian Defence Forces Geoinformation Service,*
Szilágyi E. fasor 7–9, H-1024 Budapest, Hungary
E-mail: seres.andrastamas@upcmail.hu

[2]*Hungarian Meteorological Service,*
Vitorlás u. 17, H-8600 Siófok, Hungary,
E-mail: horvath.a@met.hu

**Corresponding author*

(Manuscript received in final form June 20, 2014)

Abstract—This paper presents the results of an objective analysis on thunderstorm climatology in Hungary. The examination was based on composite PPI (plan position indicator) images made by Doppler radars of the Hungarian Meteorological Service between 2004 and 2012. In our research, thunderstorms were represented with so-called thunderstorm ellipses, and their time and spatial distribution were examined. Three types of thunderstorm ellipses and stormy days were defined with radar reflectivity set to 45, 50, or 55 dBZ. Most stormy days and ellipses happened in late spring and summer of 2007 and 2010. The daily frequency of these objects peaked in the late afternoon period. The detected ellipses had maxima in the north-eastern, north-central, and south-western parts of Hungary. Beyond information and characteristics from the past, these methods and results can be useful for forecasting severe thunderstorms.

Key-words: severe thunderstorm, Doppler radar, climatology, TITAN method, Hungary.

1. Introduction

Radar-based thunderstorm climatology has a long history in the United States. The first studies appeared in 1950s (*Braham*, 1958), followed by many other researches for different parts of the country (for example: *Myers,* 1964; *Henz,* 1974; *Falconer*, 1984; *Croft* and *Shulman,* 1989; *Mohee* and *Miller*, 2010). In the last two decades, some works have been carried out in this field in Europe (*Höller*, 1994; *Jaeneke*, 2001; *Rigo* and *Liasat*, 2002; *Weckwerth et al.*, 2010; *Rudolph et al.*, 2011; *Davini et al.,* 2012), South America (*Paiva Pereira* and

Rutledge, 2003), Canada (*Brimelow et al.*, 2004), and Australia (*Steiner* and *Houze*, 1996) as well.

The first Hungarian study on thunderstorm climatology was made by *Héjas* (1898), followed by *Raum* (1910). Some studies dealing with different aspects of thunderstorm climatology appeared in the 1960s (*Ozorai*, 1965; *Götz* and *Pápainé*, 1966; 1967). All these works were based on visual observations. Later, radar and satellite data (*Boncz et al.*, 1987; *Bodolainé* and *Tänczer*, 1991), then nowcasting methods (*Horváth* and *Geresdi*, 2003; *Horváth et al.*, 2007) appeared in the Hungarian studies. However, these works considered thunderstorms from mainly dynamical and synoptical aspects, so our work is the first attempt to examine thunderstorm climatology in Hungary using Doppler radar data. The first results of this research were presented by *Horváth et al.* (2008) but only for a shorter period.

The aim of this paper is to briefly describe the time and spatial distribution of severe thunderstorms detected by HMS's radars in the period of 2004 to 2012.

2. Methodology

2.1. Radar measurements

The first weather radar in Hungary was introduced in 1967. In the next decades, other locators were set in the country and the Hungarian Meteorological Service (HMS) built up its radar network system. By 2004, HMS's Soviet-made MRL-5 locators were replaced by modern Doppler radars.

Hungary is covered by three weather radars: (the western, the central, and the eastern locators, and they all operate on C-band (wave length = 5 cm) (*Geresdi*, 2004). During the measurement, the Doppler-wind was applied for noise filtering and the results were upgraded, filtered, and smoothened into composite fields. From each scan column, the highest reflectivity values were taken (*Collier*, 1996). The resolution of the composite PPI (plan position indicator) images was 2 km × 2 km in space and 15 minutes in time. To further reduce noises of reflectivity, median-filter method (*Tukey*, 1977) was also used before beginning the analysis.

2.2. Core of the methodology: the TITAN method

The TITAN (Thunderstorm Identification, Tracking, Analysis and Nowcasting) method was developed by *Dixon* and *Wiener* (1993). Using the identification part of this method the irregular-shaped thunderstorms detected by radar could be characterized by regular ellipses. The main point of identification is as follows: the parameters of the ellipses are determined by the covariance matrix of the isolated, irregular-shaped cluster on the image using the condition that the area of the cluster and the ellipse has to be equal. With this method, the focus

points and the equation of the ellipses could easily be determined and the objects were visualized by the Hungarian Advanced WorKstation (HAWK) system developed by HMS (*HMS*, 2012). These calculated ellipses were called thunderstorm ellipses (*Horváth et al.*, 2008). The detailed background of the identification method is given in the *Appendix*.

Two types of thresholds: the area limit ($N_{minlimit}$) and the reflectivity limit ($R_{minlimit}$) were defined. The area threshold determined the minimum area of a cluster. In our examination $N_{minlimit}$ was set to 5 radar pixels (which equals to 20 km^2). The reflectivity threshold specified that each pixel of the cluster (in our case 5 pixels) had to reach this limit. $R_{minlimit}$ was set to 45 dBZ, 50 dBZ, and 55 dBZ and these objects were named severe, highly severe, and extremely severe thunderstorm ellipses, respectively. Using these high reflectivity values, the detected cells could be considered as severe thunderstorms and the small or weak objects could be eliminated. The original radar image is presented in *Fig. 1a* for May 18, 2005 at 16:00 UTC, while ellipses with $N_{minlimit}$ = 5 pixels and $R_{minlimit}$ = 45 dBZ are visualized in *Fig. 1b*.

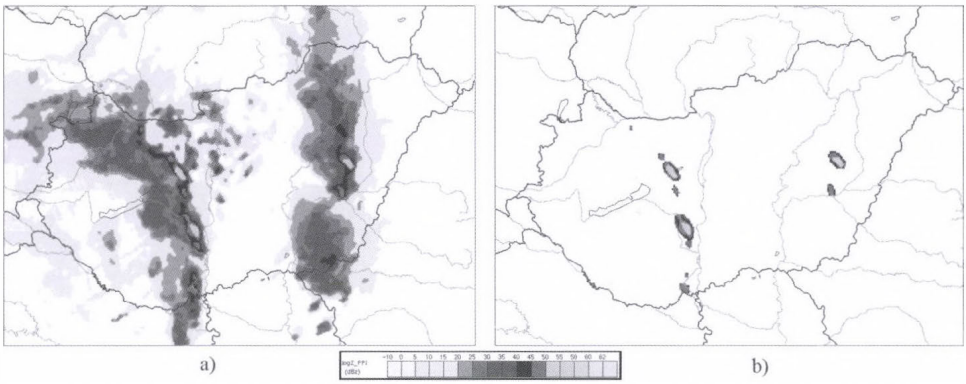

Fig. 1. Composite PPI radar images of thunderstorms observed on May 18, 2005, 16:00 UTC. Left: original image, right: image where thunderstorms were represented by ellipses.

3. Results

3.1. Time distribution of thunderstorm ellipses and stormy days

A day was called severe, highly severe, or extremely severe stormy day when at least one detected severe, highly severe, or extremely severe thunderstorm ellipse could be found on radar images. Using these data, the number of stormy days could be counted for a given time period.

The highest number of stormy days was counted in 2007 for all categories. The lowest values were detected in 2005 for extremely severe days and in 2012 for the other two types (*Table 1*). About 80 to 95% of stormy days and 97 to 98% of thunderstorm ellipses were detected between April and September, therefore this period was called thunderstorm season. The stormiest month was July followed by June, August, and May. Other months had much lower values (*Fig. 2*). On average, 118 severe, 82 highly severe, and 20 extremely severe ellipses were detected on a stormy day in the thunderstorm season. Note that these calculated values are not equal to the number of thunderstorms, because a severe thunderstorm may appear on subsequent radar images. *Table 2* shows the time distribution of days with at least 50 or 100 objects. The maxima were in 2007 and 2010, while 2004, 2005, and 2012 had the lowest values. The highest number of severe thunderstorm ellipses (1,115 objects) were detected on August 20, 2007, while for the other two types, June 14, 2010 had the highest values (527 and 139 ellipses). According to ECMWF (European Centre for Medium-Range Weather Forecast) analysis, on these days a cold front of a northern cyclone reached the country.

The daily cycle of these ellipses was also investigated (*Fig. 3*). Only results for the thunderstorm season are shown in this paper. The minima of appearance were detected at 8:30 and 9:15 for severe, 8:30 for highly severe, and 7:00 for extremely severe ellipses. The time distribution of the objects was asymmetric and the maxima were at 16:45 for severe, 16:30 for highly severe, and 16:30 and 17:30 for extremely severe ellipses.

Table 1. Annual distribution of severe, highly severe, and extremely severe stormy days in the period of 2004 to 2012.

Year	Severe stormy days	Highly severe stormy days	Extremely severe stormy days
2004	189	116	44
2005	188	101	26
2006	169	107	38
2007	190	121	69
2008	142	94	40
2009	142	102	45
2010	141	93	53
2011	136	99	52
2012	122	90	43
Average	*158*	*103*	*46*

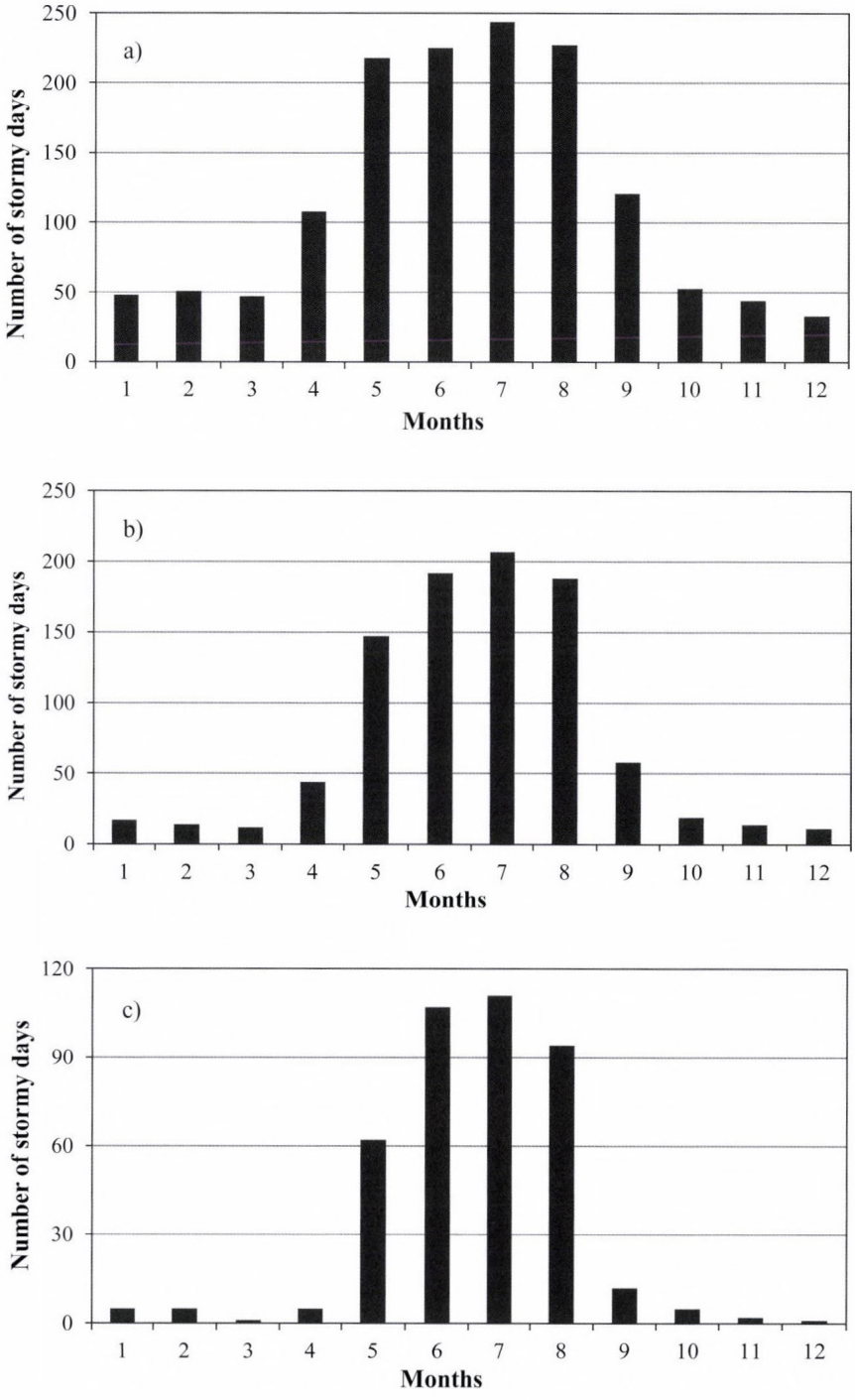

Fig. 2. Annual course of a) severe, b) highly severe, and c) extremely severe stormy days in the period of 2004 to 2012.

Table. 2. Annual distribution of days with 50 or 100 severe, highly severe, or extremely severe ellipses in the period of April to September between 2004 and 2012.

Year	Days with at least 50			Days with at least 100		
	severe	highly severe	extremely severe	severe	highly severe	extremely severe
	ellipses			ellipses		
2004	57	12	1	34	6	0
2005	45	10	0	30	2	0
2006	61	18	1	39	13	0
2007	75	40	1	59	19	0
2008	65	20	2	42	12	0
2009	62	15	1	42	4	0
2010	67	35	2	54	20	1
2011	72	32	3	53	16	0
2012	54	23	0	36	8	0
Average	*62*	*23*	*1*	*43*	*11*	*0*

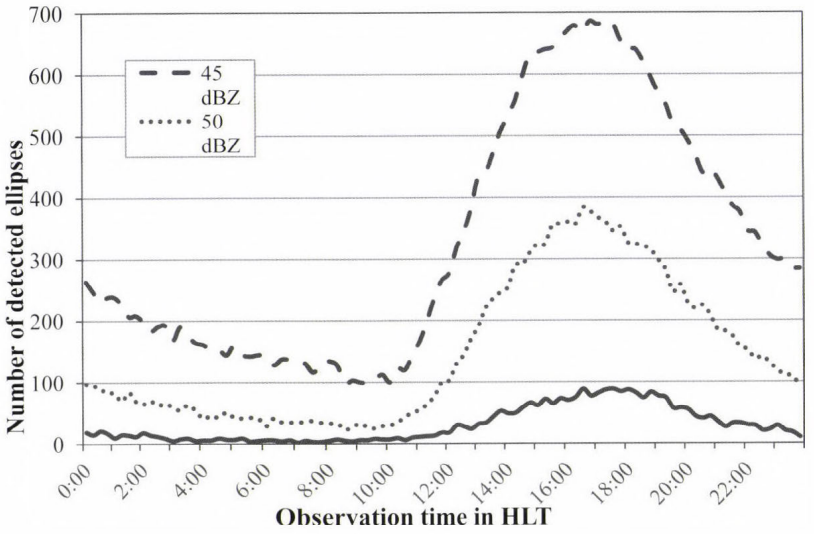

Fig. 3. Daily cycle of the detected severe (45 dBZ), highly severe (50 dBZ), and extremely severe (55 dBZ) thunderstorm ellipses in the period of April to September between 2004 and 2012. The time resolution is 15 minutes. Times are given in Hungarian Local Time (HLT = UTC + 2 hours).

3.2. Spatial distribution of thunderstorm ellipses

The spatial distribution of thunderstorm ellipses was analyzed by constructing thunderstorm statistic maps. The area resolution was set to 18 km×18 km.

Thunderstorm statistic maps were created for the entire year in the period of 2004 to 2012, but only results for the thunderstorm season are represented in this paper. Between October and March, there was only a few objects detected, while the measurement noises were high, especially in the early years. During the nine-year period, the maxima of severe, highly severe, and extremely severe thunderstorm ellipses were detected mostly in the north-eastern, north-central, and south-western parts of Hungary. Fewer objects appeared in the north-western and south-eastern parts of the country. Note that minima were mostly far from radars; these lower values could be originated to detecting problems (*Fig. 4*).

4. Summary and conclusions

This paper presents the results of an objective, radar-based analysis on thunderstorm climatology in Hungary for the nine-year period of 2004 to 2012. Most stormy days and ellipses were detected in late spring, summer and in 2007, 2010. The daily frequency of these objects peaked in the late afternoon period. The detected ellipses had maxima in the north-eastern, north-central, and south-western parts of Hungary. Beyond information and characteristics from the past, these methods and results can be useful for forecasting severe thunderstorms. The cell-detection algorithm should be more integrated into automatic warning systems or can be used in researches on supercells. In the future, this objective examination can be carried out for previous years but better noise-filtering methods should be developed. Furthermore, satellite and lightning data can be combined with these results as well.

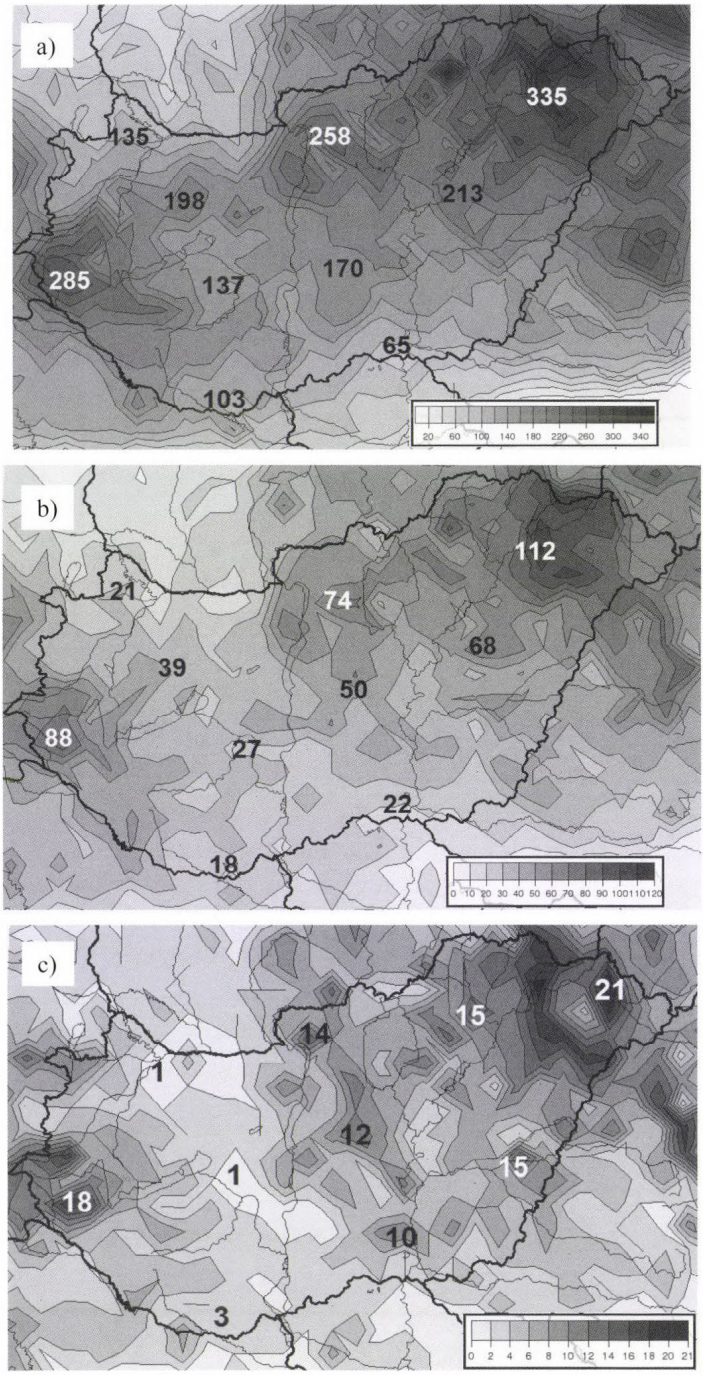

Fig. 4. Spatial distribution of a) severe, b) highly severe, and c) extremely severe thunderstorm ellipses in the period of April to September between 2004 and 2012. The area resolution is 18 km×18 km. These images were visualized by the Hungarian Advanced WorKstation (HAWK) system developed by the Hungarian Meteorological Service.

Appendix

Mathematical background of the identification

The method of calculating ellipses is as follows (*Dixon* and *Wiener*, 1993): Suppose there is an irregular cluster on a radar image which has n detected pixels. The center of a cluster is defined by

$$\bar{x} = \frac{1}{n}\sum_{i=1}^{n} x_i , \quad \bar{y} = \frac{1}{n}\sum_{i=1}^{n} y_i , \tag{1}$$

where x and y indicate the longitude and latitude of pixels which have reflectivity higher than a given threshold value. The covariance matrix of this cluster is

$$A = \mathrm{cov}_{xy} = \begin{bmatrix} d & e \\ e & f \end{bmatrix}, \tag{2}$$

where d is the deviation from the center by the x coordinate

$$d = \frac{1}{n-1}\sum_{i=1}^{n} (x_i - \bar{x})^2 , \tag{3}$$

f is deviation from the center by the y coordinate

$$f = \frac{1}{n-1}\sum_{i=1}^{n} (y_i - \bar{y})^2 , \tag{4}$$

and e is

$$e = \frac{1}{n-1}\sum_{i=1}^{n} (x_i - \bar{x})(y_i - \bar{y}) . \tag{5}$$

The eigenvalues of the covariance matrix are given by

$$\lambda_1, \lambda_2 = \frac{(d+f) \pm \left[(d+f)^2 - 4(df - e^2)\right]^{1/2}}{2} \tag{6}$$

The normalized eigenvectors of this matrix are

$$\nu = \left[\frac{1}{(1+g)^2}\right]^{1/2}, \qquad \mu = -g\nu, \tag{7}$$

where

$$g = \frac{f + e - \lambda_1}{d + e - \lambda_2}. \tag{8}$$

Then the rotation of the ellipse major axis relative to the x axis is given by these vectors

$$\theta = \tan^{-1}\left(\frac{\nu}{\mu}\right). \tag{9}$$

The eigenvalues of the covariance matrix (λ_1 és λ_2) represent the variances of the data (pixels)

$$\sigma_{major} = \lambda_1^{1/2}, \qquad \sigma_{minor} = \lambda_2^{1/2}. \tag{10}$$

The area of the detected cluster is

$$A = ndxdy, \tag{11}$$

where dx and dy are the grid spacing on the radar image.
The area of an ellipse is given by

$$T = \pi ab, \tag{12}$$

where a and b represents the major and minor axes of the ellipses.
The main idea is that the area of the irregular cluster and the area of the ellipse have to be equal, therefore

$$A = T\,. \tag{13}$$

So the major and minor axes of the ellipses can be calculated by

$$a = \sigma_{major}\left(\frac{A}{\pi\sigma_{\min or}\sigma_{major}}\right)^{1/2}, \qquad b = \sigma_{\min or}\left(\frac{A}{\pi\sigma_{\min or}\sigma_{major}}\right)^{1/2}. \tag{14}$$

With these parameters $(\bar{x}, \bar{y}, a, b, \theta)$, the focus points and the equation of the ellipse can be determined.

References

Bodolainé, J. E. és *Tänczer, T.*, 1991: Instabilitási vonal regionális ciklonban. *Időjárás 95,* 178–195.

Bodolainé, J.E. és *Tänczer T.*, 2007: Mezoskálájú konvektív komplexumok (szerk.: Horváth, Á.) A légköri konvekció, Országos Meteorológiai Szolgálat, Budapest, 35–45.

Boncz, J., Kapovits, A., Pintér, F. and *Tänczer, T.*, 1987: A method for the complex analysis of synoptic weather radar and satellite data. *Időjárás 91*, 11–22.

Braham, R.R., 1958: Cumulus cloud precipitation as revealed by radar- Arizona 1955. *J. Meteor. 15*, 75–83.

Brimelow, J.C., Reuter, W.G., Bellon, A. and *Hudak, D.*, 2004: A Radar-Based Methodology for Preparing a Severe Thunderstorm Climatology in Central Alberta. *Atmosphere-Ocean 42,* 13–22.

Collier, C.G., 1996: Application of weather radar system: A Guide to uses of radar in meteorology and hydrology. John Wiley & Sons,

Croft, P.J. and *Shulman, M.D.*, 1989: A five-year radar climatology of convective precipitation for New Jersey. *Int. J. Climatol. 9,* 581–600.

Davini, P., Bechini, R., Cremonini R. and *Cassardo, C.*, 2012: Radar-Based Analysis of Convective Storms over Northwestern Italy. *Atmosphere 3*, 33–58.

Dixon M. and *Wiener, G.*, 1993: TITAN: Thunderstorm Identification, Tracking, Analysis and Nowcasting – A radar-based methodology. *J. Atmos. Ocean. Tech. 10,* 785–797.

Falconer, P.D., 1984: A Radar-Based Climatology of Thunderstorm Days across New York State. *J. Appl. Meteorol. 23,* 1115–1120.

Geresdi, I., 2004: Felhőfizika. Dialog Campus, Budapest, 153–170.

Götz, G. és *Pápainé, Sz. G.*, 1966: Zivatartevékenység a nyári félévben Magyarországon. *Időjárás 70,* 106–116.

Götz, G. és *Pápainé, Sz. G.*, 1967: Zivatartevékenység a téli félévben Magyarországon. *Időjárás 71,* 302–309.

Henz, J., 1974: Colorado High Plains thunderstorm systems - a radar synoptic climatology. Colorado St. Univ., M.S. thesis.

Héjas, E., 1898: Zivatarok Magyarországon az 1871-től 1895-ig terjedő megfigyelések alapján. Királyi Magyar Természet Tudományi Társulat, Budapest, 174 pp.

Höller, H., 1994: Mesoscale organization and hailfall characteristics of deep convection in Southern Germany. *Beitr. Phys. Atmosph. 67,* 219–234.

Horváth, Á. and *Geresdi, I.*, 2003: Severe storms and nowcasting in the Carpathian Basin. *Atmos. Res. 67–68,* 319–332.

Horváth, Á., Ács, F. and *Seres, A. T.*, 2008: Thunderstorm climatology analyses in Hungary using radar observations. *Időjárás 112,* 1–13.

Horváth, Á., Geresdi, I., Németh, P. and *Dombai, F.*, 2007: The Constitution Day storm in Budapest: Case study of the August 20, 2006 severe storm. *Időjárás 111,* 41–65.

Hungarian Meteorological Service, 2012: HAWK-3 visualization system. http://www.met.hu/en/omsz/tevekenysegek/hawk/

Jaeneke, M., 2001: Radar Based Climatological Studies of the Influence of Orography of Thunderstorms Activity in Central Europe. In: Proceedings of the 30th International Conference on Radar Meteorology, Session 12A, Munich, Germany, 19-24 July 2001; p. 12A5.

Mohee, F.M. and *Miller, C.*, 2010: Climatology of Thunderstorms for North Dakota, 2002–06. *J. Appl. Meteorol. Climatol. 49,* 1881–1890.

Myers, J., 1964: Preliminary radar climatology of central Pennsylvania. *J. Appl. Meteor. 3,* 421–429.

Paiva Pereira, L.G. and *Rutledge, S.A.*, 2003: Convective Characteristics over the East Pacific and Southwest Amazon Regions: A Radar Perspective. EPIC 2001 Workshop, Boulder, CO, 15-16 September 2003.

Ozorai, Z., 1965: A zivatarok gyakorisága Budapest-Ferihegy repülőtéren. *Időjárás 69*, 375–377.

Raum, O., 1910: A Magyarországon észlelt 15 évi zivatarok megfigyelések eredményei az 1896–1910 időszakban. *Királyi Magyar Természettudományi Társulat Évkönyve 40, 2.*

Rigo, T. and *Liasat, M.C.*, 2002: Analysis of convective structures that produce heavy rainfall events in Catalonia (NE of Spain), using meteorological radar. Proc. ERAD, 45–48.

Rudolph, J.V., Friedrich, K. and *Germann, U.*, 2011: Relationship between Radar-Estimated Precipitation and Synoptic Weather Patterns in the European Alps. *J. Appl. Meteor. Climatol. 50,* 944–957.

Steiner, M. and *Houze, R.*, 1996: Sensitivity of the Estimated Monthly Convective Rain Fraction to the Choice of Z–R Relation. *J. Appl. Meteorol. 36,* 452–462.

Tukey, J.W., 1977: Exploratory Data Analysis. Addison-Wesley, Reading.

Weckwerth, T.M., Wilson, J.W., Hagen, M., Emerson, T.J., Pinto, J.O., Rife, D.L. and *Grebe, L.*, 2010: Radar climatology of the COPS region. *Q. J. Roy. Meteorol. Soc. 137,* 31–41.

IDŐJÁRÁS

Quarterly Journal of the Hungarian Meteorological Service
Vol. 119, No. 2, April – June, 2015, pp. 197–213

MEANDER: The objective nowcasting system of the Hungarian Meteorological Service

Ákos Horváth[1*], **Attila Nagy**[1], **André Simon**[2], and **Péter Németh**[2]

[1]*Hungarian Meteorological Service Storm Warning Observatory*
Vitorlás u. 17. H-8600 Siófok

[2]*Hungarian Meteorological Service,*
Kitaibel Pál u. 1., H-1024 Budapest, Hungary

**Corresponding author E-mail:horvath.a@met.hu*

(Manuscript received in final form March 3, 2015)

Abstract—In this paper, an overview of the complex nowcasting system of the Hungarian Meteorological Service is presented. The system named MEANDER started to work as a linear extrapolation process to provide warnings on convective storms. The role of the numerical weather prediction (NWP) models have been increased by involving the Weather Research and Forecasting (WRF) Model into nowcasting procedures. In the current state, MEANDER system consists of 2 main segments: NWP and linear parts.

In the NWP segment, WRF model is used in two steps: in the first step, WRF (WRF-ALPHA) is run at a 2.5×2.5 km horizontal resolution grid, using non-hydrostatic dynamics and ECMWF model data as initial and boundary conditions. The second step is a higher resolution (1.2×1.2 km) WRF model run – named WRF-BETA –, that uses lateral conditions and first guess data coming from WRF-ALPHA outputs and assimilates radar reflectivity, satellite and surface observation data. The domain of WRF-BETA is included in the domain of WRF-ALPHA. The applied nowcasting-specific assimilation helps the model to develop significant precipitating weather systems on the right location in the right time. WRF-BETA outputs provides such background information for the nowcasting system that makes the forecast of the linear segment more exact.

In the linear part, the actual objective analysis is considered at the beginning and the NWP prediction at the end of the nowcasting period. In the meantime, linear interpolation is applied. Radar data has key role in the nowcasting procedures in the linear segment, too. There are several derived parameters that are used for calculating the SYNOP-type present weather parameter for all grid points in the analysis and for the entire forecast time.

The MEANDER system has a warning process that is able to create weather warnings for all districts of Hungary, helping decisions of forecasters.

Key-words: nowcasting, nowcasting-systems, Weather Research and Forecasting Model (WRF), storm warning

1. Introduction

The term nowcasting is related to detailed analysis of the present state of the weather and to its very short-range (only few hours)[1] forecasts. Objective methods were developed for such purposes already in the 70-s and early 80-s of the previous century (*Browning*, 1982). Originally, the nowcasting techniques focused on the forecast of thunderstorms and on the extrapolation of radar or satellite images. Mathematical methods (e.g., fuzzy-logic techniques) or conceptual models have been developed to refine the analyses of the storms motion and to assess the development of precipitation bands (*Conway* and *Labrousse*, 1997). The extrapolation-based nowcasting systems can be cell-oriented, like the system TITAN (Thunderstorm Identification, Tracking, Analysis and Nowcasting, described by *Dixon* and *Wiener*, 1993) or can use object-tracking algorithms as the system COTREC (*Li et al.*, 1995; *Mecklenburg et al.*, 2000) or the system TREC (*Horváth et al.*, 2012). The extrapolation of radar echoes can be combined with several other kinds of observation data, parameterizations, conceptual models, thus, striving to emulate the approach of a human forecaster. An example of such (sometimes called expert) system is the NCAR Auto-Nowcaster (*Mueller et al.*, 2003). Some systems have been based on stochastic approaches to decompose the precipitation field in order to create an ensemble of nowcasts for several spatial scales – e.g., the system STEPS (*Bowler et al.*, 2006; *Foresti et al.*, 2014).

Several studies and demonstration cases showed that the performance of extrapolation methods is strongly limited. The predictability depends on the scale and intensity of the extrapolated precipitation (e.g., *Germann* and *Zawadzki*, 2002). Refinement of the extrapolation techniques (e.g., filtering of nonpredictable scales of precipitation described by *Turner et al.*, 2004) can increase the forecast lead time, but for higher intensities (occurring typically in convective environment), the forecast skills usually decrease very rapidly with time (shown e.g., by *Lee et al.*, 2009). This also motivated the use of forecasts of numerical weather prediction (NWP) models in nowcasting systems, already in the 90-s of the 20th century. NWP inputs have sometimes only support role in estimating the speed and direction of the motion of precipitation cells and their development (for example, in the GANDOLF system, described by *Pierce et al.*, 2000). Several nowcasting systems provide blending of the extrapolation methods with NWP data. This approach was used in the system NIMROD (Nowcasting and Initialization for Modeling Using Regional Observation Data System, described by *Golding*, 1998). Blending with NWP data is important for systems, which forecasts of temperature, wind, or other meteorological parameters generate besides

[1] At the beginning, the 0–1 or 0–2-hour period was denoted as nowcasting-range, but (perhaps as a consequence of increasing influence and use of numerical weather prediction models for nowcasting purposes) the 0–6-hour period is mentioned more often now.

precipitation nowcasts. For example, tendencies from NWP models are used in the nowcasting system INCA (Integrated Nowcasting through Comprehensive Analyses, described by *Haiden et al.*, 2011).

Current efforts to improve the forecasts (mainly beyond the 0–1 h forecast range) are closely related to assimilation of all available observational data (surface, radar, satellite observations, etc.) and preparation of a three-dimensional objective analysis, which can be used as initial condition in a high-resolution NWP model run. This is the basic approach for systems such as LAPS (Local Analysis and Prediction System, introduced in *Albers et al.*, 1996). The advance of the computational technology enabled frequent updates of the NWP models (so-called rapid update cycles), which can be either directly used for nowcasting purposes or for blending with extrapolation systems. Several assimilation techniques have been applied in order to improve the very short range NWP forecasts, e.g., nudging, 3DVAR, or ensemble Kalman Filter technique (an overview of these methods was given by *Sun et al.*, 2014).

Despite of advances in NWP techniques, it is recognized that the role of the conceptual models and forecasters in nowcasting is still important as shown during the WMO demonstration projects for Sidney and Beijing Olympic games (*Ebert et al.* 2004, *Wilson et al.*, 2010).

At the Hungarian Meteorological Service (OMSZ), subjective methods to forecast thunderstorm activities have been developed since the 1960-s based on surface and sounding data (*Bodolai*, 1954; *Götz* and *Bodolainé*, 1963a, 1963b, *Bodolainé et al.,* 1967). These studies were concentrating on prefrontal squall lines and severe thunderstorms. Methods were developed and applied to evaluate remote sensing data and introduce that information into weather warning (*Bodolainé*, 1980*; Boncz et al.,* 1987; *Bodolainé* and *Tänczer,* 1991; *Putsay et al.*, 2009). Because of the geographical environment, the Carpathian Basin is inherently susceptible to floods, and conceptual models were created to understand and recognize weather patterns responsible for local and regional scale floods (*Bodolainé* and *Homokiné*, 1984; *Bonta* and *Takács,* 1988; *Bodolainé* and *Tänczer*, 2003). Appearance of more accurate radar data and increasing number of automated weather stations created the need for developing objective nowcasting system MEANDER (mesoscale analysis, nowcasting and decision routines) that was introduced to operational service in the year of 2003 (*Horváth* and *Geresdi*, 2003). The first version of MEANDER was based on simple extrapolation of radar data. Later, using blending technique with NWP data, MM5 (*Dudhia*, 1993) model was applied as the background NWP tool. The analyses of MEANDER were also tested as input for the MM5 model (*Horváth*, 2005). In the last few years, several modifications and upgrades were done on the MEANDER system. In this paper the recent state of the nowcasting system of the Hungarian Meteorological Service is presented.

2. *Development of the MEANDER system*

Earlier versions of the nowcasting system used by the Hungarian Meteorological Service were linear extrapolation based procedures, and they focused on severe thunderstorms nowcast. For this reason, MEANDER considered radar-measured heavy precipitation echoes and these echoes were extrapolated using a constant motion vector field. Motion vectors were calculated from a background hydrostatic numerical model, taken the closest forecast time step to the actual time. For the motion vector calculation, density and wind component values of vertical model levels were applied. The calculation based on the idea, that thunderstorm cells are massive objects and their movement is determined by conditions in the surrounding vertical layers of the atmosphere (*Fig. 1*). The speed of the cloud is $\vec{V}^c$ and the mass of the cloud is represented by the sum of **n** vertical layers with each layer with ρ_i. The ***I*** momentum of the cloud can be written as

$$I = \sum_{i=1}^{n} \rho_i \vec{V}^c \quad .$$

The momentum of the cloud supposed to be equal to the sum of its environment momentum, thus

$$\sum_{i=1}^{n} \rho_i \vec{V}^c = \sum_{i=1}^{n} \rho_i \vec{v}_i^e \quad ,$$

where $\vec{v}_i^e$ represents the environment wind on the ith vertical level (taken from NWP). The above equation provides the cloud motion vector:

$$\vec{V}^c = \frac{\sum_{i=1}^{n} \rho_i \vec{v}_i^e}{\sum_{i=1}^{n} \rho_i} \quad .$$

The above calculated motion vector is useful for thunderstorms, but for stratiform precipitation it didn't work properly (*Horváth* and *Geresdi*, 2003).

Objective analysis of earlier MEANDER versions was based mainly on observations. The spatial and temporal resolution of available NWP was not high enough for effective use in meso-scale. Increase in density of surface observations enabled production of higher resolution surface analyses, but that was not physically consistent with higher level model data.

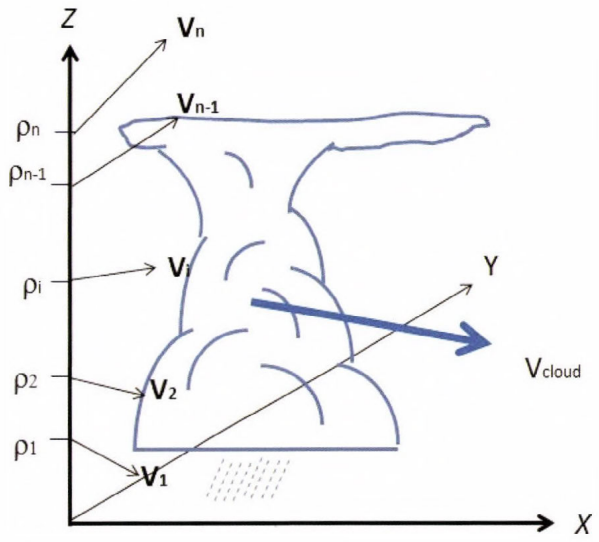

Fig. 1. Calculation of motion vectors for convective clouds. On the vertical axis ρi and Vi represents the vertical profiles of density and wind of the environment, *Vcloud* represents the cloud motion vector.

Installation of non-hydrostatic MM5 model allowed to use the blending technique for nowcasting: linear interpolation was applied instead of linear extrapolation. The system interpolated between the objective analysis at the beginning and the numerical forecast at the end of a nowcasting period (*Horváth*, 2005). The objective analysis used not only observation but, in addition, MM5 outputs as first guess information, and four dimensional data assimilation technique were applied to enhance the analysis (*Stauffer* and *Seaman*, 1990).

Motion vectors for radar echo replacement were also calculated from MM5 upper level wind data. Operational usage of high resolution satellite data also helped to improve the nowcasting, especially the cloud type and overcast part (*Putsay et al.*, 2010). Later versions of MEANDER considered not only convective but stratiform precipitation, too. A decision procedure determined that a precipitating system was stratiform or convective. For startiform systems, the average wind vector between 1000–4000 m proved to be the best parameter as motion vector.

The third generation of the MEANDER system is more NWP-based. The initial conditions provided by background NWP model are modified with

respect to certain significant, observed meteorological objects, using conceptual models. For example: radar detected thunderstorms are included in the initial model field in such a way, that convergence and divergence in the wind field and anomaly in the temperature and humidity field are placed to the appropriate location. These impacts allow the model (or at least give it a chance) to develop significant objects on the right location in the right time. The presently applied WRF model (*Skamarock et al.*, 2005) is able to manage these dynamically not balanced modification of first guess fields and, as it is shown later, WRF is able to provide corrected background data for the nowcasting system. Below, the currently used 3rd generation MEANDER system is presented.

3. Two-layer NWP background of the nowcasting system

The basic input data for the NWP segment of nowcasting are ECMWF deterministic model forecasts. Model level ECMWF data provide boundary conditions and first guess information for the non-hydrostatic WRF model. The WRF domain covers the Carpathian Basin with a 2.5×2.5 km horizontal resolution grid. This model version named WRF-ALPHA runs with 6-hour frequency and has 36-hour forecasting range. In addition to ECMWF data, surface and upper air measurements are also involved into initial conditions using WRF data assimilation tools (*Skamarock et al.*, 2005). WRF-ALPHA also uses special input coming from a stand-alone soil model that calculates soil humidity and soil temperatures on 4 soil layers. The soil model is based on the NOAH model (*Chen* and *Dudhia*, 2001), and it receives meteorological input data from MEANDER analysis (for example precipitation) and from previous WRF model run (surface fluxes, etc.). Calculated soil data are updated 4 times a day. The sensitivity of deep convection to soil condition of the Carpathian Basin was described by *Ács et al.*, 2010, and this sensitivity justifies special care of soil input data.

The second part of the NWP segment is based on a higher resolution WRF model run (1.2×1.2 km). In this model, named WRF-BETA, measured data have got higher role. First guess data originating from WRF-ALPHA input, observed temperature, humidity and wind data are assimilated using nudging facility of WRF. Two hours of nudging period are applied, i.e., the –2, –1, and 0-hour analyses are used (0 hours means the last time when analysis is available). Not only weather station data, but remote sensing information are also involved in the analyses. Especially at cases of thunderstorms, radar reflectivity can be involved into the analyses using conceptual models.

Thunderstorms can be identified by radar reflectivity in such a way, that ellipses are assigned to locations where radar reflectivity is higher than a threshold value (45 dBz). The ellipses procedure was developed in the TITAN method (*Dixon* and *Wiener*, 1993) and was applied – among of others – for

nowcasting related research (*Horváth at al.*, 2008; 2012). On locations where thunderstorms are detected, the analysis field is modified by the conceptual model as described below.

The model is based on the idea that a thunderstorm has an updraft and a downdraft channel. In the updraft channel, there is a positive temperature and humidity anomaly and there is significant convergence of the wind field at lower layers. The other pole of the thunderstorm is the downdraft channel where deficit in the absolute humidity (mixing ratio of water vapor) and divergence at lower layers can be found. The fuel of this "two-pole engine" is the humidity. Normally, the moisture is available from the basic analysis field, but the objective analysis is not necessary exact concerning the humidity analysis. To supply the thunderstorm with humidity in its initial phase, a humidity reservoir is added to the model with positive humidity anomaly and slight convergence at the lower layers (*Fig. 2*). The temperature profile of the updraft channel is calculated in such a way that equivalent potential temperature (EPT) is considered to be constant (*Fig. 3*), and EPT is calculated from the near surface layers supposing saturated air. In this way, the updraft channel of the thunderstorm appears as wet and warm bubbles in the analysis field (*Horváth*, 2006). The wind field is modified in lower layers (~lower 1000 m) to be convergent with respect to the center of the updraft channel. On the bottom of the downdraft channel the wind is divergent, blowing out of the center of the downdraft channel, and there is a weak depression in the field of absolute humidity. In the humidity reservoir, there is a weak horizontal flow in the direction of dual channels. The modification made by the conceptual model is added to the field of the objective analysis. Several numerical experiments were made to set parameters for the conceptual models. Experiments show that relatively little perturbation of humidity and wind values are enough for the conceptual model for triggering thunderstorms (*Fig. 4*). WRF model is tolerant of conceptual model made perturbations, and this triggering procedure helps to develop thunderstorms on proper place in proper time. The life time of triggered thunderstorm is more than 2 hours at about 70% of investigated cases. Sometimes the initial thunderstorms dissipated, but they made neighboring groups of incorrectly forecasted thunderstorms weaker or disappear.

Satellite data also can be used for WRF-BETA initial data by EUMETSAT provided SAFNWC information (*Derrien* and *Le Gléau*, 2005). Cloud mask and cloud type information allow to recognize opaque and thick cloudiness. Considering the mean value of cloud water mixing ratio (CLW) coming from WRF-ALPHA, it is possible to assign CLW values for cloudy areas. WRF-BETA accepts CLW as initial data and involving CLW does not increase numerical instability during the model run (numerical experiments were made to involve rain water into initial condition, but this input parameter increased the instability). Case studies showed that involving CLW has some positive influence on cloudiness, but improvement of this procedure is still under way.

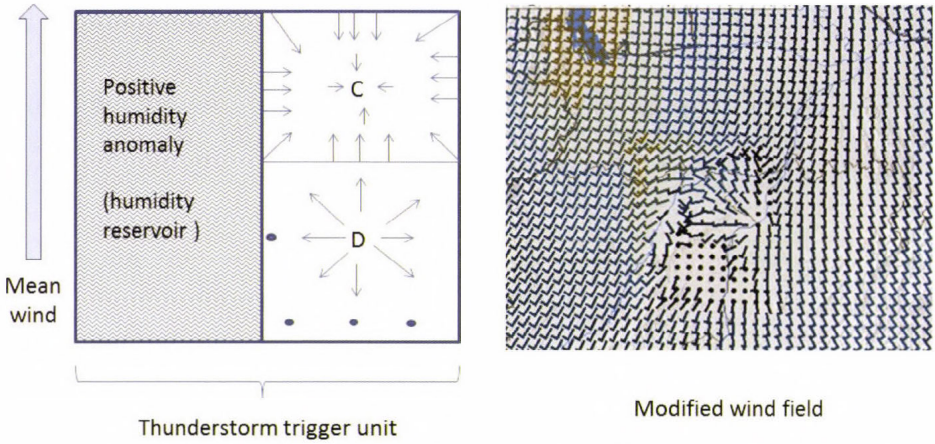

Fig. 2. The structure of a convective trigger unit (left) and the perturbed low level wind field (right). In the trigger unit, the square denoted by C represents the convergence in the updraft channel and letter D represents the divergence in downdraft channel. The right rectangle represents the humidity reservoir where is extra humidity added relative to the first guess to supply convection.

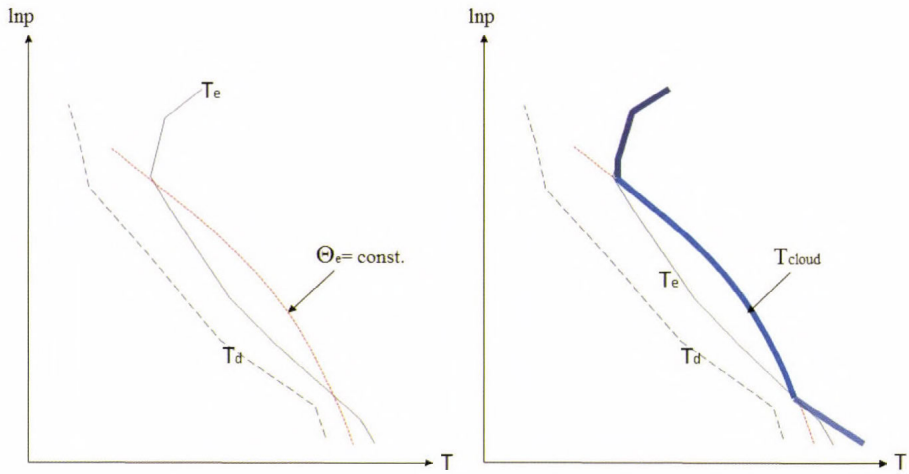

Fig. 3. Modification of the vertical temperature profile in the updraft channel of the triggering unit. In the original profile (left): T_e and T_d represents the temperature and dew point profiles of the first guess and θ_e shows the constant equivalent potential temperature (EPT) calculated from the lower 1000 m. The modified profile (right) is represented by the thick line.

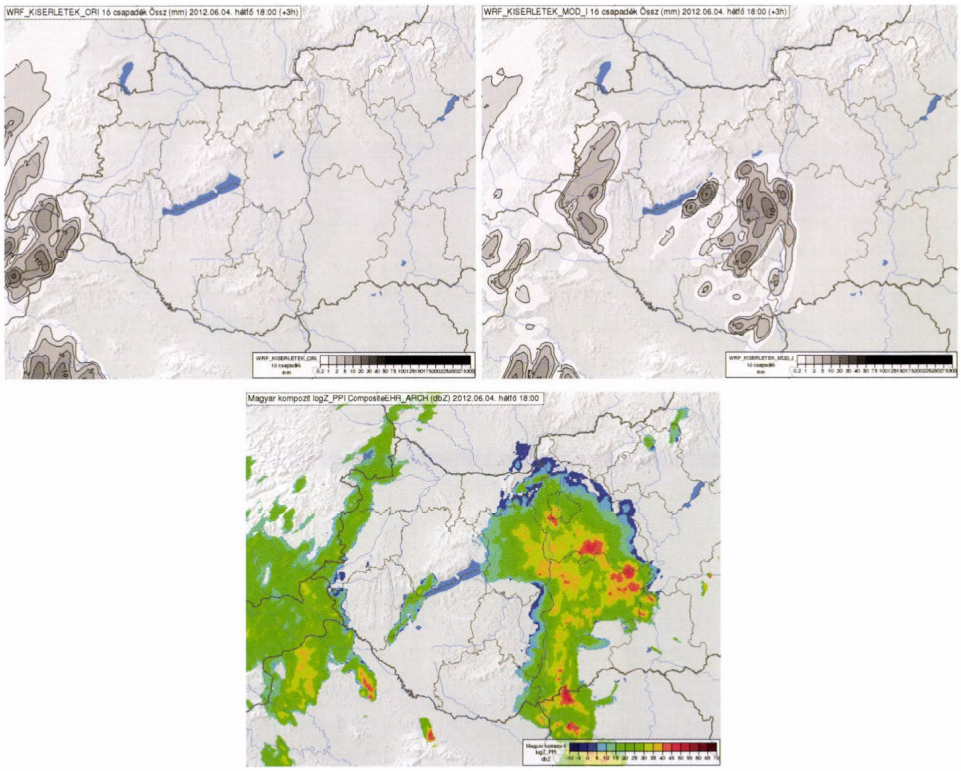

Fig. 4. 1-hour accumulated precipitation of +3-hour forecast of the WRF model at reference (upper left) and triggered forecasts (upper right) and the measured radar reflectivity (lower image). The model start time is 15:00 UTC June 4, 2012, the radar reflectivity image time is 18:00 UTC June 4, 2012. The triggered model run produced more realistic result than the reference run.

There are some derived parameters calculated as first guess data for nowcasting applications. The visibility for all grid points is computed from the lowest model level using mixing ratio of water vapor, cloud water, rain water, cloud ice, and snow (*Kunkel*, 1984). Radar motion vectors are calculated separately for convective and stratiform precipitating systems as described above.

In an ideal case, WRF-BETA should always be run when new observations are available. Because of limited computer power, WRF-BETA runs in every third hours providing NWP output for the nowcasting system for the next 8 hours with 15 minutes output frequency.

4. The linear segment of the nowcasting system

The linear segment of the MEANDER system consists of two parts: an objective analysis and a linear forecast. The objective analysis uses the coincidental WRF-BETA forecast, measured surface data, radar data, and satellite information. The grid of the objective analyses is the same as the WRF-BETA grid (1.2×1.2 km). During the objective analysis, derived parameters are also calculated, and finally, for all grid points, synoptic-type present weather code values (snow, rain, thunderstorm, etc.) are assigned. The frequency of the objective analysis is 10 minutes. From all objective analyses, a linear forecast is made for 3 hours ahead and updated in every 10 minutes.

The analysis segment uses WRF-BETA outputs as first guess data. For basic parameters, differences between observed and first guess values are calculated at all observation points. These differences are interpolated to all grid points using biharmonic spline procedure (BHS). Input for BHS are (1) coordinates of observation points, (2) coordinates of grid points of the objective analysis, (3) difference values between grid point and observation point data at the observation point. Outputs of BHS are interpolated differences at all grid points of the objective analysis. Finally, first guess data are corrected by the interpolated values at grid points.

In order to decrease representation error, grid points of first guess data are considered in the circle of radius R around an observation point. Differences between observation value and first guess values are calculated, and that grid point is chosen where the difference is the smallest. This minimum value is considered as the difference between first guess and observation as input (3) for BHS at the given observation. Coordinates of the observation point are taken to be equivalent to the coordinate of the chosen grid point as input (1) for BHS. This "wobbling observation" procedure proved to be useful on those locations, where the gradient of the considered parameter is large, for example at lake or sea side observation points or hilly regions. In practice, R is chosen 4 km for flat regions, and 5 km for hilly regions and lake side stations.

Radar data for the nowcasting system are from the Hungarian composite radar images that are created from 3 Doppler radars of the Hungarian Meteorological Service in every 5 minutes. The spatial resolution of radar information has the same order than the nowcasting grid has, so transformation of radar reflectivity data to the nowcasting grid does not cause distortion or data loss. Satellite data can also be projected to the nowcasting grid. Applied satellite data are NWCSAF products such as cloud cover, cloud type, cloud top temperature (*Derrien* and *Le Gléau*, 2013). When radar and satellite data are on the common platform of the nowcasting grid, a process compares them and eliminates large radar errors. This procedure (not detailed here) is important because of large number of commercial electromagnetic devices (for example WIFI devices) that make artificial noise and sometimes

remain in the reflectivity field despite filtering procedures of the radar facility.

The linear forecasting segment of the nowcasting system is based on the blending technique for basic parameters such as pressure, humidity, wind, and temperature. At the beginning of the 3-hour-long nowcasting period, the objective analysis is considered, and at the end there is an actual WRF-BETA forecasted data field. In the meantime, linear interpolation is applied (*Fig. 5*). Radar echoes can be advected using motion vector fields. (Motion vector fields, coming from WRF-BETA, are not permanent fields, but they are changing during the forecast time, so forecasted radar echoes are moving along fractionally linear paths.) The forecast of precipitating clouds allows the calculation of integrated precipitation using Marshal-Palmer form between radar reflectivity and rain intensity (*Marshal* and *Palmer*, 1948). In this procedure, the amount of precipitation is computed up to 3 hours, using 1 minute time step.

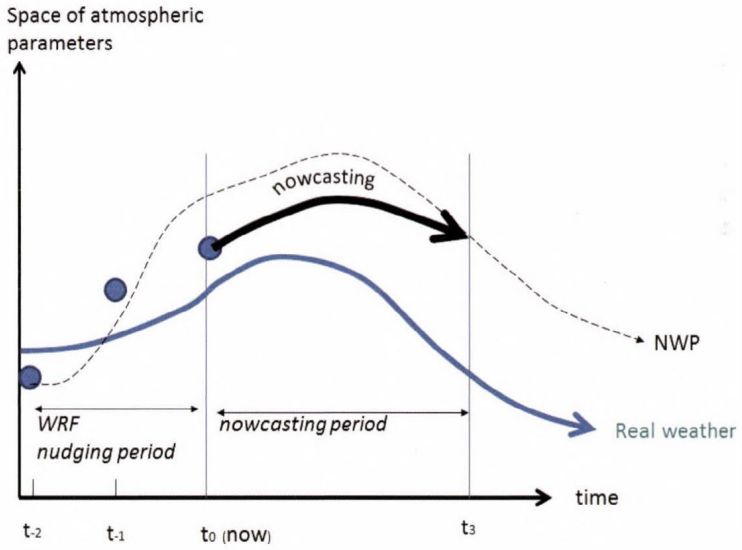

Fig. 5. Theoretical background of MEANDER system. Along the vertical axis the atmospheric parameters, on the horizontal axis the time are labeled. The continuous line represents the trajectory of the real weather, dashed line shows NWP forecast, circles represents objective analysis. The thicker solid line shows the nowcasting.

Derived parameters can be calculated at any time step of the nowcasting period. Among these parameters the precipitation phase, which frequently changes in wintertime, is especially important in the Carpathian Basin. There is a method developed by Geresdi (*Geresdi* and *Horváth*, 2000) to calculate the phase of precipitation applying cloud physics. The 1D cloud model is applied to calculate the cloud top, maximum updraft, and hailstone size of a potential thunderstorm (*Geresdi et al.*, 2004). The TREC method that was developed by the remote sensing division of the Hungarian Meteorological Service is also applied for the nowcasting system for 1 hour accumulated precipitation estimation (*Horváth et al.*, 2012). The radar based process considers previous radar reflectivity images and calculates a motion vector field taking correlations between two images. Motion vectors are applied to interpolate radar images with 1 minute temporal resolution in such a way, that radar echoes are replaced by motion vectors. Using these interpolated reflectivity images (and calculated precipitation intensity from that), the accumulated precipitation can be computed. A procedure calculates thunderstorm-associated maximum wind gust using the maximum radar reflectivity and the maximum cloud top height of cumulonimbus cells (*Bartha*, 1994). The convective wind field of a stormy day is shown in *Fig. 6*. Non-convective wind gusts are also computed from WRF-BETA, and this parameter is included in the objective analysis. During the forecast, it is blended with NWP data similarly to other basic parameters. The final result of derived parameters calculating procedure is "present weather" code values for all grid points. This parameter is depicted in similar way as the observed present weather parameters from WMO-SYNOP code.

Warning segment of the nowcasting system is designed to issue weather warning for the next 3 hours using the actual analysis and nowcasted present weather parameters. There are 3 warning levels, and the actual level is clearly defined by the previously calculated present weather code. (For example, there are three kinds of present weather code for thunderstorm in MEANDER: thunderstorm – first level; severe thunderstorm – second level; extreme thunderstorm – third warning level). There are 175 districts in Hungary, and the warning system generates individual weather warnings for those districts where it is justified by calculated present weather parameters. In the practice the forecaster on duty receives automatically generated warning maps on a special graphical user interface, and he or she can accept or interactively modify proposed information. Actual weather warnings appear on the warning page of the Hungarian Meteorological Service (http://met.hu/idojaras/veszelyjelzes/riasztas/). The flow chart of the nowcasting system is presented in *Fig. 7*.

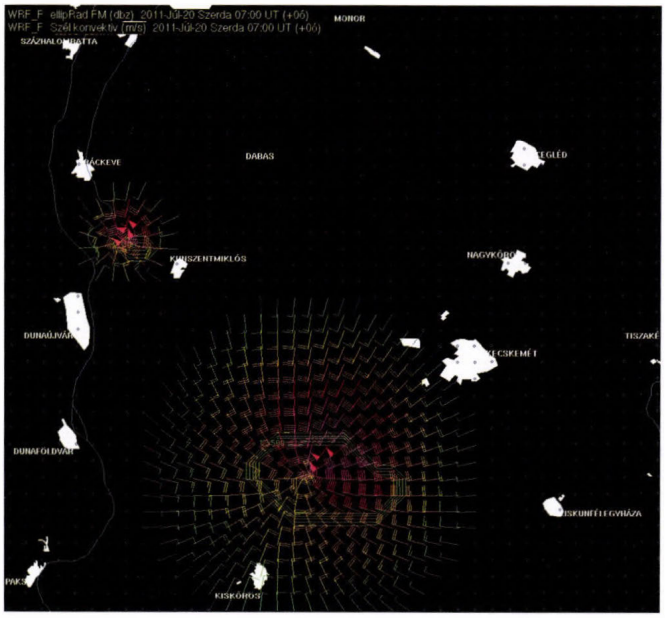

Fig. 6. Calculated convective wind field and thunderstorm contour lines on east of Danube at 07:00 UTC, July 20, 2011. That was a severe convective storm case caused serious damages near Kecskemét.

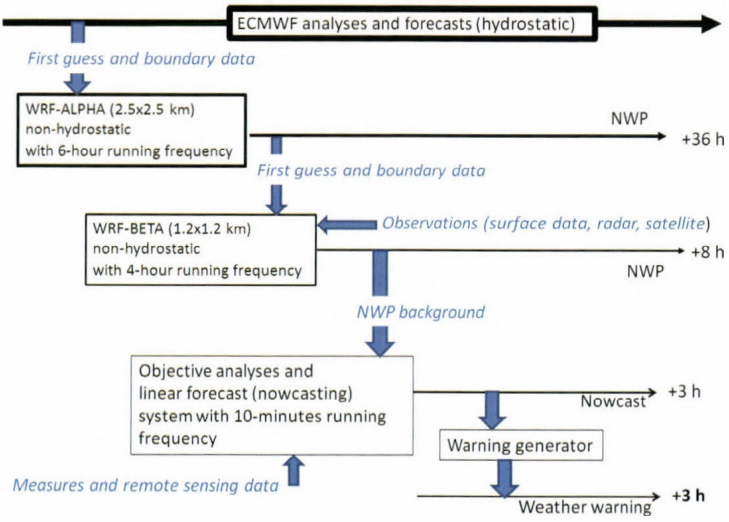

Fig. 7. Flow chart of the MEANDER system.

5. Evaluation and experiences

Concerning NWP (WRF-BETA) background, many case studies have been done to analyze the impact of radar assimilation made by the conceptual thunderstorm model. In about 70% of cases, the conceptual model has unambiguous positive impact up to 5 hours forecast. This way of introducing thunderstorm is safe, no significant gravity waves or other side effects were experienced. The limitation of the conceptual model is that it cannot be applied before first radar signs of thunderstorms appear. Currently used computer resources do not allow to run numerical models exactly in the same time when thunderstorms appear. The ideal solution would be a flexible NWP model run: WRF-BETA should run any time when the weather condition justifies that.

The nowcasting of the linear segment for basic parameters is verified by comparison of the analyses with earlier issued nowcasting at all grid points. Verification shows that basic parameters have relative small errors for the first 2 hours. The RMSE for temperature is above 0.5 °C, for pressure 0.1 hPa, for relative humidity 10%, and for wind speed 1.6 m/s. The precipitation forecast is highly dependent on the precipitation type. The forecast of stratiform precipitation is significantly better than forecast of convective precipitation (93% vs. 72%). There are problems with the verification of the derived parameters. For parameters like present weather, it is problematic to compare analysis fields with forecasts, because present weather itself is a derived parameter at the analysis time, too. Therefore, present weathers like freezing rain, severe thunderstorms can be verified via case studies, where inherently subjective visual observations are collected posteriorly. Case studies show that the most sensitive parameter is the precipitation phase and phase related present weather, especially freezing rain. Also, there is high spatial variability concerning visibility parameters. Most "nowcastable" significant present weathers are associated with stratiform precipitation like summer rain or winter snow. Severe convective storms and multicell thunderstorms can also be relative properly forecasted, especially when they are in developing phase and the advection is more decisive than developing. In the linear segment, the thunderstorm development has not been solved yet, the blending technique of radar observed cell transition to NWP simulated cell is still under development. The precipitation-associated parameters show significantly growing errors after 2 hours, hence in operational public usage only this forecast range is considered.

Evaluation of the warning segment shows better results than point-to-point comparison above. A district contains several grid points and the chance that weather objects hits at least a grid point in a district is definitely larger. Considering significant weather events, there is overestimation of weather warning for freezing rain and slight overestimation of severe convective events for 2 hours.

6. Summary

The MEANDER nowcasting system takes advantages of high resolution numerical modeling and very short range linear extrapolation. The hydrostatic ECMWF data are downscaled (in both time and space) to the resolution of the nowcasting system in two steps. During the first phase, the applied WRF (WRF-ALPHA) creates high resolution non-hydrostatic forecast 4 times a day. The WRF-ALPHA outputs are first guess and lateral condition data for a higher resolution WRF-BETA that produces forecast for the nowcasting domain with 1.2×1.2 km horizontal resolution. WRF-BETA uses nearly all available remote sensing and measured data and provides first guess information for the linear segment.

The linear segment uses observations for making analysis, which is the first pillar of the linear nowcasting. The second pillar is the WRF-BETA forecast that is considered at the end of the 3-hour-long nowcasting period. Radar located precipitating systems are moved in the linear segment using motion vector fields, calculated from WRF-BETA forecast. Derived parameters are computed during the linear segment, and finally, present weather values are assigned to all grid points. Finally, the warning segments are used to issue weather warnings for 175 districts of Hungary. The linear segment runs every 10 minutes, 24 hours a day.

Verifications and experiments show that the MEANDER system in the present stage provides usable forecast and warnings for the next 2 hours. Developing nowcasting-oriented assimilation techniques and more frequent model runs may help to extend this range in the near future.

References

Ács, F., Horváth, Á., Breuer, H., and *Rubel, F.*, 2010. Effect of soil hydraulic parameters on the local convective precipitation. *Met. Z.* 19,143–153.

Albers, S.C., McGinley, J.A., Birkenheuer, D.A., and *Smart, J.R.*, 1996: The local analysis and prediction system (LAPS): Analysis of clouds, precipitation and temperature. *Weather Forecast. 11*, 273–287.

Bartha, I., 1994: Development of a decision procedure for forecasting maximum wind gusts associated with thunderstorms. *Meteorol. Appl. 1*, 103–107.

Bodolai, I., 1954: A konvektív zivatarok aerológiai-szinoptikai feltételeiről. OMI Kisebb Kiadványai 27, OMSZ, Budapest. (in Hungarian)

Bodolainé, J.E, 1980: Radarral végzett csapadékmérések a csapadék rövidtávú előrejelzésben OMSZ Kisebb Kiadványai 48, OMSZ, Budapest. (in Hungarian)

Bodolainé, J.E, Bodolai, I. and *Böjti, B.*, 1967: Macrosynoptical conditions for the formation of Slovenian squall lines and some properties of cold fronts with thunderstorm. *Időjárás 71*, 129–143.

Bodolainé, J.E. and *Homokiné, U.K.*, 1984: A csapadékmennyiség előrejelzése az orografikus többlet figyelembevételével. *Az OMSZ Kisebb Kiadványai 57, OMSZ, Budapest.* (in Hungarian)

Bodolainé, J.E. and *Tänczer, T.*, 1991: Instabilitási vonal regionális ciklonban. *Időjárás 95*, 178–195. (in Hungarian)

Bodolainé, J.E. and *Tänczer, T.*, 2003: Mezoléptékű konvektív komplexumok. OMSZ, Budapest. (in Hungarian)

Boncz, J., Kapovits, A., Pintér, F. and *Tänczer, T.*, 1987: MÓdszer a szinoptikus-, radar- és műholdadatok complex analízisére. *Időjárás 91*, 11–22. (in Hungarian)

Bonta, I. and *Takács, Á.*, 1988: Heves esőzés veszélyét jelző rendszer kiépítése Magyarországon. OMSZ Kisebb Kiadványai 63, OMSZ, Budapest. (in Hungarian)

Bowler, N.E., Pierce, C.E., and *Seed, A.W.*, 2006: STEPS: A probabilistic Precipitation forecasting scheme which merges an extrapolated nowcast with downscaled NWP, *Q. J. Roy. Meteorol. Soc. 132*, 2127–2155.

Browning, K.A., (Ed.), 1982: Nowcasting. Academic Press.

Chen, F. and *Dudhia, J.*, 2001: Coupling an advanced land-surface/ hydrology model with the Penn State/ NCAR MM5 modeling system. Part I: Model description and implementation. *Mon. Weather Rev. 129*, 569–585.

Conway, B., and *Labrousse, J.*, 1997: Improvement of nowcasting techniques. Offices of Official Publication of the European Communities ISBN 9282787435.

Derrien, M. and *Le Gléau, H.*, 2005: MSG/SEVIRI cloud mask and type from SAFNWC. *Int. J. Remote Sens. 26*, 4707–4732.

Derrien, M. and *Le Gléau, H.*, 2013: Algorithm Theoretical Basis Document for "Cloud Products" (CMa-PGE01 v3.2, CT-PGE02 v2.2 & CTTH-PGE03 v2.2), SAFNWC documentation, available on-line: http://www.nwcsaf.org

Dixon, M., and *Wiener, G.*, 1993: TITAN: Thunderstorm Identification, Tracking, Analysis and Nowcasting – A Radar-based Methodology. *J. Atmos. Ocean. Tech. 10*, 785–797.

Dudhia, J., 1993: A non-hydrostatic version of the Penn State NCAR Mesoscale Model: validation tests and simulation of an atlantic cyclone and cold front. *Mon. Weather Rev. 121*, 1493–1513.

Ebert, E.E., Wilson, L.J., Brown, B.G., Nurmi, P., Brooks, H.E., Bally, J., and *Jaeneke, M.*, 2004: Verification of Nowcasts from the WWRP Sydney 2000 Forecast Demonstration Project. *Wea. Forecast. 19*, 73–96.

Foresti, L., Reyniers, M., and *Delobbe, L.*, 2014: Probabilistic Precipitation Nowcasting with the Short-Term Ensemble Prediction System in Belgium. Presented at the European Nowcasting Conference, Vienna, 29–30 April 2014.

Geresdi, I. and *Horváth, A.*, 2000: Nowcasting of precipitation type. Part I : Winter precipitation. *Időjárás 104*, 241–252.

Geresdi, I., Horváth, A., and *Mátyus, Á.*, 2004: Nowcasting of the precipitation type. Part II: Forecast of thunderstorms and hailstone size. *Időjárás 108*, 33–49.

Germann, U., and *Zawadzki, I.*, 2002: Scale-dependence of the predictability of precipitation from continental radar images. Part I: Description of the methodology. *Mon. Weather Rev. 130*, 2859-2873.

Golding, B.W., 1998: Nimrod: A system for generating automated very short range forecasts. *Meterorol. Appl. 5*, 1–16.

Götz, G. and *Bodolainé, J.E.*, 1963a: A mezoszinoptikus képződményekről. *Időjárás 67*, 46–53. (in Hungarian)

Götz, G. and *Bodolainé, J.E.*, 1963b: Structures and analyses of instability lines. OMI Kisebb Kiadványai 33, OMSZ, Budapest, (in Hungarian).

Haiden, T., Kann, A., Wittmann, C., Pistotnik, G., Bica, B., and *Gruber, C.*, 2011: The Integrated Nowcasting through Comprehensive Analysis (INCA) System and Its Validation over the Eastern Alpine Region. *Weather Forecast. 26*, 166–183.

Horváth, Á. and *Geresdi, I.*, 2003: Severe Storms and Nowcasting in the Carpathian Basin. *Atmos. Res. 67–68*, 319–332.

Horváth, Á., 2005: Nowcasting System of the Hungarian Meteorological Service. Proceedings. Abstracts, WWRP International Symposium on Nowcasting and Very Short range Forecasting. Toulouse, France, 5–9 September 2005

Horváth, Á., 2006: Numerical studies of severe convective phenomena using robust radar impact method. Proceedings of ERAD 2006. Barcelona, 19-22 September, 557-558.

Horváth, Á., Ács, F., and *Seres, T.*, 2008: Thunderstorm climatology analyses in Hungary using radar observations. *Időjárás 112*, 1–13.

Horváth, Á., Seres,T., and *Németh,P.*, 2012: Convective systems and periods with large precipitation in Hungary. *Időjárás 116,* 77–91.

Kunkel, A.B., 1984: Parameterization of Droplet Terminal Velocity and Extinction Coefficient in Fog Models. *J. Climate Appl. Meteor. 23*, 34–41.

Lee, H.C., Bellon, A., Zawadzki, I., and *Kilambi, A.*, 2009: McGill Algorithm for Precipitation Nowcasting by Lagrangian Extrapolation (MAPLE) applied to the South Korean to the South Korean radar network. Part 1: Sensitivity studies of the Variational Echo Tracking (VET) technique, Proceedings of the 34th Radar Conference, American Meteorological Society, 5–9 October 2009, Williamsburg, VA.

Li, L., Schmid, W., and *Joss, J.* 1995: Nowcasting of motion and growth of precipitation with radar over a complex orography. *J. Appl. Meteorol. 34*, 1286–1300.

Marshall, J.S. and *Palmer, W.M.*, 1948: The distribution of raindrops with size. *J. Meteorol. 5*, 165–166.

Mecklenburg, S., Joss, J., and *Schmid, W.*, 2000: Improving the nowcasting of precipitation in an Alpine region with an enhanced radar echo tracking algorithm, *J. Hydrol. 239*, 46–68.

Mueller, C., Saxen, T., Roberts, R., Wilson, J., Betancourt, T., Dettling, S., Oien, N., and *Yee, J.*, 2003: The NCAR Auto-Nowcast System. *Weather Forecast. 18, 545–561.*

Pierce, C.E., Hardaker, P.J., Collier, C.G., and *Haggett, C.M.*, 2000: GANDOLF: a system for generating automated nowcasts of convective precipitation. *Met. Apps.* 7, 341–360.

Putsay, M., Szenyán, I., and *Simon, A.,* 2009: Case study of Mesoscale Convective Systems over Hungary on 29 June 2006 with satellite, radar and lightning data. *Atmos. Res.* 93, 82–92.

Putsay, M.,Kocsis,Zs., and *Szenyán,I.*, 2010: Use of Satellite information in Hungarian Nowcasting System. EUMETSAT Meteorological Satellite Conference, 20–24 September 2010, Córdoba, Spain

Skamarock, W.C., Klemp, J.B., Dudhia, J., Gill, D.O., Baker, D.M., Wang, W., and *Powers, J.G.*, 2005: A description of the advanced research WRF version 2. NCAR Tech Note NCAR, TN-4681STR.

Stauffer, D.R. and *Seaman, N.L.*, 1990: Use of Four-Dimensional Data Assimilation in a Limited-Area Mesoscale Model. *Mon. Weather Rev. 118*, 1250–1277.

Sun, J., Xue, M., Wilson, J.W., Zawadzki, I., Ballard, S.P., Onvlee-Hooimeyer, J., Joe, P., Barker, D., Li, P-W., Golding, B., Xu, M., and *Pinto, J.*, 2014: Use of NWP for Nowcasting Convective Precipitation: Recent Progress and Challenges, *Bull. Amer. Meteor. Soc. 95*, 409–426.

Turner, B. J., Zawadzki, I., and *Germann, U.* 2004: Predictability of precipitation from continental radar images. Part III: Operational nowcasting implementation (MAPLE), *J. Appl. Meteorol. 43*, 231–248

Wilson, J.W., Feng, Y., Chen, M., and *Roberts, R.D.*, 2010: Nowcasting challenges during the Beijing Olympics: successes, failures, and implications for future nowcasting systems. *Weather. Forecast. 25,* 1691–1714.

IDŐJÁRÁS

Quarterly Journal of the Hungarian Meteorological Service
Vol. 119, No. 2, April – June, 2015, pp. 215–239

Overview of mesoscale data assimilation developments at the Hungarian Meteorological Service

Máté Mile[1*], **Gergely Bölöni**[1], **Roger Randriamampianina**[2], **Roland Steib**[1], and **Ersin Kucukkaraca**[3]

[1]*Hungarian Meteorological Service*
P.O. Box 38, H-1525 Budapest, Hungary

[2]*Norwegian Meteorological Institute*
P.O. Box 43, Blindern, N-0313 Oslo, Norway

[3]*Turkish State Meteorological Service*
P.O. Box 401, Ankara, Turkey

[*]*Corresponding authors E-mail: mile.m@met.hu*

(Manuscript received in final form June 03, 2014)

Abstract—The operational AROME (Applications of Research for Operations at MEsoscales) mesoscale numerical weather prediction (NWP) model has been run using interpolated analyses of the ALADIN (Aire Limitée Adaptation Dynamique Développement International) NWP model for its initialization since the end of 2010 at the Hungarian Meteorological Service (HMS). In order to improve the initial conditions, a local three-dimensional variational (3DVAR) data assimilation system was developed for the Hungarian version of AROME (AROME-Hungary). Regarding the data assimilation cycling strategy, it was shown that 3 hourly rapid update cycling (RUC), which was implemented operationally in March 2013 using conventional observations, outperforms 6 hourly cycling method. This paper describes at length the main characteristics of this local data assimilation system and its impact on the model short-range forecasts. Although the forecasts of AROME-Hungary based on a local data assimilation were already improved compared to the previous implementation (initialization via interpolated analyses of the ALADIN model), there is still a way to go to exploit the full benefit of the local 3DVAR assimilation cycle. Current development works aim at improving the system through exploitation of remote sensing observations (radar, GPS, satellite AMVs), with a special emphasis on humidity information. All tested observations showed promising performance on both the analyses and forecasts of the AROME-Hungary model, which should lead to their respective operational implementation in the near future.

Key-words: operational numerical weather prediction, mesoscale data assimilation, rapid update cycle, remote sensing observations

1. *Introduction*

State of the art mesoscale numerical weather prediction (NWP) models, such as ALADIN (*Horányi et al.,* 1996) and AROME (*Seity et al.,* 2010), describe the time evolution of small scale processes in the atmosphere (e.g., convection, sea breeze, fog), through the applied prognostic microphysical parametrization schemes and the non-hydrostatic dynamics. Advanced model dynamics and physics are, however, in vain, if the initial state does not contain appropriate information regarding the small-scale weather systems we aim to describe. The simplistic approach for the initialization of limited area models (LAMs) is to interpolate the analysis or the forecast of the driving model (i.e., a global model or another LAM) to the mesoscale grid. This approach, often referred to as spin-up initialization, is computationally cheap (i.e., there is no need to run expensive data assimilation schemes), nevertheless it implies several drawbacks, which will be demonstrated in this section. The sophisticated and scientifically sound alternative of the spin-up initialization is to run a local data assimilation system in the LAM, combining the high-resolution first guess of the mesoscale model with the available high-density observations.

Data assimilation is achieved by solving the BLUE (Best Linear Unbiased Estimation) analysis equation, which shows that the two main information used for estimating the initial state (x_a) are the background (x_b) and the actual observation set (y) (see e.g., *Kalnay*, 2003; *Lorenc*, 1986; *Evensen,* 2009):

$$x_a = x_b + K\left(y - H\left(x_b\right)\right) \tag{1}$$

In Eq.(1), K stands for the Kalman gain determining the weight of the background and the observations in each gridpoint in an optimal way, i.e., based on their reliability in a statistical sense. H denotes the observation operator, which enables the comparison of the observations with the background through a projection from the model space to the observation space.

In practice local data assimilation is substantially more expensive to implement than spin-up initialization (both computationally and regarding manpower), but in turn, it enables a more accurate representation of small-scale phenomena in the initial state. In order to demonstrate this, the kinetic energy spectra for a spin-up analysis (ALADIN analysis interpolated to the AROME-Hungary grid) and the local 3DVAR analysis of AROME-Hungary are plotted in *Fig. 1*. It can be seen that the energy spectra for the AROME analysis follows rather close the theoretical slope of energy cascade, i.e., k^{-3} for small k wavenumbers (large scales) and $k^{-5/3}$ for high k wavenumbers (small scales). In contrast, the energy spectra of the spin-up analysis is far from the theoretical slopes, especially at mesoscales (above wavenumber 50, which corresponds to spatial scales smaller than 25 km), where the energy curve is rather noisy. The mesoscale noise in the spin-up analysis is introduced by the interpolation, and it

reflects that the ALADIN analysis with its 8 km grid-length (30–45 km effective resolution) do not hold physical information on the mesoscales resolved by the AROME model with its 2.5 km grid-length. Among others, this diagnostic comparison gave a great motivation for implementing a local 3DVAR data assimilation system for the AROME-Hungary, which finally became operational in March 2013 due to approved ability to improve the forecast performance compared to the spin-up initialization approach. Similar positive impact of mesoscale data assimilation implementations have been reported by *Benjamin et al.,* (2004), *Fischer et al.,* (2005), *Bölöni* (2006), *Randriamampianina* (2006a), *Brousseau et al.* (2011).

The structure of the article is as follows: In the next section, the operational DA system will be described, with special emphasis on rapid update cycling, and also, the added value and the impact of the AROME-Hungary data assimilation system will be detailed. In Section 3, we briefly review experimental data assimilation studies with non-conventional observations added to the existing operational system. Finally, the last section gives a summary of the presented work and provides corresponding conclusions.

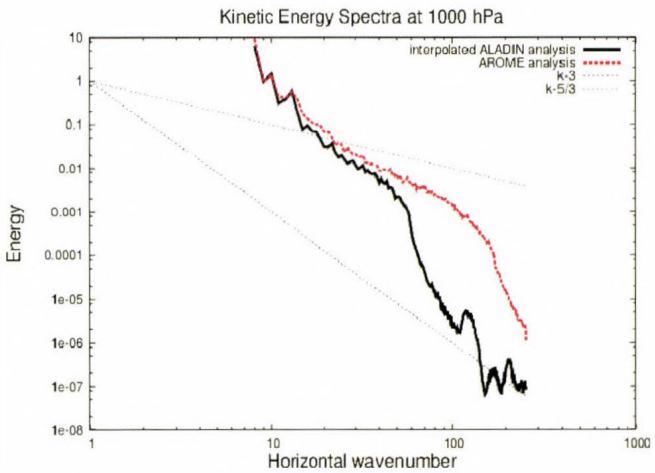

Fig. 1. Wind energy spectra (kg m^2 s^{-2}) at 1000 hPa for the AROME (dx = 2.5 km) analysis (red) and for an interpolated ALADIN (dx=8 km) analysis (black). Dotted straight lines correspond to the theoretical slopes of kinetic energy at large- (k^{-3}) and mesoscales ($k^{-5/3}$) if using a log-log scale.

2. *Operational data assimilation system of the AROME mesoscale model*

2.1. The assimilation system

The local data assimilation system of AROME-Hungary is based on a 3 hourly rapid update cycle (RUC). The organization of one particular assimilation step at 00 UTC is shown schematically in *Fig. 2*, where the lateral boundary conditions in the assimilation cycle are provided by the global ECMWF/IFS (European Centre for Medium-Range Weather Forecasts / Integrated Forecast System) model, and surface parameters are initialized either using the surface analysis of the operational ALADIN model where available (at synoptic times, i.e., 00, 06, 12, and 18 UTC) or using the previous AROME/SURFEX (SURFace Externalized) forecast (at sub-synoptic times i.e., 03, 09, 15, and 21 UTC).

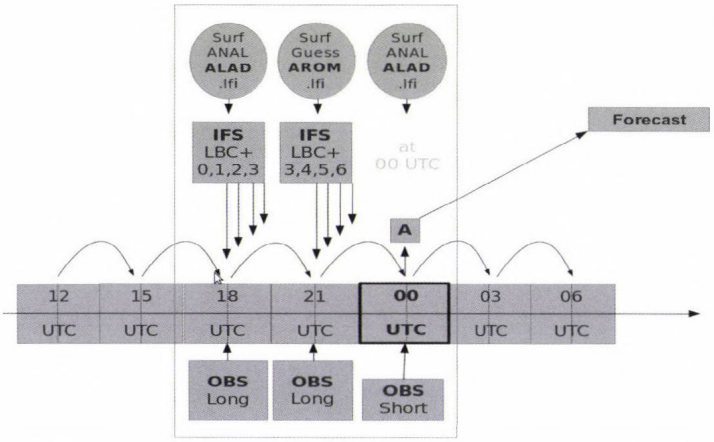

Fig. 2. Schematic figure of the data assimilation cycle applied for AROME showing the elements of a 00 UTC assimilation run.

The core of AROME-Hungary data assimilation system is an incremental 3DVAR method, where the basic mathematical formulation and its corresponding implementation is very similar to the one used in the IFS, ARPEGE, and ALADIN models (*Courtier et al.*, 1998; *Fischer et al.*, 2005; *Vasiliu* and *Horányi*, 2005; *Bölöni* 2006). An important component of the 3DVAR is the representation of background error statistics which plays a key role in filtering the information coming from observations and spreading it out to the model grid (see e.g., *Berre* 2000; *Brousseau et al.*, 2011). In the current operational system, the background error covariance matrix was sampled from

the downscaling of an ALADIN Ensemble Data Assimilation (EDA) experiment, run for a summer period using 3-hour forecast ranges and 5 EDA members to get sufficient statistical sample (*Bölöni et al.,* 2014). Input observations for the AROME-Hungary 3DVAR suite are provided by the OPLACE (Observation Preprocessing for LACE (Limited Area modeling for Central Europe)) system, which includes both conventional and non-conventional observations. Although the currently operational AROME-Hungary data assimilation system uses only conventional observations, the system is able to assimilate non-conventional observations, as described in Section 3.

Delivering the mesoscale NWP forecasts as early as possible is of high priority for every operational forecasting centre. In order to find the optimal observation cut-off time (waiting time after the nominal analysis time) of the operational AROME-Hungary data assimilation system, the timeliness of the incoming observations was diagnosed for the area of interest. In *Fig. 3*, the availability of conventional observations at 00 UTC is shown, based on the amount of data received by the OPLACE system. After gaining this result, the observation (short) cut-off time has been set to one hour, which brings the fastest possible production of AROME forecast with an almost complete input observation set. This rather early cut-off enables a faster AROME forecast production compared to the former operational version of AROME-Hungary, which was based on a spin-up initialization from the 3DVAR analysis of the ALADIN model, because the ALADIN data assimilation system uses longer cut-off.

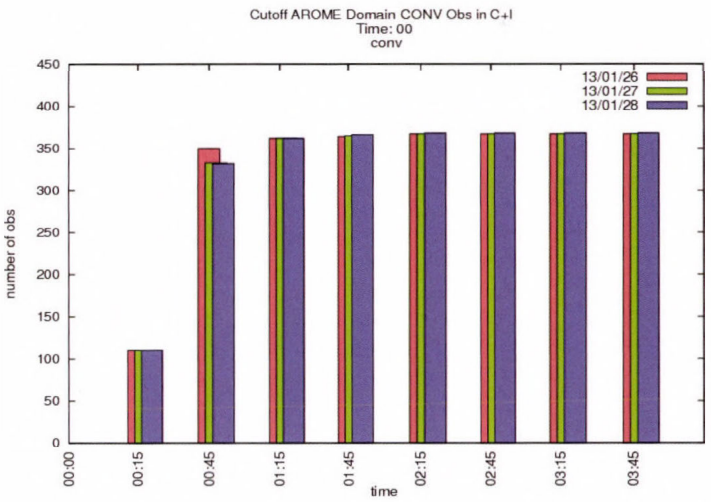

Fig. 3. Estimation of the optimal short cut-off time (considering AROME integration domain at 00 UTC) on January 26 (red columns), 27 (green columns) and 28 (blue columns) 2013.

2.2. *The Rapid Update Cycle*

In mesoscale NWP models, the accuracy of initial conditions is getting more and more crucial with an increasing resolution, hence small scale processes of the atmosphere have less and less predictability (*Fabry* and *Sun*, 2009). The rapid update cycling approach with increased analysis frequency in the assimilation cycle aims to involve more observations with reduced representativity error in time. It is assumed that the more observations we consider for the update of the model state, the better initial conditions we will get when starting a forecast from an analysis of the assimilation cycle. Considering conventional observations for instance, the different amount of used observations between a 6 hourly data assimilation cycle and a 3 hourly RUC is plotted in *Fig. 4* for a short period. At sub-synoptic times, mainly aircraft and SYNOP reports provide almost a double amount of data per day, due to the 4 extra analyses. To further emphasize the benefits of a RUC, it should be mentioned that many remote sensing observations are available with high temporal frequency, which are potentially beneficial in a data assimilation system with high frequency cycling. Also, many of the remote sensing observations are available in a very timely manner, almost immediately after analysis time, which allows to keep the operational observation cut-off time rather short, and thus to provide the forecasts with an early delivery.

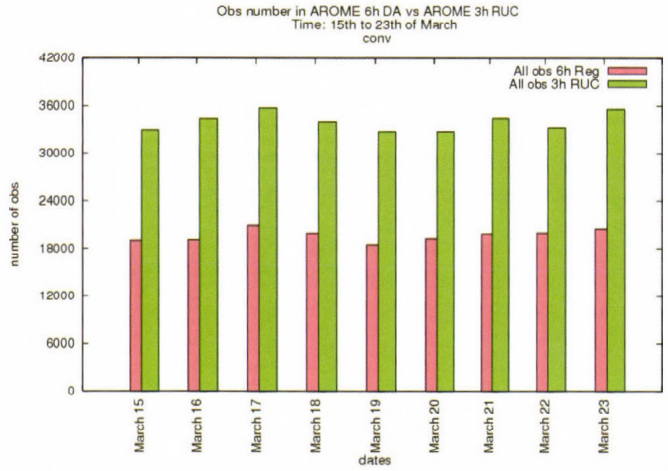

Fig. 4. The number of conventional observations used in a day in the RUC implementation (green) and in a 6 hourly cycling (red). The amount of data was counted in the period of March 15-23, 2014.

Beside these attractive features of the RUC system, there are some issues which have to be treated carefully in case of using a frequent assimilation cycle,

and thus, shorter background forecast lengths. The forecast model integration may imply spin-up effects (noise due to spurious gravity waves or imbalances between dynamics, atmospheric and soil physics) at the very short ranges, which can be accumulated in the assimilation cycle through the background forecasts, and thus, lead to degradation in the analyses and the forecasts. A usual practice in NWP, and in the Hungarian version of the ALADIN model as well, is the use of initialization techniques e.g., digital filter initialization (DFI) (*Daley*, 1991; *Lynch et al*, 1997), which is a low-pass spectral filter removing high-frequency components of the initial conditions. In case of AROME-Hungary, no DFI is applied because such filtering is assumed to be too strong in case of a mesoscale non-hydrostatic model, where gravity waves are described by the dynamics. To diagnose spin-up effects in AROME-Hungary, surface pressure tendencies have been examined for very short-range forecasts (+2 hours) for an arbitrarily chosen case. In *Fig. 5*, time evolution of the surface pressure tendency provided by three different forecasts is shown for a particular gridpoint over orography. The red curve corresponds to a forecast, which was started from an AROME 3DVAR analysis, using a time-consistent coupling scheme, i.e., when the lateral boundary condition (LBC) at initial time is the interpolated global IFS forecast. The blue curve stands for a similar run with the only difference of using a space-consistent coupling scheme, i.e., when the lateral boundary condition (LBC) at initial time is the AROME 3DVAR analysis itself. As an additional reference, the tendency from an AROME forecast using a spin-up initialization is added (green curve), i.e., where both the initial condition and the LBC at initial time is the interpolated global IFS forecasts. As the high amplitude oscillation in the time evolution of surface pressure tendency is an indicator of noise, it has been concluded based on *Fig. 5*, that AROME forecasts using a RUC assimilation with a space-consistent coupling scheme imply less noise than a RUC with a time-consistent coupling approach or the spin-up initialization. Supposedly, the higher amplitude oscillation in case of the spin-up initialization is caused by the interpolation noise which is more emphasized over orography. It should be also mentioned that plotting the evolution of surface pressure tendency on a horizontal map (not shown) supports the choice for the space-consistent coupling scheme. Namely, in the time-consistent case, noise patterns (indicated by large tendencies) penetrate from the domain borders towards the middle of the domain in a rectangular shape. In *Fig. 5*, this is captured by the red curve at integration steps 40–45 as an outstanding wave. An explanation for this structured noise might be that imbalances between the local 3DVAR analysis and the LBC at initial time arise, due to the inconsistent model states of the AROME and IFS models near the boundaries. The final decision on implementing a 3 hourly RUC instead of a traditional 6 hourly cycling was based on a comparison study over a 1 month period during summer 2012, where the skill of these two cycling options was measured. Verification results – which will be studied in the next section – reflected a better performance of the 3 hourly RUC, leading to its operational implementation.

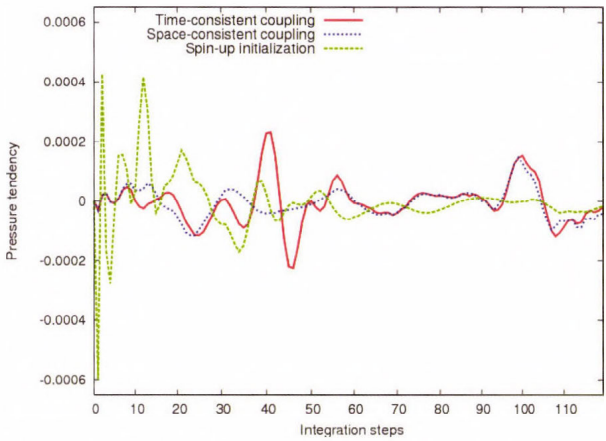

Fig. 5. Temporal evolution of surface pressure tendency (Pa/min) over orography during the first 2 hours of a forecast concerning spin-up initialization (green dashed line), time-consistent coupling approach (red line), and space-consistent coupling approach (blue dashed line).

2.3. The impact of local data assimilation scheme on the analysis and forecast

For measuring the impact of the local data assimilation scheme, three experiments with AROME-Hungary have been run and compared for several periods based on objective verification scores primarily. The three experiments are an AROME suite based on spin-up initialization (called DYNA), and two AROME suites based on local 3DVAR data assimilation, one of them using a 6 hourly cycling (called CONV6H) and another one using a 3 hourly rapid update cycling (called CONV). Forecasts have been run up to +36 hours starting at 00 UTC network times. Concerning the verification, both point-based and object-based scores have been computed. In the point-based verification, surface and radiosonde observations have been used as reference. The applied object-based method calculates average precipitation of forecasted weather objects (or alternatively the full domain average), and compares with calibrated radar precipitation measurements as reference. In *Figs. 6a* and *6b*, 10 m wind and mean sea level pressure scores are shown for the period between June 25 and July 25, 2012. It is rather clear from these figures that both the 6 hourly and the 3 hourly RUC 3DVAR provide an added value compared to the spin-up initialization with respect to both RMSE and BIAS. Moreover, the 3 hourly RUC provides slightly better scores than the 6 hourly cycling during daytime, while during the night, scores show a rather low sensitivity to the cycling frequency. To demonstrate the impact on precipitation, object-based verification score (domain average precipitation) is shown in *Fig. 7*. It can be seen, that in comparison with the spin-up initialization, both the 6 hourly 3DVAR cycling

and the 3 hourly RUC could reduce the overestimation of the precipitation maximum linked to convective activity in the afternoon. It is also clear from *Fig. 7*, that the 3 hourly RUC provides slightly better precipitation forecasts than the 6 hourly cycling, by reducing the overestimation further.

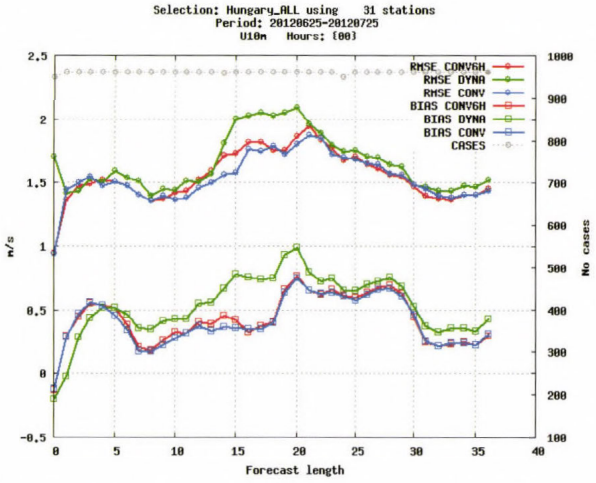

Fig. 6a. RMSE and BIAS scores corresponding to the spin-up initialization scheme (green), 3 hourly RUC (blue), and 6 hourly cycling (red) for 10 m wind speed (m/s).

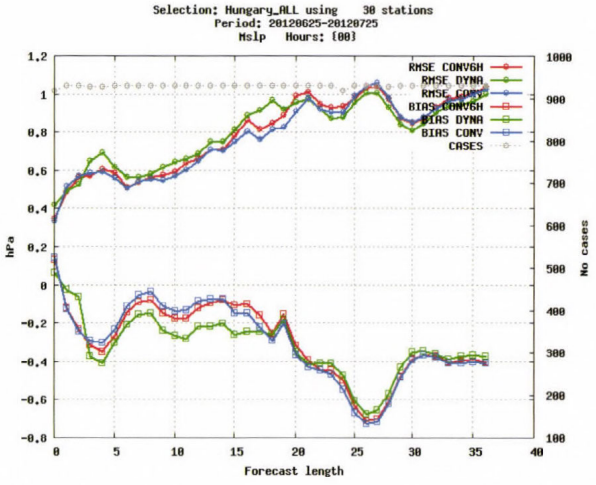

Fig. 6b. RMSE and BIAS scores corresponding to the spin-up initialization scheme (green), 3 hourly RUC (blue), and 6 hourly cycling (red) for mean sea level pressure (hPa).

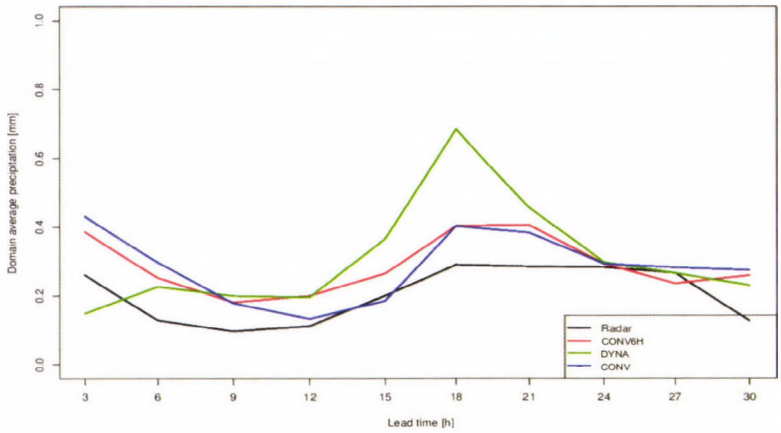

Fig. 7. Comparison of 3h RUC (blue), 6 hourly cycling (red) and the spin-up initialization scheme (green) regarding domain average precipitation (mm/h). The reference is the calibrated radar measurement (black).

Based on the success of the RUC approach (*Figs. 6a, 6b,* and *7*), a parallel suite with a 3 hourly RUC data assimilation system was compared with the former operational AROME-Hungary system (based on spin-up initialization) over the period from February 20 to March 12, 2013. This parallel suite was set up in a fully operational environment, providing real time outputs for the forecasters of the Hungarian Meteorological Service (this time both for 00 and 12 UTC base times), with the main aim to make a final decision about the operational implementation of the RUC system, in case of preferable scores and positive feedbacks from the forecasters. Based on the verification results, the RUC system clearly outperformed the forecasts of the former operational AROME-Hungary suite with spin-up initialization, which is demonstrated in *Figs. 8a, 8b* for 2 m temperature and in *Fig. 9* for precipitation. Feedbacks of the forecasters also confirmed the slight but consistent improvements implied by the RUC system, and this led to its operational implementation on March 17, 2013.

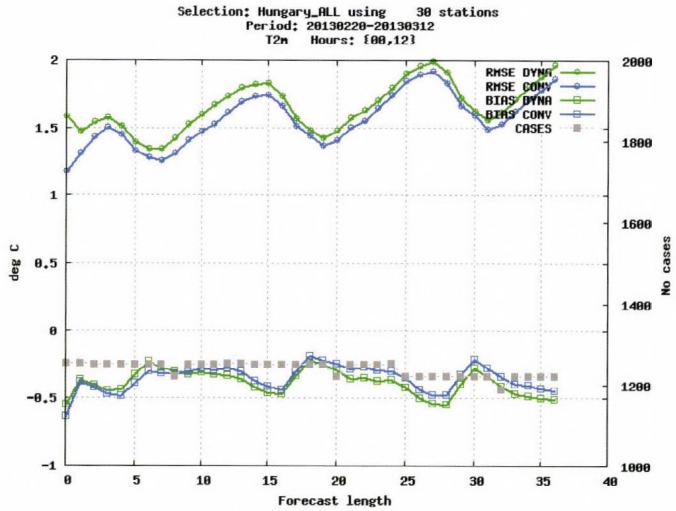

Fig. 8a. RMSE and BIAS scores of AROME forecasts according to the spin-up initialization (DYNA – green), and the 3 hourly rapid update cycle (CONV – blue) for 2 m temperature (°C).

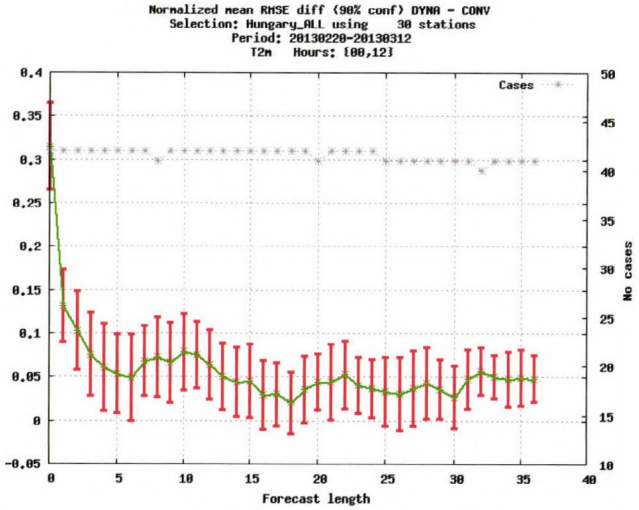

Fig. 8b. Normalized RMSE differences according to the spin-up initialization (DYNA – green), and the 3 hourly rapid update cycle (CONV – blue) for 2 m temperature (°C).

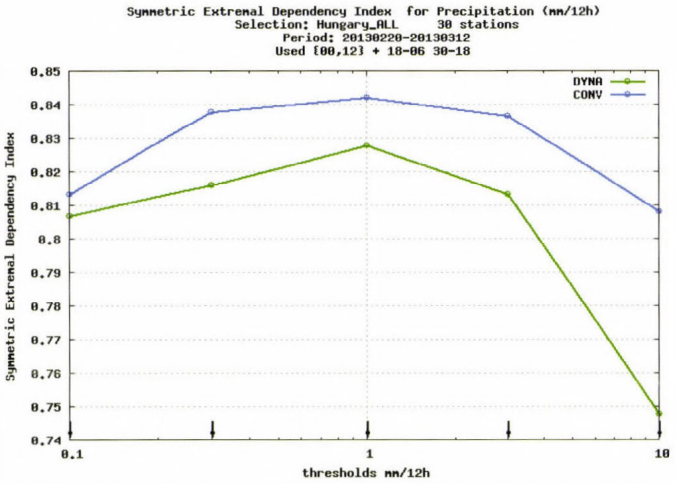

Fig. 9. Symmetric Extremal Dependency Index (SEDI) for precipitation according to the spin-up initialization (DYNA – green), and the 3 hourly rapid update cycle (CONV – blue) for precipitation (mm/12h).

2.4. Diagnosing analysis sensitivity to observations

An obvious way for the further development of the operational RUC is to bring non-conventional observations to its analysis system. In order to figure out, which observations would contribute the most to the analysis, the DFS (Degrees of Freedom for Signal) diagnostic tool (*Chapnik et al.*, 2006; *Cardinali et al.*, 2004) has been adapted and applied at the Hungarian Meteorological Service. The DFS tool diagnoses the observation influence on the analysis, thus, if applied for the available observation types, it provides an indication on their relative contribution. The DFS diagnostic is computed as the trace of the Kalman gain matrix projected to observation space:

$$DFS = Tr(HK) \tag{2}$$

where K and H denote respectively the Kalman gain matrix and the observation operator introduced in Eq. (1). In practice, this trace cannot be computed, because the gain matrix K is not known explicitly. *Girard* (1987) suggested a solution which enables to evaluate the above mentioned trace with the following approximation:

$$Tr(HK) \approx \left(y' - y\right)^T R^{-1}\left(H\left(x_a'\right) - H\left(x_a\right)\right) \tag{3}$$

where $H(x_a)$ gives the analysis state at observation locations using a background and the observations (y), and $H(x'_a)$ stands similarly for the analysis at observation space but using the perturbed observations (y') (and the same background). In Eq. (3), R stands for the observation error covariance matrix.

Therefore, DFS can be calculated through a random perturbation of the observations, and the method is flexible in a sense that DFS values can be computed for any subset of the available observational data. For a given date, the DFS was computed with conventional and some experimentally used non-conventional observations. In order to verify the influence of the available observations, both the absolute and the relative DFS diagnostics were computed (*Fig. 10*). Absolute DFS stands for what have been explained above in Eqs. (2) and (3), while relative DFS is the absolute DFS normalized by the number of observations within the given observation subset. The first conclusion based on the absolute DFS is that the largest contribution to the analysis is provided by wind observations, i.e., the largest amount of information is extracted from these observations in the current data assimilation system. On the other hand, relative DFS reflects the importance of humidity (from surface SYNOP stations and TEMP radiosondes), RADAR reflectivity (RADAR-Z), and GNSS (global navigation satellite system) ZTD (zenith total delay) observations. In conclusion, DFS diagnostics show that radar reflectivity and GNSS ZTD observations are promising candidates for assimilation in the future version of the RUC system. It should be mentioned that DFS provides a theoretical measure of the information content projected from the observations to the analysis and it does not provide any indications on the impact attributed to the forecasts. Another point to be added here is that no radiance observations have been considered and diagnosed in the recent RUC system.

3. *Use of non-conventional observations in the AROME 3DVAR system*

In the following section, we present the latest developments of the RUC system since its operational implementation. The need of using more observations, especially non-conventional ones, was already mentioned. Specifically, the observations measuring humidity are potentially good candidates based on the results of the DFS analysis sensitivity study shown in the previous section. At the same time, to gain advantage of the RUC system, early accessible observations with high frequency and high density are also required. Taken into account these objectives, the atmospheric motion vectors (AMV) from Meteosat Second Generation (MSG) geostationary satellite, RADAR measurements as reflectivity and radial wind, and GNSS ZTD observations have been investigated in the operational data assimilation system of AROME-Hungary.

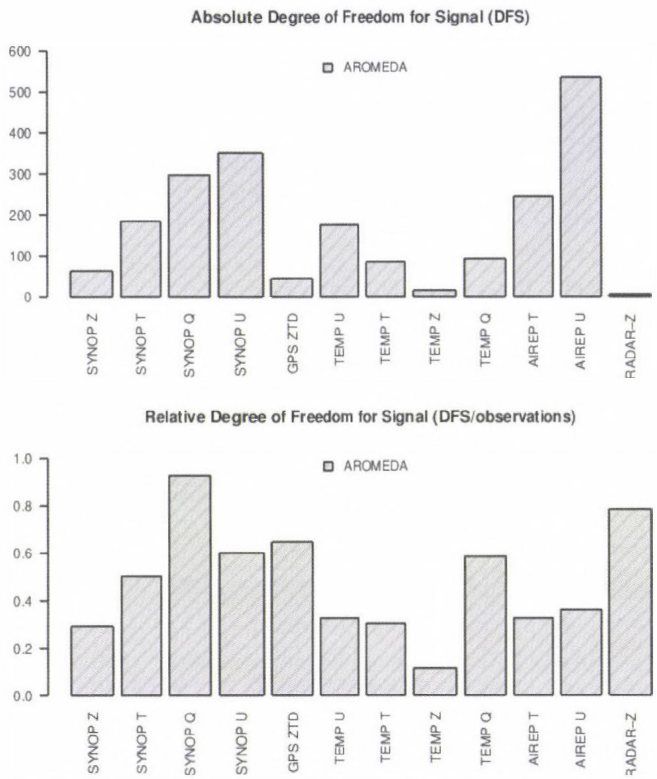

Fig. 10. Absolute and relative degrees of freedom for signal (DFS) for experimental data assimilation of AROME-Hungary at 12 UTC, January 3, 2014.

3.1. The impact of the Atmospheric Motion Vectors

EUMETSAT (European Organization for the Utilization of Meteorological Satellites) MSG provides sets of satellite winds (AMVs) extracted from sequences of well-navigated and calibrated images produced by the SEVIRI (Spinning Enhanced Visible and Infrared Imager) instrument. Accordingly, AMVs are derived from SEVIRI infrared, water vapor, and visible channels. At the HMS MSG AMV date is received through the EUMETCast broadcasting service of EUMETSAT with hourly frequency and processed in OPLACE for data assimilation purposes.

MSG AMV data is proved to be beneficial in nowcasting applications and in data assimilation systems (*Randriamampianina*, 2006b). Furthermore, numerous examples exist (*Forsythe et al.*, 2014), where AMVs are operationally assimilated in a similar way like the adopted technique used in the ALADIN

model in Hungary. As MSG AMV observations possess many advantages needed for a RUC data assimilation, a summertime impact study has been run with AROME-Hungary, where MSG AMV observations were added to the conventional observations. The implementation of the AMV data in AROME-Hungary was done according to *Randriamampianina* (2006b). To assess the impact of AMVs two experiments were conducted during the period of June 25 – July 25 in 2012. The AROME-Hungary forecasts initialized at 00 and 12 UTC were verified against SYNOP and radiosonde observations. Regarding the impact of MSG AMV observations, in *Figs. 11a* and *11c* RMSE and BIAS scores are plotted with the corresponding (*Figs. 11b* and *11d*) normalized RMSE differences for 10 m wind speed and 2 m dew point temperature forecasts. In these figures, CONV stands for the operational AROME-Hungary and GEOW denotes the experimental run, where MSG AMV was assimilated as well. In case of 10 m wind speed forecasts, the AMV experiment provides better skill for the shorter range forecasts up to 15 hours. Concerning the 2 m dew point temperature verification scores, the overall decrease of the error is perceptible and it is even statistically significant for some longer ranges. To conclude, AMV data in AROME-Hungary provides small contribution with respect to the amount of assimilated data, but with positive signal on the short-range forecasts.

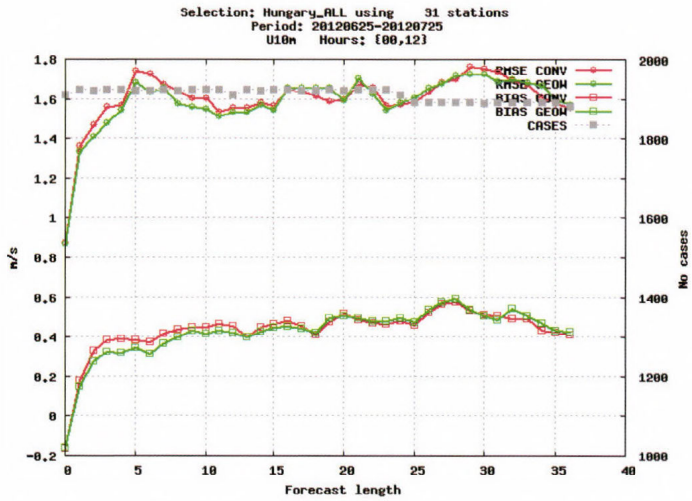

Fig. 11a. Experimental assimilation study of AROME-Hungary for the period between June 25 and July 25, 2013. RMSE and BIAS scores of AROME forecasts corresponding operational AROME with conventional observations (CONV – red) and AROME with conventional plus AMV observations (GEOW – green) are plotted for 10 m wind speed (m/s).

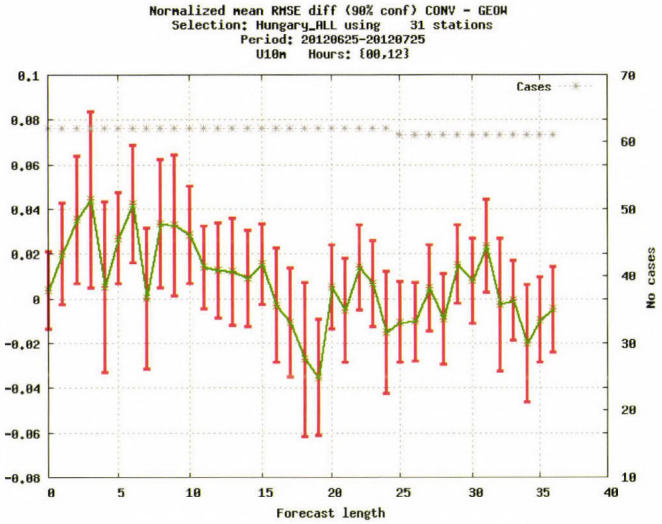

Fig. 11b. Experimental assimilation study of AROME-Hungary for the period between June 25 and July 25, 2013. Normalized RMSE differences between operational AROME with conventional observations (CONV – red) and AROME with conventional plus AMV observations (GEOW – green) are plotted for 10 m wind speed (m/s).

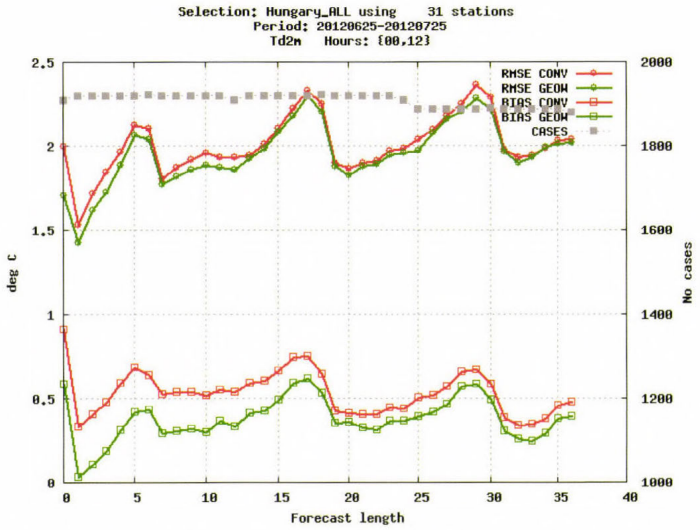

Fig. 11c. Experimental assimilation study of AROME-Hungary for the period between June 25 and July 25, 2013. RMSE and BIAS scores of AROME forecasts corresponding operational AROME with conventional observations (CONV – red) and AROME with conventional plus AMV observations (GEOW – green) are plotted for 2 m dew point temperature (°C).

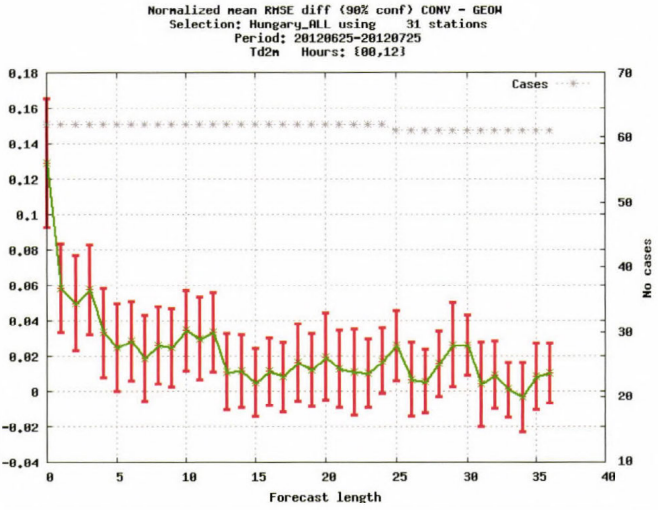

Fig. 11d. Experimental assimilation study of AROME-Hungary for the period between June 25 and July 25, 2013. Normalized RMSE differences between operational AROME with conventional observations (CONV – red) and AROME with conventional plus AMV observations (GEOW – green) are plotted for 2 m dew point temperature (°C).

3.2. The impact of the radar reflectivity and radial wind observations

Radar measurements play an important role in nowcasting, and nowadays they also contribute to the initial conditions of mesoscale NWP models. The weather RADAR instrument receives emitted electromagnetic signal to measure the reflectivity of the atmosphere's elements along the emitted ray's path. From the backscattered radiation one can estimate the reflectivity, i.e., the precipitation intensity, and from the phase shift of the backscattered signals the radial wind can be measured using Doppler's law.

Focusing on data assimilation, the utility of radar observations has been already demonstrated by different studies (see, e.g., *Lindskog et al,* 2004; *Snyder* and *Zhang,* 2003; *Montmerle* and *Faccani,* 2008). However, assimilating the observed quantities of the radar is not straightforward since the relationship between the measured quantities and the control variables of the data assimilation scheme is complex and non-linear. This relation in case of radial wind observation is less complex than that with reflectivity, where the radar equation gives the direct relationship between the observed hydrometeors and the 3DVAR control variables. Instead of extending the control variables to account also for hydrometeors, an alternative solution was worked out by *Caumont et al.* (2010) and *Wattrelot et al.* (2014) using 1D+3DVAR method, which enables to retrieve columns of relative humidity and temperature from reflectivity profiles as pseudo-observations. This approach is based on a 1D Bayesian estimate, which uses the assumption that a

well-chosen linear combination of model simulated reflectivities in the neighborhood of the observation provides comparable quantities to what is observed (see *Wattrelot et al.* (2014) for more details).

In the observing system of the Hungarian Meteorological Service dual-polarized Doppler radars are used which provide reflectivity and radial wind observations with 240 km and 120 km range, respectively. Raw radar data requires specific pre-processing in consideration of data assimilation which consists of the elimination of non-meteorological and noisy signals. Due to this quality control, for instance, reflectivity data under 7 dBz is filtered to avoid clear-sky echo and also unwanted RLAN (Radio Location Area Network) signals are rejected. After a thorough pre-processing with quality control, RADAR data is presented in Cartesian coordinates and in BUFR, which is one of the accepted format of the current 3DVAR system.

An observing system experiment with AROME-Hungary was made for an early, but convective summer period of May 15 – June 18, 2012. Point- and object-based verifications were computed to evaluate the performance of the operational AROME-Hungary and experimental runs including a combination of radar reflectivity and radial wind. In the first experiment with assimilation of both the radar Doppler wind and reflectivity, skill scores showed positive impact on forecasts of precipitation, but we observed also a cold and wet bias for surface parameters (not shown). A possible explanation of the observed bias might be that the assimilation of reflectivity data over-saturates the planetary boundary layers (PBL), which degrades the forecast of surface parameters through physical process along the model integration. To verify this assumption, another experiment was run avoiding the use of reflectivity observations below 1000 m from all 3 used radar stations. As a result, no degradation on surface parameters was observed, but on the other hand, the impact on precipitation forecasts was also reduced. The average intensity of the precipitation objects was verified against objects measured by the radar (*Fig. 12*). The four curves are respectively the operational AROME-Hungary (AromeCONV), the experimental AROME with complete set of radar data (AromeFULL), AROME runs with blacklisted reflectivity (AromeBLACK), and radar observations (RADAR). In *Fig. 12*, one can see that AromeBLACK provides the closest estimation to radar, however, the diurnal cycle of the maximum precipitation is still slightly shifted with delay in time. Additionally, a case study is shown in *Fig. 13*, where 3 hourly accumulated precipitation forecasts are plotted for all the three tested runs. One can see that the AromeFULL run predicts more realistic precipitation over north-eastern Hungary than AromeCONV, but it overestimates slightly in the mid-western part of the country. AromeBLACK is able to correct this overestimation, but the positive signal is also suppressed by filtering reflectivity. To conclude, the assimilation of radar data has major impact on forecasts of precipitation, but the quality control has to be further investigated and improved for better accounting of all potential measurements.

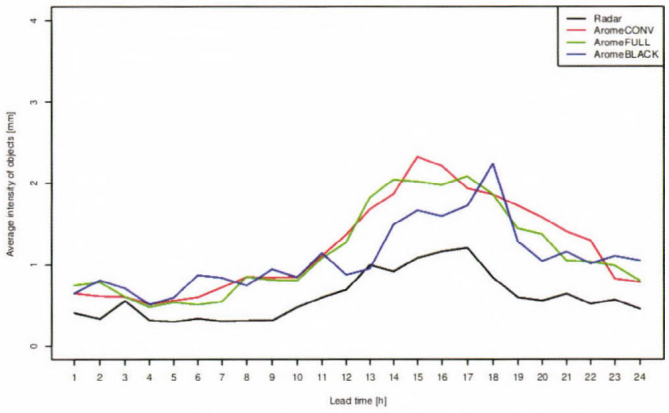

Fig. 12. Object-based verification of radar data assimilation experiments where average intensity of precipitation (mm/h) objects is verified against radar measurements for the period June 7 – June 18, 2012. AromeCONV: Operational AROME-Hungary (red line), AromeFULL: experimental AROME with RADAR reflectivity and radial wind observations added to conventional ones (green line), AromeBLACK: experimental AROME with same set of observations except reflectivity which was blacklisted below 1000 m elevation (blue line).

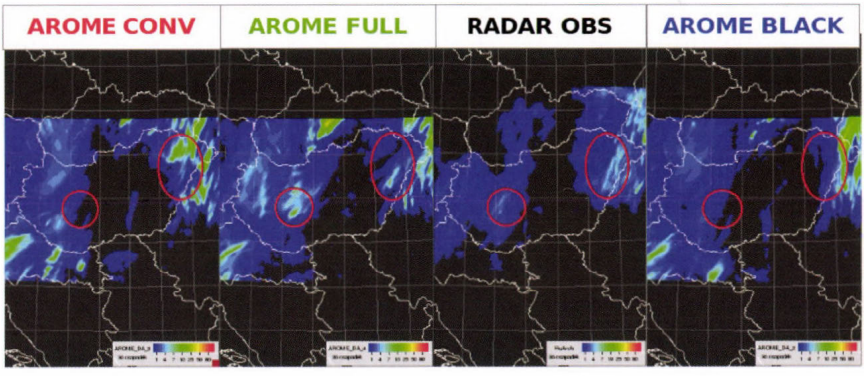

Fig. 13. A case study at 03 UTC, June 5, 2012 for 3 hourly accumulated precipitation forecast according to AROME model with operational configuration (AROME CONV), experimental AROME with radar reflectivity and radial wind (AROME FULL), experimental AROME with blacklisted low level reflectivity (AROME BLACK), and radar composite image (RADAR OBS).

3.3. The impact of the GNSS ZTD observations

Signal delay originating from different constituents of the troposphere and stratosphere can be extracted from satellite constellations of GNSS. The zenith tropospheric delay (ZTD), which is the converted-to-distance time delay,

provides valuable information on atmospheric water vapor content expressed in length units along the zenithal direction above the ground-based GPS receiver station. *Bevis et al.*, (1992) describes at length the principle of such measurement. The number of ground-based GPS stations over Europe has been increasing during the last years, and their use for meteorological purposes is coordinated by EUMETNET GNSS Water Vapour Programme (E-GVAP). E-GVAP also provides a data hub allowing the assimilation of GNSS ZTD observations with high spatial and temporal resolution. The Hungarian GNSS network (so called SGOB) operated by the Satellite Geodetic Observatory of Hungary was added to E-GVAP officially at the end of 2013, which provides access to a dense station network of ground-based GPS over the Carpathian Basin. This was a good motivation for us to assimilate the GNSS ZTD data.

The impact of GPS ZTD observations in data assimilation systems has been already investigated in the ARPEGE/ALADIN/AROME model family (see e.g., *Yan et al,* 2008; *Poli et al,* 2007; *Storto* and *Randriamampianina,* 2010). For the assimilation of E-GVAP ZTD data, a whitelist approach is used containing only stations with good-quality measurements. The whitelist is created according to the following criteria evaluated during a passive assimilation for a period of 15 days: i) the availablility of data is more than 40%, ii) observation minus background departures have Gaussian distribution, the absolute bias and also the standard deviation are both less than 40 mm, iii) the difference between station altitude and corresponding model orography height is less than 250 meter. We were able to choose 67 active stations inside our area of interest. The computed bias at each selected station is used as static bias correction in the assimilation scheme.

The impact of ground-based GNSS ZTD was investigated with AROME-Hungary over a winter period of 2014, namely January 5 to 27. The operational AROME-Hungary forecasts and the experimental AROME run with GNSS ZTD were compared with verification against SYNOP and radiosonde observations. In *Fig. 14a*, RMSE and BIAS scores are plotted for 2 m dew point temperature forecasts and the corresponding (*Fig. 14b*) normalized RMSE differences with significance test check. It can be seen that the experimental run (marked PGPS) has better skill scores on forecast of surface dew point temperature than the operational one (marked CONV), however, it is not statistically significant. In addition, one case study is presented in *Fig. 15*, showing the accumulated precipitation during the first 3 hours of the forecasts. In this case, the operational AROME-Hungary (CONV) provided a strong overestimation of precipitation as compared to the measured SYNOP observations plotted with numbers, probably due to spin-up effects. By assimilating ZTD observations (PGPS), the AROME forecast became more realistic with a reduction in the amount of predicted precipitation. This example showed, that the assimilation of GNSS ZTD observations is advantageous for improving short-range model forecasts, particularly regarding humidity, which is very promising to further improve the current operational AROME system.

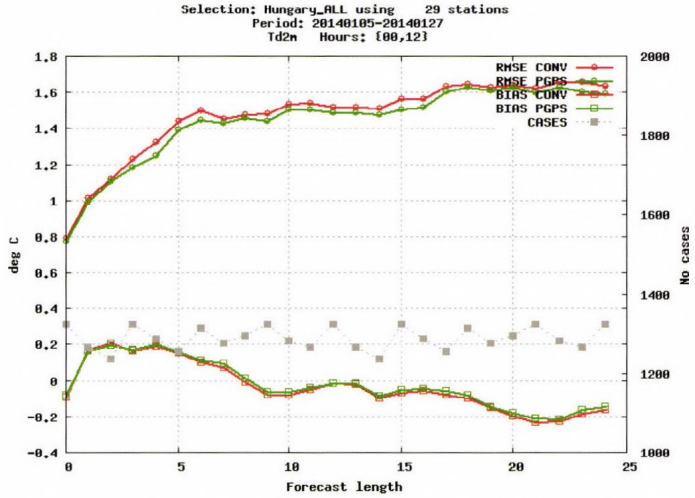

Fig. 14a. RMSE and BIAS scores of AROME forecasts corresponding to the operational AROME with conventional observations (CONV – red) and AROME with conventional plus GNSS ZTD observations (PGPS – green) for 2 m dew point temperature (°C).

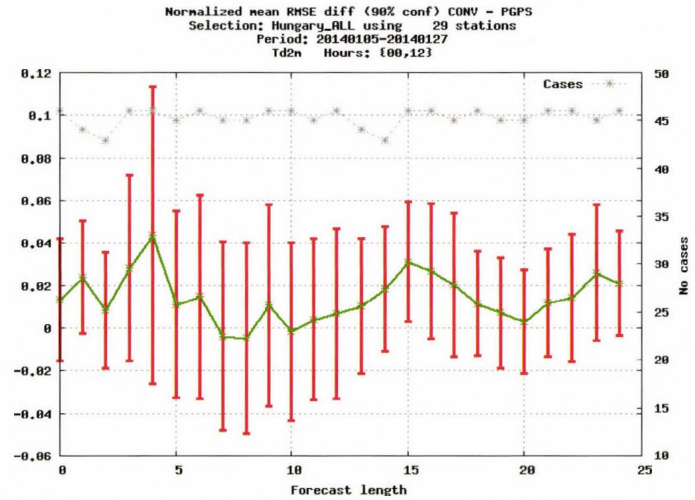

Fig. 14b. Normalized RMSE differences between operational AROME with conventional observations (CONV – red) and AROME with conventional plus GNSS ZTD observations (PGPS – green) for 2 m dew point temperature (°C).

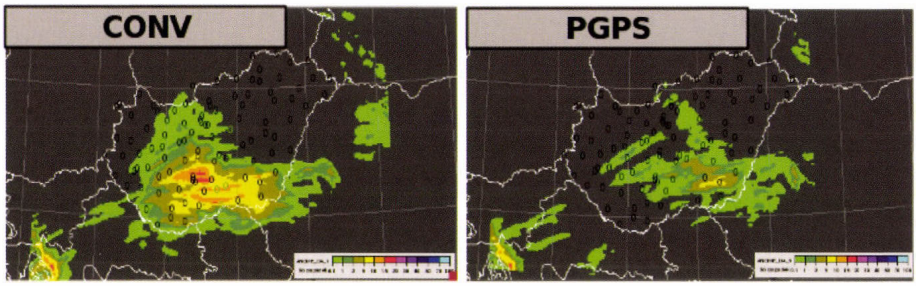

Fig. 15. A case study at 15 UTC, January 3, 2014 for 3 hourly accumulated precipitation forecast, AROME model with operational configuration (CONV), experimental AROME with GNSS ZTD (PGPS) and SYNOP precipitation (in numbers) are plotted.

4. ***Summary and conclusions***

The current operational RUC data assimilation system of the AROME-Hungary mesoscale model has been described with a special emphasis on the design of the assimilation cycle and the use of observations. It has been demonstrated, that the RUC system using conventional observations (surface, radiosonde, and aircraft measurements) improves the reliability of short-range forecasts compared to the spin-up initialization technique (former operational configuration) and also compared to the use of a 6 hourly data assimilation cycle.

The most important attempts for improving the current operational RUC system so far consisted of impact studies using remote sensing observations, such as MSG AMV, radar reflectivity, radial wind, and GNSS ZTD. The impact of AMV data assimilation was found to be significantly positive on the forecast of surface parameters, up to a forecast range of 15 hours. These results imply an operational use of MSG AMV data in the near future. The assimilation of radar data has been found to be useful in ameliorating precipitation forecasts, however, as a side effect of radar data assimilation, a bias have been found in surface parameters. The cause of these systematic errors has to be understood in order to achieve an operational implementation of radar data assimilation. The impact of GNSS ZTD data assimilation has been found to be slightly positive regarding the forecasts of surface parameters. Given that GNSS ZTD data provide information on atmospheric humidity also in clear-sky conditions, their importance is high in mesoscale data assimilation. This is reflected in some of our case studies through the preferable feature that ZTD data assimilation allows to reduce possible humidity and precipitation overestimations originating from the model first guess. Based on the overall impact of ZTD data, they are anticipated for an operational implementation in the near future.

Apart from the observation impact studies, an overview has been given about the relative importance of observing networks and observed variables based on the DFS method. The main message to be extracted out of these analysis sensitivity studies is that humidity observations are really important in mesoscale data assimilation, as they have relatively large influence on the analysis as compared to other observed variables. This indicates that the density of humidity observations have to be increased in the coming years either by using cloudy information from satellites or by implementing humidity sensors on board European aircrafts, similarly to the practice applied at the USA.

The paper gives an indication, that by increasing the resolution of mesoscale models, it becomes highly important to implement local data assimilation at the full resolution of the model, using high-resolution observations. It is shown that doing so, the spin-up initialization scheme can be outperformed both in terms of verification scores and case studies. This experience justifies that data assimilation will remain one of the major directions for improving mesoscale forecasts at the Hungarian Meteorological Service, with a special emphasis on remote sensing data. Besides the implementation of new observations to the RUC system, attention will have to be paid to the development of the background error covariance representation, which is responsible for the efficient filtering and spreading of observed information to the model space. It is foreseen that the background error covariance matrix for AROME-Hungary will be recalculated based on AROME ensembles of data assimilations similarly to the work of *Brousseau et al.* (2011).

Acknowledgements: The authors would like to thank *András Horányi, Edit Adamcsek, Helga Tóth* for their earlier work on data assimilation developments at the Hungarian Meteorological Service. Also we are grateful to *Balázs Szintai* for providing the object-based verification for RADAR assimilation experiments, *Ulf Andrae* for installing the Harmonie verification package at HMS, *Szabolcs Rózsa* to preparing test ZTD data for the assimilation study, and to *Xin Yan* who provided useful advices for ZTD pre-processing. We would like to thank also *László Kullmann* for the great support of AROME configurations and *István Sebők* for the important development of RADAR BUFR converter. Last but not least we are grateful to the organizers of the 39th Meteorological Scientific Days to found the possibility of this IDŐJÁRÁS special issue.

References

Benjamin, S.G., Dévényi D., Weygandt S.S., Brundage K.J., Brown J.M., Grell G.A., Kim D., Schwartz B.E., Smirnova T.G. and *Smith T.L.*, 2004: An hourly assimilation-forecast cycle: The RUC. *Mon. Weather Rev. 132,* 495–518.

Berre, L., 2000: Estimation of synoptic and mesoscale forecast error covariances in a limited area model. *Mon. Wea. Rev. 128*, 644-667.

Bevis, M., Businger, S., Herring, T., Rocken, C., Anthes, R., and *Ware, R.H.*, 1992: GPS meteorology: Remote sensing of atmospheric water vapor using the global positioning system. *J. Geophys. Res. 97,* 15787–15801.

Bölöni, G., 2006: Development of a variational data assimilation system for a limited area model at the Hungarian Meteorological Service. *Időjárás 110*, 309–327.

Bölöni, G., Berre, L., and *Adamcsek, E.*, 2014: Comparison of static mesoscale background error covariances estimated by three different ensemble data assimilation techniques. *Q. J. Roy. Meteor. Soc., 141*, 413-425.

Brousseau, P., Berre, L., Bouttier, F., and *Desroziers, G.*, 2011: Background-error covariances for a convective-scale data-assimilation system: AROME–France 3D-Var, *Q. J. Roy. Meteor. Soc., 137*, 409–422.

Cardinali, C., Pezzuli, S. and *Andersson, E.* 2004: Influence matrix diagnostic of data assimilation system. *Q. J. Roy. Meteor. Soc. 130*, 2767–2786.

Chapnik, B., Desroziers, G., Rabier, F., and *Talagrand, O.*, 2006: Diagnosis and tuning of observational error in a quasi-operational data ssimilation setting, *Q. J. Roy. Meteor. Soc. 132*, 543–565.

Caumont, O., Ducroq, V., Watterlot, E., Jaubert, G., and *Pradier-Varbe, S.*, 2010: 1D+3DVar assimilation of radar reflectivity data: a proof of concept, *Tellus A 62*, 173–187.

Courtier, P., Andersson, E., Heckley, W., Pailleux, J., Vasiljevic. D., Hamrud, M., Hollingsworth, A., Rabier, F., and *Fisher, M.*, 1998: The ECMWF implementation of three dimensional variational assimilation (3D-Var). Part I: Formulation. *Q. J. Roy. Meteor. Soc., 124*, 1783–1808.

Daley, R., 1991: Atmospheric Data Analysis. Atmospheric and Space Science Series, Cambridge.

Evensen, 2009: Data Assimilation, The Ensemble Kalman Filter, Springer.

Fabry, F. and *Sun, J.*, 2009: For How Long Should What Data Be Assimilated for the Mesoscale Forecasting of Convection and Why? Part I. *Mon. Weather Rev. 138*, 244–255.

Fischer, C., Montmerle, T., Berre, L., Auger, L., and *Stefanescu, S.* 2005: An overview of the variational assimilation in the Aladin/France numerical weather prediction system, *Q. J. Roy. Meteor. Soc. 131*, 3477–3492.

Forsythe M, C Peubey, C Lupu and *J Cotton*, 2014: Assimilation of wind information from radiances: AMVs and 4D-Var tracing, *ECMWF Annual Seminar*, September 2014, available in-line at: http://www.ecmwf.int/sites/default/files/ecmwf_sep14.pdf.

Girard, D., 1987: A fast Monte-Carlo cross-validation procedure for large least-squares problems with noisy data. *Technical Report 687-M, IMAG, Grenoble, France*

Horányi, A., Ihász, I. and *Radnóti, G.*, 1996: ARPEGE/ALADIN: a numerical weather prediction model for Central-Europe with the participation of the Hungarian Meteorological Service. *Időjárás 100*, 277–301.

Kalnay, E., 2003: Atmospheric Modeling, Data Assimilation and Predictability. Cambridge University Press.

Lindskog, M., Salonen, K., Järvinen, H.,Michelson, D., B., 2004: Doppler Radar Wind Assimilation with HIRLAM 3DVAR. *Mon Wea. Rev., 132*, 1081-1092.

Lorenc, A., 1986: Analysis methods for numerical weather prediction. *Q. J. Roy. Meteor. Soc. 112*, 1177–1194.

Lynch, P., D. Giard, and *V. Ivanovici*, 1997: Improving an efficiency of Digital Filtering Scheme for Diabatic Initialization. *Mon. Wea. Rev. 125*, 1976–1982.

Montmerle T. and *Faccani, C.*, 2008: Assimilation of Doppler wind into the French mesoscale model AROME. Proceedings of the ERAD 2008 conference (http://erad2008.fmi.fi/proceedings/index/session_wednesday.html)

Poli, P., Moll, P., Rabier, F., Desroziers, G., Chapnik, B., Berre, L., Healy, S. B., Andersson, E., and *El Guelai, F.-Z.* 2007: Forecast impact studies of zenith total delay data from European near realtime GPS stations in Meteo France 4DVAR, *J. Geophys. Res. 112*, D06114.

Randriamampianina, R., 2006a: Impact of high resolution observations in the ALADIN/HU model. *Időjárás 110*, 329–349.

Randriamampianina, R., 2006b: Investigation of the AMV data derived from Meteosat-8 in the ALADIN/HU data assimilation system. Eighth International Winds Workshop. 24-28 April 2006 Bejing, China, Available from: http://www.eumetsat.int/website/wcm/idc/idcplg?IdcService=GET_FILE&dDocName=PDF_CONF_P47_S2_06_RANDRIAMA_V&RevisionSelectionMethod=LatestReleased&Rendition=Web

Seity, Y., Brousseau, P., Malardel, S., Hello, G., Bénard, P., Bouttier, F. Lac, C., and *Masson, V.,* 2010: The AROME-France Convective-Scale Operational Model, *Mon. Weather Rev. 139,* 976–991.

Snyder, C. and *Zhang, F.,* 2003: Assimilation of Simulated Doppler Radar Observations with an Ensemble Kalman Filter, *Mon. Weather Rev. 131,* 1663–1677.

Storto, A. and *Randriamampianina, R.,* 2010: A new bias correction scheme for assimilating GPS zenith tropospheric delay estimates, *Időjárás 114,* 237–250.

Vasiliu S. and *Horányi A.,* 2005: An evaluation of the performance of the three-dimensional variational data assimilation scheme for the ALADIN/HU spectral limited area model, *Időjárás 109,* 233–257.

Wattrelot, E, O Caumont, and *J-F Mahfouf,* 2014: Operational Implementation of the 1D+3D-Var Assimilation Method of Radar Reflectivity Data in the AROME Model. *Mon. Weather Rev. 142,* 1852–1873.

Yan, X., Ducrocq, V., Poli, P., Jaubert, G., and *Walpersdor,f A.,* 2008: Mesoscale GPS Zenith Delay assimilation during a Mediterranean heavy precipitation event, *Adv. Geosci.* 17, 71–77.

IDŐJÁRÁS

Quarterly Journal of the Hungarian Meteorological Service
Vol. 119, No. 2, April – June, 2015, pp. 241–265

Application of the AROME non-hydrostatic model at the Hungarian Meteorological Service: physical parameterizations and ensemble forecasting

Balázs Szintai[1]*, **Mihály Szűcs**[1], **Roger Randriamampianina**[2], and **László Kullmann**[1]

[1]*Hungarian Meteorological Service,*
Kitaibel Pál u. 1., H-1024 Budapest, Hungary

[2]*Norwegian Meteorological Institute*
P.O. Box 43, Blindern, N-0313 Oslo, Norway

**Corresponding author E-mail:szintai.b@met.hu*

(Manuscript received in final form November26, 2014)

Abstract—At the Hungarian Meteorological Service (HMS), the AROME non-hydrostatic numerical weather prediction model has been running operationally since the end of 2010. The horizontal resolution is 2.5 km, thus it is assumed that deep convection is explicitly resolved. To achieve this, apart from increasing the horizontal and vertical resolution of the model, advanced physical parameterizations have to be applied. In this paper, some recent developments in connection with dynamics and physical parameterizations performed at the HMS are described. Model sensitivities related to horizontal diffusion, microphysics, turbulence, and shallow convection are discussed. Main features of the applied surface scheme "SURFEX" are highlighted as well as developments in connection with the prognostic treatment of vegetation. Recent work focusing on high resolution probabilistic forecasting with the AROME model is also summarized. It is shown that the AROME model is able to adequately predict severe weather events, however, as resolution increases, the importance of a probabilistic forecasting approach increases. An initial condition perturbation method and a model error representation scheme are described and their impact in an AROME-EPS test configuration is also presented.

Key-words: numerical weather prediction, physical parameterization, semi-Lagrangian horizontal diffusion, convection permitting ensemble system

1. Introduction

Thanks to the fast evolution in computing technology, more national numerical weather prediction centers can run models with increased resolutions. Using high-resolution models is very important in predicting fast-developing and intense atmospheric events. Good prediction of such hazardous events can protect lives and properties. Hence, investing in development of such models is very important for environmental and societal protection.

Hungary, together with several other European countries, has been participating in the ALADIN (Aire Limitée Adaptation Dynamique Développement International) consortium since 1991. The ALADIN consortium was initiated by France. The aim of this consortium is to develop a short-range limited-area numerical weather prediction (NWP) model. As a result of this collaboration, the ALADIN/AROME model family has emerged and is constantly being developed in the participating countries.

At the beginning of the ALADIN collaboration, the ALADIN model was a hydrostatic NWP model and was designed to run at relatively coarse horizontal resolutions (i.e., not higher resolution than 8 km), where the hydrostatic approximation (vertical acceleration of air is neglected) is valid. By the beginning of the new millennium, it became possible to run operational non-hydrostatic models at a horizontal resolution of 2–3 km. At Météo-France, the AROME (Application of Research to Operations at Mesoscale) project was initiated in 2002 with the aim to develop a non-hydrostatic NWP model running at 2.5 km horizontal resolution (*Seity et al.*, 2011). The AROME model has three main components: the non-hydrostatic ALADIN dynamical core (*Bubnová et al.*, 1995; *Benard et al.*, 2010), the atmospheric physical parameterizations, which are taken from the French Meso-NH research model (*Lafore et al.*, 1998), and the SURFEX surface model (*Le Moigne et al.*, 2009). A mesoscale data assimilation system with a three-dimensional variational (3D-VAR; *Fischer et al.*, 2005) scheme for the upper-air and an optimum interpolation (OI) technique for the surface analysis provides reliable initial condition for the AROME model.

The AROME model is now used in several countries of the ALADIN and HIRLAM (HIgh Resolution Limited Area Model) consortia. At the Hungarian Meteorological Service (HMS), work related to the AROME model started in 2006. After five years of scientific and technical development, the AROME model became operational in December 2010. In the beginning of the operational implementation, the model ran four times a day (at 00, 06, 12, and 18 UTC) at a horizontal resolution of 2.5 km, and provided forecasts up to 48 hours for a domain covering the Carpatian Basin (*Fig. 1*). The initial conditions were provided by the ALADIN/Hungary (Hereafter ALADIN/HU) limited area model (LAM) (*Horányi et al.*, 1996), while lateral boundary conditions are obtained from the ECMWF/IFS (European Centre for Medium-

Range Weather Forecasts / Integrated Forecast System) model. The ALADIN/HU model has its own three-dimensional variational (3DVAR) data assimilation system (*Bölöni*, 2006, *Randriamampianina,* 2006), which is partly inherited by the AROME model. The AROME assimilation system, using only conventional observations, was operationally implemented in March 2013 (*Mile et al.*, 2014). The short-range forecasts of AROME are mainly used by the forecasters of HMS to produce early warnings of severe weather events. Furthermore, products derived from AROME are utilized by wind energy farms to plan their production.

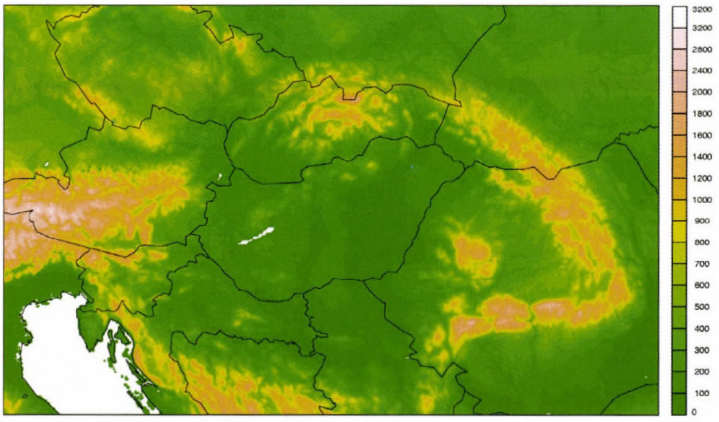

Fig. 1. Domain and orography of the AROME model as run operationally at the Hungarian Meteorological Service.

The aim of this paper is to present recent developments of the AROME model performed at HMS regarding dynamics, physical parameterizations, and ensemble prediction. In Section 2, the dynamical core of the model is briefly described and developments related to horizontal diffusion are presented. In Section 3, an overview of the physical parameterizations applied in AROME is given, together with the description of certain developments related to the turbulence parameterization and surface processes. Section 4 presents new developments regarding non-hydrostatic probabilistic forecasting. Finally, results are summarized in Section 5.

2. Dynamics

At horizontal mesh sizes at or below two kilometers, vertical accelerations could be of the order of the gravitational acceleration (g) and cannot be neglected any more, thus the hydrostatic approach is not recommended. Consequently, a new

equation has to be carried for the vertical momentum in the non-hydrostatic dynamical cores. The advantage of this approach is that certain atmospheric phenomena (like deep convection or orographic gravity waves) are resolved explicitly by the model, therefore no parameterization of these processes is required. The AROME model uses the non-hydrostatic dynamical core which was developed by the ALADIN consortium (*Bubnová et al.*, 1995).

The application of high resolution atmospheric models is a computationally demanding task, due to the increased number of grid points, the additional equation for vertical momentum in the dynamical core, and the increased complexity of certain parameterization schemes (e.g., microphysics). These requirements are only partly compensated by the fact that the deep convection scheme could be switched off in the model. In the case of the AROME model, this high computational demand is tackled by the application of advanced and efficient numerical schemes. AROME is a spectral model, which means that in the dynamical part of the model, the prognostic equations are handled in spectral space, which enables a fast computation of horizontal derivatives. Regarding the time integration, a very efficient semi-implicit, semi-Lagrangian time integration scheme is applied in AROME. This scheme permits a rather long time step even at fine horizontal resolutions. In the current operational version at the HMS, a time step of 60 s is used in AROME at 2.5 km horizontal resolution. This is approximately five times larger than the time step applied in other widely used non-hydrostatic models.

2.1. Horizontal diffusion

In current mesoscale NWP models, one dimensional physical parameterizations are applied. The reason for this is that above 1 km horizontal resolution, vertical gradients of meteorological variables are much larger than the horizontal gradients. However, due to numerical stability constraints, it is necessary to ensure a horizontal communication of grid cells. Apart from advection, this can be realized by the application of a numerical horizontal diffusion filter operator. In the case of the ALADIN/AROME model family, there are two main options for numerical horizontal diffusion. The first one is the spectral diffusion which is calculated in spectral space and consequently acts on the full model domain. The second option is the semi-Lagrangian horizontal diffusion (SLHD, *Váňa et al.*, 2008), which is calculated in grid point space as a function of wind deformation, hence it has a physically based and more local effect. It is important to note that in the AROME model, SLHD is used in combination with the spectral diffusion. In fact, next to SLHD, two other spectral diffusion operators are used: a fourth order spectral diffusion which acts mainly at the upper part of the model domain to prevent the reflection of gravity waves from the model top and a sixth order spectral diffusion to filter noise due to orography.

At HMS, several experiments have been done in connection with SLHD. The main goal of these experiments was to tackle some known deficiencies of

the AROME model during convective conditions (e.g., too strong updrafts, too high precipitation peaks in the cells, too strong gust fronts). In the original configuration, SLHD is applied to all (falling and non-falling) hydrometeors. The experiment presented here is based on the work of *Bengtsson et al.* (2010). SLHD is applied only to non-falling hydrometeors, and additionally it is also applied to the dynamical fields (wind, temperature, and humidity) and turbulent kinetic energy (TKE). Characteristics of the fourth order spectral diffusion have also been changed: while in the original configuration spectral diffusion acts on all levels (although with increasing intensity upwards), in the experiments spectral diffusion was only applied above 100 hPa. *Fig. 2* presents the impact of SLHD changes on a convective event. With the new SLHD configuration, the AROME simulation is closer to observations: the intensity of convective precipitation is reduced, convective wind gusts are weaker and the number of convective cells is decreasing. Apart from case studies, the new SLHD settings were tested on longer summer and winter periods, and the forecasts were compared against the surface (SYNOP) observations and radar-based precipitation data. Verification scores against SYNOP data show a clear improvement in the wind speed, wind gust, and cloudiness forecast, while the impact on temperature and humidity is neutral (*Fig. 3*). The diurnal cycle of convective precipitation is also improved, as the overestimation in the late afternoon is decreased (*Fig. 4*).

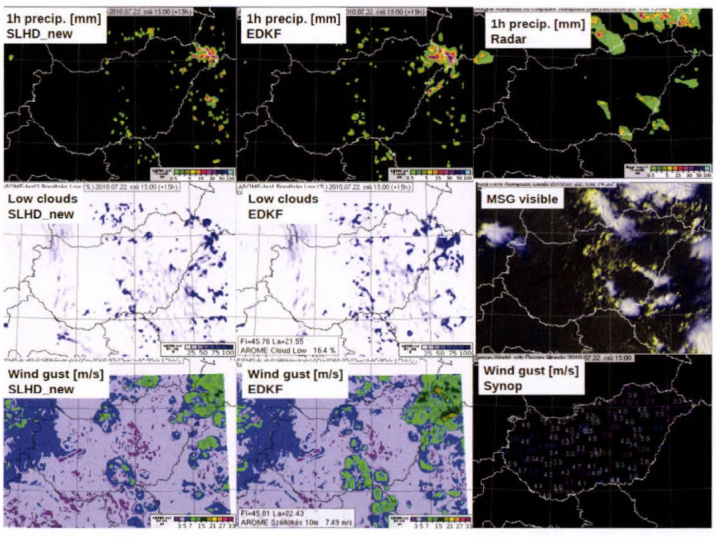

Fig. 2. Forecasted fields of two AROME experiments and measurements for July 22, 2010, at 15 UTC (+15 h forecasts). Left column: AROME with new SLHD settings, middle column: AROME with original SLHD settings, right column: measurements. First row: hourly precipitation, second row: low cloud cover, third row: hourly maximum wind gust.

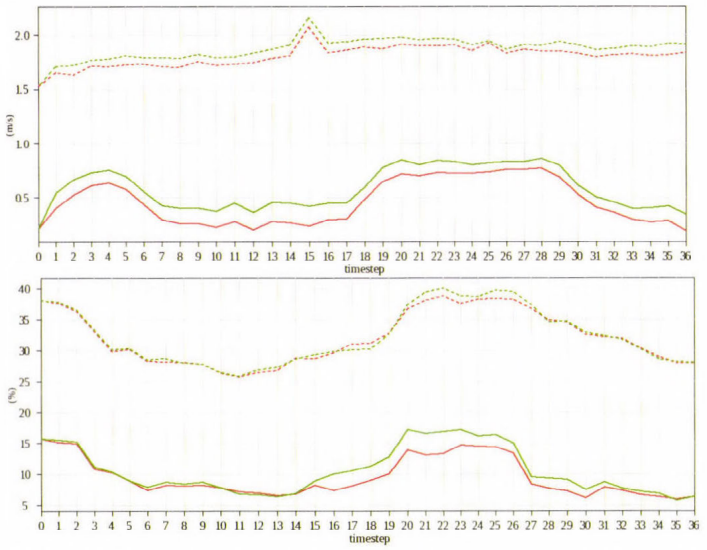

Fig. 3. Verification scores for the period between May 1, and June 1, 2013 as a function of lead time (in hours). Upper panel: 10-meter wind speed, lower panel: cloudiness. Green line: original SLHD settings, red line: new SLHD settings. Dashed line: root mean square error, solid line: bias. Always the 00 UTC forecasts were verified against low-altitude (station altitude below 400 m) SYNOP observations above sea level on the operational AROME domain.

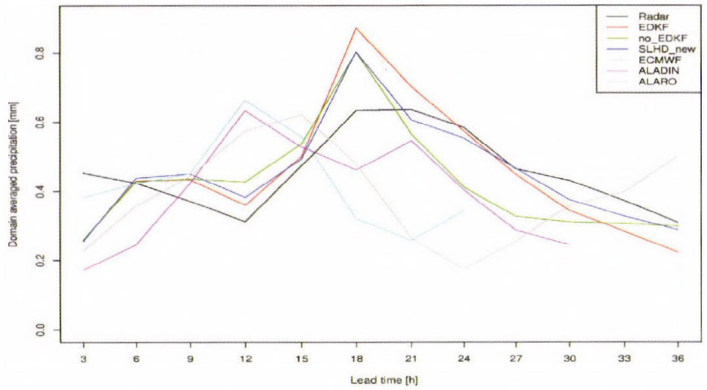

Fig. 4. Observed (radar) and predicted diurnal cycle of convective precipitation (area averaged precipitation on the AROME domain) for the period between July 17 and August 17, 2010. AROME experiments mentioned in the text: green: without EDKF parameterization and original SLHD settings; red: with EDKF parameterization and original SLHD settings; blue: with EDKF parameterization and new SLHD settings. Forecasts of the 8 km resolution limited area regional model run at the Hungarian Meteorological Service with two different physical parameterizations (ALADIN and ALARO) and of the ECMWF model are also indicated.

3. Physical parameterizations

Numerical weather prediction models are not able to resolve explicitly those processes which are smaller than the grid scale of the model, thus these processes have to be parameterized. Parameterization means the description of the overall effect of a given subgrid scale process on the grid scale values, using the given grid scale variables. The AROME model uses the physical parameterizations of the Meso-NH French research model. In the following, an overview is given on the components of this physical parameterization package, and the corresponding developments performed at HMS are described.

3.1. Microphysics

Phase changes occurring in clouds are described by the microphysical parameterization. In convection permitting NWP models, the choice of the microphysical scheme is of great importance. As these models do not apply a deep convection parameterization, the convective cloud should explicitly be simulated by the model, and thus the non-hydrostatic dynamical core and the microphysical parameterization play a crucial role. Consequently, the microphysical scheme has to be rather sophisticated to be able to simulate all the relevant processes during a lifetime of a convective cloud.

In AROME, the so-called ICE3 scheme (*Pinty* and *Jabouille*, 1998) is used, which carries six prognostic microphysical variables (vapor, cloud water, cloud ice, rain, snow, graupel), and describes the phase change processes among these variables. In the AROME model this means 35 processes: warm-cloud and mixed-phase processes are distinguished. Warm-cloud processes are autoconversion, accretion, evaporation, sedimentation, while mixed-phase processes are nucleation, ice-crystal autoconversion, aggregation, raindrop contact freezing, riming, melting, deposition, Bergeron-Findeisen effect, and ice-crystal sedimentation. The ICE3 scheme is a bulk one-moment scheme. This means that the mixing ratio of each hydrometeor is written as the third momentum of the size distribution of the given hydrometeor. The advantage of this approach is that the microphysical processes become analytically resolved processes. It has to be noted that a new two-moment microphysical scheme is currently under development in Meso-NH and is planned to be available in AROME soon. Next to the mixing ratios, this scheme handles the number concentration of hydrometeors prognostically as well.

Several tests were performed in connection with the initialization of the hydrometeor fields in the microphysics parameterization at the Hungarian Meteorological Service. The problem regarding hydrometeors is that these variables are not measured regularly, thus it is not possible to initialize these model fields based on measurements in an operational setting. In the early years of AROME development, it was considered that the formation of hydrometeors

is a relatively fast process, and consequently, it is possible to initialize these fields with zero. It was assumed that if the initial temperature and humidity fields are correct, then the hydrometeors would form within a couple of time steps. As a contrary to this assumption, case studies showed that if the hydrometeors are initialized with zero, then precipitation events could be missed by AROME in the early hours of the forecast. To overcome this problem, the following procedure was applied: the hydrometeors are "cycled" from the previous run, so, e.g., the initial hydrometeor fields of an AROME forecast starting at 06 UTC are the +6 h forecasted hydrometeor fields of the 00 UTC AROME forecast. With this approach, several previously missed precipitation objects could be well simulated by AROME (*Fig. 5*).

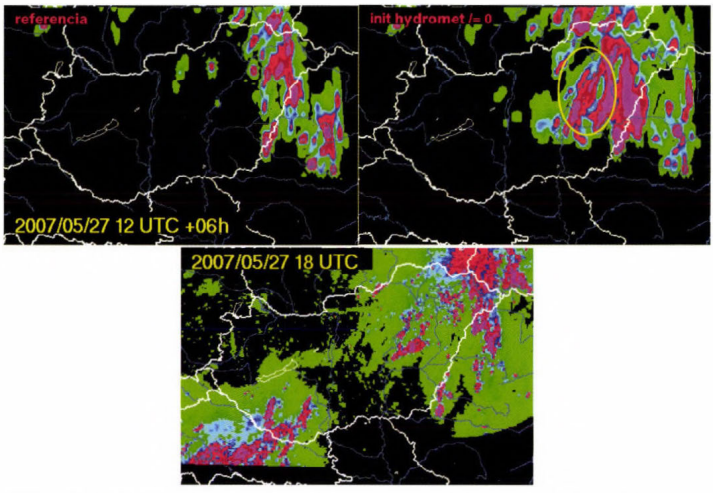

Fig. 5. Impact of hydrometeor initialization on the AROME forecast. Left: hydrometeors are initialized with zero; middle: hydrometeors are initialized from the 6 hour forecast of the previous run; right: hourly accumulated radar precipitation. A +6 h forecast of hourly precipitation is shown valid for 12 UTC, May 27, 2007.

3.2. Turbulence and shallow convection

Shallow convection refers to the warm updrafts (thermals) which originate from the surface and reach the top of the planetary boundary layer (PBL). These thermals are usually indicated by small non-precipitating clouds (Cumulus humilis). Boundary layer turbulence refers to those eddies which are generated either by wind shear (mechanical turbulence generation) or buoyancy, with a characteristic size much smaller than the depth of the PBL. Until recently, shallow convection was parameterized separately from boundary layer turbulence in NWP models, however, nowadays these two processes are handled in a unified way in several schemes.

In the AROME model, the eddy diffusivity – mass flux (EDMF) approach is followed to parameterize turbulence and shallow convection. The eddy diffusivity part of the parameterization uses the CBR scheme (*Cuxart et al.*, 2000) to describe the effect of boundary layer turbulence. This is a 1.5 order closure which carries a prognostic equation for the turbulent kinetic energy. The diffusion coefficients are then calculated based on TKE, a turbulent length scale and stability functions. In the AROME model, the length scale formulation after *Bougeault* and *Lacarrere* (1989) is applied. Originally, the CBR scheme has both one and three dimensional versions, however, currently the one dimensional version is applied in AROME. Based on recent experiments, it is assumed that a three dimensional turbulence scheme is not necessary above 1 km horizontal resolution (*Yann Seity* and *Rachel Honnert*, personal communication). The main drawback of the CBR scheme is that it is a local scheme, which means that turbulent fluxes at a given vertical level are determined by the local vertical gradients of wind and temperature at that level. Consequently, with a local turbulence scheme, it is not possible to reproduce the correct behavior of the convective boundary layer, which has a strong non-local nature: thermals originating at the surface result in considerable vertical transport in the middle part of the PBL, where the local vertical gradients are very close to zero. To resolve this problem, in the EDMF framework a mass flux parameterization is applied next to the CBR scheme.

In the AROME model, the mass flux parameterization of a shallow convection thermal is divided to two parts (*Pergaud et al.*, 2009). On vertical levels below the shallow convective cloud base, the parameterization of *Lappen* and *Randall* (2001) is used. This scheme is closed with the surface sensible heat flux, consequently, the entire mass flux part of the EDMF parameterization is inactive if the surface sensible heat flux is negative (stable conditions). Above the cloud base, the *Kain* and *Fritsch* (1990) parameterization is applied (this is why the EDMF parameterization is mentioned as EDKF in connection with the AROME model). The closure of this scheme is performed by taking the mass flux at cloud base from the parameterization of the non-cloudy part of the thermal. The cloudy part uses a diagnostic cloud scheme where the cloud fraction at a given level is proportional to the area fraction of the updraft.

At the Hungarian Meteorological Service, the impact of the EDKF parameterization on the overall performance of the AROME model has been investigated before the operational introduction of the scheme. As the scheme is only active during unstable conditions, largest impact was expected for summer convective events. *Fig. 6* shows the impact of EDKF on a summer convective case. Here, two AROME simulations are compared; one with EDKF, and a second one which parameterized turbulence and shallow convection separately (with the CBR and Kain-Fritsch schemes, respectively). The run without EDKF significantly overestimates the number of convective cells during early afternoon, while during the evening it fails to simulate the heavy thunderstorms

(not shown here). Also, convection itself is initiated too early (around 8 UTC) in this experiment (see also in *Fig. 4*), and consequently, convective wind gusts are overestimated until the early afternoon hours.

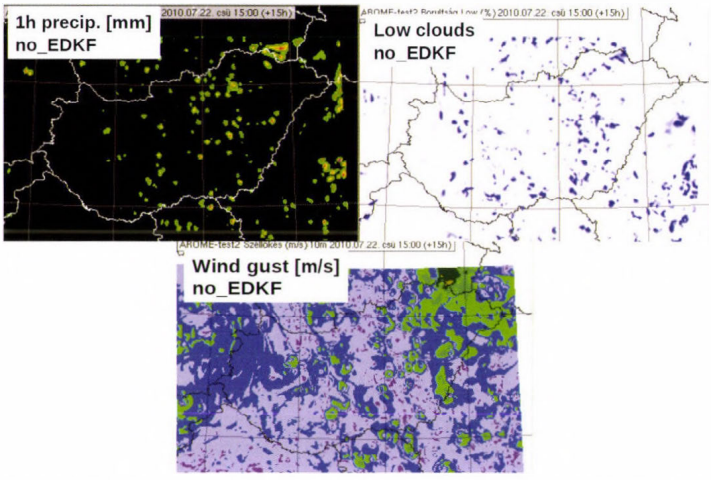

Fig. 6. Same AROME forecast of hourly precipitation, low clouds and wind gusts as in *Fig. 2*, but the EDKF parameterization is switched off, thus turbulence and shallow convection is parameterized separately (CBR scheme for turbulence and Kain-Fritsch scheme for shallow convection). Colour scales are the same as in *Fig. 2*.

3.3. Surface

Surface processes are calculated using the SURFEX (SURFace EXternalisée, *Le Moigne*, 2012) platform.

SURFEX uses the tiling approach: each grid point is divided into 4 different surface types (tiles): sea, inland water, town, and vegetated land. Each tile uses the same atmospheric forcing (air temperature, humidity, wind speed, long and shortwave radiation, pressure, precipitation), but the parameterizations are different and independent of each other. The resulting surface fluxes (momentum, sensible- and latent heat) are averaged according to the area fraction of the tiles and returned to the atmosphere. Surface parameters are determined by physiographic databases: GTOPO30 for orography, ECOCLIMAP for surface covers, and FAO for soil texture.

In the current operational version, over sea and inland water (lakes) SURFEX uses simple schemes: surface temperatures are kept constant, roughness length and fluxes are computed with the Charnock's approach. However, there is a more advanced scheme for lakes, FLAKE (Freshwater lake, *Mironov et al.*, 2010), in which lake temperature is a prognostic variable.

Over artificial surfaces, the TEB scheme (Town Energy Budget, *Masson,* 2000) is used. Towns are represented by the canyon concept: there is a single road with two buildings and a canyon between them. Each surface (road, wall, roof) consists of 3 layers and has a different temperature , while the temperature inside the buildingsis constant. The time evolution of the temperatures are calculated by heat conduction equations. In the radiative forcing, trapping and shadowing effects are also taken into account. The scheme also accounts for anthropogenic heat and water fluxes (traffic and industry).

Vegetated land surfaces are parameterized with the ISBA scheme (*Noilhan* and *Planton*, 1989; *Noilhan* and *Mahfouf,* 1996). The current operational version uses a 3-layer (surface, root zone, and deep soil) force-restore scheme. Over snow mantel, a one layer snow scheme (*Douville et al.* 1995) is used in which snow albedo and density are prognostic variables.

The 2 m temperature and 10 m wind are calculated by the Canopy scheme (*Masson* and *Seity*, 2009) ,which is a one dimensional vertical turbulence scheme in the surface boundary layer.

Vegetation is constant and determined from climatology databases. However, a more advanced version of the ISBA scheme, called ISBA-A-gs (*Calvet et al.* 1998), uses a simplified photosynthesis model which is able to describe the evolution of vegetation. In this model version, biomass is a prognostic variable. Growing of the active biomass is due to assimilation of CO_2 (photosynthesis), while the decline (or mortality) can be due to soil moisture stress, senescence, or transport of organic molecules from active biomass to structural one. Since the photosynthesis process depends on the vegetation type, the vegetated land tile in SURFEX is further divided into 12 patches according to the vegetation or surface type, like grass, crops, trees, etc. Beside the prognostic treatment of the vegetation, the scheme also calculates the carbon fluxes (assimilation and soil respiration).

In the framework of the Geoland2 EU-FP7 project, the task of the Hungarian Meteorological Service was to simulate the natural carbon fluxes and the evolution of vegetation over Hungary. SURFEX was used in offline mode (no influence on the atmosphere) with the ISBA-A-gs photosynthesis model. To improve the accuracy of the initial soil moisture and biomass fields, assimilation of satellite observations (surface wetness index and leaf area index) was developed and used. Results have shown that the model is able to describe the seasonal cycle of the vegetation and the natural carbon fluxes, and that assimilation of the above mentioned satellite observations (SWI and LAI) gives some improvement in spring (*Fig. 7*).

The Hungarian Meteorological Service also takes part in the IMAGINES EU-FP7 project. Our task – besides the simulation of vegetation and carbon fluxes – is the development of the model to be able to assimilate surface albedo from new generation Proba-V satellite observations and to calculate agricultural indicators like drought indices.

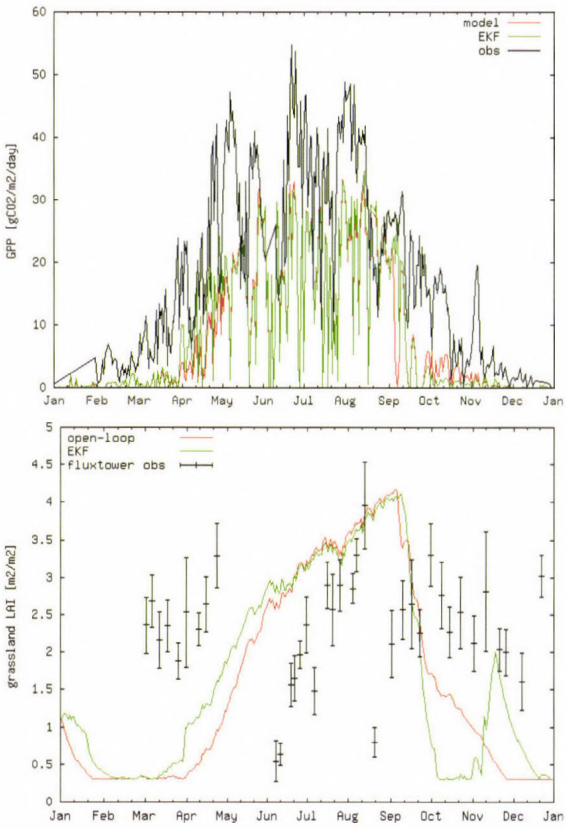

Fig. 7. Simulated and measured carbon flux (up) and leaf area index, LAI (down). Black line is observation, red line is without and green line is with assimilation.

3.4. General performance of the AROME model

As a result of the developments described in the previous sections, the AROME model has become a robust and reliable operational NWP model at HMS. The quality of AROME forecasts is comparable to that of other operational models used at HMS. In this section we show verification scores of a longer period, where the performance of AROME is compared to two operational hydrostatic models: the IFS global model run at ECMWF at 16 km horizontal resolution and the ALADIN regional model run at HMS at 8 km resolution.

The time period for the comparison was chosen in a way that no major changes should be applied in any of the three models. According to this criteria the period between September 16, 2013 and July 2, 2014 was selected. In this period, AROME was running with the model cycle 36, and the 3DVAR data assimilation system was operational using conventional upper air observations.

In the following, verification scores for screen and surface level variables (using SYNOP stations) as well as upper level variables (using radiosounding stations) are presented. Only forecasts with 00 UTC initial time were verified, and the verification scores were investigated as a function of lead time.

Regarding temperature and dew point at 2 meters, performance of AROME is comparable with the ECMWF model, while these two models outperform the ALADIN model for these variables (*Figs. 8a* and *8b*). The model bias has a diurnal dependency, daytime temperatures are underestimated, while nighttime temperatures are overestimated in AROME. Wind speed and wind gusts at 10 meters are generally overestimated by all three models (*Figs. 9a* and *9b*). For wind speed, ECMWF gives the best forecasts followed by AROME and ALADIN. Wind gusts are best captured by AROME, while ALADIN and ECMWF have similar performance for this variable.

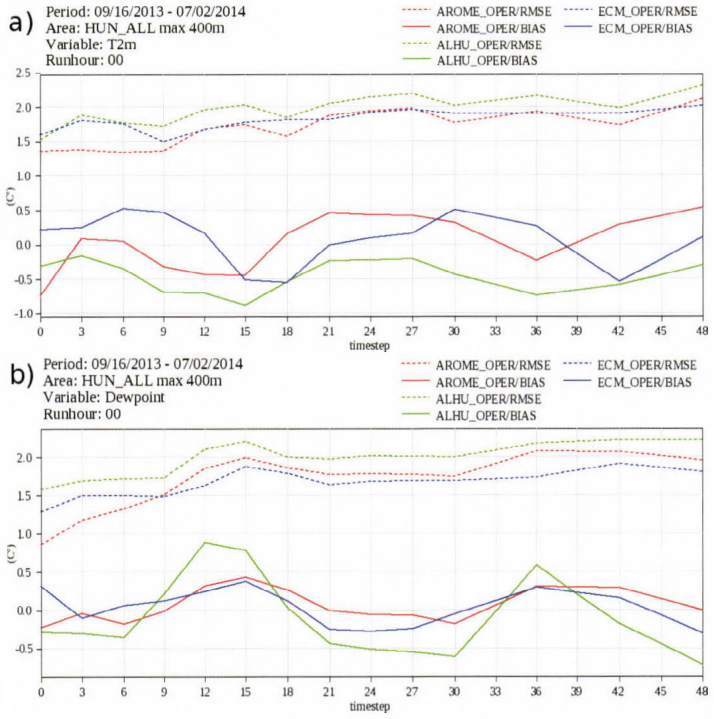

Fig. 8. Verification scores as a function of forecast lead time for temperature (a) and dew point (b) at 2 meters for operational NWP models at HMS between September 16, 2013 and July 2, 2014. Red: AROME, green: ALADIN, blue: IFS; dashed line: root mean square error, solid line: bias.

High resolution non-hydrostatic models are mainly applied for the forecasting of severe weather events, thus it is important to assess the quality of forecast performance for heavy precipitation. *Fig. 10* presents the symmetric extremal dependence index (SEDI), which is often used to verify high threshold events and the frequency bias for forecasted 12 hourly precipitation amounts. The SEDI score shows that for higher thresholds, the AROME model gives the best precipitation forecasts out of the three operational models. However, the frequency bias score points out a serious problem of AROME, namely that the model tends to forecast intensive convective cells more often than in reality. This erroneous model behavior is currently investigated at HMS.

Model performance at upper levels is mainly important for aviation forecasting. Based on the investigation of geopotential, temperature, wind, and humidity at several vertical levels, it can be concluded that the three models have similar performance, and the AROME model has usually a low bias but somewhat higher RMSE scores than the other two models (*Figs. 11a* and *11b*).

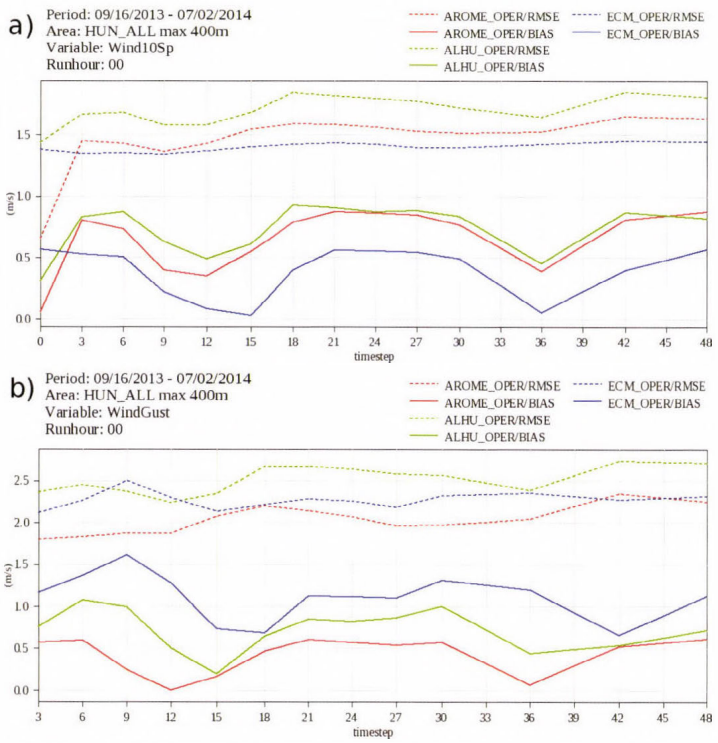

Fig. 9. Same as *Fig. 8* but for wind speed (a) and wind gusts (b) at 10 meters.

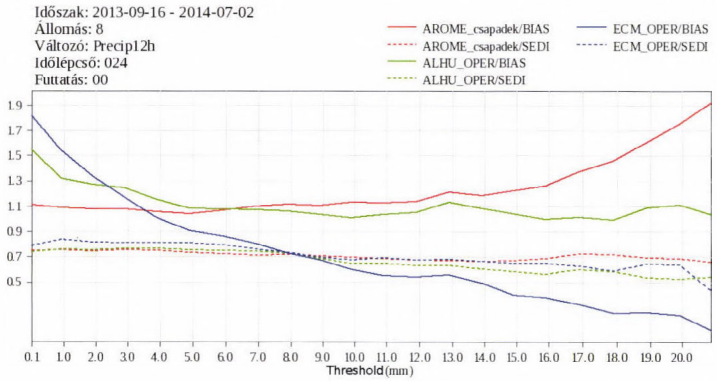

Fig. 10. Verification scores for 12 hourly accumulated precipitation for operational NWP models at HMS between September 16, 2013 and July 2, 2014. Red: AROME, green: ALADIN, blue: IFS; dashed line: SEDI, solid line: frequency bias.

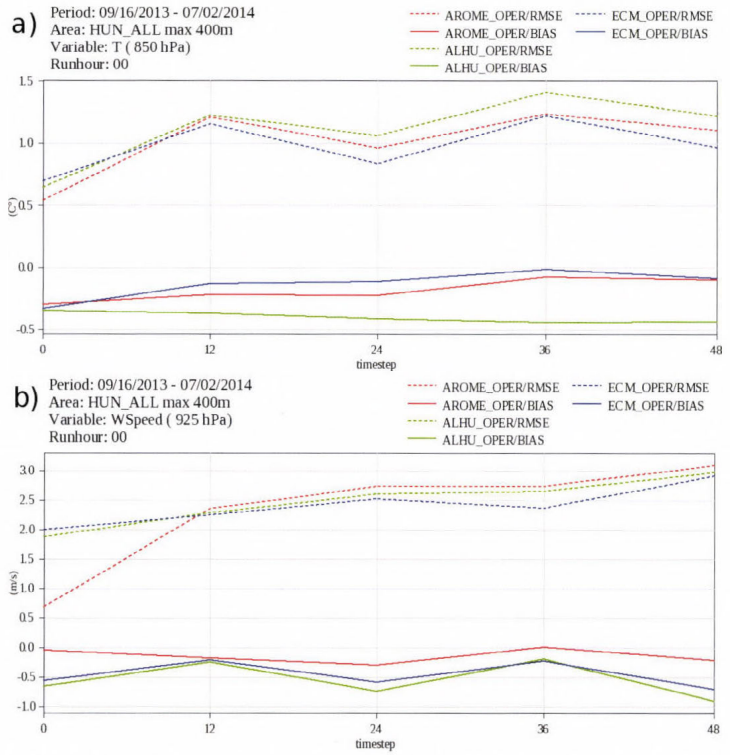

Fig. 11. Same as *Fig. 8* but for temperature at 850 hPa (a) and wind speed at 925 hPa (b).

4. Ensemble prediction system with AROME model

4.1. Motivation for a convection-permitting EPS

The uncertainty of numerical weather predictions is usually thought to originate from two main sources (*Palmer* and *Tibaldi*, 1988):
– Initial condition (IC) errors which evolve with time in the models due to the chaotic nature of the non-linear atmospheric system;
– Model errors which are based on limited human knowledge about atmospheric processes and finite resolution and representation possibilities of our models.
In reality, these errors can not be absolutely separated and they evolve together with time in the numerical models. Instead of giving a single-value as a forecast of a meteorological variable, it is more correct to give a probability density function (PDF) of it which contains information about forecast uncertainty. Until now, ensemble prediction systems (EPS) have been the only feasible and widely used tools to estimate such PDF. The main idea behind EPS is to run not only a single-forecast but an ensemble of numerical integrations where members can differ from each other in various aspects. These differences are defined by the perturbation generation methods which are designed to address different sources of error, so basically IC perturbation methods and model error representation can be separated.

The first ensemble prediction systems (EPS) were implemented in the early 90's with global models of ECMWF and NCEP (*Buizza et al.*, 1993; *Toth* and *Kalnay*, 1997). These global systems described synoptic-scale motions on medium-range. Consequently, their error is dominated by the chaotic growth of IC error, and that is why early methods focused on IC perturbations (singular vector and breeding methods). Later it was realized that classic methods can not always ensure sufficient spread at the early stage of the forecast, so new methods were implemented, which aim is usually to identify the most uncertain parts of analysis fields where bigger initial spread is needed. One possible way is to run an ensemble of data assimilation cycles (EDA) with perturbed observations. This method has been successfully used for example in ECMWF's EPS or in Meteo-France's global ensemble, called PEARP (*Desroziers et al.*, 2009; *Vié et al.*, 2011).

In the improving ensemble systems, it was recognized that the representation of model error is also a very important challenge, so the perturbation of the model formulations is also necessary. Generally, it is assumed that model physics is more uncertain than dynamics because of the fluctuation of sub-grid scale processes and the bigger error of the parametrization methods. For that purpose, ensemble members can run with different parametrization schemes (multi-physics approach, used e.g., in PEARP) or with slightly different parameter settings in physics (parameter

perturbations). Another possible way of representing model error is the stochastic perturbation of the total tendencies coming from the physics. Such a method is the so-called stochastically perturbed parameterized tendencies (SPPT) which was first implemented at ECMWF (*Buizza et.al.*, 1999).

Limited area ensemble prediction systems (LAMEPS) have become also popular tools to refine global probabilistic forecasts on a shorter time range and for a smaller domain. LAMEPS have to be coupled to global EPS, which results in some additional challenges. Global perturbations have to be taken into account through the interpolated lateral boundary conditions (LBC) of the perturbed members. The potential benefit of LAMEPS motivated the HMS to start its own researches on that field and established an operational system in 2008. This EPS uses the hydrostatic ALADIN model and runs with 8 km horizontal resolution. It has 11 members which are the simple dynamical downscaling of the control and the first 10 perturbed members of the 18 UTC run of the Prevision Ensemble ARPege (PEARP). While no local perturbation or data assimilation have been implemented yet, its quality depends highly on PEARP, and the impact of the changes in global system can be also measured in the LAMEPS. The slightly positive impact of a simple EDA implementation was shown, where only near-surface observations were perturbed in an ensemble of surface optimal interpolations (*Horanyi et al.*, 2011).

The quality of numerical weather prediction has been improving for the previous decades because of the better model formulations and the finer resolution which was enabled by the growing computer capacity. As it has been already mentioned in Section 2, at around 2 km resolution, models become non-hydrostatic and they can resolve such small-scale phenomena like deep convection. This way, finer structures can be produced and more realistic fields can appear. Unfortunately, this type of improvement is not necessarily associated with better scores, because resolving smaller scales can cause more uncertainty in model results (e.g., localization problems can lead to double-penalty effect). To overcome this problem, more and more national meteorological services in Europe started to develop non-hydrostatic model based ensemble systems. This new generation of EPS is also referred to as convection-permitting EPS. The introduction of such systems has already happened at Deutscher Wetterdienst (DWD) with COSMO-DE which has 20 members and runs with 2.8 km resolution (*Gebhardt et.al.*, 2008). Met Office has also started its operational convection-permitting EPS based on the 1.5 km resolution version of Unified Model (*Migliorini et.al.*, 2011). Météo-France has also joined the bigger services and runs its 12-member EPS with AROME model (*Vié et al.*, 2011).

HMS started its own research around convection-permitting EPS in 2012, and many tests have been run since then. Some of the results will be presented in this chapter. In this paper, an 11-member test configuration is called as a reference, which is, similarly to the operational LAMEPS, the simple dynamical downscaling of the first 11 PEARP member. AROME model runs with very

similar settings to what was detailed in previous parts for single-forecasts. The only notable difference was that the SLHD settings were not changed (cf. Section 2.1). In the following parts, the impact of two perturbation methods will be presented, which have been already mentioned as successfully used approaches in global EPS. The EDA method is addressed to IC error (see Section 4.2), while the SPPT method represents the model error (see Section 4.3).

4.2. Impact of Ensemble Data Assimilation Method

Modern data assimilation methods are based on complex algorithms which usually combine model forecasts as background fields and different types of observations. Similarly to the atmospheric models, these algorithms also have their limitations, while background fields and observations are also sources of additional errors. As a result of the above mentioned weaknesses, it has to be admitted that analysis fields are imperfect. A plausible way for handling this imperfection is to define the most uncertain areas of the analysis, which is possible with generating not only a single analysis field but running an ensemble of data assimilation cycles. This ensemble can provide flow dependent information about the accuracy of the background fields which is very useful to the data assimilation itself (*Brousseau et al.*, 2006; *Desroziers et al.*, 2009). From the aspect of an ensemble, it is even more important that more analysis fields are generated in EDA which can be the initial conditions of different ensemble members in an EPS.

The differences between the members of EDA originate usually from the perturbations which are added to the observations:

$$y'_j = y + \sigma(y) r_j \tag{1}$$

where it is assumed that observations y are imperfect but they are not biased and their uncertainty can be described by σ, which is estimation of the accuracy of the instrument. There is an r random number for the jth member, picked from a Gaussian-distribution, which has 0 mean, unit variance, and bounded in a [–3;3] interval. Observation perturbations can evolve in assimilation cycles, so in new steps there are always uncertainty information in the system which comes from the background fields. Additionally, LBCs are needed in LAM EDA during the model integration when background fields are generated. These LBCs are usually interpolated from different members of a global EPS, so they can be also sources of perturbations inside an EDA system.An EDA was implemented to construct better perturbed initial conditions for our test AROME-EPS compared to those obtained by simple downscaling of the global EPS. In this implementation of EDA (very similar to the EPS itself), different members were coupled to the different members of PEARP. The data assimilation methods are very similar to the operational AROME system of

HMS (*Mile et al.*, 2014). Conventional data (SYNOP, radiosonde, aircraft measurements) were used in a 3D-VAR data assimilation which generated atmospheric fields. Surface fields were simply interpolated from HMS's operational ALADIN model, where an optimal interpolation method is used to improve surface variables with observations.

In comparison with the reference, it is expected from the EDA based configuration that the quality of all members can be improved simply because of the positive impact of data assimilation itself. It is also expected that additional perturbations can increase the spread of the system. These two effects can result in a better relationship between the root mean square error (RMSE) of the ensemble mean and the system's spread. These expectations are verified on spread-skill relationship plots (*Figs. 12a, 12b, 12c, 12d*), where RMSE is smaller and spread is bigger in the early stage of the forecast. Later the difference between reference and EDA based version are smaller, because on such a small domain, the effect of LBC's become dominant quite fast. For total cloudiness scores, *Fig. 12c* underlines another advantage of EDA which is valid in AROME-EPS framework: hydrometeors can be initialized from background, which importance have been already mentioned in Section 3.1. In this paper, mainly near-surface scores are presented because of the big number and high frequency of independent SYNOP observations (*Figs. 12a. 12b, 12c*). ECMWF analysis was chosen as a reference for upper-air verification (*Fig. 12d*). It has to be noted that the remarkable resolution difference between AROME model (2.5 km) and reference analysis (16 km) can be questionable. Unfortunately, the short test period and the small domain resulted a very limited number of radiosonde measurements, what has not permitted to calculate atmospheric scores on higher level with observations.

a)

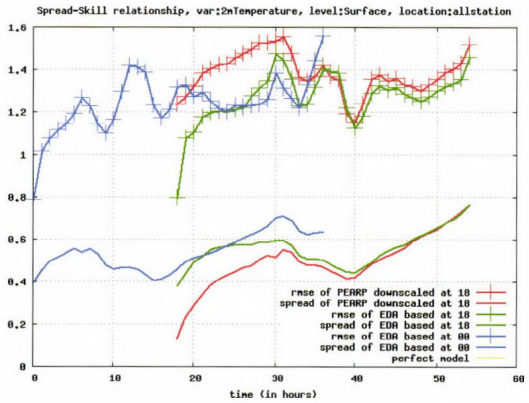

Fig. 12 a. Spread-skill relationship of 2 meter temperature. Red is a simple PEARP downscaling as a reference; blue and green are the test versions where IC is generated in an EDA system. Scores are calculated for the period between December 26, 2011 and January 8, 2012.

b)

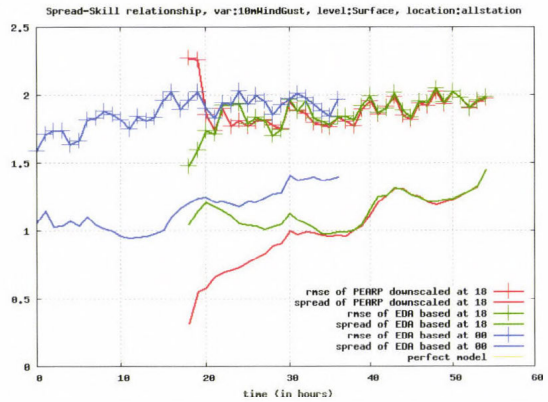

c)

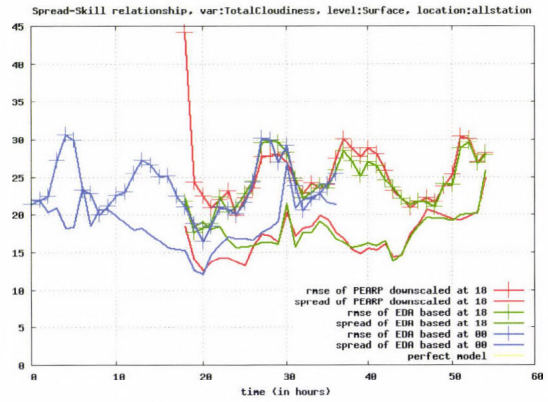

d)

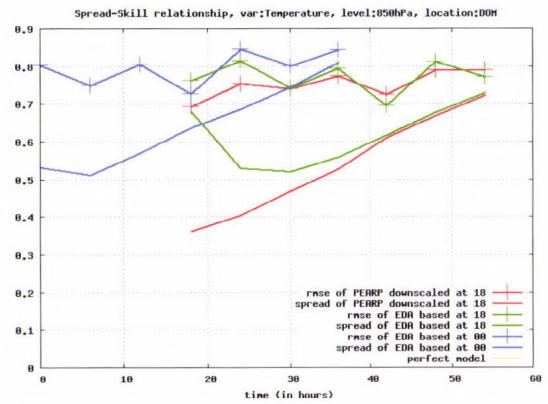

Fig. 12 b-d. Spread-skill relationship of 10 meter wind gust values (b), and total cloudiness (c), temperature on 850hPa pressure level Red is a simple PEARP downscaling as a reference; blue and green are the test versions where IC is generated in an EDA system. Scores are calculated for the period between December 26, 2011 and January 8, 2012.

4.3. Impact of Stochastically Perturbed Parametrized Tendencies

The original version of Stochastically Perturbed Parameterized Tendencies (SPPT) scheme was developed at ECMWF and called just as stochastic physics or BMP (*Buizza et al.*, 1999). Later it has been revised (*Palmer et al.*, 2009) and used as a successful tool to increase ensemble spread during the whole range of the forecast. It had positive impact even on the quality of single-model runs, especially in the tropical region.The concept can be expressed by the following equation:

$$e_j(T) = \int \{A(e_j;t) + P'(e_j;t)\} dt \,, \tag{2}$$

where e is the model state of the jth member at time T, which can be simply evolved from the integration of two processes: A is the contribution of the resolved scales (model dynamics) and P is the total tendency coming from the parametrized processes (model physics). While model physics is assumed to be a more uncertain part, in SPPT (as in other methods representing model error), this term is perturbed and P' is calculated from the original P :

$$P'(e_j;t) = (1 + \alpha r_j) P_j(e_j;t) \,, \tag{3}$$

where r is random number.

In the revised SPPT scheme, a spectral pattern generator is introduced, which provide horizontally smooth fields of r. Its horizontal structure is defined by an L horizontal correlation length parameter. The scheme has been implemented in AROME model (*Bouttier et al.,* 2012), where r is represented by biFourier functions and r' spectral coefficients are defined as first order auto-regressive processes:

$$(r')_{mn}(t + \Delta t) = \Phi (r')_{mn}(t) + \sigma_n \mu_{nm}(t) \,, \tag{4}$$

where σ sets the size of the perturbation and μ is a random number picked from a Gaussian-distribution, which has 0 mean, 1 variance, bounded in interval [–2;2], and it is a white process in time. The correlation between time-steps is determined via a τ decorrelation time parameter:

$$\Phi = \exp(-\Delta t / \tau) \,. \tag{5}$$

In Eq. (4) α is an attitude dependent number which varies on [0;1] interval and it has 0 value at the highest and the lowest model levels because of numerical stability reasons, and it is set to 1 in middle-troposphere.

In our AROME-EPS tests, SPPT was active in the case of perturbed members and inactive in the case of the control forecast. σ=0.5 and τ=2 hours

settings were used and two different L parameters were applied: in the so-called 'SpptLong' test L=500 km and in the so-called 'SpptShort' test L=125 km. As it was in EDA related experiments, simple dynamical downscaling of PEARP is referred to as reference forecast. The impact of SPPT scheme is represented also via spread-skill relationship. This impact was found quite limited in this research: neither the RMSE of the ensemble mean has improved, nor the spread of the ensemble members has increased for the examined variables (*Fig. 13a*). The most sensitive parameter was the total cloudiness, but unfortunately, some model quality degradation in connection with the growth of the system's spread (*Fig. 13b*) was observed.Further examination is needed for better understanding of this limited impact. More tests are needed on summer periods, when a 'more active' atmosphere is expected to behave differently. The importance of control parameters (σ, τ, and L) also needs some additional clarification in our AROME model.

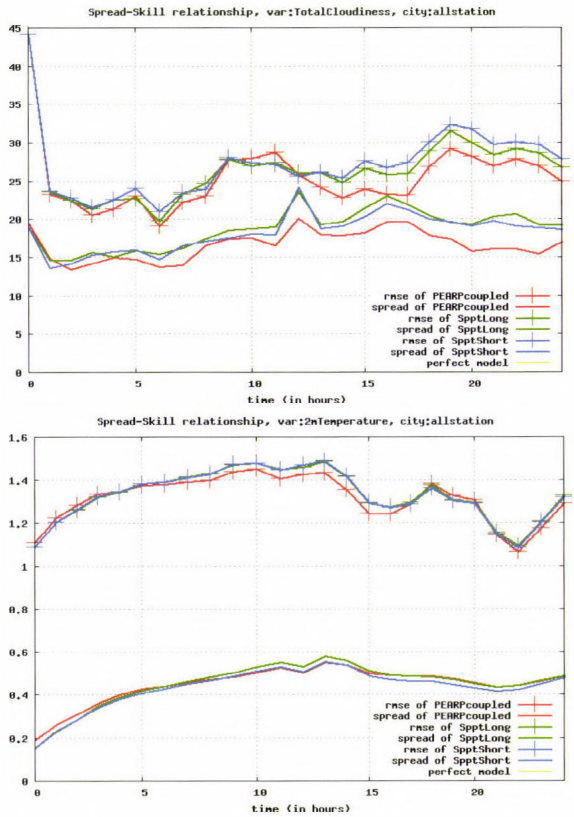

Fig. 13. Spread-skill relationship of 2 meter temperature (a) and total cloudiness (b). Red is a simple PEARP downscaling as a reference; blue and green are the test versions where SPPT scheme has been activated. Scores are calculated for the period between December 26, 2011 and January 8, 2012.

5. Summary and conclusions

In this paper, the AROME non-hydrostatic numerical weather prediction model as implemented at the Hungarian Meteorological Service was described with a focus on physical parameterizations and ensemble prediction. It was shown that high resolution NWP models are capable of predicting severe weather events. To achieve this, apart from increasing the horizontal and vertical resolution of the model, a non-hydrostatic dynamical core and advanced physical parameterizations have to be applied.

In connection with the dynamical core, aspects of horizontal diffusion in AROME were discussed. Recent developments regarding the semi Lagrangian horizontal diffusion scheme (SLHD) were described. It was shown that if SLHD is applied to all dynamical fields and not to falling hydrometeors then model performance – especially convective precipitation and wind gusts – could be improved.

The AROME model uses a state-of-the-art physical parameterization package, which was originally developed for the Meso-NH French research model. In this paper, some recent developments in connection with physical parameterizations performed at the Hungarian Meteorological Service were described. Regarding microphysics, the importance of the correct initialization of hydrometeor fields was highlighted. In connection with turbulence and shallow convection, the main ideas behind the eddy diffusivity – mass flux (EDMF) approach were discussed, and the positive impact of this parameterization on the resolved deep convection in the AROME model was shown. As the horizontal resolution of NWP models increases, surface processes are getting more and more important. In AROME, the SURFEX externalized surface model is utilized. Basic features of SURFEX were summarized as well as a recent development in connection with the prognostic treatment of vegetation.

To conclude the description of the deterministic AROME model, some verification scores were presented both for surface variables and upper levels. The performance of AROME was compared to other operational NWP models used at HMS. It was found that AROME has good performance for those meteorological variables (wind gusts and high precipitation amounts) which are linked to severe weather events.

As the horizontal resolution of NWP models is increasing, models are getting able to resolve even finer scales atmospheric phenomena. However, this not necessarily lead to better forecasts if forecast skill is measured locally (which is the case for most model applications). This is mainly related to localization problems in space and time. The application of the probabilistic approach could be a path to overcome this problem and handle the chaotic error growth in the model. In this paper, certain aspects of convection-permitting ensemble forecasts were highlighted and their impact was demonstrated using ensemble forecasts based on the AROME model. First, the ensemble data assimilation (EDA) method was

described, which aims at the correct determination of perturbed initial conditions for ensemble members. Secondly, one possible solution for the representation of model errors, namely, the stochastically perturbed parametrized tendencies (SPPT) approach was described. Based on the experiments performed with the AROME-EPS, it can be concluded that the EDA approach could significantly improve the high resolution ensemble forecasts, while the SPPT scheme has limited impact in its current configuration.

Acknowledgements: Useful discussions in the framework of the COST ES0905 project ('Basic concepts for convection parameterization in weather forecast and climate models') which contributed to the sections about dynamics and physics are greatly acknowledged. The authors are thankful to *Filip Vana* and *Lisa Bengtsson* for discussions about the SLHD scheme. The work about prognostic vegetation with the SURFEX model was carried out in the frameworks of the Geoland2 and ImagineS EU FP7 projects. AROME-EPS related tests were realized in the framework of an ECMWF's special project, called 'Continental winter weather prediction with the AROME ensemble prediction system', where HMS participate together with Météo France. We are really grateful to the project partners, and personally to *Francois Bouttier*. Remarks of the anonymous reviewer which lead to an improvement of the manuscript are greatly acknowledged.

References

Benard, P., Vivoda, J., Masek, J., Smolikova, P., Yessad, K., Smith, C., Brozkova , R., and *Geleyn, J.-F.,* 2010: Dynamical kernel of the Aladin-NH spectral limited-area model: Revised formulation and sensitivity experiments. *Q. J. Roy. Meteor. Soc., 136*, 155–169.

Bengtsson, L., Tijm, S., Váňa, F., and *Svensson, G.,* 2012: Impact of Flow-Dependent Horizontal Diffusion on Resolved Convection in AROME. *J. Appl. Meteor. Climatol. 51*, 54–67.

Bougeault, P. and *Lacarrere, P.,* 1989: Parameterization of orography-induced turbulence in a meso-beta-scale model. *Mon. Weather Rev. 117*, 1870–1888.

Bouttier, F., Vié, B., Nuissier, O., and *Raynaud, L.,* 2012: Impact of Stochastic Physics in a Convection-Permitting Ensemble. *Mon. Weather Rev., 140*, 3706–3721.

Bölöni, G., 2006: Development of a variational data assimilation system for a limited area model at the Hungarian Meteorological Service. *Időjárás 110*, 309–327.

Brousseau, P., Berre, L., Bouttier, F., and *Desroziers, G.,* 2011: Background-error covariances for a convective scale data-assimilation system: Arome-France 3D-Var. *Q. J. Roy. Meteor. Soc. 137*, 409–422.

Bubnová, R., Hello, G., Bénard, P., and *Geleyn, J.-F.,* 1995: Integration of the fully elastic equations cast in the hydrostatic pressure terrain-following in the framework of the ARPEGE/ALADIN NWP system. *Mon. Weather Rev. 123*, 515–535.

Buizza, R., Tribbia, J., Molteni, F., and *Palmer, T.,* 1993: Computation of optimal unstable structures for a numerical weather prediction model. *Tellus 45A*, 388–407.

Buizza, R.,. Miller, M., and *Palmer, T.N.,* 1999: Stochastic representation of model uncertainties in the ECMWF Ensemble Prediction System, *Q. J. Roy. Meteorol. Soc. 125*, 2887–2908.

Calvet, J.C., Noilhan, J., Roujean, J.L., Bessemoulin, P., Cabelguenne, M., Olioso, A., and *Wigneron, J.P.,* 1998: An interactive vegetation svat model tested against data from six contrasting sites. *Agr. Forest Meteorol. 92*, 73–95.

Cuxart, J., Bougeault, P., and *Redelsberger, J.-L.,* 2000: A turbulence scheme allowing for mesoscale and large-eddy simulations. *Q. J. Roy. Meteor. Soc. 126*, 1–30.

Desroziers, G., Berre, L., Chabot, V., and *Chapnik, B.,* 2009: A posteriori diagnostics in an ensemble of perturbed analyses. *Mon. Weather Rev. 137*, 3420–3436

Douville, H., Royer, J.-F., and *Mahfouf, J.-F.,* 1995: A new snow parameterization for the French community climate model. Part I: Validation in stand-alone experiments, *Clim. Dynam., 12*, 21–35.

Fischer, C., Montmerle, T., Berre, L., Auger, L., and *Stefanescu, S.E.,* 2005: An overview of the variational

assimilation in the Aladin/FranceNWP system. *Q. J. Roy. Meteor. Soc. 131,* 3477–3492.

Gebhardt, C., Theis, S., Krahe, P. and *Renner, V.,* 2008: Experimental ensemble forecasts of precipitation based on a convection-resolving model. *Atmos. Sci. Lett. 9,* 67–72.

Horányi A., Ihász I. and *Radnóti G.,* 1996: ARPEGE/ALADIN: A numerical weather prediction model for Central-Europe with the participation of the HMS. *Időjárás 100,* 277–301.

Horányi A., Mile M., and *Szűcs M.,* 2011: Latest developments around the ALADIN operational short-range ensemble prediction system in Hungary, *Tellus 63A,* 642–651.

Kain, J.S., and Fritsch, J.M., 1990: A one-dimensional entraining/detraining plume model and its application in convective parameterizations. *J. Atmos. Sci.* 47, 2784–2802.

Lafore, J.-P., Stein, J., Asencio, N., Bougeault, P., Ducrocq, V., Duron, J., Fischer, C., Héreil, P., Mascart, P., Masson, V., Pinty, J. P. , Redelsperger, J. L. , Richard, E. and Vilà-Guerau de Arellano J., 1998: The Meso-NH atmospheric simulation system. Part I: Adiabatic formulation and control simulations. *Ann. Geophys., 16,* 90–109.

Lappen, C.L. and *Randall, D. A.,* 2001: Toward a unified parameterization of the boundary layer and moist convection, Part 2: lateral mass exchanges and subplume-scale fluxes. *J. Atmos. Sci. 58,* 2037–2051.

Masson, V., 2000: A physically-based scheme for the urban energy budget in atmospheric models, *Bound.-Lay. Meteorol. 94,* 357–397.

Masson, V. and *Seity, Y.,* 2009: Including atmospheric layers in vegetation and urban offline surface schemes, *J. Appl. Meteorol. Clim. 48,* 1377–1397.

Migliorini, S., Dixon, M., Bannister, R., and *Ballard, S.,* 2011: Ensemble prediction for nowcasting with a convection-permitting model. I: Description of the system and the impact of radar-derived surface precipitation rates. *Tellus 63A,* 468–496.

Mile, M., Bölöni, G., Randriamampianina, R., Steib, R., and *Kucukkaraca, E.,* 2015: Overview of mesoscale data assimilation developments at the Hungarian Meteorological Service. *Időjárás 119,* 215–239.

Mironov, D., Heise, E., Kourzeneva, E., Ritter, B., Schneider, N., and *Terzhevik, A.,* 2010: Implementation of the lake parameterisation scheme flake into the numerical weather prediction model COSMO. *Boreal Env. Res. 15,* 218–230.

Le Moigne, P., 2012: SURFEX scientific documentation. Note de centre du Groupe de Météorologie a Moyenne Echelle, 87, Météo-France, CNRM, Toulouse, France, on-line available at: http://www.cnrm.meteo.fr/surfex/

Noilhan, J., and *Planton, S.,* 1989: A simple parameterization of land surface processes for meteorological models, *Mon. Weather Rev. 117,* 536–549.

Noilhan, J., and *Mahfouf, J.-F.,* 1996: The ISBA land parameterization scheme, *Global Planet. Change 13,* 145–159.

Pergaud, J., Masson, V., Malardel, S., and *Couvreux, F.,*2009: A parameterization of dry thermals and shallow cumuli for mesoscale numerical weather prediction, *Bound.-Lay. Meteor., 132,* 83–106.

Randriamampianina, R., 2006: Impact of high resolution observations in the ALADIN/HU model, *Időjárás 110,* 329–349.

Palmer, T.N., and *Tibaldi, S.,* 1988: On the prediction of forecast skill, *Mon. Weather Rev. 166,* 245.

Palmer, T., Buizza, R., Doblas-Reyes, F., Jung, T., Leutbecher, M., Shutts, G., Steinheimer, M., and *Weisheimer, A.,* 2009: Stochastic parametrization and model uncertainty. *Tech. Rep., ECMWF Tech. Memo. 598.* Available online at http://www.ecmwf.int/publications/.

Pinty, J.-P., and *Jabouille, P.,* 1998: A mixed-phased cloud parameterization for use in a mesoscale non-hydrostatic model: Simulations of a squall line and of orographic precipitation. *Preprints, Conf. on Cloud Physics, Everett, WA, Amer. Meteor. Soc.,* 217–220.

Seity, Y., Brousseau, P., Malardel, S., Hello, G., Bénard, P., Bouttier, F., Lac, C., and *Masson, V.,* 2011: The AROME-France Convective-Scale Operational Model. *Mon. Weather Rev. 139,* 976–991.

Toth, Z. and *Kalnay, E.,* 1997: Ensemble forecasting at NCEP and the breeding method. *Mon. Weather Rev. 127,* 3297–3318.

Vána, F., Bénard, P., Geleyn, J.-F., Simon, A., and *Seity, Y.,* 2008: Semi-Lagrangian advection scheme with controlled damping: An alternative to nonlinear horizontal diffusion in a numerical weather prediction model. *Q. J. Roy. Meteor. Soc. 134,* 523–537.

Vié, B., Nuissier, O., and *Ducrocq, V.,* 2011: Cloud-resolving ensemble simulations of Mediterranean heavy precipitating events: Uncertainty on initial conditions and lateral boundary conditions. *Mon. Weather Rev. 139,* 403–423.

IDŐJÁRÁS

Quarterly Journal of the Hungarian Meteorological Service
Vol. 119, No. 2, April – June, 2015, pp. 267–275

Meteorological support, weather warnings and advisories in the Hungarian Defence Forces

Richárd Büki[1]* and **Kornélia Radics**[2]

[1]*Geoinformation Service of the Hungarian Defence Forces*
Szilágyi Erzsébet fasor 7–9., H-1024 Budapest, Hungary

[2]*Hungarian Meteorological Service,*
Kitaibel Pál u. 1., H-1024 Budapest, Hungary

**Corresponding author E-mail: buki.richard@mhtehi.gov.hu*

(Manuscript received in final form April 25, 2014)

Abstract—During the history, it has been proved several times that ignoring the quickly changing meteorological circumstances and atmospheric phenomana or their insufficient assessement can result in catastrophic impacts on military operations. Weather plays a very significant role in flight operations, and it can be vital even for planning and executing operations of land forces and for any other open air activities involving armed forces (e.g., disaster relief activities, industrial and natural catastrophes, and in assessement of chemical, biological, radiological, and nuclear events). The possible course of weather and the range of the climatological factors should be taken into consideration for protecting life, property and infrastucture.

In the Hungarian Defence Forces, the focus of the meteorological support is on providing the necessary meteorological information for decision makers supporting the planning and executing certain military activities, and enhancing efficiency. This is a very complex task and that is the reason for having specialized meteorological service and capability within the Hungarian Defence Forces which can meet these requirements.

The military weather warnings and advisories ("military weather warnings") are specialized type of forecasts. They alert the military users on the possible or expectable severe weather, which can significantly impact life and property in order to mitigate the unfavorable effects of the severe weather. For avoiding misinformation in the meteorological support in our daily routine, the military weather warnings should be in harmony with the weather warnings issued by the Hungarian Meteorological Service for civilian users, which is enabled by the strong and efficient cooperation between the two services.

This paper describes some effects of weather on military activities in general and military weather warnings within the Hungarian Defence Forces.

Key-words: weather impact, warning, advisory, severe weather, military

1. Introduction

In order to deeply understand how civilian and military meteorology differ, firstly it is needed to be defined. By definition, the military meteorology is the science concerned with the collection and analysis of the understandings of the physical characteristics of the past, current, and predicted states of the atmosphere, including space, and the ability to exploit this information for the planning and conduct of military activities.

This paper highlights those weather elements that affect the different branches of the Hungarian Defence Forces.

2. Impacts of different meteorological elements on military activities

2.1. Barometric pressure

The weight of the air affects gunnery computations and ballistic preformance in armour operations.

The air pressure affects artillery operations due to projectile trajectory, barofuzing, and fire control calculations. Moreover, the vertical pressure profiles are essential in both baroarming and barofuzing as they are required for calculating densities for ballistic firing data (*METOC Effects Smart Book, (http://www.fas.org)* – Homepage of the Federation of American Scientist, 2002).

Aviation is one of the main user of barometric pressure data. Densitiy altitude, which is in strong connection with the barometric pressure, determines if an aircraft has enough lift capabilities and performance to get off the ground. Too much densitiy altitude limits fuel, weapons, and passenger loads.

2.2. Clouds and sky cover

Low overcast clouds limit the effectiveness of aerial illumination devices. Overcast clouds tend to limit heating of inactive targets and lower target detection ranges for thermal sights. NVG (night vision googles) are limited by clouds blocking natural light from the moon and stars. Close air support and aerial resupply missions are degraded by low clouds. Low ceilings affect target acquisition systems and terminally guided munitions. Low overcast clouds will limit the effectiveness of aerial illumination devices (*METOC Effects Smart Book, (http://www.fas.org)* – Homepage of the Federation of American Scientist, 2002).

Clouds are always a major consideration for aviation operations. Low overcast clouds will limit the effectiveness of aerial illumination devices. Overcasts tend to limit heating of inactive targets and lower target detection range for thermal sights. NVG are limited by clouds blocking natural illumination from the moon or the stars. Best use of most NVG requires about a

quarter of the moon, 30 degrees above the horizon, scattered clouds, and the sun more than 5 degrees below the horizon. Close air support and aerial resupply missions are degraded by low clouds.

From a CBRN (chemical biological radiological and nuclear) point of view, persistent overcast low clouds usually indicate a neutral condition for the hazardous materials, while broken low clouds indicate an unstable condition during the day and a moderately stable condition at night.

Overcast skies with low cloud bases reduce the effectiveness of infrared and photographic collection systems, and may restrict the use of UAVs (unmanned aerial vehicle).

2.3. Humidity

Coupled with high temperatures, high humidity decreases crew effectiveness in closed vehicles. The humidity should be taken into consideration in artillery operations due to its use to compute virtual temperatures for ballistic firing data.

High humidity destroys some chemical agents such as lewisite and phosgene because of rapid hydrolysis. High humidity increases the effectiveness of HC and phosphorous smokes, some chemical agents, and both wet and dry forms of biological agents. High humidity improves the effectiveness of wet aerosols by reducing evaporation, while low humidity assists agent aerosols (*METOC Effects Smart Book, (http://www.fas.org)* – Homepage of the Federation of American Scientist, 2002).

Extreme humidities affect handling, storage, and use of building materials. When coupled with high temperatures, humidity affects personnel and significantly increases the time to perform physical work.

2.4. Precipitation and icing

Rain and snow degrade trafficability and limit visibility. They also degrade target acquisition and NVG. Rain and snow affect visibility and the safety of both crew and airframe.

Rain and snow will effect the persistence of chemical agents and may produce radioactive rainout and hot spots. Snow may cover and neutralize certain liquid agents. Rain may even work as a decontaminate. On the other hand, some agents may be very persistent on snow (*METOC Effects Smart Book, (http://www.fas.org)* – Homepage of the Federation of American Scientist, 2002).

High rainfall rates influence river currents, water depth, and bridging operations. It complicates other construction or maintenance jobs, affects flooding, rivercrossings, soil bearing strength, and explosives.

Ice on lifting surfaces affects the aerodynamics of the aircraft. Even a little ice is a big problem.

Even moderate amounts of rain and snow will obstruct vision and degrade photographic and infrared data collection systems (*METOC Effects Smart Book, (http://www.fas.org)* – Homepage of the Federation of American Scientist, 2002).

2.5. Wind and turbulence

Trajectory projections and first round hit capability can be affected by high crosswinds. Winds affect the accuracy of rocket fire and firefinder radar trajectory computations (*METOC Effects Smart Book, (http://www.fas.org)* – Homepage of the Federation of American Scientist, 2002).

Strong winds aloft impact all ballistic projectile aiming calculations. Accurate and timely meteorological data can compensate for the problem. Wind profiles play a major role in ballistic wind compensations for artillery firing.

Strong winds, especially cross-winds, affect aircraft control near the ground during take-off and landings. Turbulence is a critical condition affecting all aviation assets and missions. It may cause aircraft structural damage or even crashes during take-offs and landings. Severe turbulence may cancel all operations.

Winds play a significant role in CB (chemical and biological) agent dispersion, chemical agent persistence, and aerial delivery methods. Very light and strong winds degrade effectiveness of smoke and CBRN operations. Wind direction is considered for fallout pattern determination.

Ground level winds affect river crossings, port management, and all watercraft. Construction projects in chronic wind areas may need to recalculate structural strength figures. Strong winds may damage or prevent installing antennas.

2.6. State of the ground

Frozen ground improves mobility and significantly increases the time available to prepare fighting positions. Deep snow slows movement of tracked vehicles. Frozen ground and mud affects munitions, sensors, and indirect fire.

Soil conditions impact the effectiveness of chemical agents. Bare, hard ground favors short-term effectiveness and high-vapor concentrations. If the surface is porous, such as sand, the liquid agent quickly soaks in. Vegetative cover reduces exposure to ultraviolet light and favors the survival of wet aerosols (*METOC Effects Smart Book, (http://www.fas.org)* – Homepage of the Federation of American Scientist, 2002). Wet soil degrades the effectiveness of smoke munitions.

Ground conditions impact mining operations, trenching, and any excavation job. Snow cover can impact the emplacement of scatterable mines.

Ground state affects trafficability and movement rates. Frozen ground improves mobility and will increase the time available for preparing fighting positions.

Wet grounds can affect trafficability and movement rates. Frozen ground improves mobility and significantly increases time available for preparing fighting positions. Deep snow slows movement of tracked vehicles. Frozen ground affects systems such as mines, sensors, and indirect fire.

2.7. Temperature, frost line, and thaw depth

High and low temperatures influence the type of lubricants to be used, engine warm-up periods, and sustained rates of fire for weapons.

High temperatures decrease the time personnel can remain in vehicles. High temperatures cause gun tube droop, shimmering, mirages, and vehicle exteriors to be too hot to touch. Extremely high temperatures increase water consumption.

Low temperatures degrade the ballistics of main guns, require frequent starting of engines, and may increase maintenance problems and possible detection by the enemy. Extremely low temperatures reduce personnel effectiveness and decrease the availability of water because of freezing.

Temperature profile affects calculations of ballistic artillery firing. The profile is used to compute virtual temperatures for artillery firing. Extreme cold affects gun accuracy and fuse functioning.

High temperatures reduce lift capability. Cold temperatures increase maintenance requirements and the time needed to accomplish each task. The number of personnel that can be carried on a flight is reduced due to the weight of cold-weather gear.

Some agents are more persistent at low temperatures. Vaporization may be a problem with higher temperatures. Normal atmospheric temperatures have little direct effect on a biological agent aerosol. Sub-freezing temperatures make water-based decontamination methods ineffective.

High temperatures impact trafficability, influence flood control, and dictate the use of certain construction materials. Cold weather influences ice thickness and river crossings, while ice flow problems affect bridges. For example, armored vehicle launched bridges are affected by warming if they were set up on frozen ground. Alternating freezing and thawing (frost heaves) may destroy the effectiveness of emplaced mines.

Frozen soil increases the difficulty of grounding equipment. At extreme cold temperatures, cables snap and wire is unmanageable. Extreme cold also shortens battery life and may put systems requiring a good source of battery power out of service.

Too cold or too hot conditions dictate the type of lubricants to be used, engine warm-up periods, and sustained rate of fire for weapons. Extreme low temperatures reduce personnel effectiveness, and decrease the availability of water because of freezing. Temperatures changing from above to below freezing can freeze stationary tracks into the mud. High temperatures cause gun tube "droop," shimmering, mirages, and vehicle exteriors to be too hot to touch.

The frost line impacts site selection, construction, excavation, and trafficability.

2.8. Visibility

Visibility affects visual target acquisition, fire adjustment, and electro-optical (E-O) target designation. Reduced visibility affects the placement of forward observers and fire support teams (*METOC Effects Smart Book, (http://www.fas.org)* – Homepage of the Federation of American Scientist, 2002).

The lack of good visibility affects landings and take-offs, terminally guided munitions, and the ability to distribute scatterable mines.

Low visibility decreases the effectiveness of visual, photographic, infrared, and E-O collection systems.

Poor visibility increases the survivability of infantry units.

2.9. Thunderstorms and lightning

Electrical storms restrict the use of and handling some munitions and fuse types because of safety.

Extreme weather that includes thunderstorms and lightning is very hazardous to inflight operations, refueling, and rearming operations.

Electrical storms, and the associated rain and wind, affect electronic systems in general and antennas, shelters, and mobility in particular.

3. Weather warnings and advisories

Certain weather conditions endanger life and/or property, pose a safety hazard, or adversely impact operations. Weather units should monitor these phenomena and provide products and services to support the possbily affected services and units when these conditions are observed or forecasted. These items include weather advisories and warnings.

A weather warning (WW) is a special notice provided to supported customers that alerts them to very likely weather conditions of such intensity that could pose a hazard to life or property.

A weather advisory (WA) is a special notice provided to supported customer that alerts them the likely potential of weather conditions that could affect their operations.

Within the Hungarian Defence Forces (HDF), the meteorological support is clearly defined in a Manual on Supporting Military Activities signed by the Chief of General Staff. This manual is the highest level document, and it is a framework for the main principles, duties ans goals in the field of military meteorological support.

Each unit involved in military meteorological support has its Standard Operating Procedure (SOP). This SOP deals with the aspects of military meteorolgical support at a certain unit in detail (including range of product, duties and responsibilities, order of reporting, threshold values for different weather elements if they apply). The SOPs are completed by the respective meteorological unit and approved by the Geoinformation Service of the HDF (GEOS).

GEOS is the supervising unit in the field of military meteorology in Hungary. There is a Weather Forecast and Training Department within the GEOS providing the personnel for the continuous meteorological support and professional supervision over the meteorolgical support acitivities carried out in the HDF.

As the leading professional meteorological unit of the HDF, GEOS is entitled to issue WWs and WAs for the whole activity spectrum of the HDF and MoD including excercises, troop movement, tansport, and any other open air activities.

There are three types of WAs and WWs isued by GEOS:

- Preliminary General WA is a forecast in plain text format for general military users with 24–72 hours lead time.
- General WA is a forecast in plain text format for general military users with 3–24 hours lead time.
- WW is a forecast in plain text for general military users with 1–3 hours lead time (*Fig. 1*).
- In every case when a WA or WW has been issued, its receipton is verified by phone call and sent via electronically as well.

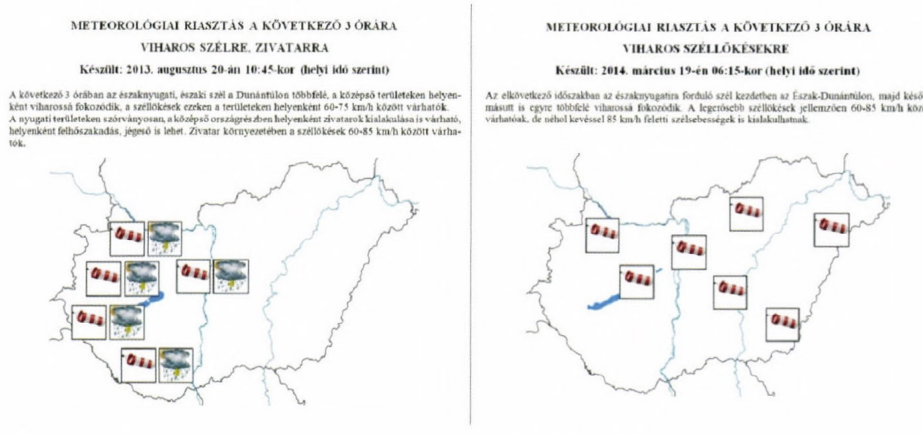

Fig. 1. Two examples for weather warnings issued by GEOS.

The Meteorological Center of the Air Command and Control Center of HDF (ACCC) provides meteorological support for the military aviation in Hungary and entitled to issue aviational WWs in harmony with the WWs and WAs issued by GEOS. The WWs are in a text and map combination format with an abbreviated form of text explanation (*Fig. 2*). The issued WWs are sent to GEOS and the MSUs at the airfields.

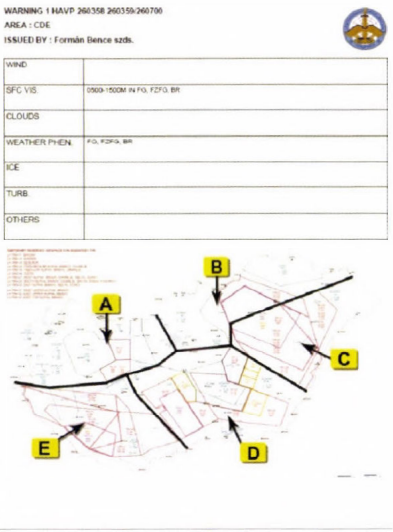

Fig. 2. An example for weather warning issued by ACCC.

Different weather warnings and advisories by Hungarian military MSUs are summarized in *Table 1*.

Table 1. WAs and WWs

No.	Station	Airbase	Lon [° E]	Lat [° N]	Altitude [m]	To
1	Kecskemét	59. Szentgyörgyi Dezső Air Base	19.75	46.91	114.0	designated local users GEOS ACCC
2	Szolnok	86. Szolnok Helicopter Base	20.13	47.17	90.0	designated local users SARS GEOS ACCC
3	Pápa	Pápa Airbase	17.50	47.37	146.6	designated local users Heavy Airlift Wing Search and Rescue Service GEOS ACCC

4. Conclusions

The weather and its effect can pose significant threat to life and property. This is valid to a wide range of military activities; therefore, it is vital to operate a capable, well structured, and regulated system of meteorological support. In order to fulfil its mission, every level of the military meteorological support in Hungary provides in-time weather warnings and weather advisories to mitigate the possible negative effects of weather.

References

METOC Effects Smart Book, (http://www.fas.org) – Homepage of the Federation of American Scientist, 2002

IDŐJÁRÁS

Quarterly Journal of the Hungarian Meteorological Service
Vol. 119, No. 2, April – June, 2015, pp. 277–306

Forecasting of wet- and blowing snow in Hungary

Katalin Somfalvi-Tóth[1], **János Tordai**[2], **André Simon**[1*], **Kornél Kolláth**[1], and **Zsuzsanna Dezső**[2]

[1]*Hungarian Meteorological Service,*
Kitaibel Pál u. 1., H-1024 Budapest, Hungary

[2] *Department of Meteorology, Eötvös Loránd University,*
Pázmány Péter sétány 1/a, 1117 Budapest, Hungary

**Corresponding author E-mail:simon.a@met.hu*

(Manuscript received in final form September 8, 2014)

Abstract—Deep cyclones, originating in the Mediterranean area, are frequently the cause of heavy precipitation and environments characterized by large temperature gradients and strong wind. In winter period, several types of precipitation can be observed in such situations, including freezing rain and wet snow, which can cause serious damage on the electricity power lines or other infrastructure. On March 14–15, 2013, deep snowdrifts resulted in blocking of thousands of vehicles on Hungarian highways. Similar cases motivated the research of these phenomena in Hungary, using and adapting empirical approaches to calculate wet snow loads on wires or to calculate the blowing snow index (BSI) to assess the intensity of the snowdrifts development. Forecasting of these parameters is possible by using inputs from global and limited numerical weather prediction models (ECMWF, WRF). The paper describes methods for wet- and blowing snow diagnostics and classification of their intensity. The results are demonstrated on case studies and supported by observations and available damage reports. The possibility of further refinement of the diagnostics and its operational application is also discussed.

Key-words: wet snow, blowing snow, forecasting, winter weather, numerical models, WRF, diagnostics

1. Introduction

Wet snow is defined as "deposited snow that contains a great deal of liquid water" (*Glickman et al.*, 2000). It typically occurs during snowfall within the temperature range between 0 and +3 °C (*ISO*, 2001), though, snow accretion on structures have sometimes been observed also by temperatures below zero

(*Sakamoto*, 2000). The liquid water content of the accreted wet snow is usually between 5 and 40% (*Admirat*, 2008). Heavy and long-lasting snowfall in such conditions can develop considerable snow loads on wires, sometimes in order of several tens of N/m (*Makkonen* and *Wichura*, 2010). Serious problems with electricity failures caused by wet snow are frequently reported in cold regions or in mountains (*Eliasson et al.*, 2013; *Bonelli et al.*, 2011).

The study of wet snow occurrence in Hungary started in 2009, and it was related to situation with heavy snowfall and large damage on electricity power lines in the southwest part of Hungary on January 27–28, 2009 (*Tóth et al.*, 2009). Methods of *Sundin* and *Makkonen* (1998), *Poots* (1996), and *Admirat* (2008) were tested with use of both observational data and analysis and forecasts of the WRF (Weather Research and Forecasting) model (*Skamarock et al.*, 2008). The method of Admirat has recently been refined and adapted with respect to long- term observations (*Nygaard et al.*, 2013). In Hungary, in some years, up to 35 wet snow events can occur (*Gulyás et al.*, 2012) a substantial portion of these events is related to intense cyclogenesis in the Mediterranean area and frequent passages of cyclones over or near Hungary. These are characterized by widespread and high amount of often mixed-phase precipitation, including wet snow. Adjusted diagnostics of wet snow accretion and estimation of the snow sleeve mass and diameter was tested in these types of situations and the analyses and forecasts obtained from the WRF model run at relatively high (2.7 km) resolution were investigated and compared with available observations and reports. Drifting or blowing snow occurrence in Hungary can be sometimes related to intense cyclogenesis over the Mediterranean as well (it usually develops on the northwestern flanks of propagating cyclones). Similarly to wet snow, combination of several meteorological parameters (snowfall, wind, snow density, snow depth, surface temperature) must be taken into account during forecasting of blowing snow. Over the past years, several methods were elaborated in order to study and forecast its development (*Baggaley* and *Hanesiak*, 2005). There were attempts to parameterize the blowing snow as function of wind, temperature, and state of the snow surface (*Li* and *Pomeroy*, 1997). These studies motivated the development of a comprehensive index (blowing snow index or BSI) for forecasting blowing snow in Hungary. The index was proposed with a purpose of easier evaluation of blowing snow conditions and more precise determination of areas eventually threaten by snow drifts. The method was developed upon several case studies and recently tested during severe wind- and snowstorms of January 18 and March 14–15, 2013, which hit the western part of Hungary. Above all, the usefulness of the short-range (mainly 24h) forecasts of the BSI distribution in the forecasting praxis was evaluated and compared with available observations.

This paper is divided in five sections. In the next one, we describe the methods of the wet- and blowing snow diagnostics, in Section 3 we explain the synoptic background of some major (or interesting) weather events, and we

present the corresponding results (forecasts compared with observations) in Section 4. Conclusions are given in Section 5.

2. Methodology

2.1. Method of wet snow diagnostics

Admirat (2008) proposed a formula for calculation of the diameter Φ (m) of the snow sleeve accumulated on the wire. He expected that the snow sleeve has nearly cylindrical shape and started from the relationship between the variation of Φ and the mass M (kg/m), supposing that the density of the accreted snow ρ_s (kg/m^3) is constant:

$$\Phi \frac{d\Phi}{dt} = \frac{2}{\pi \rho_S} \frac{dM}{dt}. \tag{1}$$

The time variation of the mass is proportional to flow R of the snow, which passes a rectangle surface S (of unitary length and of width equal to Φ). It is expected that the airflow in front of the wire is perpendicular with respect to this surface. The basic formula for the flow (similar to the formula for accretion intensity in *Nygaard et al.*, 2013) yields:

$$R = c \sqrt{u^2 + w^2}\, S, \tag{2}$$

where u is the horizontal wind speed, w is the terminal velocity of snowflakes (both in m/s), and c is the mass concentration of wet snow in the air. Because c is usually not directly measured, it is often parameterized from water equivalent precipitation intensity at the ground P (mm/h):

$$c = \frac{P}{3600 w}. \tag{3}$$

Thus, the time variation of the mass can be expressed as:

$$\frac{dM}{dt} = \beta R = \frac{\beta P}{3600} \sqrt{1 + \frac{u^2}{w^2}}\, \Phi. \tag{4}$$

In Eq. (4), the parameter β is the collection coefficient (sometimes named also as coefficient of sticking efficiency). It expresses that only a part of the snowflakes crossing the area of the wire is accreted (some snowflakes will not accrete due to curvature of the flow around the wire or some snowflakes break up).

The final formula of *Admirat* (2008) for the diameter variation can be obtained from the combination of Eqs. (1) and (4):

$$\frac{d\Phi}{dt}=\frac{2K}{\pi\rho_S}, \tag{5}$$

where $K=\frac{\beta P}{3600}\sqrt{1+\frac{u^2}{w^2}}$.

Neither β nor ρ_S are measured or calculated in the used numerical models and these variables had to be parameterized. It is often expected that β is indirectly proportional to wind speed (*Admirat*, 2008), however, it was shown that such approach significantly decreases the role of wind in the snow accretion model described by Eq. (5). *Nygaard et al.* (2013) proposed a computation of beta, denoted BETA_U, in which beta is indirectly proportional to the square root of the wind speed u ($\beta=1/\sqrt{u}$), which has been used in this study. The density of the accreted snow can vary between 100 and 800 kg/m^3 (including extreme cases), and laboratory studies indicate that it is also dependent on the wind speed. One of the suggested empirical formulas (*Admirat*, 2008) used in the presented wet snow calculations yields:

$$\rho_S = 200 + 20u. \tag{6}$$

Because w is usually also not observed at synoptic stations, it is supposed to be constant in many wet snow studies. Here a value of 1.5 m/s was used, which is in the middle between w=1 m/s proposed by *Admirat* (2008) and the average fall velocities of wet snow (w=2 m/s) reported by *Yuter* (2006).

For diagnostics, based on data from synoptic stations with direct observation of the weather type, wet snow was considered if the 2 m temperature was between 0 and +3 °C and if snowfall, corresponding to 70–75 codes of the SYNOP report (*WMO*, 1995), was present at the same time. Because there were no reports of the liquid water content, we used the assumption that there must be a positive heat flux from the environment to the snowflakes, so that the snow surface can melt and accrete. It can be shown that this is equivalent to condition that the environmental wet-bulb temperature t_w is positive (*Makkonen*, 1989):

$$t_w > 0 \tag{7}$$

For NWP data, the same temperature conditions for wet snow were used as in case of observed data. It was supposed that the fraction of frozen precipitation (FR)

had to be between 0.7 and 0.98 as used in the BETA_U model (denoted as FR method in this paper). We also tested a method, where snowfall was distinguished from liquid precipitation upon the 850/1000 hPa relative topography – $RT_{850/1000}$ (*Cantin* and *Bachand*, 1993). *Hirsch* (2006) showed that in the area of Hungary snowfall might be usually expected by $RT_{850/1000} \leq 1300\ gpm$. This method was chosen because it is often used in the operational forecasting, and it could be very simply applicable on basic model fields or sounding data. Because the $RT_{850/1000}$ method does not provide any information about the liquid water content of the precipitation, we used the condition Eq. (7) to distinguish between wet- and dry snow. The FR and the $RT_{850/1000}$ criterions calculated from model forecasts were also applied on wet snow diagnostics at synoptic stations, where no direct observation of the precipitation type was available.

Eq. (5) has been integrated for a 24-hour period with 1-hour timesteps, during which P and u were considered to be constant (u was equal to the average of the wind at the start and end of the step). As final output, we visualized the difference ($\Delta\Phi$) between the diameter of the snow sleeve and the diameter of the wire without snow d, which is taken equal to 0.031 m (typical diameter of transmission wires). The advantage of calculating $\Delta\Phi$ is that it can be relatively easily measured or even visually estimated (e.g., upon photographs).

The estimation of the snow mass on the wire was based on combination of Eqs. (4) and (5):

$$\frac{dM}{dt} = K\Phi. \tag{8}$$

If the wind is assumed to be constant for the whole wet snow period, the diameter can be converted to snow mass with use of a simple geometrical relationship (expecting nearly cylindrical shape of the snow accumulation):

$$M = \frac{\rho_S \pi}{4}\left(\Phi^2 - d^2\right). \tag{9}$$

Upon several cases and damage reports in Hungary, it was proposed to issue warning in cases where certain threshold of calculated snow mass or increase in the diameter would be exceeded (*Table 1*). However, alertness in some situations can be recommended already by lower values (2–3 cm diameters of snow accumulation), especially if higher snow density can be expected or if the wet snow event is combined with strong wind (so-called wind-on-ice load).

Melting of snow is not yet included in the presented wet snow diagnostics. This can eventually cause overestimation, especially when the wet snow parameters are integrated for a long period, during which the character of the weather significantly changes (but this was not typical for the evaluated cases).

Table 1. Proposal on wet snow warning thresholds upon calculated mass and diameter of snow accumulation on wires (*Somfalvi-Tóth*, 2014). The values of $\rho_S = 300$ kg/m^3 and d=0.031 m were chosen for this conversion, based on Eq. (9)

Wet snow mass M [kg/m]	Increase of the snow-sleeve diameter $\Delta\Phi$ [cm]	Proposed level of warning
1.5	5.5	1
3	8.6	2
5	11.8	3

2.2. *Method of blowing snow diagnostics*

In situations with blowing snow we evaluated the so-called blowing snow index (BSI) parameter (*Tordai*, 2012). The index evaluates six meteorological parameters, which can influence the development of snowdrifts. This influence is represented by weighting functions *f*. These can be negative – thus, one term itself can counteract positive contributions of other terms (e.g., snowdrifts are improbable by very low windspeed, even if other conditions would be optimal). The maximum values of the weighting functions are 1. The final formula for BSI sustains from the sum of the functions:

$$BSI = f(T)+f(T_s)+f(U)+f(G)+f(H)+f(\rho_H)\,, \tag{10}$$

where $f(T)$ represents temperature at 2 m, T_s is the surface (skin) temperature, U is the wind speed at 10 m, G is the wind gust at 10 m, H is the snow depth, and ρ_H is the snow density. The criteria and formulas for determination of each weighting function (given in *Table 2*) were based on the work of *Tordai* (2012), and it was only slightly modified for mathematical reasons. The thresholds in the weighting function calculations were determined upon observations and several case studies of blowing snow. The BSI can acquire negative values (if impact of certain components would strongly inhibit the development of blowing snow). The maximum possible value is 6 (very high probability of snowdrift development). Although BSI is rather related to probability of blowing (or drifting) snow occurrence, higher values of BSI usually also indicate higher intensity of snowdrift production. It has been observed that blowing snow is probable by BSI exceeding 2, values exceeding 3.5 are already significant and are usually accompanied by light or moderate development of snowdrifts.

Table 2. Determination of respective weight functions (f) in the calculation of the BSI index

State determinating parameter	Interval	Weight function
T [°C] (2 m temperature)	$T \leq -6.5$	$f(T)=1$
	$-6.5 < T \leq 0.5$	$f(T)=-0.0087T^2-0.1727T+0.2447$
	$T > 0.5$	$f(T)=-(0.0181T)^2-0.139T+0.2257$
T_S [°C] (Surface temperature)	$T_S \leq -3.0$	$f(T_S)=1$
	$-3.0 < T_S \leq -0.5$	$f(T_S)=-0.0406T_S^2-0.2436T_S+0.6342$
	$-0.5 < T_S \leq 2.0$	$f(T_S)=0.3397\exp(-1.5717\,T_S)$
	$T_S > 2.0$	$f(T_S)=-0.1264T_S^2+0.5056T_S-0.4915$
U [m/s] (10m wind)	$U < 4.0$	$f(U)=1.014U-4.014$
	$4.0 \leq U < 15.0$	$f(U)=-0.0076U^2+0.2314U-0.7616$
	$U \geq 15.0$	$f(U)=1$
G [m/s] (10m wind gust)	$G < 6.0$	$f(G)=-0.075G^2+1.1192G-3.9657$
	$6.0 \leq G \leq 21.0$	$f(G)=-0.0029G^2+0.1416G-0.6952$
	$G > 21.0$	$f(G)=1$
H [cm] (snow depth)	$H < 5.0$	$f(H)=0.0732H^2+0.6711H-4.9321$
	$5.0 \leq H < 31.0$	$f(H)=-0.0007H^2+0.0538H+0.0022$
	$H \geq 31.0$	$f(H)=1$
ρ_H [kg/m^3] (snow density)	$\rho_H < 100.0$	$f(\rho_H)=1$
	$100.0 \leq \rho_H < 240.0$	$f(\rho_H)=-1.83\times10^{-5}\rho_H^2+0.0019\rho_H+0.9912$
	$\rho_H \geq 240.0$	$f(\rho_H)=-0.0534\rho_H+13.207$

At the Hungarian Meteorological Service, warnings on blowing snow have already been issued prior to development of BSI, although the criteria for it were arbitrary. Upon these criteria, we developed a simple warning decision index (WDI) in order to compare the original formulation (*Table 3*) with a warning system proposed upon BSI thresholds (*Tordai*, 2012). When using BSI, it was recommended to issue first level (yellow) warning on blowing snow for values higher than 3.5. Strong development and second level (orange) warnings can be expected by BSI exceeding 4, and very severe blowing snow and third level of warnings (red) can occur by BSI equal to 4.5 or higher.

Both BSI and WDI were estimated upon data from synoptic station observations (and compared with forecasts of these parameters from numerical models). We considered only stations, where measurements of snow depth and density were available, or where it was possible to assess them using spatial and temporal interpolations. Instead of the skin surface temperature (which can eventually be the temperature of the snow surface, and it is usually not measured at the stations), we used the near-surface temperature measured 5 cm above the terrain. We also checked the reports on drifting- and blowing snow, which are

coded at certain synoptic stations (*WMO*, 1995). We assumed that the code on slight or moderate drifting snow (36) would nearly correspond to current yellow warning, the codes 37 (heavy drifting snow), 38 (slight or moderate blowing snow) to orange and the 39 code (heavy blowing snow) to red warning. Though, the original definitions of drifting and blowing snow are rather related to visibility conditions as to height or intensity of snowdrift production.

Table 3. Blowing snow warning criteria of the Hungarian Meteorological Service and corresponding WDI codes and algorithms. The meaning of parameters is the same as in Table 2, except for R_{24} (snow precipitation of past 24 hours, in mm) and R_{03} (snow precipitation of past 3 hours, in mm)

HMS warning criteria	Level of warning	WDI algorithm	WDI code
The wind produces snowdrifts of low depth occurring on territories covered by fresh snow	Yellow 1	$U \geq 4 m/s \quad H \geq 5 cm$	1
The wind accompanied by strong gusts (> 60 km/h) produces deep (depth locally > 0.5 m) snowdrifts on territories covered by fresh snow	Orange 2	$U \geq 4 m/s \quad H \geq 5 cm$ $G \geq 16.7 m/s \quad R_{24} \geq 1 mm$	2
The wind accompanied by strong gusts (> 60 km/h) produces deep (depth > 0.5 m at many places) snowdrifts on territories covered by fresh snow. Besides, snowfall can be still expected (several cm of fresh snow).	Red 3	$U \geq 4 m/s \quad H \geq 5 cm$ $G \geq 16.7 m/s \quad R_{24} \geq 1 mm$ $R_{03} \geq 0.1 mm$	3

2.3. Description of numerical models and their setup used in the study

Blowing snow parameters were calculated from operational forecasts of the deterministic ECMWF global numerical model (*Persson*, 2011), which outputs were available in a regular latitude-longitude grid of 0.125 degree (nearly 16 km) horizontal resolution. The wet snow has been diagnosed upon outputs of non-hydrostatic limited area model WRF (*Skamarock et al.*, 2008). The WRF model, implemented and computed at the Hungarian Meteorological Service (HMS), provides data at nearly 2.7 km horizontal resolution and 37 vertical levels. In the HMS implementation, WRF is using the microphysics scheme of Thompson (*Thompson et al.*, 2004) and the YSU PBL scheme (*Hong et al.*, 2006) for the parameterization of planetary boundary layer processes. The higher horizontal resolution (compared to global models) and advanced physical parameterizations are important to obtain finer, mesoscale structures in the precipitation, temperature, and wind fields and the estimates of the precipitation type (fraction of frozen precipitation, *FR*). This seems to be currently more important by wet snow, which occurrence fits a relatively narrow temperature interval and which parameters (snow sleeve diameter and mass) are more sensitive on the precision and exact quantity of input parameters than in the BSI case.

3. Selected synoptic situations

3.1. Blowing snow on January 18, 2013

On January 18, 2013, the weather over Hungary was largely influenced by a deep cyclone, which centre was over the Adriatic Sea (*Fig. 1*). The cyclone had initially developed over the Bay of Genoa (on January 15) and became deeper as a result of interaction with an upper air potential vorticity (PV) anomaly, which centre was situated over the southwest flank of the surface low. The cyclone later moved toward east-northeast. The drop of the pressure over the Balkan Peninsula and increase of the pressure gradient in the north-south direction induced a low-level jet and cold-air advection over the western part of Hungary (*Fig. 2*). This was the primary reason for strong wind and gusts observed at several places in northwestern Hungary (the maximum wind gust, 21.4 m/s was reported at Sármellék at 09:40 UTC). The depth of the snow cover over western Hungary had already been high (20–50cm at many places) as a result of previous snowfalls. In the same region, moderate snowfall (up to 10 mm of precipitation) occurred on January 18 as well (*Fig. 3*). Although, at several stations, where blowing snow was observed, only light precipitation was measured (or estimated from radar measurements) during the event.

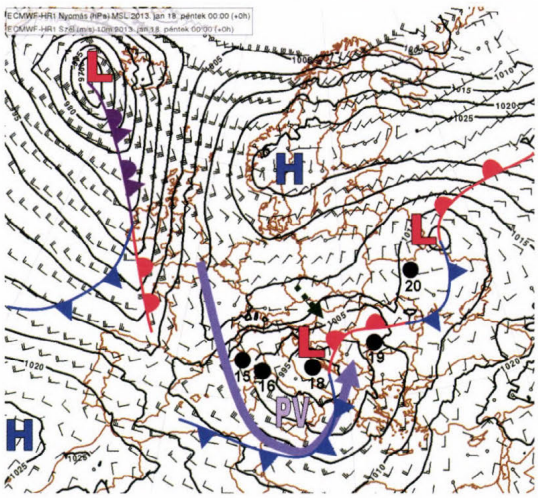

Fig. 1. ECMWF analysis of mean sea level pressure (lines, by 5 hPa), 10 m wind (barbs), and fronts valid for January 18, 2013, 00:00 UTC. The letters L and H represent lows and highs, respectively. The letter "PV" marks the position of the center of the upper-air PV anomaly; the arrow-headed line shows the segment of the upper-air jet surrounding the anomaly (at nearly 250 hPa height). The dots show the positions of the centre of the studied Mediterranean cyclone on January 15, 16 (and 17), 18, 19, and 20, 2013. The dashed line points toward northwestern Hungary, where the blowing snow event occurred.

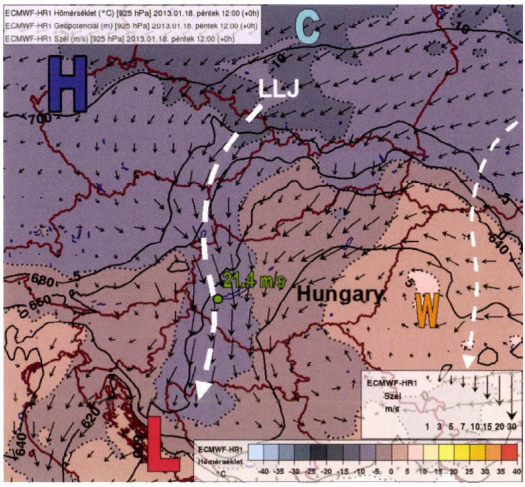

Fig. 2. ECMWF analysis of 925 hPa geopotential (lines, by 20 gpm), temperature (°C, shaded), and 925 hPa wind (arrows, m/s) valid for January 18, 2013, 12:00 UTC. The letters L, H represent low and high pressure, respectively; C, W the cold (warm) airmasses. The dashed line approximately shows the axis of the low level jet (LLJ). A point is placed on the area of the station Sármellék, where the maximum wind gust (21.4 m/s) was recorded on January 18, 2013, 09:40 UTC.

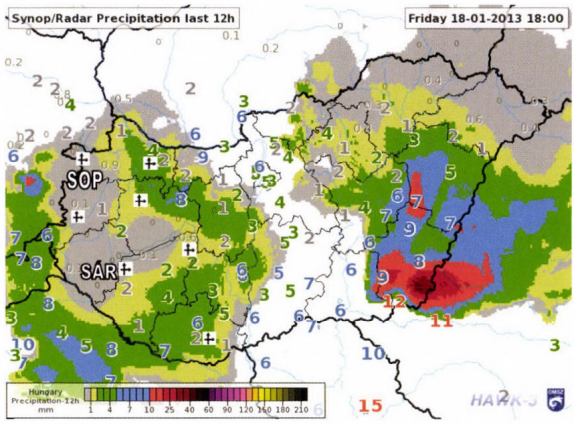

Fig. 3. 12 h precipitation amounts valid for January 18, 2013, 18:00 UTC from stationary measurements (numbers) and radar estimates (shaded). Stations, where drifting or blowing snow was coded in the past weather (–01 h) section are emphasized by square and symbol of blowing snow. Meteorological stations Sopron Kuruc-domb and Sármellék are denoted by abbreviations SOP and SÁR.

3.2. Wet snow on February 6–7, 2013

The weather in central Europe was governed by large area of low pressure (exhibiting several centres) and by a frontal system, which evolved in the Mediterranean region. On February 6–7, 2013, one of the centers of the low pressure was situated over Hungary and east Slovakia (*Fig. 4*). The eastern part of the countries was located in the warm zone of the system, while the colder air propagated around the low-pressure center and forced the mild air toward the mountainous region in northeast Hungary and east Slovakia (*Fig. 5. a–b*). There was an intensive positive temperature advection and high (almost 100%) mean relative humidity between 925–600 hPa (not shown), especially in east Slovakia, where heavy snowfall occurred. Vertical cross-sections of temperature show that across Hungary and Slovakia, over the localities, where wet snow was reported/diagnosed, there was a 200–300 meters deep layer of 0–2 °C temperature (*Fig. 6. a–b*). This layer was well expressed over the northern part of Hungary and the central-eastern part of Slovakia, where 10–20 mm precipitation occurred (*Fig. 7*). Upon precipitation estimates from radars and temperature profiles, favorable wet snow conditions could have developed on the southern slopes of the mountains in the central part of Slovakia, but surface observations were sparse in this region. Damage reports and photographs (*Railpage.net,* 2013) indicate that wet snow occurred also in the valley of the river Hornád (on the railway between Krompachy and Margecany). There was no positive temperature layer on the vertical cross-sections in this region, probably because the valley is not yet resolved by the ECMWF model orography by current resolution (nearly 16 km). The cross-sections also show that the area of the positive temperature layer reduced in time as the cold-air advection was progressing (marked by the decrease of the near-surface equivalent potential temperature).

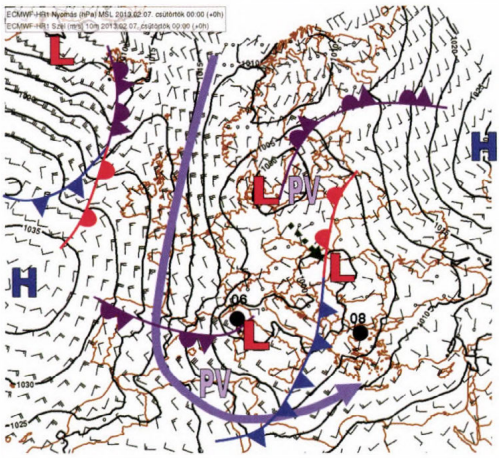

Fig. 4. As in *Fig. 1* but for February 7, 2013, 00:00 UTC. The dots show the positions of the (deepest) centre of the Mediterranean cyclone on 6, 7, and 8 February, 2013. The dashed line points toward the border region of northeastern Hungary and southeastern Slovakia, where the wet snow event occurred.

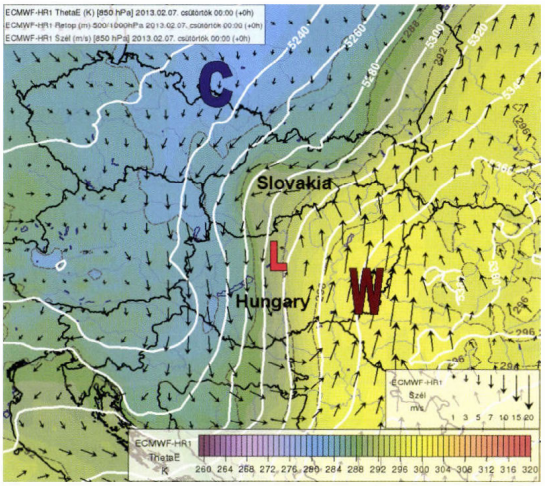

Fig. 5a. ECMWF analysis of the 850 hPa equivalent potential temperature (color shades and dashed lines, K), wind field (arrows, m/s), and the 500/1000 hPa relative topography (white lines, m) valid for February 7, 2013, 00:00 UTC. The letter L denotes the center of the cyclonic circulation over Hungary, letters W, C show the warm and cold air-masses.

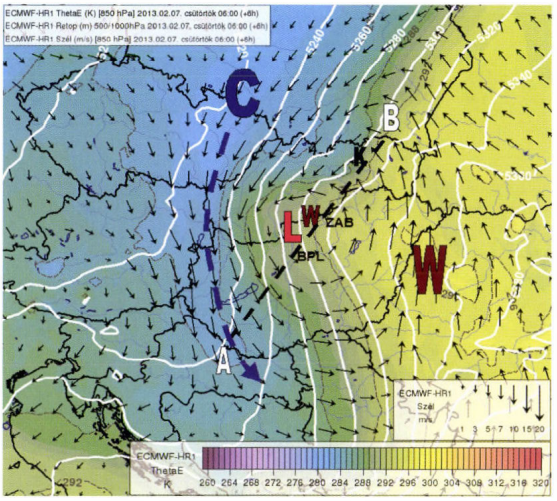

Fig. 5b. As in *Fig. 5a* except for the 6h ECMWF forecast valid for February 7, 2013, 06:00 UTC. The dashed, arrow-headed line schematically shows the flow of the colder airmass, which started to surround and force the warmer air away. The AB line shows the direction of the cross-section in *Fig. 6a-b*. The abbreviations BPL, ZAB emphasize the positions of the weather stations at Budapest Lőrinc and Zabar, respectively (mentioned also later in the text). The letter K denotes the town Krompachy in Slovakia (wet snow caused damages were reported in its neighborhood).

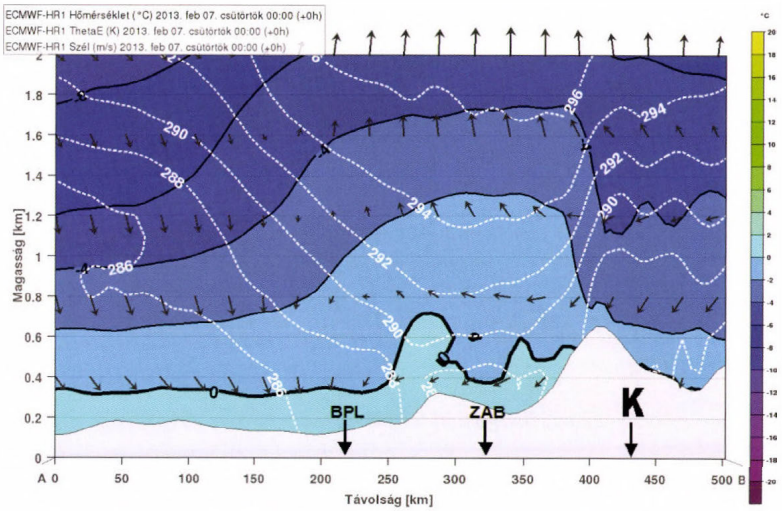

Fig. 6a. ECMWF analysis of temperature (shades and solid lines by 2 °C), equivalent potential temperature (dashed lines, by 2 K) and wind (arrows, m/s) valid for February 7, 2013, 00:00 UTC in a vertical cross-section, which direction is shown in *Fig. 5b*. The abbreviations and arrows mark places, where wet snow was diagnosed/reported (see also *Figs. 5b* and *14a-b*).

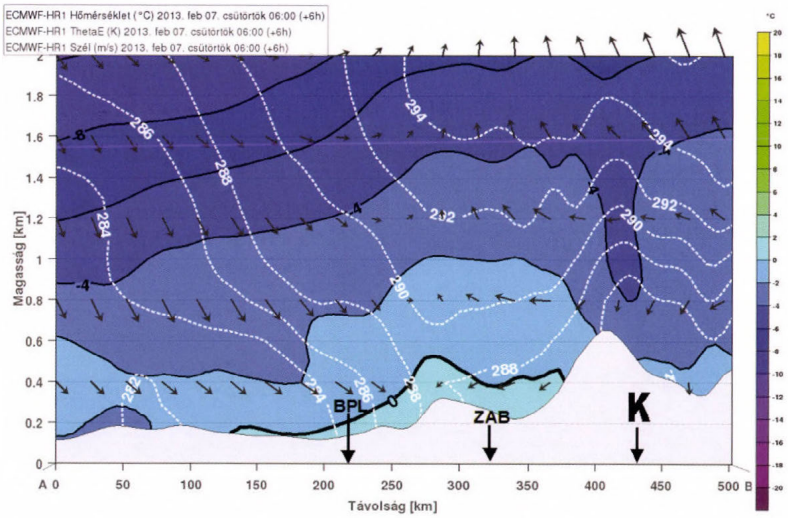

Fig. 6b. As in *Fig. 6a* but for the ECMWF forecast of temperature valid for February 7, 2013, 06:00 UTC.

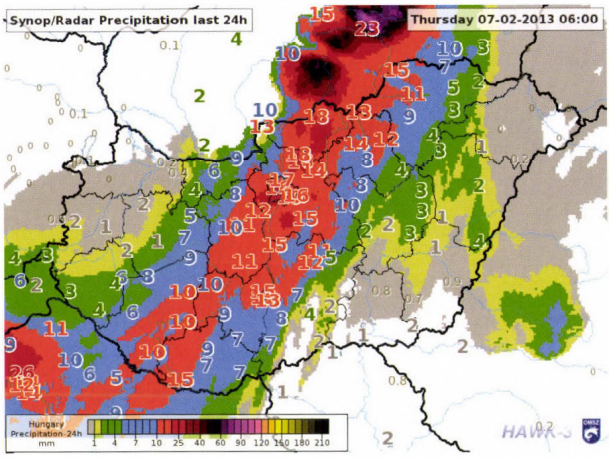

Fig. 7. As in *Fig. 3* but for 24 h precipitation amounts valid for February 7, 2013, 06:00 UTC.

3.3. Wet- and blowing snow on January 24–25, 2014

On January 25, 2014, a cyclone with centre over southern Italy and the Adriatic Sea was moving eastwards (*Fig. 8.*). Its frontal system affected several countries of southern and central Europe causing extraordinary heavy snowfall (Slovenia, Croatia, Serbia, Bulgaria). The northern flank of the warm frontal precipitation band also reached the southern part of Hungary (already on January 24, 2014). At 850 hPa level ECMWF analyses (*Fig. 9*), it was possible to observe that while the cold-air advection already started over large part of western Hungary, there was still a "tongue" of warmer and moist air overturning toward the southwest part of Hungary, where the intense snowfall occurred. This is likely a signature of an occlusion process (in rather mesosynoptic scale), similar to the one observed in the February 6–7, 2013 wet snow situation. The maximum of 20 mm precipitation in Hungary was also reported close to this area (*Fig. 10*).

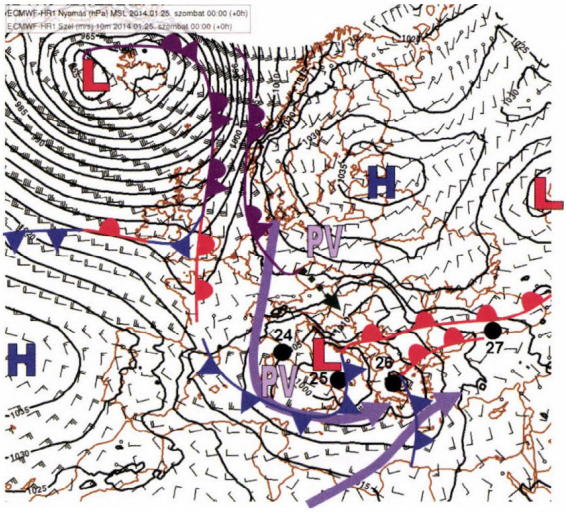

Fig. 8. As in Fig. 1 but for January 25, 2014, 00:00 UTC. The dots show the positions of the (deepest) centre of the Mediterranean cyclone on January 24–27, 2014. The dashed line points toward southwestern Hungary, where both wet snow and blowing snow were observed.

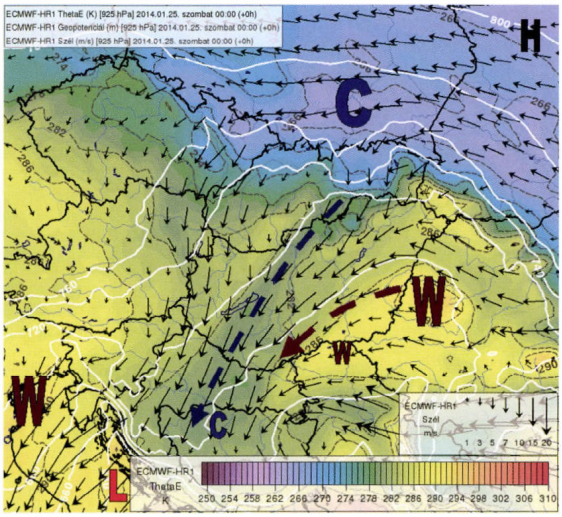

Fig. 9. ECMWF analysis of the 925 hPa equivalent potential temperature (color shades and dashed lines, K), wind field (arrows, m/s), and geopotential (solid lines, m) valid for January 25, 2014, 00:00 UTC. The letters L, H represent low and high geopotential, respectively; C and W represent the cold (warm) regions. The dashed lines schematically show the flow of colder/warmer air over Hungary.

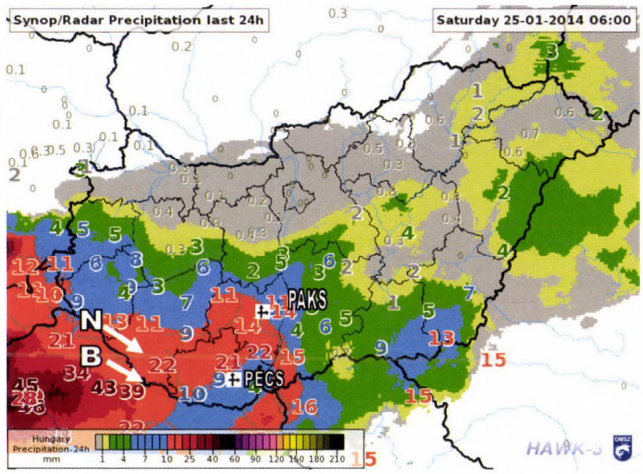

Fig. 10. As in *Fig. 3* but for 24 h precipitation amounts valid for January 25, 2014 06:00 UTC. Meteorological stations Pécs-Pogány and Paks, which reported blowing snow on January 24, 2014, are displayed. Arrows denoted by letters B and N point toward the position of settlements Barcs and Nagyatád, respectively. Damage due to wet snow was reported in their surroundings on January 24–25, 2014.

4. Results for wet- and blowing snow diagnostics

4.1. Blowing snow on January 18, 2013

The January 18, 2013 weather situation was one of the most serious blowing-snow events of the past ten years in Hungary. The blowing snow developed at a large area (almost entire western Hungary), causing serious problems in transport and requiring numerous actions of the disaster management (*Fig. 11*). Such cases are relatively rare – for example, between 2007 and 2012 there was only one case that the highest, third-level warning was issued on blowing snow (18 second- and 60 first-level warnings were issued during the same period). Only light-to-moderate snowfall (few mm of precipitation) had been expected upon available NWP forecasts a day before this event, hence, the intensity of the snowdrift developments had been debated in the HMS forecasters team. The 24h forecast of BSI from the January 17, 2013, 12:00 UTC ECMWF run indicated a possibility of very intense blowing snow for the area northwest of the Lake Balaton (*Fig. 12a*). This area was also emphasized in the WDI outputs (*Fig. 12b*). Though, there would hardly be any transition between the yellow and red warning in WDI (the red warning is distinguished from the orange one only upon the presence of precipitation, which had been forecast by the ECMWF

model for the entire area with strong wind). The analysis of respective weighting functions present in Eq. (10) reveals that all of them positively contributed to BSI in the model forecast for the localities (meteorological stations Sopron Kuruc-domb and Sármellék), where snowdrifts were expected (*Table 4*).

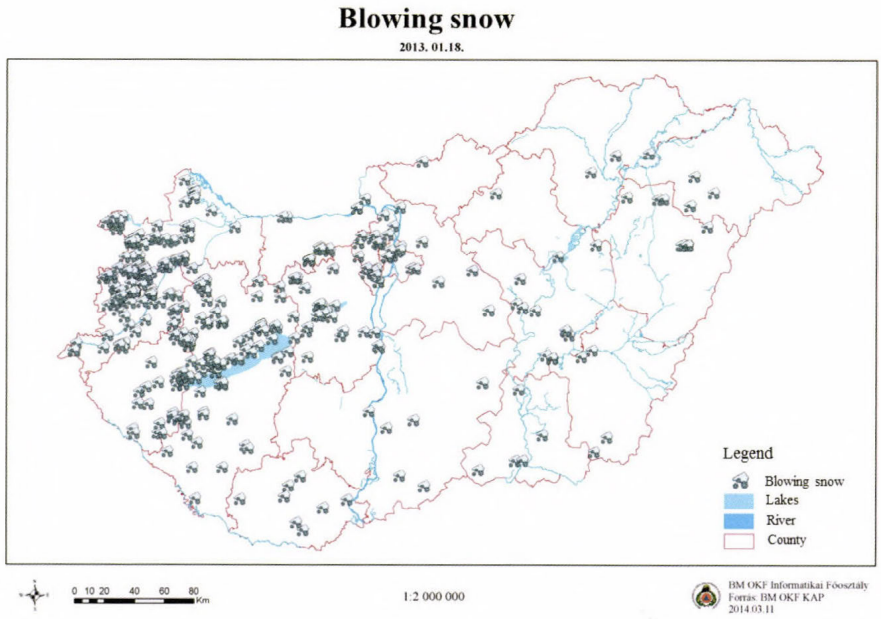

Fig. 11. Actions of the disaster management on January 18, 2013. (source: National Disaster Management Directorate General, with permission)

Table 4. Weighting functions, BSI, and WDI for Sopron Kuruc-domb and Sármellék, derived from the ECMWF 24h forecast valid for January 18, 2013, 12:00 UTC.

Station	$f(T)$	$f(T_S)$	$f(U)$	$f(G)$	$f(H)$	$f(\rho_H)$	***BSI***	***WDI***
Sopron	0.77	1	0.83	0.97	1	0.81	5.4	3
Sármellék	0.84	1	0.71	0.91	1	0.78	5.2	3

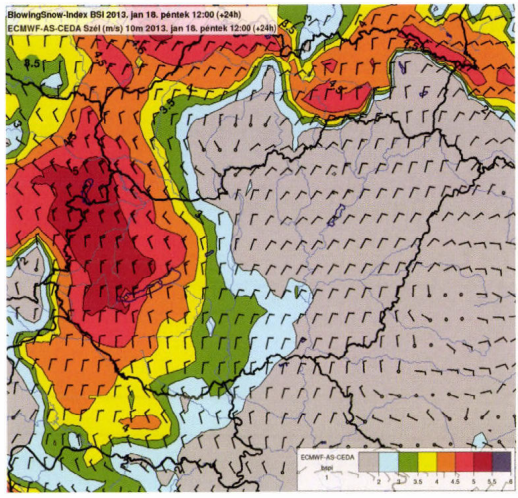

Fig. 12a. ECMWF 24 h forecasts of BSI (shades and solid lines) and 10 m wind (barbs, m/s) valid for January 18, 2013, 12:00 UTC.

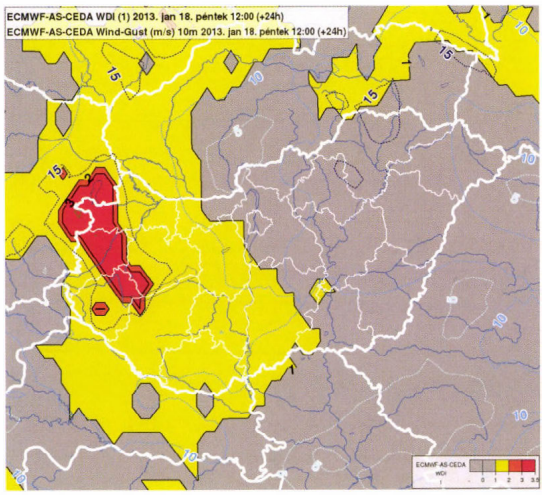

Fig. 12b. ECMWF 24 h forecasts of WDI (shades and solid lines, by 1) and of wind gusts (dotted lines, by 5 m/s) valid for January 18, 2013, 12:00 UTC.

Available observations, close to the time of the forecast validity (January 18, 11:40 UTC), show that drifting or moderately blowing snow was really coded at several stations in western Hungary (*Fig. 13*). Though, heavy blowing snow (code 39) was not observed and BSI estimated from the measurements did not exceed 5. This could have been caused by the use of temperature measured

close to terrain surface, instead of the skin surface temperature (of the snow cover), because the weights of surface temperature are significantly lower in the observations (*Table 5*) than in the forecasts. Interestingly, WDI would suggest only 1st level of warning for the evaluated stations. The main reason for it is that only low precipitation amounts were reported at stations concerned (although light or moderate snowfall had been coded at some observation dates). One possible explanation is that the strong wind blew the snow off the measuring devices. The radar-estimated precipitation indicates that the real snow precipitation could have been somewhat bigger compared to surface observations, though this was not typical in the area of highest gust and snowdrift occurrences (refer to *Fig. 3*).

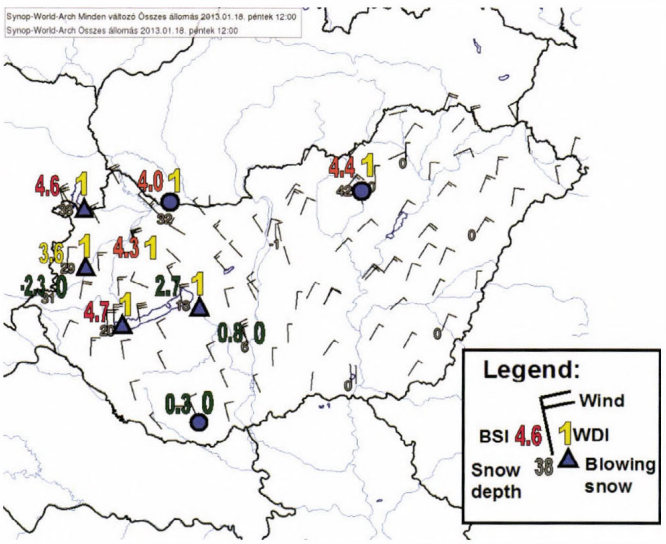

Fig. 13. Observations of 10m wind (barbs, m/s) and snow depth (numbers, cm) from Hungarian meteorological stations on January 18, 2013, 12:00 UTC. Further numbers (see the description in the legend) denote the estimated value of BSI and WDI valid for 11:40 UTC. The circles are drawn at stations, where drifting snow (code 36) was reported on January 18, 2013, triangles are for blowing snow (code 38).

Table 5. As in *Table 4* but derived from observations at Sopron Kuruc-domb and Sármellék, on January 18, 2013, 11:40 UTC.

Station	$f(T)$	$f(T_S)$	$f(U)$	$f(G)$	$f(H)$	$f(\rho_H)$	***BSI***	***WDI***
Sopron	0.68	0.18	0.85	0.91	1	0.96	4.6	1
Sármellék	0.73	0.84	0.78	0.86	0.8	0.74	4.7	1

4.2. Wet snow on February 6–7, 2013

Wet snow calculations were provided upon WRF model run based on February 6, 2013, 12:00 UTC. In the first calculation, the FR criterion was chosen for wet snow diagnostics (*Fig. 14a*).

Wet snow was detected at several places in Hungary and Slovakia (mostly in the southern part of central Slovakia and in the valley between the towns Košice and Prešov), though, the values of $\Delta\Phi$ were mostly below the proposed warning thresholds (maximum detected values were 5–6 cm). When using the $RT_{850/1000}$ criterion, the area of potential wet snow occurrence became considerably bigger (*Fig. 14b*), and the condition for first-level warning according to *Table 1* would be fulfilled on several places. The maximum detected $\Delta\Phi$ was about 8 cm. If we assume, that the density of the wet snow on wires was between 250 and 300 kg/m^3 (according to mean wind speed in this area), this diameter would be equivalent to 2.2–2.7 kg/m snow-mass, which can potentially cause damage on the overhead lines, particularly if the wind speed is strong. The comparison of the diagnostics on observations (*Table 6a*) and on the corresponding model outputs (*Table 6b*) showed that the FR-criterion largely reduced the precipitation, which potentially occurred in wet snow form. This is the main cause of the differences between the forecast diameters (wet snow loads) and the ones diagnosed upon observations, because forecasts of other parameters (wind-speed, temperature) were relatively close to the observed ones. Examination of the course of FR (e.g., for station Košice, *Fig. 15*) showed that this parameter was rather low when the temperature was higher than 1 °C, although, in the reality, snowfall was reported in such conditions. The low *FR* could have been partially also influenced by somewhat higher (by 0.5–1 °C) temperature in the model compared to observations. The $RT_{850/1000}$ criterion seemed to be more successful in detection of wet snow occurrence, but it is possible that the diagnosed values of the snow sleeve diameter were too high when using this method (especially in the area of Budapest, where wet snow accretion on wires corresponding to $\Delta\Phi$ of 5 cm or bigger probably did not occur).

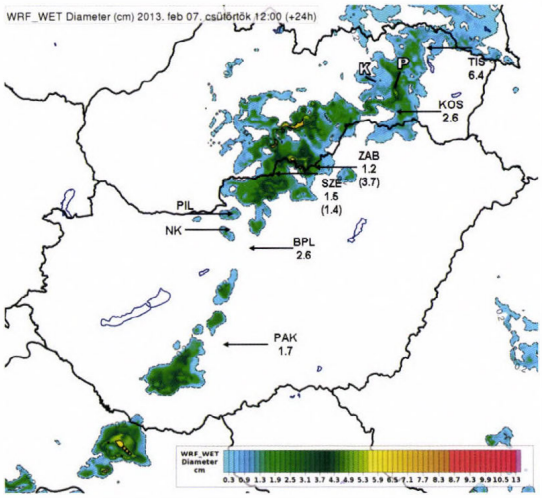

Fig. 14a. WRF 24 h forecast of the snow sleeve diameter increase (shades, in cm) valid for February 7, 2013, 12:00 UTC calculated using the FR method. The solid lines denote the diameters of 5.5 and 8.6 cm corresponding to warning thresholds. The arrows and abbreviations denote the positions of weather stations and localities, where wet snow was reported/diagnosed (PAK-Paks, BPL-Budapest Lőrinc, SZE-Szécsény, ZAB-Zabar, KOS-Košice, TIS-Tisinec, NK- Nagy-Kevély, PIL-Pilis). The numbers show the increase of the snow sleeve diameter (cm) assessed from the observations (as in *Table 6a*). The thick line denoted K (P) shows the direction of the railway between Krompachy and Margecany (Prešov and Kysak), where damage due to wet snow was reported.

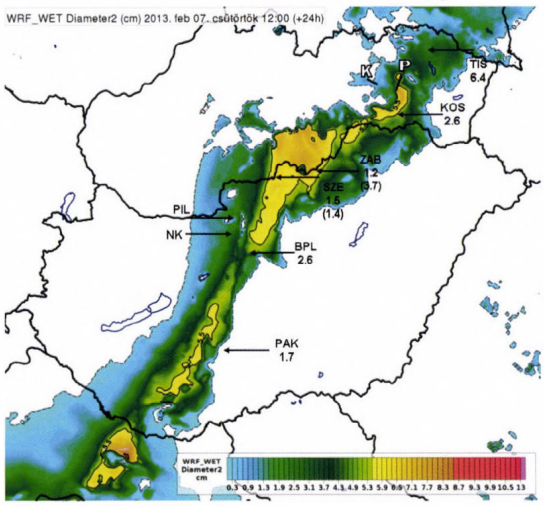

Fig. 14b. As in *Fig. 14a* but for the $RT_{850/1000}$ method.

Table 6a. Parameters of wet snow precipitation observed or derived from observations of several synoptic stations in Hungary and Slovakia during the period of February 6, 2013, 12:00 UTC – February 7, 2013, 12:00 UTC. There were no weather-type observations on the star-marked stations (Szécsény and Zabar), the wet snow period was assessed from the WRF model data (upper record using the FR, lower record in parenthesis the $RT_{850/1000}$ method). At the station Tisinec (marked by two stars), weather-type observations were not available between 20:00 and 05:00 UTC, but from the amounts and course of other parameters (snow-depth, temperature, wet-bulb temperature) it is probable that all the precipitation in this period was in wet snow form.

Synoptic station: / **Parameter:**	**Paks (PAK)**	**Budapest Lőrinc (BPL)**	**Szécsény (SZE)***	**Zabar (ZAB)***	**Košice Letisko (KOS)**	**Tisinec (TIS)****
Station height (*ASL*) [m]	97	139	153	226	230	216
P [mm] Total precipitation	7.9	12.1	15.8	11.6	19.0	26.0
Pw [mm] Wet snow precipit.	5.15	8.3	4.35 (4.3)	3.7 (11.6)	8.08	20.5
U [m/s] Average wind	1.66	1.93	0.97 (0.73)	1.18 (0.99)	5.34	1.98
Δϕ [cm] Snow-sleeve diameter increase	1.68	2.60	1.50 (1.43)	1.18 (3.72)	2.64	6.41
M [kg/m] Wet snow mass	0.236	0.436	0.199 (0.185)	0.157 (0.639)	0.528	1.526

Table 6b. Parameters of wet snow precipitation derived from the WRF model forecasts valid for the period of February 06, 2013 12:00 UTC – February 07, 2013 12:00 UTC and for the grid-points nearest to observations listed in the *Table 6a*. The upper (lower) values are for the *FR* ($RT_{850/100}$) method of snowfall determination. The abbreviation NR (Not Relevant) means that wet snow was not detected.

Synoptic station: / **Parameter:**	**Paks (PKS)**	**Budapest Lőrinc (BPL)**	**Szécsény (SZE)**	**Zabar (ZAB)**	**Košice Letisko (KOS)**	**Tisinec (TIS)**
Grid-point height (*ASL*) [m]	87.7	124.1	161.2	301.2	250.2	258.7
P [mm] Total Precipitation	10.86	17.63	19.37	18.49	17.83	8.06
Pw [mm] Wet snow precipitation	0 (0)	0 (16.81)	5.22 (19.37)	5.77 (18.49)	3.03 (17.24)	0 (6.7314)
U [m/s] Wet snow period average wind	NR (NR)	NR (2.19)	2.83 (2.26)	2.74 (2.12)	4.15 (3.33)	NR (2.64)
Δϕ [cm] Snow sleeve diameter increase	NR (NR)	NR (5.26)	1.64 (6.09)	1.83 (5.85)	0.98 (5.56)	NR (2.11)
M [kg/m] Wet snow mass	NR (NR)	NR (1.153)	0.26 (1.475)	0.297 (1.368)	0.157 (1.420)	NR (0.342)

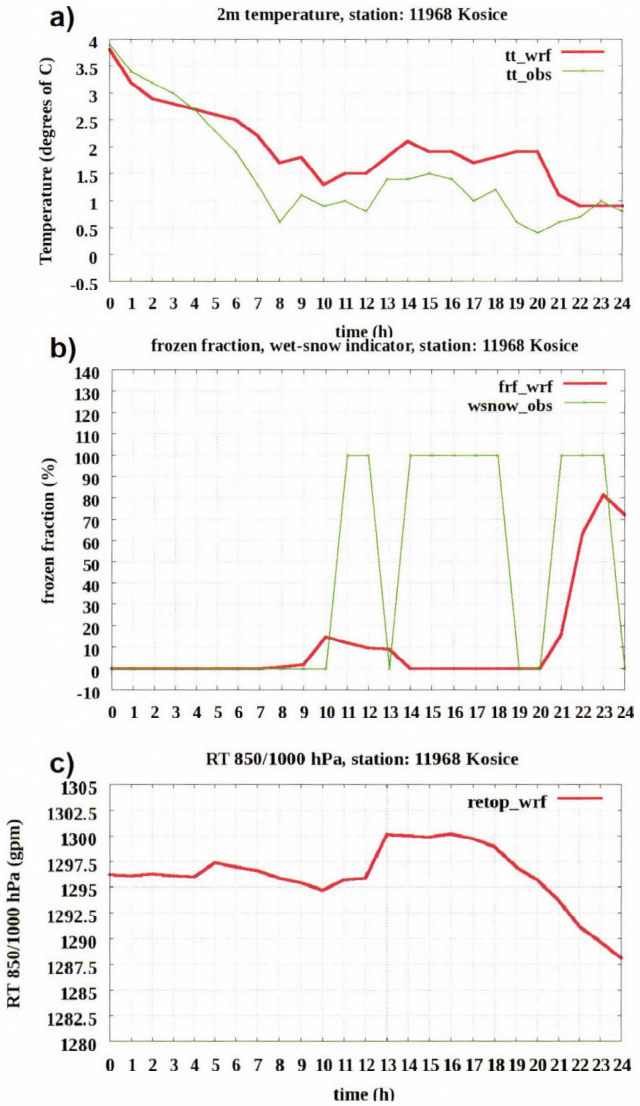

Fig. 15. Course of observed/diagnosed (thinner lines) and forecasted (thicker lines) meteorological parameters valid for the station Košice and for the period of February 6, 2013, 12:00 UTC –February 7, 2013, 12:00 UTC. The February 6, 2013, 12:00 UTC WRF run outputs were used for this visualization. The horizontal axis shows the time (h) from the start of this run. Evolution of the 2 m temperature is shown in a), figure b) shows the change of the model-computed fraction of frozen precipitation (FR). This is depicted together with an index showing detection of wet snow upon observed precipitation type, temperature, and wet-bulb temperature (0 – no wet snow, 100-wet snow). Figure c) shows the evolution of the $RT_{850/1000}$ parameter forecast by WRF.

Available reports (*Pilis parkerdő,* 2013) mentioned damage in the forest due to high snow loads in Pilis mountains, and there is also photographic evidence (*Kolláth*, 2013) of wet snow accumulated on wires in this region (e.g., in the area of the Nagy-Kevély mountain). Although, this region seemed to be only marginally affected by wet snow in the WRF forecasts (see *Figs. 14a–b*). In Slovakia, wet snow was reported on the railway electric power lines between the railway stations Margecany and Krompachy and also between stations Kysak and Prešov. Though, the damage on the power lines was probably not only direct, due to high loads on the wires, but it was also caused by trees, which broke under the weight of heavy, accumulated wet snow (*Railpage.net*, 2013). Wet snow was forecast for the surrounding of both above-mentioned railways. A local maximum of $\Delta\Phi$, close to the Kysak-Prešov railway, appeared in the diagnostic outputs, using both FR and $RT_{850/1000}$ methods.

4.3. Wet- and blowing snow on January 24–25, 2014

Most reports of the wet snow occurrence in Hungary and associated damage (electric power failures) were concentrated to the southwestern border of Hungary (region of Barcs and Nagyatád), yet, several thousands of inhabitants were concerned (*E.O.N. Hungária Zrt.*, 2014, data on power failures, photographs, and personal communication). The wet snow was diagnosed using both FR and $RT_{850/1000}$ criterions in this territory.

In case of *FR*, the forecast diameters of snow-sleeve mostly did not reach the proposed warning thresholds (5.5 cm, not shown). In the second diagnostics, significant, up to 8–9 cm diameters were predicted during the 24-hour accretion period, until January 25, 06:00 UTC (*Fig. 16*). Very high accumulation of wet snow was also forecast for the region close to the synoptic station Paks. However, here the development of wet snow was questionable: though the forecast 2 m temperature fitted the wet snow criterions (between 0 and 3 °C), in the reality, it was probably well below 0 °C during most of the investigated period, as indicated by observations of the Pécs and Paks stations.

During this situation, blowing snow was reported at synoptic stations Pécs and Paks. Its intensity was probably highest in the evening of January 24, 2014 (at around 21:00 UTC), when wind gusts of 12–15 m/s were observed. Upon available observations, the BSI was estimated to be 3.54 for Pécs and 3.49 for Paks. There were no snow density measurements in this case, thus, a mid-value of 170 kg/m^3 between the two thresholds mentioned in *Table 2* was used in this calculation. But, because of the uncertainty in both skin-surface temperature and snow density, it is probable that the true BSI values were bigger (e.g., in case of fresh snow, these parameters could have been lower and their weight functions higher). The more simple WDI index also indicated the possibility of blowing snow, corresponding to the first level warning at the two evaluated locations (*Fig. 17*).

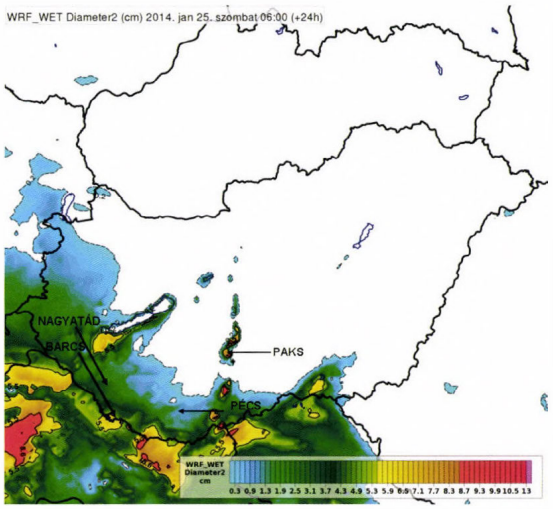

Fig. 16. As in *Fig. 14b* but for the 24 h forecast valid for January 25, 2014, 06:00 UTC. The arrows point toward Nagyatád and Barcs, where wet snow damages were reported and toward meteorological stations Pécs and Paks (mentioned in the text).

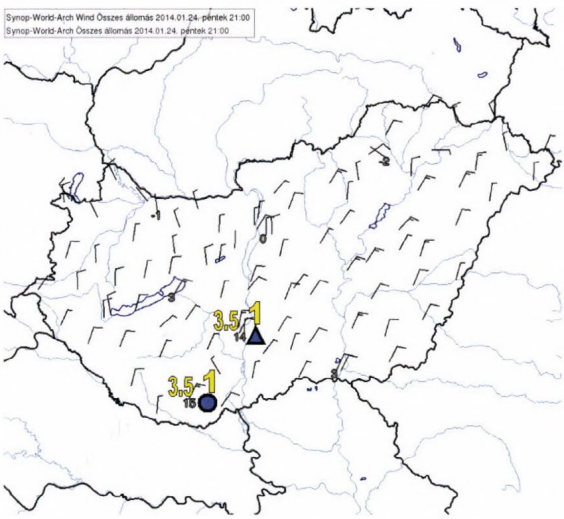

Fig. 17. As in *Fig. 13* except for January 24, 2014, 21:00 UTC. The BSI/WDI indices are valid for 20:40 UTC, the observations of drifting/blowing snow for 21:00 UTC (note that the station Pécs-Pogány reported blowing snow as well but only until 20:20 UTC).

The short-range ECMWF-based BSI forecasts showed maximum values exceeding 4 between Pécs and Paks but 3 hours later, on January 25, 2014, 00:00 UTC (*Fig. 18*). Evaluation of the BSI contributions showed that the temperature and snow-surface state were of at least same importance for snow-drift generation than wind, because the wind- and windgust speed were not as high as in the January 18, 2013 case (*Table 7*).

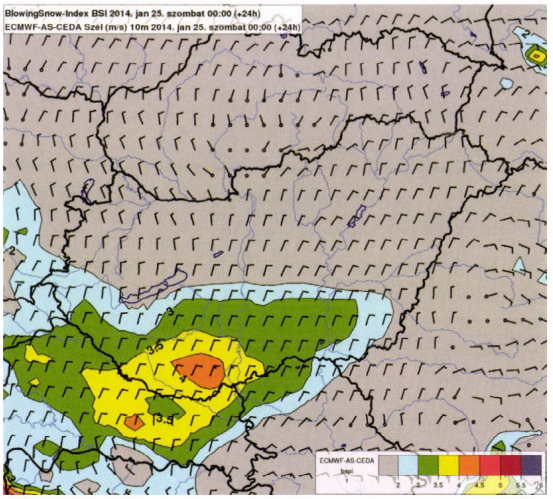

Fig. 18. As in *Fig. 12a* except for the 24-hour ECMWF forecast valid for January 25, 2014, 00:00 UTC.

Table 7. As in Table 4 but for the stations Pécs-Pogány and Paks, derived from the ECMWF 24 h forecast valid for January 25, 2014, 00:00 UTC.

Station	$f(T)$	$f(T_S)$	$f(U)$	$f(G)$	$f(H)$	$f(\rho_H)$	***BSI***	***WDI***
Pécs	0.63	1.0	0.44	0.70	0.5	0.83	4.1	1
Paks	0.56	0.97	0.17	0.38	0.3	0.83	3.2	1

5. Conclusion

The previous examples showed that the wet- and blowing snow occurrence is influenced by several factors (precipitation, wind, temperature) at once. Thus, foreseeing of such events only upon basic model outputs is not easy, and it requires a lot of forecasting experience and continuous study of typical synoptic

and mesosynoptic situations favorable for wet- or blowing snow. There could be, for example, cases with one dominant factor (e.g., very strong wind), when significant snowdrifts can develop even in areas, where there is currently no or only very weak snowfall. Or, there are limit cases, where existence of blowing snow is determined by reaching of some sufficient (but not extreme) intensity for all contributing parameters, including skin-surface temperature and snow density (which are generally rarely studied in forecasting practice). Thus, indices like BSI or snow sleeve diameter can help the forecaster to immediately turn attention to areas, where such conditions could appear providing guidance for further analysis of the potential causes of the event. Another advantage of these methods is that they are relatively simple from computational point of view (extraordinary computational time and power are not required) and can be easily applied on outputs of various NWP models.

The deficiency of the above-described diagnostic methods is that they can be interpreted or verified rather in qualitative sense. At Hungarian Meteorological Service, there is no parameter for blowing snow, which would forecast a directly measurable quantity (e.g., the height of the snowdrift), and such parameters are also not measured. Though, the statistically based BSI seems to be somewhat better in specifying the intensity of the event than indices based on arbitrary criterions (WDI). The BSI forecasts were also more consistent with the observed values than the simple WDI index in the evaluated cases. For future, it could be recommended to develop and test a "cumulative" form of BSI as well (e.g., a simple time-integral of this index), which could help to distinguish between short- and long-period blowing snow events, which can eventually cause especially high snowdrifts.

In contrary to blowing snow parameters, the algorithms for calculation of the wet snow mass on wires and diameter of snow accumulation give measurable quantities on outputs (although at the cost of several assumptions and simplifications). However, there are rarely precise reports based on such measurements in Hungary – generally no wet snow accumulation measurements are provided at the meteorological stations, estimates of the significance of wet snow loads can be currently done rather upon damage reports (e.g., from electricity companies) or upon photographs. The verification of the forecasts of wet snow or blowing snow parameters is further complicated by the fact that even observations of some "basic" input parameters (like precipitation type, snow depth, or snow density) are relatively sparse. These could be partially replaced by using interpolations or calculated from outputs of numerical models or nowcasting systems analyses – which is not an optimal solution, but even partial use of observations would still give better estimates of the real intensity of such events as if we would use only NWP model forecasts.

The determination of the type of precipitation and of the fraction of solid precipitation is very important for both blowing- and wet snow forecasting (essential for the latter one). It seems that numerical forecast of snowfall by

positive temperature is still difficult, even in LAM models which use parameterization of microphysical processes. Although, we tested only the scheme of Thompson, which is currently operationally used, and which was suggested in other winter precipitation studies (e.g., *Nygaard et al.*, 2011, *Podolskiy et al.*, 2012, *Liu et al.*, 2011). The inaccuracy of some forecast parameters (e.g. temperature) and of the model parameterizations can be one of the reasons, why relatively simple, empirical approaches (e.g., the $RT_{850/1000hPa}$ method) can be still more successful than criterions, based on the direct outputs of the model microphysics or precipitation schemes. Improved parameterization of the type of precipitation and of other characteristics (terminal velocity of snowflakes, collection coefficient, accreted snow density, etc.) is necessary to get quantitatively useful results. The accretion models (e.g., of the one described by Eq. 5) are often tested under laboratory conditions with nearly constant wind or density of the accreted snow. But even in such cases, it is difficult to directly measure some input characteristics, e.g., the collection coefficient. Although it was shown that the evaporation/condensation processes do not have substantial effect on the accreted snow diameter or snow mass (*Admirat*, 2008), it can be expected that (especially for long accretion periods) the changes of the snow density or fall speed of snowflakes can have a non-negligible impact on the forecast wet snow characteristics.

The analyses of the pressure, geopotential, and temperature fields in Section 3 indicate that there are some similarities in the macro- or mesosynoptic situations, in which the wet- or blowing snow appears in Hungary. The most typical feature is a deep cyclone with center over Italy or the Adriatic Sea moving (extending) toward east-northeast; a deep upper-air trough (eventually a cut-off low) surrounded by a jet and situated on the west-southwest flank of the surface cyclone (indicating a strongly meridional type of circulation). The blowing snow can develop in presence of a mesoscale, low-level jet, which was observed in other cases as well, e.g., during the March 14–15, 2013 blowing snow event in western Hungary (*Simon et al.,* 2013). Wet snow often appears at or behind the warm frontal boundaries characterized by large temperature gradients but sometimes also in the neighborhood of stationary occlusions at the rear side of the cyclone. Although the BSI and wet snow parameters were developed in order to make the recognition of wet- and blowing snow conditions easier, we are convinced that the knowledge of typical types of synoptic situations, favorable for such events, is also important for their successful forecasting and should be further studied.

Acknowledgements: The authors are indebted to *Attila Nagy* and *Kornél Locher* (HMS) for their support and for providing the NWP data. We are also grateful to *Jozef Csaplár* (SHMÚ) for additional information and for sending us useful materials. The study has been prepared in the frame of the COST Action ES1002 WIRE and INCA-CE (2CE120P3) CENTRAL EUROPE projects, with the support of the European Regional Development Fund.

References

Admirat, P., 2008: Wet Snow Accretion on Overhead lines. In: Atmospheric Icing of Power Networks. Springer Netherlands, 119-169.

Baggaley, D.G. and *Hanesiak, J.M.*, 2005: An Empirical Blowing Snow Forecast Technique for the Canadian Arctic and the Prairie Provinces. *Weather Forecast. 20*, 51–62.

Bonelli, P., Lacavalla, M., Marcacci, P., Mariani G., and *Stella, G.*, 2011: Wet snow hazard for power lines: a forecast and alert system applied in Italy. *Nat. Hazard. Earth Sys. 11*, 2419–2431.

Cantin, A. and *Bachand, D.*, 1993: Synoptic pattern recognition and partial thickness techniques as a tool for precipitation types forecasting associated with a winter storm. Centre Meteorologique du Quebec Tech. Note 93N-002.

Elíasson, Á.J., Ágústsson, H., and *Hannesson, G.M.*, 2013: Wet-Snow accumulation - A study of two severe events in complex terrain in Iceland. 15th IWAIS conference. St. John's, Newfoundland and Labrador, Canada.

E.O.N. Hungária Zrt., 2014: Összesített üzemzavari adatok 2014.01.24. 15:00 - 2014.01.26. 15:00 (in Hungarian)

Glickman, T.S. (ed.), 2000: Glossary of Meteorology, 2d. ed., American Meteorological Society, Boston.

Gulyás, K., Somfalvi-Tóth, K., and *Kolláth, K.*, 2012: A tapadó hó statisztikus-klimatológiai viszonyai hazánkban. *Légkör 57*, 49–54. (in Hungarian)

Hirsch, T., 2006: Téli magyarországi nagy csapadékos helyzetek vizsgálata és előrejelzése. PhD thesis. ELTE, Budapest. (in Hungarian)

Hong, S.Y., Noh Y., and *Dudhia J.*, 2006: A new vertical diffusion package with an explicit treatment of entrainment processes. *Month. Weather Rev. 134*, 2318–2341.

ISO, 2001: Atmospheric icing of structures. International Standardization Organisation (ISO) International Standard 12494, Geneva, Switzerland.

Kolláth, K., 2013: 2013.02.07. Tapadó hó. Website http://mrstratus.blogspot.hu/2013/02/20130207-tapado-ho.html (in Hungarian).

Li, L. and *Pomeroy, J.W.*, 1997: Probability of occurrence of blowing snow. *J. Geophys. Res. 102*, 21955–21964.

Liu, C., Ikeda, K., Thompson, G., Rasmussen, R., and *Dudhia, J.*, 2011: High-Resolution Simulations of Wintertime Precipitation in the Colorado Headwaters Region: Sensitivity to Physics Parameterizations. *Month. Weather Rev. 139*, 3533–3553.

Makkonen, L., 1989: Estimation of wet snow accretion on structures. *Cold Reg. Sci. Technol. 17*, 83–88.

Makkonen, L. and *Wichura, B.* 2010: Simulating wet snow loads on power line cables by a simple model. *Cold Reg. Sci. Technol. 61*, 73–81.

Nygaard, K., Egil, B., Kristjánsson, J.E., and *Makkonen, L.*, 2011: Prediction of In-Cloud Icing Conditions at Ground Level Using the WRF Model. *J. Appl. Meteorol. Climatol. 50*, 2445–2459.

Nygaard, K., Egil, B., Ágústsson H., and *Somfalvi-Tóth K.*, 2013: Modeling Wet Snow Accretion on Power Lines: Improvements to Previous Methods Using 50 Years of Observations. *J. Appl. Meteorol. Climatol. 52*, 2189–2203.

Persson, A., 2011: User guide to ECMWF forecast products. Meteorological Bulletin M3.2, ECMWF.

Pilis parkerdő, 2013: Hótörés a Pilisben – balesetveszélyes az erdő Website, http://www.parkerdo.hu/index.php?pg=news_1_667. (in Hugarian)

Podolskiy, E.A., Nygaard, B.E.K., Nishimura, K., Makkonen, L., and *Lozowski, E.P.*, 2012: Study of unusual atmospheric icing at Mount Zao, Japan, using the Weather Research and Forecasting model, *J. Geophys. Res.: Atmospheres, 117(D12)*, 1984–2012.

Poots, G., 1996: Ice and snow accretion on structures. Research Studies Press Ltd. – Wiley, Taunton, England.

Railpage.net, 2013: Sneh opäť ochromil železničnú dopravu. Website http://www.railpage.-net/modules/news/article.php?storyid=2560. (in Slovak)

Sakamoto, Y., 2000: Snow accretion on overhead wires. *Philos. T. R. Soc. Lon. A 358(1776)*, 2941–2970.

Simon, A., Kolláth, K., Somfalvi-Tóth, K., Dezső, Zs., and *Tordai, J.*, 2013: A 2013-as év veszélyes időjárási jelenségei. Presentation. *39. Meteorológiai Tudományos Napok*, 2013. November 21–22. http://www.met.hu/doc/rendezvenyek/metnapok-2013/21_Simon.pdf. (in Hungarian)

Skamarock, W.C., Klemp, J.B., Dudhia, J., Gill, D.O., Barker, D.M., Duda, M.G., Huang, X.-Y., Wang, W., and *Powers, J.G.*, 2008: A description of the Advanced Research WRF version 3. *NCAR Technical Note NCAR/TN-475+STR.*

Somfalvi-Tóth, K., 2014: *Tapadó hó számolása HAWK3-ban.* Technical report, OMSZ. (in Hungarian),

Sundin, E. and *Makkonen, L.*, 1998: Ice Loads on a Lattice Tower Estimated by Weather Station Data. *J. Appl. Meteorol. 37*, 523–529.

Thompson, G., Rasmussen, R.M., and *Manning, K.*, 2004: Explicit forecasts of winter precipitation using an improved bulk microphysics scheme. Part-I: Description and sensitivity analysis. *Mont.Weather Rev. 132*, 519–542.

Tordai, J., 2012: A hófúvás előrejelzése Magyarország térségére. MSc thesis, ELTE, Budapest. (In Hungarian)

Tóth, K., Lakatos M., Kolláth K., Fülöp R., and *Simon A.*, 2009: Climatology and forecasting of severe wet-snow icing in Hungary. In: Proceedings of the 13th International Workshop on Atmospheric Icing of Structures, IWAIS 2009 and the Final Workshop of the COST Action 727 "Measuring and Forecasting Atmospheric Icing on Structures". Andermatt, Switzerland, 8–11 September 2009.

WMO, 1995: *WMO* Manual on codes. International Codes VOLUME I. 1 Part A — Alphanumeric Codes. WMO–No. 306.

Yuter, S.E., Kingsmill, D.E., Nance, L.B., and *Löffler-Mang, M.*, 2006: Observations of precipitation size and fall speed characteristics within coexisting rain and wet snow. *J. Appl. Meteorol. Climatol. 45*, 1450–1464.

INSTRUCTIONS TO AUTHORS OF *IDŐJÁRÁS*

The purpose of the journal is to publish papers in any field of meteorology and atmosphere related scientific areas. These may be

- research papers on new results of scientific investigations,
- critical review articles summarizing the current state of art of a certain topic,
- short contributions dealing with a particular question.

Some issues contain "News" and "Book review", therefore, such contributions are also welcome. The papers must be in American English and should be checked by a native speaker if necessary.

Authors are requested to send their manuscripts to

Editor-in Chief of IDŐJÁRÁS
P.O. Box 38, H-1525 Budapest, Hungary
E-mail: journal.idojaras@met.hu

including all illustrations. MS Word format is preferred in electronic submission. Papers will then be reviewed normally by two independent referees, who remain unidentified for the author(s). The Editor-in-Chief will inform the author(s) whether or not the paper is acceptable for publication, and what modifications, if any, are necessary.

Please, follow the order given below when typing manuscripts.

Title page: should consist of the title, the name(s) of the author(s), their affiliation(s) including full postal and e-mail address(es). In case of more than one author, the corresponding author must be identified.

Abstract: should contain the purpose, the applied data and methods as well as the basic conclusion(s) of the paper.

Key-words: must be included (from 5 to 10) to help to classify the topic.

Text: has to be typed in single spacing on an A4 size paper using 14 pt Times New Roman font if possible. Use of S.I. units are expected, and the use of negative exponent is preferred to fractional sign. Mathematical formulae are expected to be as simple as possible and numbered in parentheses at the right margin.

All publications cited in the text should be presented in the *list of references*, arranged in alphabetical order. For an article: name(s) of author(s) in Italics, year, title of article, name of journal, volume, number (the latter two in Italics) and pages. E.g., *Nathan, K.K.,* 1986: A note on the relationship between photosynthetically active radiation and cloud amount. *Időjárás 90,* 10-13. For a book: name(s) of author(s), year, title of the book (all in Italics except the year), publisher and place of publication. E.g., *Junge, C.E.,* 1963: *Air Chemistry and Radioactivity.* Academic Press, New York and London. Reference in the text should contain the name(s) of the author(s) in Italics and year of publication. E.g., in the case of one author: *Miller* (1989); in the case of two authors: *Gamov* and *Cleveland* (1973); and if there are more than two authors: *Smith et al.* (1990). If the name of the author cannot be fitted into the text: *(Miller,* 1989); etc. When referring papers published in the same year by the same author, letters a, b, c, etc. should follow the year of publication.

Tables should be marked by Arabic numbers and printed in separate sheets with their numbers and legends given below them. Avoid too lengthy or complicated tables, or tables duplicating results given in other form in the manuscript (e.g., graphs).

Figures should also be marked with Arabic numbers and printed in black and white or color (under special arrangement) in separate sheets with their numbers and captions given below them. JPG, TIF, GIF, BMP or PNG formats should be used for electronic artwork submission.

More information for authors is available: journal.idojaras@met.hu

Published by the Hungarian Meteorological Service

Budapest, Hungary

INDEX 26 361

HU ISSN 0324-6329